: Uncooled bolometer based on La0.7Sr0.3MnO3 thin films: Thermal model, electrical and optical characterizations

Ammar Aryan

UNIVERSITE DE CAEN BASSE-NORMANDIE

UFR Sciences

Ecole doctorale **SIMEM**

Thèse de doctorat

Présentée et soutenue le : **08 Juillet 2013**

par

Ammar ARYAN

pour obtenir le

Doctorat de l'Université de Caen Basse-Normandie

Spécialité : Électronique, microélectronique et nanoélectronique

Arrêté du 07 août 2006

Bolomètres non refroidis à base de $La_{0,7}Sr_{0,3}MnO_3$: modèle thermique, caractérisations électrique et optique

Directeur de thèse : **M. Jean-Marc ROUTOURE**
Co-directeur de thèse : **Mme. Laurence MECHIN**

Membres du jury

M. Alain GIANI, Professeur des universités, UM2/IES Montpellier, (Rapporteur)
M. François PESTY, Maître de conférences, Université Paris Sud / LPS Orsay (Rapporteur)
M. Didier ROBBES, Professeur des universités, UNICAEN (Examinateur)
M. Geoffroy KLISNICK, Maître de conférences, UPMC - Paris 6/ L2E (Examinateur)
M. Jean-Marc ROUTOURE, Professeur des universités, UNICAEN (Directeur de thèse)
M. Bruno GUILLET, Maître de conférences, UNICAEN (Encadrant)

To the memory of my father
To my mother, sisters, and brothers
To my wife and my kids

Acknowledgment

It is my pleasure to acknowledge the many people who helped me directly or indirectly during this work. To start with, I would like to thank all my supervisors for their support during this work. I would like to thank especially Jean-Marc Routoure and Laurence Méchin for their guidance, suggestions and new ideas throughout this work.

I extend my sincere thanks to all persons of the electronic group at GREYC laboratory for the warm atmosphere that I found during my stay in the laboratory. Special thanks to Mr. cedric Fur for the fabrication of all my tested samples. Also, thanks for Slyvain Lebargy, Julien Gasnier, and Philippe Poupard for their helpful technical intervention. I am most grateful to Nicole Delamotte for her assistance and administrative support.

I would also want to thank all of my present and former colleagues at the Electronic group: Olivier, Basile, Rimond, Rachida, Hakim, Maria, Alice, Geeta, Dalal, Sheng, Shuang, Xin, Kamel. All of you have contributed to this work in your own way.

Finally, it is my pleasure to express my sincere gratitude to my kids: Sama, Sara and Karam for the joy and happiness they offered me, and to my wife Tharwa whose understanding made this study possible.

Thank you all.

Ammar ARYAN

Caen, France

July 2013

TABLE OF CONTENTS

Table of contents

Table of contents

INTRODUCTION

GENERAL INTRODUCTION

Uncooled infrared (IR) detectors have been studied in recent years due to a wide range of applications such as thermal cameras, night vision cameras, thermal sensors, surveillance, etc. The IR detectors are generally classified into photon detectors and thermal detectors. The choice of detector type depends on the intended application. Achieving higher performance, like high response speed or high responsivity, is associated to higher cost. Each type of detector has its specific characteristics depending on the detection mechanism and material properties. This result in advantages and disadvantages for each type of detector when it is used in field applications.

Photon detector converts photon energy directly into electrical signal. Thermal detector, on the other hand, has a temperature-sensitive electrical property. The photon detectors have high signal to noise ratio and very fast response, but most of them require a cooling system, which is heavy and expensive. In contrast, most of thermal detectors operate at room temperature even for far IR radiation, thus reducing the cost of operation and then they can be used for commercial hand-held infrared applications. Even if their response time is still larger than that of photon detectors; they have no limitation on the wavelength response. Thermal detectors achieve lower responsivity than photon detectors, but they exhibit lower cost and better ease of use. They have found widespread use in low cost applications, which do not require high performance and speed.

Thermal detectors are based on three different approaches, namely, bolometers, pyroelectric and thermoelectric effects. Uncooled microbolometers take a large part of infrared imaging application business. A bolometer is a thermal detector whose electrical resistance changes as a function of radiant energy. So, the larger the resistance changes, the higher the Temperature Coefficient of Resistance (TCR), and the higher the responsivity.

The present efforts in infrared detector researches are directed towards improving the performance of room temperature infrared detectors. This includes elaborating a new sensing material and developing enhanced pixel geometries and thermal isolation. The recent advances in microelectromechanical systems (MEMS) technology allow fabricating sensitive thermal bolometric detectors. Since the discovering of the first bolometer in 1880, many materials have been investigated as IR active layer of the bolometer. The most commonly used materials as thermometer in uncooled bolometers are metals (like Pt and Ti), vanadium oxides (VO_x), and the amorphous semiconductor films.

Other existing promising bolometer materials are manganese oxides. It has been realized that these materials have a promising potential for bolometric infrared detection. The large change of their electrical resistance at the metal-to-insulator transition, which takes place for some materials at or around 300 K, makes them potential materials for the fabrication of uncooled thermal detectors. Thus, many experimental and theoretical efforts have been recently devoted to the study of these materials.

Preliminary results in our laboratory, GREYC, showed that the manganese oxide $La_{0.7}Sr_{0.3}MnO_3$ (LSMO) is a competitive candidate for uncooled thermal detector. Even if it does not exhibit the highest TCR values at room temperature, compared to other possible manganite compositions, we study LSMO because it shows low 1/f noise at the metal-to-insulator transition. In addition, good quality LSMO films deposited on silicon substrates were realized, which enables the compatibility with silicon microelectronic fabrication process and makes possible development of more complex systems.

The aim of this thesis is to evaluate LSMO thin films as room temperature radiation detector, and then optimize its performance in terms of geometry. I will first try to propose a detailed thermal model of “thin-film-on-substrate” structure, which has to interpret the variation of the optical voltage responsivity versus the modulation frequency of a heating radiation power. This model will be then analyzed and validated using the measurement results of many detection surfaces and substrate materials. I will try here to investigate the effect of film-substrate interface thermal resistance on this performance, and try to estimate its value for different substrate materials. Once the model is validated, it can be used to optimize the detector geometry and estimate its performance for any pixel surface, and maybe for other substrate material. Then I will study the role of detector geometry and substrate material on the detector’s performance, therefore, optimizing the detector geometry to achieve an optimal performance for the intended application. Indeed, achieving the measurement of the optical responsivity of LSMO films implies design and realize an optical measurement test stand. This involves expertise optics, optoelectronics, signal conditioning, and instrumentation knowledge.

In the first chapter, I will present the fundamentals of infrared detectors, with introducing the principle of IR radiation and detectors. Then, the thermal detector types and principle of operation will be given. Also, a detailed discussion of bolometer (principle, types, model, and figures of merit) will be presented. I will also introduce the different fundamental properties of the LSMO material. This includes its structure, transport properties, and thermal

properties. Finally, a state of the art of the performance of uncooled bolometers will be exposed.

Chapter II is devoted to present a detailed explanation of the measurement setup, including the design considerations and background principles. The characteristics of all components of this setup, like the current source and the amplification stage, will be explored in details. This setup has been used during the thesis to characterize the LSMO samples as thermal radiation detector. This includes the measurement of the optical responsivity and the noise for each sample in order to estimate the classical figures of merit such as noise equivalent power and specific detectivity. At the end of this chapter, I will provide a detailed list of all the tested samples, including samples fabricating using the old and the new mask.

In the beginning of chapter III an explanation of the used practical method to characterize a thin film bolometer made on a substrate will be presented. This methodology intends to explore thermal and electrical parameters needed to qualify the performance of the bolometer by indentifying the figures of merit. Then, a detailed discussion on the thermal model of thin film on substrate will be offered. This includes presenting the heat diffusion into substrate, the thermal boundary resistance between film and substrate, the thermal properties of the different materials that were used in our samples. Finally, analysis and experimental validation of the proposed model for film-on-substrate structure will be given. I then will study the influence of substrate material on the parameters that characterize the bolometer. Thus, a whole paragraph of this chapter is devoted to analyze the effect of pixel geometry on the performance of a bolometer, using the measurement results and calculation data issued from the proposed thermal model. The geometry parameters include pixel surface, film thickness, and number of strips.

This page has been left blank intentionally

CHAPTER I

Uncooled infrared detectors

1. Fundamentals of Infrared detectors

1.1. Infrared radiation

1.1.1. Infrared spectra

The Infrared (IR) radiation is an electromagnetic radiation in the wavelength (λ) range between visible radiation (λ = 380-780 nm) and microwave radiation (see Figure 1-1). It was discovered in 1800 by the British astronomer William Herschel [1]. He passed sunlight through a prism to separate the light into its spectrum as usual. Then, he observed that when a thermometer is placed below the red light region, the temperature increases. He thus predicted that the reason was an invisible radiation, which he called “infrared” using the Latin word “infra” for “below”. After that, many researches had been attempted to detect the IR radiation energy.

In 1821 Seebeck discovered the thermoelectric effect (*Seebeck effect*) from the ends of connection of two different wires, later called thermocouple. Later, using this thermoelectric effect, the first thermopile was demonstrated by Nobili in 1829 by connecting a number of thermocouples in series.

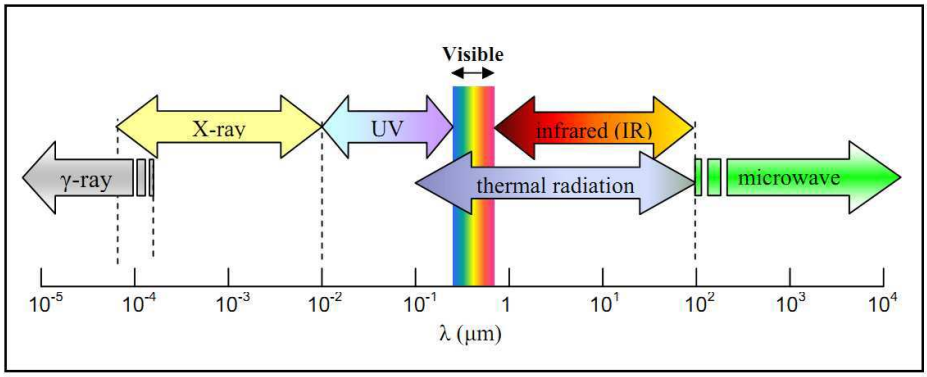

Figure 1-1. Spectra of electromagnetic radiation [2]

1.1.2. Infrared light types

The infrared range covers all electromagnetic radiation longer than the visible and shorter than millimeter waves (see Figure 1-1). Many proposals in the division of IR range have been published, and these shown in Table 1-1 are based on limits of spectral bands of commonly used IR detectors [3][4]. The wavelength of 1 μm is a sensitivity limit of Si

detectors. Similarly, the wavelength 3 μm is a wavelength sensitivity of PbS and InGaAs detectors. Wavelength 6 μm is a sensitivity limit of InSb, PbSe, PtSi detectors, and HgCdTe detectors optimized for a 3–5 μm atmospheric window. Finally, wavelength 15 μm is the wavelength sensitivity limit of HgCdTe detectors optimized for 8–14 μm range [1].

The near infrared is used in telecommunications and is itself subdivided into several regions. Short and medium wavelength infrared can be used to detect some gases. Long wavelength infrared finds its main use in thermal imaging.

Table 1-1. Division of Infrared radiation [3]

Region (Abbreviation)	Wavelength λ(μm)
Near Infrared (NIR)	0.78-1
Short wavelength Infrared (SWIR)	1-3
Medium wavelength Infrared (MWIR)	3-6
Long wavelength Infrared (LWIR)	6-15
Very Long wavelength Infrared (VLWIR)	15-30
Far Infrared (FIR)	30-100
Submillimeter (SubMM)	100-1000

1.1.3. Atmospheric Transmission

Infrared radiation emitted by distant objects generally has to traverse through some distance in air before being detected by infrared detectors. However, being influenced by dispersion and absorption of air molecules (H_2O, CO_2), the energy that can be detected decreases as distances increase.

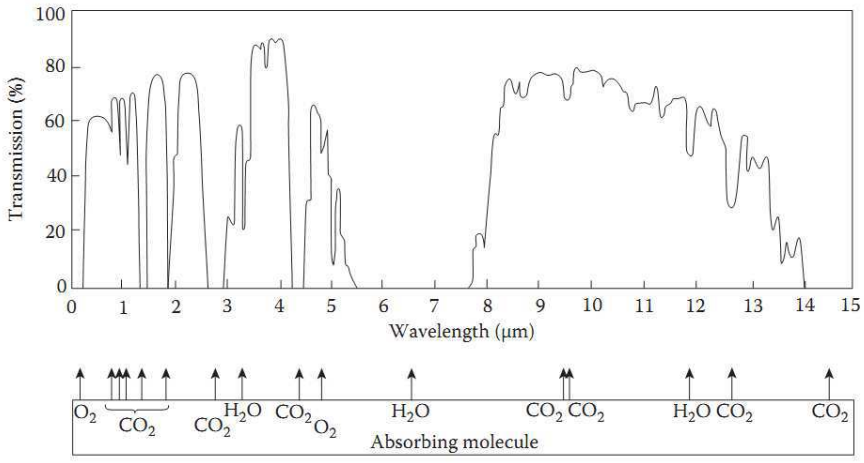

Figure 1-2. Atmospheric transmission spectra [3]

Figure 1-1 shows the transmitting characteristics of visible to infrared radiation through the atmosphere as a function of wavelength [3]. Specific absorption bands of water, carbon dioxide, and oxygen molecules are indicated, which restricts atmospheric transmission to two windows at 3–5 μm and 8–14 μm.

1.1.4. Radiation laws

In 1879, Joseph Stefan concluded from experimental data that the power transferred between two bodies was proportional to the difference of the fourth power of their temperature, a result later theoretically proven by Ludwig Boltzmann in 1884 [5]. In 1896, Wilhelm Wien experimentally found that the wavelength of maximum radiation, λ_{max}, of a blackbody is inversely proportional to its absolute temperature [6]. This relation, known as Wien's displacement law, is given by:

$$\lambda_{max}\, T = 2898 \ \ [\mu m \cdot K] \qquad \text{(I- 1)}$$

In 1901 Max Planck had published the correct blackbody radiation law. It describes the spectral radiance of the electromagnetic radiation emitted by a perfect blackbody as function of its temperature (T) and the wavelength (λ) of the emitted radiation, and is in the form,

$$M(\lambda, T) = \frac{2\pi h c_0^2}{\lambda^5}\left[\exp\left(\frac{h c_0}{\lambda\, k_B T}\right) - 1\right]^{-1} \ \ [W \cdot m^{-3}] \qquad \text{(I- 2)}$$

Where h is the Planck's constant, c_0 is the velocity of light in vacuum, k_B is the Boltzmann's constant. According to the Planck's radiation law, all objects having a surface temperature above 0 K emit infrared radiation. The power and the spectral content of the emitted radiation are determined by the temperature of the object. With an increasing object temperature, the peak of the emitted radiation shifts towards shorter wavelengths. The blackbody is an ideal object that absorbs all radiation, which is incident on it, and the radiation thus emitted is known as blackbody radiation (Figure 1-3). For example, a normal light bulb emits radiation with a color temperature of about 3000 K, which corresponds to a peak wavelength of 970 nm. A normal human has a body temperature of about 37 °C and a skin temperature of about 34 °C. Maximization of the radiation emitted by a human will therefore occur at wavelengths of around 10 μm [4].

The total radiation energy of a blackbody can be expressed by Stefan-Boltzmann law:

$$E_b(T) = \int_0^\infty M(\lambda, T)\, d\lambda \;=\; \sigma_{SB}\, T^4 \quad [W{\cdot}m^{-2}] \tag{I-3}$$

where σ_{SB} is called the Stefan–Boltzmann constant and has an approximate value of 5.67×10^{-8} $W{\cdot}m^{-2}{\cdot}K^{-4}$. From Equation (I-3), total radiation energy can be calculated given the absolute temperature T.

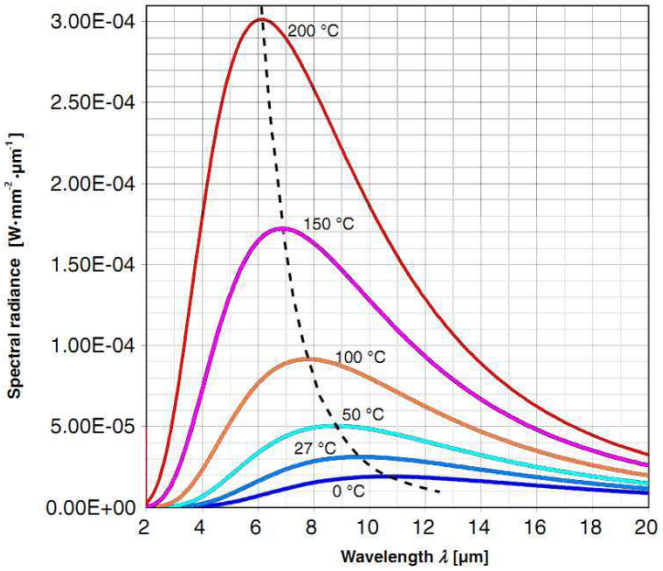

Figure 1-3. Blackbody radiation versus wavelength. The dashed line marks Wien's displacement law [4]

1.1.5. Infrared applications

Infrared detection technology is employed in a wide range of applications in a variety of areas, like medical, industrial and military. Radiation can be detected either quantitatively or qualitatively. Radiometry is the quantitative determination of the absolute amount of radiation present via temperature (pyrometry) or as a spectral distribution (spectroscopy). Thermal imaging, on the other hand, typically relies on qualitative detection of radiation, in which images are obtained using thermal contrast.

Applications of thermal imaging systems are vast. Military applications include battlefield surveillance, minefield detection. In the medical field, IR detection can be used to analyze blood flow, observe muscular functions for physical therapy, image wounds or burns, determine body temperature, or locate tumors. Industrial applications include monitoring equipment, circuit boards, piping, furnaces, insulation coverage [1],[3]-[5]. Finally, other

important infrared techniques and devices are: non-contact thermometers, radiometers, and NDIR gas sensors.

1.2. Radiation detectors

1.2.1. Brief history

Many materials have been investigated as IR detector. A simple theorem, after Norton [1], can be stated: "All physical phenomena in the range of about 0.1-1 eV will be proposed for IR detectors". Among these effects are: thermoelectric power (thermocouples), change in electrical conductivity (bolometers), gas expansion (Golay cell), pyroelectricity (pyroelectric detectors), fundamental absorption (intrinsic photodetectors), impurity absorption (extrinsic photodetectors), low dimensional solids (superlattice, quantum well and quantum dot detectors), different types of phase transitions, etc.

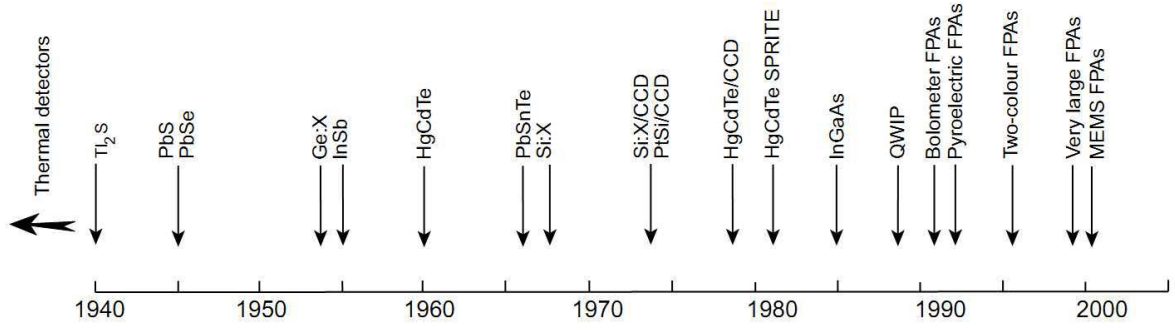

Figure 1-4. History of the development of infrared detectors and systems [1]

Figure 1-4 gives approximate dates of significant development efforts for the materials mentioned above. The birth of modern IR detector technologies was during the World War II. The development of high performance infrared detectors has been made over the last six decades. Photon IR technology combined with semiconductor material science, and the development of photolithography technology for integrated circuits, have boosted many advances in IR capabilities within a short time period during the last century [1].

1.2.2. Classification of infrared detectors

A radiation detector must have the ability to convert the energy associated with incident electromagnetic radiation into an electrical signal. Infrared detectors are generally classified into two main groups, namely photon detectors (also called quantum detectors) and thermal detectors. The choice of detector very much depends on the intended applications.

Some applications require a high response speed and high responsivity, whereas others can settle for lower speed and responsivity, but at a lower cost.

Photon detectors convert photons energy directly into free current carriers by photoexciting electrons across the energy bandgap of the detector material. This produces a current, voltage or resistance change of the detectors. To achieve this, the received photons energy must be greater than the energy bandgap [8]. Therefore, the energy bandgap of the detector material determines its cut-off wavelength.

Photon detectors depend on the wavelength of the incident radiation. Hence, it has a narrow and selective spectral response. In contrast, thermal detectors are wavelength independent because the signal does not depend on the photon nature of the radiation, thus they have flat and wide spectral response. Furthermore, photon detectors have a higher sensitivity and faster response in comparison with thermal detectors (see Figure 1-5). Indeed, most photon detectors require a cooling system, while most thermal detectors operate at room temperature even for far IR radiation. The cooling of detectors reduces thermal generation of charge carriers, but adds to the system bulk and weight, and tends to increase system cost.

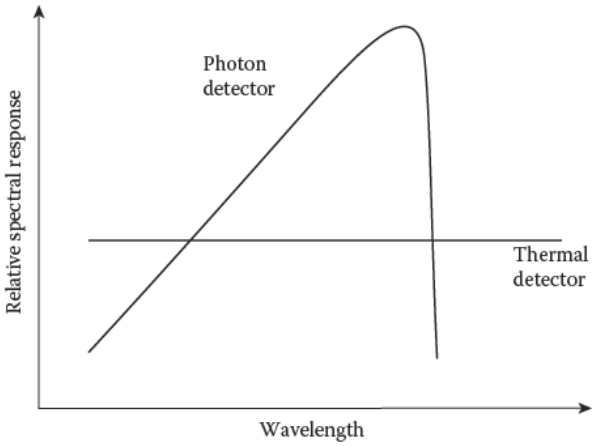

Figure 1-5. Relative spectral response of thermal and photon detector [9]

Depending on the detection mechanism, nature of interaction and material properties, the various types of detectors have their own characteristics. These characteristics result in advantages and disadvantages when the detectors are used in field applications. Table 1-2 shows a comparison of various IR detectors.

Table 1-2. Comparison of infrared radiation detectors; adapted from[3]

Type		Principles	Materials	Advantages	Disadvantages
THERMAL	**thermocouple /thermopile**	induced thermoelectric voltage	BiTe-TiSbTe poly-Si	- low cost - operated in room temperature - rugged system	- slow response time (order ms) - low detectivity at high frequency
	pyroelectric	change of polarization or charge	$(Ba,Sr)TiO_3$ $Pb(Sc_{0.5}Ta_{0.5})O_3$, $LiTaO_3$		
	bolometer	electrical conductivity change	VO_x a-Si SiGe manganite oxide		
PHOTON	**intrinsic**	optical excitation of free carriers (electron or hole) photoconductive or photovoltaic effect	IV-VI (PbS, PbSe,PbSnTe) II-VI (HgCdTe) III-V (InGaAs, InAs, InSb, InAsSb)	- stable material	- high thermal expansion coefficient - large permittivity - Nonuniformity over large area - High cost in growth & processing - Surface instability - Heteroepitaxy with large lattice mismatch
	extrinsic		Si:Ga Si:As Ge:Cu Ge:Hg	- detect long wavelength - simple technology	- high thermal generation - operated at very low temperature
	free carrier		PtSi Pt_2Si IrSi	- low cost - Large 2D arrays - high yield	- low efficiency - low temperature operation
	quantum wells		Type I (GaAs/AlGaAs, InGaAs/AlGaAs)	- matured material - Good uniformity over large area - multi color	- high thermal generation - complicated design - films growth difficulty
			Type II (InAs/InGaSb, InAs/InAsSb)	- low Auger recombination rate - easy wavelength Control - Multicolor detectors	
	quantum dots		InAs/GaAs InGaAs/InGaP Ge/Si	- low thermal generation - Normal incidence of light	- complicated design - films growth difficulty

1.3. Performance parameters

There are many parameters that are used to describe the detector performance. These parameters are usually defined in terms of radiometric inputs and detector outputs. These parameters are [3][8]: responsivity, noise, specific detectivity, and noise equivalent power.

However, to provide ease of comparison between detectors, certain figures of merit, computed from the measured data, will be defined in this section.

1.3.1. Responsivity

The responsivity of an IR detector is defined as the ratio of the value of the electrical output signal of the detector to the value the input radiation power. The units of responsivity are volts per watt ($V \cdot W^{-1}$) or amperes per watt ($A \cdot W^{-1}$). The responsivity is usually a function of the bias voltage or current, the operating frequency, and the wavelength.

1.3.2. Noise & Noise Equivalent Power

In this document, noise refers to an electrical signal that perturbs the desired signal. The ability of a radiation detector to detect an incoming light signal is limited by the intrinsic fluctuations, or noise, both of incoming light itself and of the background electrical current fluctuations generated by the detector. If the noise signal is too high, it can obscure or completely hide the signal.

The noise equivalent power (NEP) is the incident power on the detector generating a signal output equal to the rms noise output. Stated another way, the NEP is the signal level that produces a signal-to-noise ratio (SNR) of 1. It can be written in terms of responsivity as,

$$\text{NEP} = \frac{\text{noise spectral density}}{\text{responsivity}} \qquad \text{(I-4)}$$

The NEP is quoted for a fixed reference bandwidth, which is often assumed to be 1 Hz. This “NEP per unit bandwidth” has a unit of watts per square root hertz ($W \cdot Hz^{-1/2}$).

1.3.3. Signal to noise ratio and detectivity

The signal to noise ratio (S/N) is a simple way to describe the “cleanliness” of a given signal level. It is simply the signal voltage divided by the root mean square noise voltage. However, the S/N does not characterize the detector itself: we can get a better S/N for same detector just by applying a higher incidence level. The most commonly used parameter to characterize the minimum power a sensor can detect is the specific detectivity (D*). D* is the signal to noise ratio that would result if the performance of detector were scaled to a detector of standard size, under standard test conditions:

$$D^* = \frac{\sqrt{\text{detector area}}}{\text{NEP}} \qquad \text{(I-5)}$$

The significance of D* is that this figure of merit permits a comparison of detectors that have different areas. D* is expressed by the unit $cm \cdot Hz^{1/2} \cdot W^{-1}$, which has also been called a "Jones." [3], where the detector area is expressed in cm^2.

1.4. Comparison of radiation detectors

Spectral detectivity (cf. paragraph 1.4.3) curves for a number of commercially available IR detectors are shown in Figure 1-6. Interest has centered mainly on the wavelengths of the two atmospheric windows 3–5 µm and 8–14 µm, though in recent years there has been increasing interest in longer wavelengths stimulated by space applications.

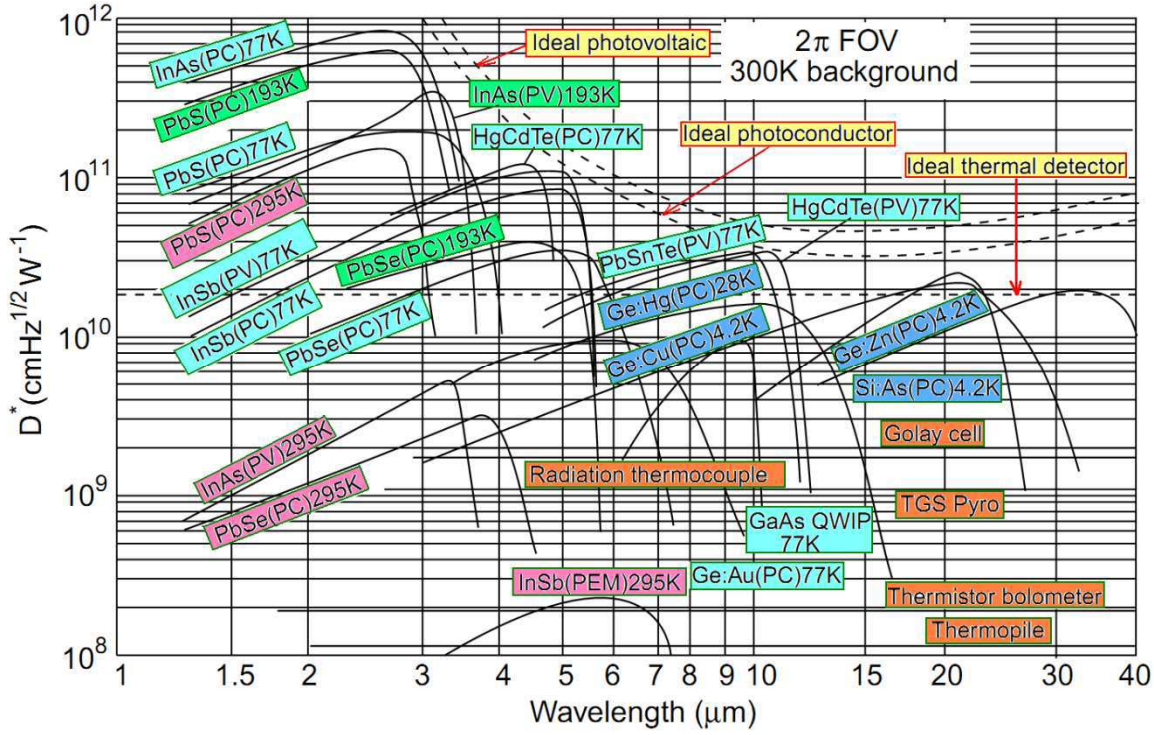

Figure 1-6. Comparison of specific detectivity, D, of various commercially available infrared detectors when operated at the indicated temperature. Chopping frequency is 1000 Hz for all detectors except the thermopile (10 Hz), thermocouple (10 Hz), thermistor bolometer (10 Hz), Golay cell (10 Hz) and pyroelectric detector (10 Hz). Each detector is assumed to view a hemispherical surrounding at a temperature of 300K. Theoretical curves for the background-limited D* (dashed lines) for ideal photovoltaic and photoconductive detectors and thermal detectors are also shown. PC-photoconductive detector, PV-photovoltaic detector, and PEM-photoelectromagnetic detector. [4]*

As seen in this figure, a color code was used to distinct working temperature of detectors. Indeed, cooled detectors show the best performance. Room temperature detectors (rose color) are centered mainly in short wavelength infrared. For higher wavelength, cooled detectors are still dominant. The best uncooled detector (PbS) achieves a specific detectivity more than 10^{11} cm·Hz$^{1/2}$·W^{-1} in 1.5–3 µm wavelength range. Thermal detectors are less sensitive and slower than photon detectors, but they may have a sensibility over a wide range of wavelengths.

2. Infrared thermal detectors

Up until the 1990s, thermal detectors have been considerably less exploited in commercial and military systems in comparison with photon detectors. In the last decade, however, it has been shown that extremely good imagery system can be obtained from large thermal detector arrays operating uncooled at TV frame rates [1]. The use of modern microelectronic and micromechanical manufacturing methods has resulted in a rapid development of miniaturized and high-resolution detectors that are inexpensive and open up an ever increasing number of new application areas, such as thermography.

2.1. Principe and operation

In a thermal detector**,** the incident radiation is absorbed to change the material temperature and the resultant change in some physical property is used to generate an electrical output. The signal does not depend upon the photonic nature of the incident radiation. Thus, thermal effects are generally wavelength independent (see Figure 1-5); the signal depends upon the radiant power (or its rate of change) but not on its spectral content. Attention is directed toward three approaches that have found the greatest utility in infrared technology, namely, bolometers, pyroelectric, and thermoelectric effects [1][3]. In contrast with photon detectors, thermal detectors are typically operated at room temperature. They are usually characterized by modest sensitivity and slow response (because heating and cooling of a detector element is a relatively slow process), but they are cheap and easy to use. They have found widespread use in low cost applications, which do not require high performance and speed. Being unselective, they are frequently used in IR spectrometers. A list of thermal effects related to each thermal detector is listed in Table 1-3.

Table 1-3. Infrared Thermal detectors [3]

Detector	Method of operation
Bolometer	Change in electrical conductivity
Thermocouple/thermopile	Voltage generation, caused by change in temperature of the junction of two dissimilar materials
Pyroelectric	Change in spontaneous electrical polarization
Golay cell	Thermal expansion of a gas

The simplest representation of the thermal detector is shown in Figure 1-7. The detector is represented by the thermal capacitance C coupled via the thermal conductance G to a heat sink at the constant temperature T_0. When a radiation input is received by the detector, the rise in temperature is found by solving the heat balance equation. The change in temperature of any thermal detector due to incident periodic radiant power is ΔT.

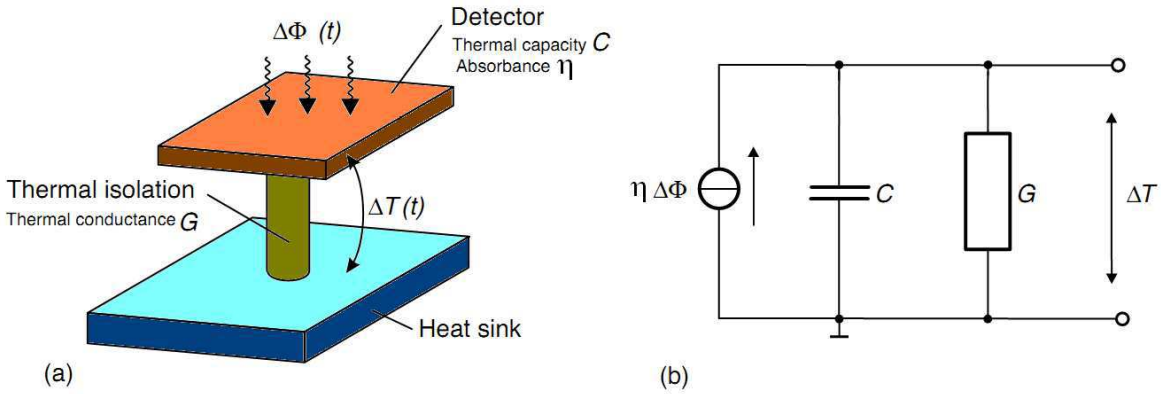

Figure 1-7. Simple model of a thermal IR detector. (a) Principle; (b) thermal model; adapted from [4]

Here, ΔT presents the temperature difference due to modulated IR radiation signal $\Phi = \Phi_0 \mathrm{Exp}(j\omega t)$, of power amplitude Φ_0 , and is given by [3][5]:

$$\Delta T(\omega) = \frac{\eta \Phi_0}{(G^2 + \omega^2 C^2)^{1/2}} \qquad \text{(I- 6)}$$

Equation (I- 6) illustrates that, at low frequency, a more sensitive thermal detector can be achieved if its thermal coupling to its surroundings (G) might be as small as possible.

A characteristic thermal response time for the detector can therefore be defined as:

$$\tau = \frac{C}{G} \qquad \text{(I- 7)}$$

Typical value of thermal time constant for thermal detectors is in the millisecond range, which is much longer than the typical time of photon detectors (microsecond range). There is a trade-off between sensitivity, ΔT, and frequency response. If one wants a high sensitivity, then a low frequency response is forced upon the detector.

Several physical mechanisms can be used to measure this change in temperature. The main types of thermal detectors are briefly described below.

2.2. Thermocouples/Thermopiles

The thermocouple was discovered in 1821 by the German physicist, J. Seebeck [3]. He discovered that at the junction of two dissimilar conductors a voltage could be generated by a change in temperature (see Figure 1-8). Then, in 1883, Melloni produced the first bismuth cooper thermocouple detector. But the output voltage of thermocouples is still small, thus preventing the measurements of very small temperature differences. Nobili, in 1829, connected several thermocouples in series to generate a higher and consequently measurable output voltage [3].

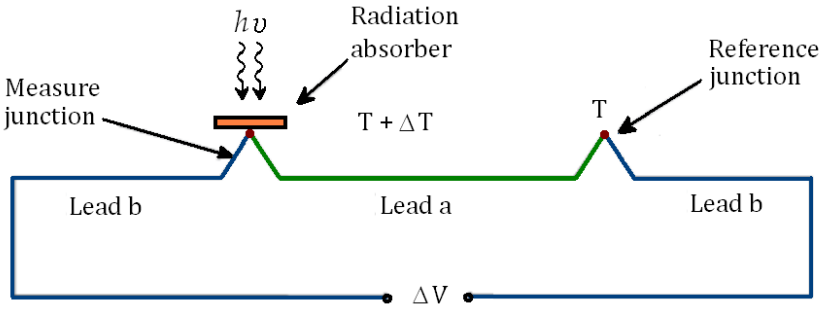

Figure 1-8. Principle of thermocouple [3]

The output voltage (ΔV) of a thermocouple is directly proportional to the temperature difference between the two junctions (ΔT), and is given by the relation:

$$\Delta V = \alpha_s \Delta T \qquad \text{(I- 8)}$$

Where α_s is the thermoelectric (or Seebeck) coefficient of the thermocouple, commonly expressed in $\mu V \cdot K^{-1}$, which is a material constant (see Table 1-4).

Table 1-4. Thermoelectric coefficient of some thermocouple materials; adapted from [3]

Material	α_s (μV/K)	Material	α_s (μV·K^{-1})
p-Si	100-1000	Ni	-19.5
p-poly-Si	100-500	Constantan	-37.25
p-Ge	420	Bi	-73.4
Sb	48.9	n-Si	-450
Cr	21.8	n-poly-Si	-100 to -500
Fe	15	n-Ge	-548

The thermopile is one of the oldest IR detectors. It results from connecting many thermocouples in series in order to achieve better temperature sensitivity [9]. Even though thermopiles have relatively low sensitivity and slow response, it can be optimized of specific application. In addition, the development of semiconductors produced materials with much higher Seebeck coefficients offers the possibility of constructing thermopiles with increased sensitivities. Although thermopiles are not as sensitive as bolometers and pyroelectric detectors, they can replace these in many applications due to their reliable characteristics and good cost/performance ratio [3].

2.3. Pyroelectric detectors

The first theory of the pyroelectric detector was presented by Cooper in 1962 using the barium titanate material. Also in the same year, Lang proposed the use of pyroelectric devices for measuring temperature changes as small as 0.2 μK. Afterward, a lot of research activities towards the pyroelectric infrared detectors had begun [3].

Pyroelectric detectors utilize dielectric materials, particularly crystalline materials, which exhibit temperature dependent spontaneous polarization. Most of the pyroelectric materials used as thermal detector are the lead-based ‘‘perovskite’’ oxides. These materials have the basic formula ABO_3 where A is lead, O is oxygen, and B may be one or a mixture of cations. Examples of these materials are: lead zirconate titanate $PbZrTiO_3$ (PZT), barium strontium titanate $BaSrTiO_3$ (BST), and lead scandium tantalate $PbScTaO_3$ (PST) [4]. Above Curie temperature, T_c, these materials becomes paraelectric and do not exhibit any pyroelectric activity.

The current flowing into or out of a pyroelectric detector, made of two electrodes and a pyroelectric material between them, is given by:

$$I = \pi_p A \frac{dT}{dt} \qquad \text{(I- 9)}$$

Where A is the area of the electrodes, π_p is the pyroelectric coefficient which is material specific (see Table 1-5) and dT/dt the rate of temperature change.

Table 1-5. The most known pyroelectric materials; adapted from [3]

Type	**Material**	**Pyroelectric coefficient π_p [$\mu C \cdot m^{-2} \cdot K^{-1}$]**	**Curie temperature T_c [K]**
Single crystals	TGS *(triglycine sulphate)*	280	49
	DTGS (*Deuterated triglycine sulfate*)	550	61
	$LiTaO_3$	170	603
	$LiNbO_3$	80	480
Ceramics	PZT	400	230
	BST	7000	25
	PST	3500	25
Polymer	PVDF *(Polyvinalidene Fluoride)*	27	80

2.4. Golay cell

In 1936, Hammond Hayes published a paper proposed a new type of thermal detector based on the principle of gas expansion [10]. Based on the same idea of gas expansion, Harold Zahl and Marcel Golay fabricated a “pneumatic infrared detector” in 1946 [11]. Later, in 1947, Golay published another paper presenting an improved version using light deflection from a flexible mirror as a way to detect the gas expansion [12]. Even though he was not the first to use gas expansion as a way to detect infrared light, this type of infrared detector is known as a “Golay Cell”. They are still commercially available today.

A Golay cell consists of a closed, thermally well-isolated gas volume (cell) that increases its temperature due to the absorption of radiation [4][12]. Usually, we measure the deflection of the cell wall that is deformed due the increased pressure and consequently we can calculate the temperature change of the gas.

The performance of Golay cell is only limited by the temperature noise associated with the thermal exchange between the absorbing film and the detector gas. Therefore, the detector can be extremily sensitive with D* around 3×10^9 $cm \cdot Hz^{1/2} \cdot W^{-1}$ and responsivity of

10^5-10^6 $V \cdot W^{-1}$. In contrast, the response time is quite long, typically about 15 ms. Also, the detector is fragile and very susceptible to vibration, and is only suitable for use in controlled environement such as a laboratory [1].

2.5. Bolometers

Another widely used thermal detector is the bolometer. The bolometer is a resistive element constructed from a material with large temperature coefficient, so that the absorbed radiation produces a large change in resistance. In contrast to the thermocouple, the device is operated by passing an accurately controlled bias current through the detector and monitoring the output voltage. The basic detection mechanism is that a radiant power produces heat within the material, which in turn produces a resistance change. There is no direct photon-electron interaction. More details on the principle of types, operation and thermal model of bolometer will be presented in section 3.

2.6. Comparison of thermal detectors

The several types of thermal sensors can only be differentiated by the way they convert temperature change ΔT into an output signal, mainly voltage ΔV. Therefore, the design of thermal detector intends to reach a maximum of ΔT, which can be achieved, according to Equations (I- 6), by a maximum thermal isolation of the sensor elements. In other side, to achieve a small thermal time constant a minimum thickness of detector element is needed. Table 1-6 provides a comparison of the most important characteristics of the thermal detectors presented before.

Table 1-6. Comparison of uncooled thermal detectors; adapted from [4][13]

	Thermopile	**Pyroelectric**	**Golay cell**	**Bolometer**
Principle	Energy converter		Parametric converter	
Physical effect	Seebeck effect	Dielectric polarization	Gas expansion	Carrier density mobility
Object	Temperature gradient ΔT	Temperature change dT/dt	Temperature T	Temperature T
Signal	Voltage	Polarization	Volume	Resistance
Material parameter	α_s	π_p	TCC	TCR
Temperature control	unnecessary	Unnecessary/ necessary	necessary	necessary

Figure 1-9 shows the performance of a number of thermal detectors operating at room temperature. Typical values of detectivities of thermal detectors at 10 Hz change in the range between 10^8 to 10^9 cm·Hz$^{1/2}$·W^{-1} [3]. Pyroelectric TGS detectors show the higher D* but with high decreasing slope relative to frequency. The metal oxide bolometer shows lower D* and wider pass band.

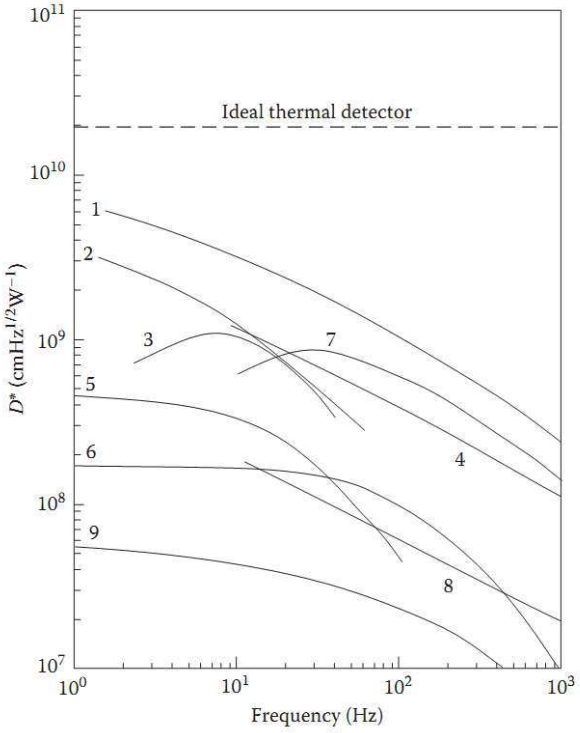

Figure 1-9. Performance of uncooled thermal detectors. 1- alaine doped TGS pyroelectric detector (1.5×1.5 mm²); 2- spectroscopic thermopile (0.4 mm², τ_{th}=40 ms); 3- Golay cell; 4- TGS pyroelectric detector in ruggedized encapsulation (0.5×0.5 mm²); 5- Sb/Bi evaporated film thermopile (0.12×0.12 mm², τ_{th}=13 ms); 6- immersed thermistor (0.1×0.1 mm², τ_{th}=2 ms); 7- $LiTaO_3$ pyroelectric detector; 8- Plessey PZT ceramic pyroelectric detector; and 9- Metal oxide thin film bolometer(0.5mm², τ_{th}=1 ms) [3]

3. Basics of Bolometers

The first bolometer was designed in 1880 by American astronomer S. P. Langley. It was consisting of blackened platinum absorber element [9]. Langley was able to make bolometers that were more sensitive than the thermocouples available at that time. Although other thermal devices have been developed since that time, the bolometer remains one of the

most used infrared detectors [3]. Many materials have been investigated as bolometers. The first thin film resistive micobolometers were proposed by R. Hartmann and K.C. Liddiard in 1982 and 1984 respectively. Today, the most common bolometer temperature sensing materials are vanadium oxide (VO_x) and amorphous silicon (a-Si).

The key factor is to find a high performance temperature sensing material, in terms of responsivity and signal to noise ratio, together with high thermal isolation in the smallest possible area. At the same time, it must be possible to integrate this material together with signal readout electronics.

3.1. Principle of operation

The basic detection mechanism of a bolometer is the change of electrical resistance R as reaction to absorption of radiant power. The parameter used to quantify the temperature dependence of electrical resistance R is the Temperature Coefficient of Resistance (TCR) expressed in K^{-1}, defined as seen in equation (I-10). It is independent of geometry, so it is useful to compare resistive materials. The larger the electrical resistance changes, the higher the TCR and the higher the responsivity (cf. paragraph 3.5.1).

$$\beta = \mathrm{TCR} = \frac{1}{R}\frac{dR}{dT} \tag{I-10}$$

When biasing the bolometer with a constant current (I_b), the change of voltage across it will be,

$$\Delta V = I_b \times \Delta R = I_b R \beta \times \Delta T \tag{I-11}$$

In steady state, when the bolometer material absorbs an amount P_i of radiated power from a light source, a temperature change ΔT occurs:

$$\Delta T = \eta \frac{P_i}{G_{eff}} \tag{I-12}$$

where G_{eff} is the effective thermal conductance of bolometer material (expressed in $W \cdot K^{-1}$), and η is the absorption coefficient (dimensionless). G_{eff} is related to the self-heating effect and given by the relation:

$$G_{eff} = G - I_b^2 \frac{dR}{dT} \tag{I-13}$$

where G is the geometrical thermal conductance of the bolometer. The variation of the temperature causes a change in the electrical resistance R of the bolometer material, and therefore a variation of voltage across it will be:

$$\Delta V = \eta \frac{P_i I_b R \beta}{G_{eff}} \quad \text{(I-14)}$$

3.2. Types of bolometer

Bolometers may be divided into several types. The most commonly used are the metal, the thermistor, and the semiconductor bolometers. A fourth type is the superconducting bolometer [3]. This bolometer operates on a conductivity transition in which the electrical resistance changes dramatically over the transition temperature range. These materials will not be described in this thesis since there is no such one at 300 K. Figure 1-10 shows schematically the temperature dependence of electrical resistance of different types of bolometers.

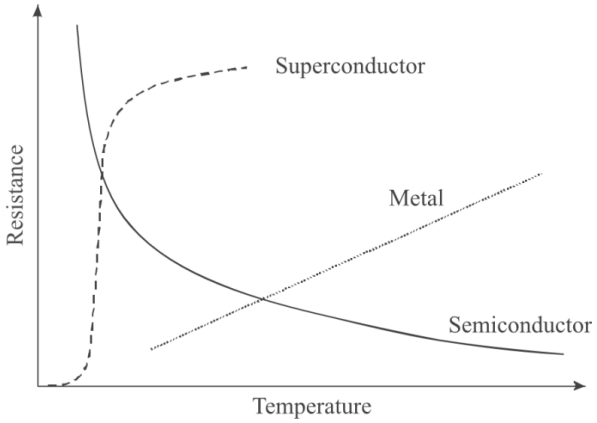

Figure 1-10. Temperature dependence of electrical resistance of bolometer material types [9]

3.2.1. Metal bolometers

Typical materials used for metal bolometers are nickel, bismuth, platinum, or titanium. The metal bolometers are easy to integrate with CMOS process and have low noise, but their TCR value is relatively very low (e.g. Titanium up to 0.35% K^{-1}), which results in low performance detectors. Most metal bolometers are formed as film strips, about 100-500 Å

thick, via vacuum evaporation or sputtering. They are often coated with a black absorber such as evaporated gold or platinum [3].

Metal bolometers have a positive temperature coefficient with typical value of about 0.3% K^{-1}. Giani [14] has reported a TCR value of 0.33% K^{-1} for Pt thin films on SiN_x/Si substrates, and Liddiard [15] has proved a TCR 0.33% K^{-1} for same the material. The metal bolometers operate at room temperature and have specific detectivity of the order 1×10^8 $cm\cdot Hz^{1/2}\cdot W^{-1}$ [3][15] with response times of approximately 10 ms. Unfortunately, metal in thin film form has a TCR value of 0.4% K^{-1}, much lower than for competitor materials, which causes it to be of little use in uncooled bolometer arrays.

3.2.2. Semiconductor bolometers

Semiconductor bolometers are the most highly developed thermal detectors for low light levels. They present the best choice detectors for many applications, especially in the infrared and submillimeter spectral range [3]. Over most of the far infrared spectrum, the performance of a germanium bolometer is comparable to that of the best photon detectors with the added advantage of being a broadband device [4]. More attention has been recently given to the use of amorphous Si (a-Si) as an alternative to Ge. In comparison with Ge, Si has a lower specific heat (by a factor of 5), easier materials preparation, and more advanced device fabrication technology. An alternative to a-Si are different types of amorphous germanium-silicon-oxygen compounds ($Ge_xSi_{1-x}O_y$), and poly crystalline silicon germanium (SiGe). Table 1-7 states some typical TCR values for different metals and semiconductor materials. Note that the TCR values of semiconductors are heavily dependent on the manufacturing process.

Table 1-7. Comparison of uncooled thermal detectors at room temperature. Adapted from [4]

Metals		Semiconductors	
Material	TCR (% K^{-1})	Material	TCR (%K^{-1})
Ag	0.38	VO_x	-2.7
Au	0.34	YBCO	-3.5
Cu	0.39	GaAs	-9
Ni	0.60	a-Si	-3.0
Ni-Fe (thin layer)	0.23	a-Ge	-2.1
Pt (thin layer)	0.18	Poly-Si :Ge	-1.4

3.2.3. Thermistor bolometers

Thermistor bolometers are constructed from a sintered mixture of various semiconducting oxides that have a higher TCR than metals (2–4% K^{-1}). The negative TCR value depends on the bandgap, the impurity states, and the dominant conduction mechanism. This coefficient is not constant but varies as T^{-2}, which is a result of exponential dependence of semiconductor resistivity [3]. The sensitive material in a thermistor bolometer is typically made of wafers of manganese, cobalt, and nickel oxides. They can be made in sizes ranging from 50 μm^2 to 5 mm^2. Thermistors have a time constant value in the range of 1-10 ms. They exhibit a large value of 1/f noise. Therefore, thermistor thin films were not practically used for uncooled bolometer thermal imaging arrays.

3.2.4. Sensitive materials for bolometers

Uncooled bolometers have dominantly taken over the IR market. A variety of materials have been used as thermo-sensing elements in microbolometers, such as vanadium oxide, polycrystalline and amorphous semiconductors. Next, we will present an overview of these materials. More details on their properties and performance will be presented later in paragraph 5 of this chapter.

Vanadium Oxides

Vanadium oxides are the most popular thermistor material in fabrication of today's IR detectors. Early tests of TCR, electrical resistivity, and l/f noise indicated that this material would perform better than a metal resistor [13]. Some of the vanadium oxides, like V_2O_3 and VO_2, show semiconductor to metal phase transition with a significant change in electrical and optical properties. The electrical resistivity change and optical properties of VO_2 films strongly depend on the fabrication conditions and the resulting crystallographic structure and stoichiometry. For film thickness of 100-300 nm a TCR value of -3% to -5% K^{-1} were reported at 300 K [1]. Finally, vanadium oxides are transparent in the infrared range of the wavelength; they therefore require the addition of an absorbing layer. Also, VO_2 material show a hysteresis phenomenon related to a phase transition which occurs near 50 °C [16], thus it must be heated.

Amorphous Semiconductor films: a-Si, a-Si: H, a-Ge: H, a-$Si_{1-x}Ge_x$: H et a-Si: N

The amorphous silicon (a-Si) appears to be the most promising material. TCR values for a-Si range from -2.5% K^{-1} for doped, low electrical resistivity films at room temperature, to -8% K^{-1} for high electrical resistivity materials [1]. Although high TCR values are achievable, they are accompanied by high level of 1/f noise.

Hydrogenated amorphous silicon (a-Si: H) is very attractive to be used as thermo-sensing material for uncooled microbolometers, since it provides a very large TCR value of about -13% K^{-1} [17]. However, it has a very low room temperature electrical conductivity resulting in a very high pixel electrical resistance ($\geq 10^9$ Ω). For commercial microbolometers, boron doping is commonly used in order to decrease the undesirable resistivity, but this also results in a reduction of the TCR (-2.8 %/K). Intrinsic a-Ge_xSi_y: H has better performance characteristics than a-Si: H,B when is used as thermo-sensing element, since it has a high TCR (-4.7% K^{-1}), a moderated room temperature electrical conductivity and therefore a moderated pixel electrical resistance ($\approx 10^7$ Ω) [18].

In general, films of a-Si: H, a-Ge: H, a-$Si_{1-x}Ge_x$: H and a-Si: N have comparable relative sensitivities with variable 1/f noise characteristics depending on the manufacturing process and imperfection contacts.

Semiconductor $YBa_2Cu_3O_{6+x}$

The electrical resistivity of this compound has a semiconducting behavior at room temperature. These thermometers are very interesting because of their relative sensitivity and are potentially compatible with CMOS technology. Very encouraging results have also been obtained using semiconducting $YBa_2Cu_3O_{6+x}$ (YBCO) thin films on silicon. This material has a high and relatively constant TCR value of -3% K^{-1} at room temperature. Amorphous YBCO thin films deposited on silicon wafers with MgO buffer layer have exhibited TCRs as high as -4% K^{-1} [19]. Unfortunately, these compounds have a very high 1/f noise.

Manganese oxides $Ln_xM_{1-x}MnO_3$

Manganese oxides are compounds based on manganese oxide, lanthanide Ln = La, Pr, Sm, Nd, Gd, Y and alkaline earth metal or divalent ions M = Ca, Sr, Pb, Ba. The remarkable electronic and magnetic properties of rare-earth manganite oxides have raised lot of interests for applications. Manganite thin films showing a large change of electrical resistivity at the

metal-to-insulator transition, which takes place for some materials at or around 300 K, also makes them potential material for the fabrication of uncooled bolometers (see Figure 1-11) [20]. They may have a TCR coefficient of about 8% K^{-1} at 300 K [54], so can be a good candidate as room temperature thermal detectors. More details on the bolometric performance of these materials will be presented later in paragraph 5 of this chapter.

We did choose the manganite oxide $La_{0.7}Sr_{0.3}MnO_3$ (LSMO) as thermometer in this thesis to realize and characterize an uncooled bolometer. Even if it does not exhibit the highest TCR values at room temperature, compared to other possible manganite compositions, we study LSMO because it shows low 1/f noise at the metal-to-insulator transition [21]-[24].

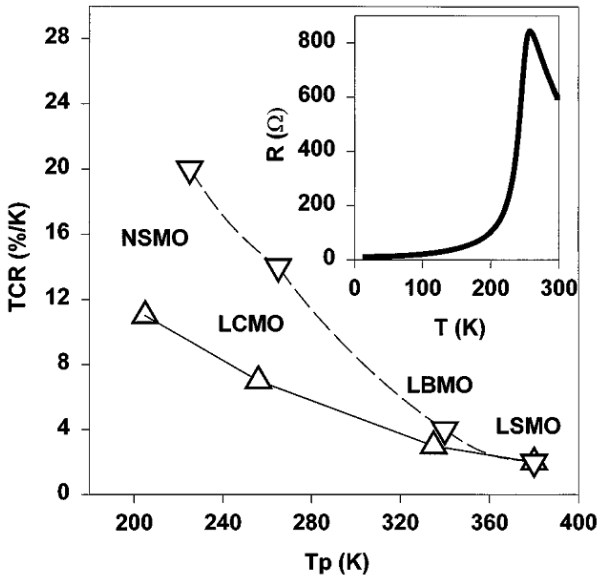

Figure 1-11. TCR values versus electrical-resistivity-peak temperature, T_p, for many manganite oxides materials. Inset shows temperature dependence of electrical resistivity for $La_{0.7}Ca_{0.3}MnO_3$ (LCMO) thin film [20]

Other Materials:

Recently, the carbon nanotube has been studied as infrared uncooled detectors. It shows a TCR value of -0.2% K^{-1}[25]. Karanth *et al* [26] proposed the material Mn-Ni-Co-O material as infrared detector which has a specific detectivity value of 4.4×10^8 cm·$Hz^{1/2}$·W^{-1} at 10 Hz. In other hand, Fobes *et al* [27] proved the potential application in bolometric detection in doped Ca_2RuO_4 material at the metal-insulator transition. It shows a high TCR value of about -40% K^{-1}.

3.3. Basic thermal model (RC model) of bolometer

A simple model describes a bolometer as an absorber with heat capacity C connected to a thermal bath at temperature T_0 by a thermal conductance G. The temperature of absorber changes in response on changes in incident power. These temperature changes are converted into voltage changes by means of a current biased thermometer. The thermometer is a thin layer of material possessing a high temperature coefficient of resistance (TCR). Relation between temperature changes and incident power can be found from the energy balance equation:

$$C\frac{d(T-T_0)}{dt} + G(T-T_0) = \eta P_i + P_J(T) \qquad \text{(I-15)}$$

where T is the absorber temperature, T_0 is the temperature of thermostat, P_i is the incident radiation power, R is the thermometer resistance and $P_J(T)$ is the energy released in the absorber due to the Joule heat. The thermal conductance G describes the heat conduction from thermometer to the surroundings.

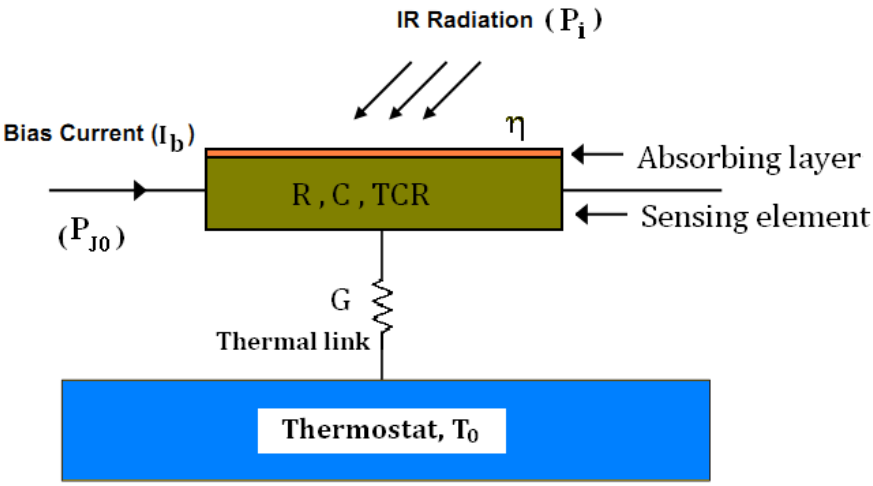

Figure 1-12. Schematic representation of simple bolometer thermal model

Within the linear approximation the electrical resistance of thermometer in the presence of small temperature changes could be written as $R(T) = R_0 + (dR/dT)\times(T-T_0)$. Thus, with this approximation, the dissipated power $P_J(T)$ can be presented:

$$P_J(T) = I_b^2 R(T) = I_b^2 R_0 + I_b^2 \frac{dR}{dT}(T-T_0) \qquad \text{(I-16)}$$

Thus, using equation (I-13), the final energy balance equation will be:

$$C\frac{d(T-T_0)}{dt}+G_{eff}(T-T_0)=\eta P_i+P_{j0} \qquad \text{(I-17)}$$

where $P_{J0}=I_b^2R_0$ and R_0 presents the thermometer electrical resistance at the temperature T_0.

If the incident radiation is harmonically modulated with modulation frequency $\omega=2\pi f$, $P_i=P_0e^{j\omega t}$, then equation (I-17) gives the solution for the thermometer temperature:

$$T=T_0+\frac{\eta P_0 e^{j\omega t}}{G_{eff}(1+j\omega\tau_{eff})} \qquad \text{(I-18)}$$

here the term τ_{eff} presents the effective thermal time constant, which is given by the relation:

$$\tau_{eff}=\frac{C}{G_{eff}} \qquad \text{(I-19)}$$

The thin film detector element with area A_f and thickness t_f, has a heat capacitance C given by:

$$C=c_p\,\rho_v\,A_f\,t_f \qquad \text{(I-20)}$$

where c_p is the specific heat capacity at constant pressure expressed in $J\cdot kg^{-1}\cdot K^{-1}$, ρ_v is the mass density of detector material expressed in $kg\cdot m^{-3}$.

3.4. Figures of merit

In order to characterize and quantify the performance of bolometers, we used some common figures of merit which are the temperature coefficient of resistance TCR (=β), optical voltage responsivity ($\Re_v$), Noise Equivalent Power (NEP), and specific detectivity (D*). All of these parameters are inter-related. They also depend on some parameters such as thermal conductance (G), heat capacitance (C) and effective thermal time constant (τ_{eff}). Although these parameters enable us to compare the relative detector performance, only one figure of merit cannot completely characterize bolometer performance, except perhaps for specific detectivity. However, in order to calculate the specific detectivity of bolometer optical responsivity and noise equivalent power have to be known. Next, we will describe all these parameters in more details.

3.4.1. Optical Responsivity ($\Re_v$)

The voltage optical responsivity ($\Re_v$) of a bolometer is defined as the output voltage per radiated power when a bias current I_b is applied to the bolometer device. It has the units of volt/watt [$V \cdot W^{-1}$], and is written as [28]-[30]:

$$\Re_v(\omega) = \frac{\Delta V}{\Delta P_i} = \eta . \frac{I_b . R . \beta}{G_{eff}\sqrt{1 + \omega^2 \tau_{eff}^2}} = \frac{\Re_v(0)}{\sqrt{1 + \omega^2 \tau_{eff}^2}} \qquad \text{(I-21)}$$

Thus the responsivity is frequency-independent at low modulation frequencies and rolls off with frequency at higher frequencies. It shows that the responsivity bolometer exhibits a first-order frequency response. The value of responsivity at zero frequency $\Re_v(0)$ is controlled by G_{eff}. Thus, bolometers with a high thermal conductance are fast, but their responsivity is low since $\tau_{eff}=C/G_{eff}$. The key factor to developing highly sensitive bolometers is having a high temperature coefficient β and excellent thermal isolation (low thermal conductance G) [3].

In order to maximize the responsivity a main consideration, especially for bolometers with positive TCR, is to do not exceed a certain bias current value which is set by "thermal runaway" inequality: $I^2_b < I^2_{emb} = G\,(dR/dT)^{-1}$. Above this current value, the bolometer can be destroyed. Therefore, to avoid damage, the maximal bias current [28] is set by the equation (I-22), which is called the optimal bias current.

$$I_{opt} = \sqrt{0.3}\, I_{emb} = \sqrt{0.3 \frac{G}{dR/dT}} \qquad \text{(I-22)}$$

The power dissipated by Joule heat leads to a bolometer temperature increase (ΔT usually called "thermal overheating"), which can be found from steady state solution of equation (I-15) in the absence of incident radiation:

$$\Delta T = \frac{P_{J0}}{G_{eff}} = \frac{I_b^2 R_0}{G_{eff}} \qquad \text{(I-23)}$$

The basic model, presented in the previous paragraph, can well explain the optical voltage responsivity of bolometer at low chopping frequency regions. However at very high frequencies, an advanced model has to be taken into account, as we will see in chapter 3.

3.4.2. Response time

The response time constant of a detector, expressed in seconds, reflects its rapidity of converting the light signal into an electrical signal. It can be extracted from the dependence of the optical responsivity to the modulation frequency of the radiant incident signal. The -3 dB value ($0.707\times\Re_v(0)$) is determined by the condition $\omega\tau_{eff} = 1$ for first order system. The basic model of bolometer incorporates equation (I-19) as definition of response time, or is the effective thermal time constant.

We sometimes call it time constant or response time by abuse of language. It actually indicates the minimum time that must elapse between two consecutive signals so that they are differentiated by the detector. This is a limiting factor of the flow of information that can be received by the sensor.

3.4.3. Noise Equivalent Power (NEP)

The NEP of the bolometer is calculated as the ratio of the square root of the voltage noise spectral density, $S_v(\omega)$ expressed in $V^2\cdot Hz^{-1}$, over the bolometer responsivity $\Re_v(\omega)$ expressed in $V\cdot W^{-1}$. The NEP thus is expressed in the unit $W\cdot Hz^{-1/2}$. In order to determine the noise equivalent power of a bolometer, we have first to determine the noise sources that influence the bolometer.

Noise is the undesirable random electrical signal output which contributes to the desired electrical signal from various sources. It is not possible to eliminate noise from the system entirely, also it is not easy to measure and quantify noise. Although elimination of environment noise sources is relatively easy, there is no possibility to get rid of noise in the material because some of it depends on crystal structure and device fabrication quality, while others such as Johnson noise is a fundamental phenomenon. Some known sources and mechanisms of noise are widely investigated both experimentally and theoretically [28][30][31][32]. There are several main noise sources which limit detector performance: photon fluctuations, phonon fluctuations, thermal fluctuations, low frequency noise (1/f noise), and the preamplifier noise (noise of measuring system itself).

Photon noise. According to Stefan-Boltzmann law, all objects can radiate photons at any non-zero temperature. Energetic photons that are randomly exchanged between environment and detector cause photon noise. In order to reduce this type of noise the detector

needs to be shielded from environment and must be kept sufficiently cold. In practice, this noise is negligible for not ultimate bolometers.

Phonon noise. Most of this noise is due to the random exchange of energy carriers between absorber element of bolometer and heat bath through thermal conductance (G). This energy is quantized in the form of phonons. The random exchange of energy leads to fluctuations in temperature, thus fluctuations of bolometer electrical resistance. Noise equivalent power for phonon fluctuations is given by [31]:

$$\mathrm{NEP_{phonon}}(\omega) = \frac{\sqrt{S_v^{\mathrm{phonon}}(\omega)}}{\Re_v(\omega)} = \sqrt{4k_B T^2 G} \qquad \text{(I-24)}$$

where $S_v^{\mathrm{phonon}} = \Re_v(\omega)\sqrt{4k_B T^2 G}$ is the phonon voltage noise spectral density. It depends on temperature, voltage optical responsivity, and thermal conductance of the system.

Thermal noise. All resistive materials exhibit thermal (or Johnson) noise. The random scattering of electrons from the core ions or imperfections in the crystal causes thermal noise as they are moving in the direction of the current. Noise equivalent power for thermal fluctuations for bolometer of electrical resistance R is given by:

$$\mathrm{NEP_{therm}}(\omega) = \frac{\sqrt{S_v^{\mathrm{therm}}(\omega)}}{\Re_v(\omega)} = \frac{\sqrt{4k_B T\, R}}{\Re_v(\omega)} \qquad \text{(I-25)}$$

where S_v^{therm} is the thermal voltage noise spectral density. It depends on temperature, bolometer electrical resistance, and is independent of frequency.

1/f noise. It strongly depends on the material used for the detector. Indeed, the origin of this noise is still not completely known. Generally, the quality of material (epitaxial growth of thin film) and of electrical contacts, with using suitable measurement technique, allow to reduce this noise. In addition to the structure of thin films, the operating frequency also affects this type of noise, because it is inversely proportional to the frequency. The empirical relation of Hooge [32] normalizes the density of fluctuations relative to the total carrier number N_p and a normalization parameter α_H by the relation:

$$\frac{S_v^{1/f}(\omega)}{V^2} = \frac{\alpha_H}{N_p} \times \frac{1}{(\omega/2\pi)} = \frac{\alpha_H}{n} \times \frac{1}{(\omega/2\pi)\,\Omega} \qquad \text{(I-26)}$$

Where the carrier number N_p is defined as the product of carriers concentration n by the real volume of the sensitive element Ω (in m^3). The parameter α_H/n is called the normalized Hooge parameter, which has a unit of m^3.

Noise equivalent power for 1/f fluctuations for bolometer is given by:

$$NEP_{1/f}(\omega) = \frac{\sqrt{S_v^{1/f}(\omega)}}{\Re_v(\omega)} \qquad \text{(I-27)}$$

Measurement system noise. This noise contributes to the total measured noise, but it can be clearly identified. We can subtract its contribution to retain only the specific detector noise. A good choice of measurement system parameters can reduce this noise. In the model e_n-i_n without sources correlation, the noise equivalent power of the measurement system NEP_{Amp} associated to source resistance R is equal to:

$$NEP_{Amp}(\omega) = \frac{\sqrt{S_v^{Amp}(\omega)}}{\Re_v(\omega)} = \frac{\sqrt{e_{nA}^2(\omega) + (R\ i_{nA}(\omega))^2}}{\Re_v(\omega)} \qquad \text{(I-28)}$$

where S_v^{Amp} is the amplifier voltage noise spectral density, and e_{nA} and i_{nA} are the voltage and current noise sources of the amplifier.

The noise equivalent power of the bolometer NEP can finally be written as the quadratic sum of the different major noise sources, since they are statistically independent:

$$NEP_{tot}^2(\omega) = \frac{S_v(\omega)}{\Re_v^2(\omega)} = NEP_{1/f}^2(\omega) + NEP_{therm}^2(\omega) + NEP_{phonon}^2(\omega) + NEP_{Amp}^2(\omega) \qquad \text{(I-29)}$$

Further optimization of bolometer material requires minimizing the magnitude of electrical fluctuations down to the ultimate limit, which in the ideal case is set by photon fluctuations [33].

3.4.4. Specific detectivity D* and impulse detectivity D_i

The specific detectivity D* (expressed in $cm \cdot Hz^{1/2} \cdot W^{-1}$) provides information that is equivalent to NEP, but with the possibility to compare bolometer pixels of different areas. It

is calculated as the ratio of the square root of effective area of bolometer (expressed in cm²) over the NEP,

$$D^* = \frac{\sqrt{A_f}}{NEP} \qquad \text{(I-30)}$$

The specific detectivity of an ideal thermal detector (absorption coefficient and emission equal to one) only depends on the detector temperature T_D and the background temperature T_B. If the detector is only limited by the photon noise of the environment, then it's the case of BLIP (Background Limited Infrared Photodetector) detector. If the receiving surface can detect under a solid angle of 2π steradians, we obtain [34]:

$$D^*_{BLIP} = \sqrt{\frac{\eta}{8\, k_B \sigma_{SB} (T_D^5 + T_B^5)}} \qquad \text{(I- 31)}$$

where T_D is the detector temperature, T_B is the background temperature, and $\sigma_{SB}=5.67\times10^{-8}$ $W\cdot m^{-2}\cdot K^{-4}$ is the Stefan-Boltzmann constant.

For an ideal uncooled detector, $T_D=T_B=300$ K and $\eta=1$, we get $D^*_{BLIP}=1.8\times10^{10}$ $cm\cdot Hz^{1/2}\cdot W^{-1}$, which presents the maximal detectivity of an ideal uncooled thermal detector.

Finally, another important figure of merit is the impulse detectivity [35], which is defined as:

$$D_i = \frac{D^*}{\sqrt{\tau_{eff}}} \qquad \text{(I-32)}$$

It is expressed in $cm\cdot J^{-1}$. This parameter illustrates the necessary compromise between optical responsivity and effective time thermal constant.

4. Properties of $La_{0.7}Sr_{0.3}MnO_3$ (LSMO)

Recently, considerable experimental and theoretical efforts have been devoted to the study of perovskite manganites. The term manganites refers to a whole range of perovskite manganese oxide compounds of the generic formula $B_xA_{1-x}MnO_3$ ($0 \le x \le 1$), where B is a rare-earth atom (e.g., La, Pr, Nd) and A is an alkaline-earth metal atom (e.g., Ca, Sr, Ba). The doping parameter x is equal to the density of carriers [38]. Indeed, the interest in manganites

originated from the discovery of their ferromagnetism and its correlation with electrical conductivity by Jonker [39]. Then, the discovery of a colossal magnetoresistance CMR effect in manganites [40], as well as the metal-insulator phase transition (observed in the vicinity of the Curie temperature T_c) and granular magnetoresistance [41]-[43], gave arise more interest in these compounds for their potential applications, like room temperature bolometers and magnetic sensors [44]-[46].

A brief description about the different fundamental properties of the manganite $La_{0.7}Sr_{0.3}MnO_3$ (LSMO) is presented in this paragraph. This includes its structure, transport properties, and thermal properties.

4.1. Crystal structure

The LSMO, like all manganese oxides, has a Perovskite structure (which is named after Russian mineralogist L. A. Perovski), as seen in Figure 1-13. The trivalent La and the divalent Sr are located at all corners, and the oxygen ions occupy the center of all the faces in the unit cell. The smallest Mn (transition metal) ions exist in the center of the octahedral oxygen ions. The perovskite structure is ideally cubic. But for LSMO, with x = 0.3, the structure is rhombohedral, with a = 0.549 nm and c = 1.3356 nm. Deposited as thin films, structure becomes pseudo-cubic with a = 0.3889 nm [47].

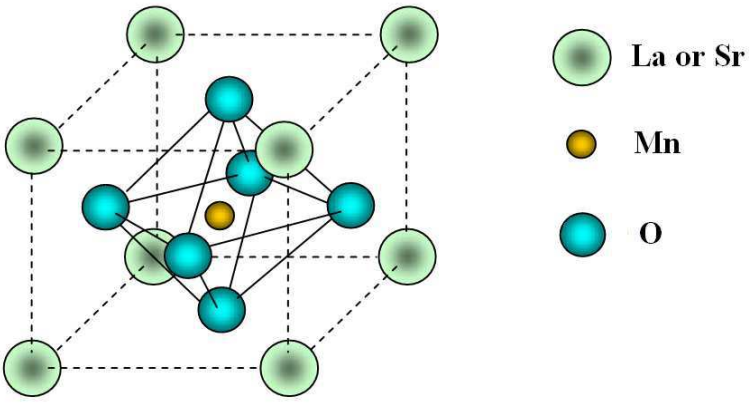

Figure 1-13. Schematic crystal structure of LSMO manganite [2]

Traditionally, LSMO has been grown on substrates such as strontium titanate (STO), lanthanum aluminate (LAO), and magnesium oxide (MgO). LSMO Films grows epitaxially (The term “epitaxy” describes the phenomenon of the thin crystalline films grown in a well-defined orientation on a single crystal substrate. The term epitaxy comes from the Greek roots epi, meaning “above”, and taxis, meaning “in ordered manner”[38]) with (001) orientation on (001) oriented substrates due to the cubic symmetry and constraints imposed by epitaxy. However, the small lattice mismatch between the LSMO film and these substrates cannot be released easily and built-in stresses are produced, that might lead to interesting effects on transport and magnetic properties [38].

Figure 1-14 shows the electronic phase diagram of $La_{1-x}Sr_xMO_3$ with the evolution of transition temperature as function of doping concentration x [36]. This graph reveals that it has an ferromagnetic insulating (FI) behavior at low doping concentration ($0.1 \leq x \leq 0.15$) values and ferromagnetic metallic (FM) behavior in the high-doped region ($x > 0.15$). The ferromagnetic transition temperature, or Curie temperature T_C (filled triangles), increases with x and reaches the maximum (about 370 K) around x=0.3, so it is considered for the use in various devices such as magnetic field sensors and magnetic random access memories and magnetic sensors [46][49]. Also, above the magnetic transition temperatures (T_N and T_C) the insulator (PI) to metal (PM) transition appears to occur around x = 0.3. This is the reason why LSMO (x=0.3) is considered as a good candidate for room temperature applications, like uncooled detectors.

4.2. Transport properties

The temperature behavior of the electrical resistivity depends strongly on the doping level (Figure 1-15 (a)). As we can notice in this graph, for x=0.3 we have a large variation of electrical resistivity near 300K, so that this composition considered as potential material for room temperature thermal detector. This variation is more evident in Figure 1-15 (b), which shows the electrical resistivity curve as a function of the temperature for x=0.3. This composition has Curie temperature of about 370 K, which is the highest value for the family $La_{1-x}Sr_xMnO_3$.

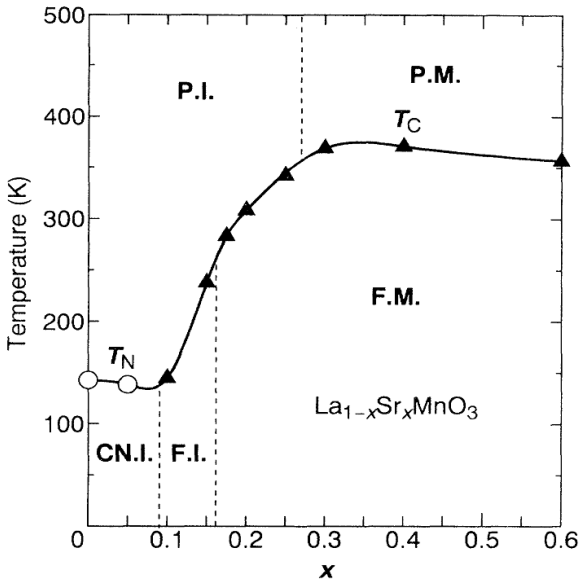

Figure 1-14. Phase diagram of $La_{1-x}Sr_xMnO_3$. Open circles and filled triangles are the Neel (T_N) and Curie (T_C) temperatures, respectively. The abbreviations mean paramagnetic insulator (PI), paramagnetic metal (PM), spin-canted insulator (CNI), ferromagnetic insulator (FI), and ferromagnetic metal (FM) [36]

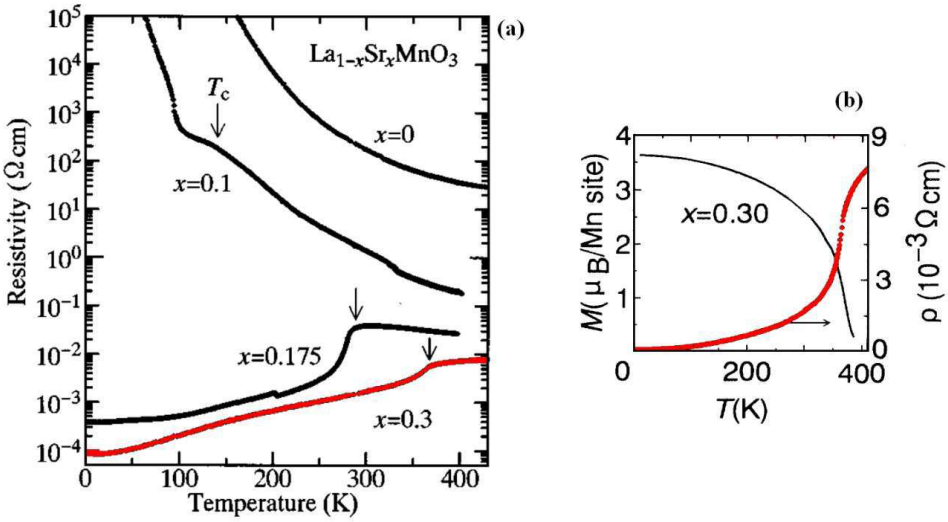

Figure 1-15. (a) Temperature dependence of the electrical resistivity in crystals of $La_{1-x}Sr_xMnO_3$. Arrows indicate the respective Curie temperature Tc [37], (b) electrical resistivity versus temperature for x=0.3 [36]

4.3. Thermal properties

Up to now, although a large number of investigations focused on the electronic and magnetic properties of the LSMO compounds, only a few studies regarding thermal properties were reported in the literature. Wang *et al* [49] and Kuo *et al* [50] have reported a throughout investigation of, between many others, the specific heat and thermal conductivity of $La_{0.7}Sr_{0.3}Mn_{1-x}Ru_xO_3$. Also, Khlopkin *et al* [51] have investigated the specific heat of $La_{0.7}Sr_{0.3}MnO_3$ single crystal. We can notice that the specific heat of LSMO (x=0) increase almost linearly near 300K with a value of 568 $J{\cdot}kg^{-1}{\cdot}K^{-1}$. It reaches its maximum value at ferromagnetic-paramagnetic phase transition (370K).

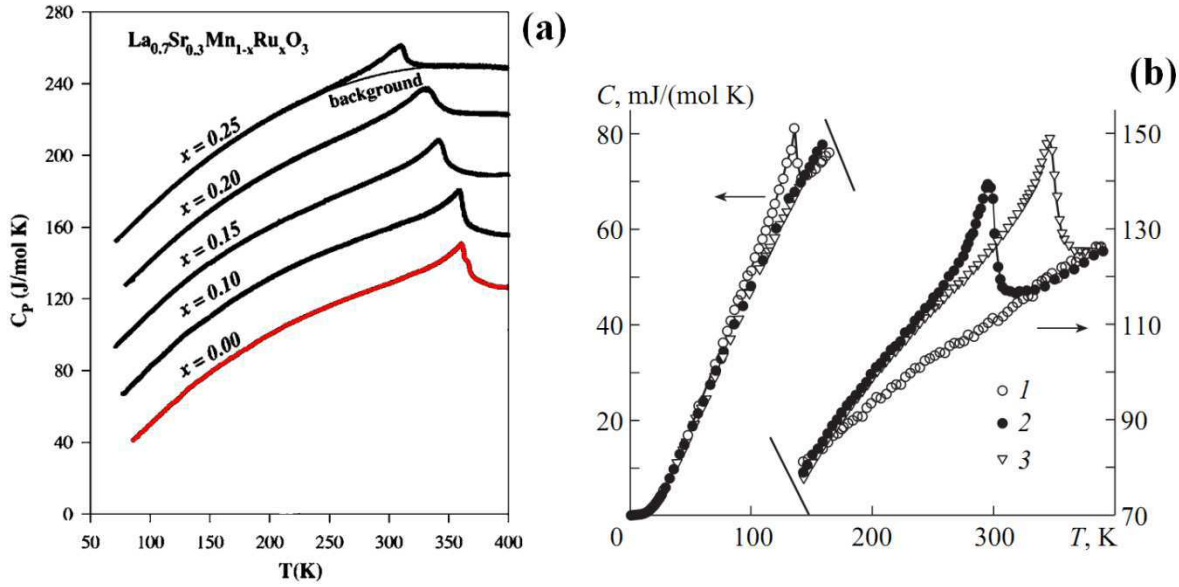

Figure 1-16. Temperature dependence of specific heats for: $La_{0.7}Sr_{0.3}Mn_{1-x}Ru_xO_3$ with $0 \leq x \leq 0.25$ (a) [49] and for 1- $LaMnO_3$, 2- $La_{0.8}Sr_{0.2}MnO_3$, and 3- $La_{0.7}Sr_{0.3}MnO_3$ single-crystal samples(b) [51]

The variation of thermal conductivity of LSMO as function of temperature has been reported by Wang *et al* [49] and El-Kassab *et al* [52] (see Figure 1-17). It is almost constant near 300 K, with a value of 2.5 $W{\cdot}m^{-1}{\cdot}K^{-1}$.

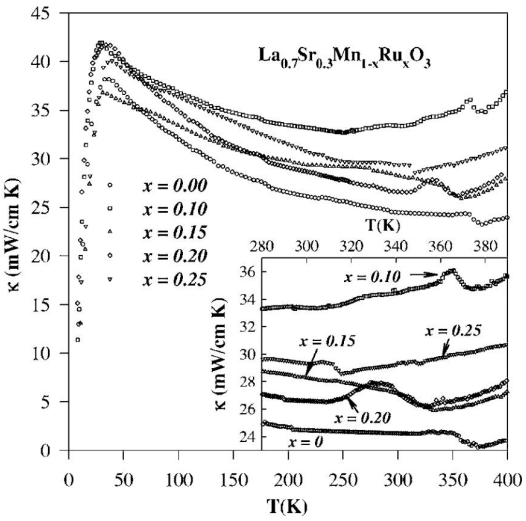

Figure 1-17. Temperature-dependent thermal conductivities for $La_{0.7}Sr_{0.3}Mn_{1-x}Ru_xO_3$ with $0 \leq x \leq 0.25$. The inset shows the blow-up plot near phase transitions [49]

Another important property, which is important for bolometric radiation detector application, is the value of LSMO optical absorption. Indeed, few studies have tried to investigate this property. Okimoto *et al* [37] studied the reflectivity of LSMO at various temperatures (Figure 1-18). For wavelength of 635 nm (so, a photon energy of 1.95 eV), the reflectivity equals 16%, thus the absorption plus the transmission equals 84%. Mechin *et al* [21] have measured independently an absorption coefficient of 85% for LSMO at 533 nm wavelength. At 635 nm wavelength, Liu [53] has reported an absorption coefficient of around 90% for suspended LSMO microbridge.

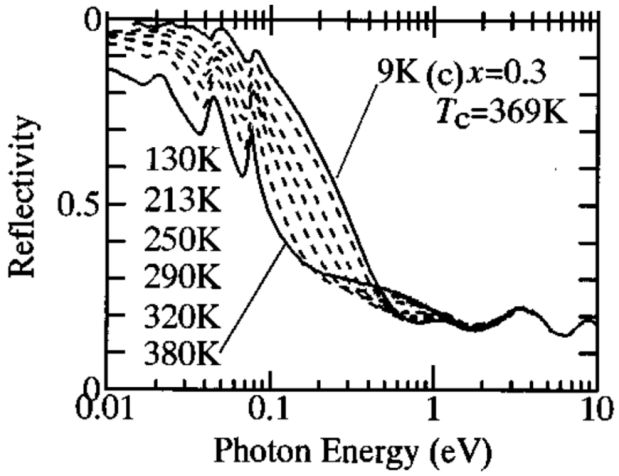

Figure 1-18. Reflectivity spectra at various temperatures in $La_{0.7}Sr_{0.3}MnO_3$ [37]

5. Uncooled bolometer: state of the art

Infrared (IR) radiation detectors have absorbed a large attention during the last two decades due to its application in both civil and military applications. Thermal detectors are presently taking more interest in the IR technology field. One of these detectors is microbolometers, which are manufactured through micromaching of many temperature sensing materials. The requirements for the temperature sensing materials used in microbolometers are: high temperature coefficient of resistance (TCR), low noise, and compatibility with standard microelectronic fabrication processes. Modern bolometer technology development started in the early 1980s with the work of Honeywell on vanadium oxide (VO_x) and Texas Instruments on amorphous silicon (a-Si) [3].

Other existing promising bolometer materials are manganese oxides, which have high TCR in the vicinity of metal-to-insulator phase transition. This makes them suitable for uncooled radiation thermal detectors. We report next a state of the art of the performance of these bolometers at room temperature.

5.1. Manganites based bolometer

In the past two decades, there has been increasing interest in doped manganites because of their extraordinary electrical and magnetic properties. In addition, to the observed colossal magnetoresistance (CMR) effect near the Curie temperature, their large temperature coefficient of resistance (TCR), which is close to the insulator-metal transition temperature, T_C, makes the manganite materials suitable for infrared detector applications [20].

Next, as seen in Table 1-8, we have extracted the main characteristics of manganites based bolometers using the figures of merit that describe these detectors. The N/A abbreviation will be used for all not available values.

Table 1-8. Thermal detectors based on manganites materials

Ref.	Composition/ Substrate	Area/ Form/ thickness	TCR (%K^{-1})	G (W·K^{-1})	R_m (Ω)/ ρ (Ω·m)	Time constant τ(ms)	$\Re_v$ (V·W^{-1})	NEP (W·Hz$^{-1/2}$)	D* (cm·Hz$^{1/2}$ ·W^{-1})
[54]	$La_{0.7}(Pb_{0.63}Sr_{0.37})_{0.3}MnO_3$/ $LaAlO_3$	2.5×3 mm² / rectangular/ 450 nm	5.5 @300K	3×10^{-3} @ 295K	1.1k / 4.1×10^{-4} @ 300K	τ_1=500 τ_2=1.9 τ_3=0.09	0.6 @ 1.2mA, 295K	3×10^{-8} @30Hz, 1.2mA, 295K	0.9×10^{7}
[21]	$La_{2/3}Sr_{1/3}MnO_3$/ $SrTiO_3$	300×100 µm²/ rectangular/ 200 nm	1.7 @335K	1.6×10^{-3} @ 335K	390 / 26×10^{-6} @ 300K	N/A	4.2 @ 2mA 10.4 @ 5mA @ 335K	8.1×10^{-10} @30Hz, 5mA, 330K	1.64×10^{6}
[55]	$(Bi,La)_{1-x}Sr_xMnO_3$/ Si (x>0.2)	38×38 µm² / rectangular/ 160 nm	3.1 @300K	1.3×10^{-7} @ 300K	250k / 4×10^{-2} @ 300K	N/A	4.8×10^{5} @ 323K	1.2×10^{-9} @30Hz, 5mA, 300K	N/A
[56]	La_xMnO_3/ $LaAlO_3$	3×6 mm² / rectangular/ 250 nm	11 @218K -1.1 @300K	4×10^{-3} @ 300K	1.8k / 35×10^{-5} @ 300K	N/A	22 @ 50mHz, 0.5mA, 218K	N/A	N/A
[57]	$La_{0.67}Ca_{0.33}MnO_3$/ $LaAlO_3$	N/A	7.9 @260K -0.84 @300K	N/A	950 @300K	10 @255K	34 µV @100µA, 255K, 20Hz	N/A	N/A
[58]	$La_{0.67}Ca_{0.33}MnO_3$/ $SrTiO_3$ (500µm)	50×1300 µm²/ µbridge/ 200 nm	1.8 @260K	9×10^{-6} to 9×10^{-4}	125k/ 96×10^{-5} @ 223K	N/A	685 @ 5Hz, 0.1mA, 223K	2.92×10^{-11} @ 5Hz, 0.1mA, 223K	2.76×10^{9} @ 5Hz, 0.1mA, 223K
[59]	$La_{2/3}Ca_{1/3}MnO_3$/ $LaAlO_3$	N/A N/A 300 nm	N/A	N/A	4k @240K	0.45 @300K	33 µV @400µA, 300K, 60Hz	N/A	N/A
[60]	$La_{2/3}Ca_{1/3}MnO_3$/ $NdGaO_3$	1cm×0.5mm or 1cm×1mm/ rectangular/ 300 nm	1.8 @230K	N/A	1.6k @230K	0.43 @188K	50 µV @50µA, 188K, 74Hz	N/A	N/A
[61]	LCMO/Si	4×10^{-6} cm²/ 200 nm	7 @300K	N/A	8.6×10^{-3}	N/A	6.3×10^{4}	1.5×10^{-11} @ 30Hz	1.3×10^{8} @ 30Hz
[61]	LBMO/ Si	4×10^{-6} cm²/ 200 nm	1.5 @300K	N/A	5.8×10^{-3}	N/A	1.4×10^{4}	2.0×10^{-11} @ 30Hz	1.0×10^{8} @ 30Hz
[53]	LSMO/CTO/Si	150×4 µm² / sus. µbridge/ 50 nm	2.4 @325K	7×10^{-8}	30k @330 K/ 2×10^{-5} @ 300K	3.12	78.3×10^{3} @ I_{limit},	2×10^{-13} @ 330 K @ 30 Hz	1.1×10^{10} @ 330 K @ 30 Hz

5.2. Other material bolometer

Several materials have been used as thermo-sensing elements in microbolometers, but the most employed are vanadium oxide (VO_x), amorphous and polycrystalline semiconductors, and semiconducting YBCO.

Vanadium oxide presents a high value of TCR, but it is not a standard material in IC fabrication technology. Hydrogenated amorphous silicon (a-Si:H) have shown a high value of TCR (13% K^{-1}) and are fully compatible with the silicon technology, but intrinsic amorphous semiconductors have a very high electrical resistance. Amorphous germanium-silicon (a-Ge_xSi_y:H) thin films deposited by plasma (PECVD) is another material alternative for bolometer application. Intrinsic a-Ge_xSi_y:H has better performance characteristics than a-Si:H since it has a high TCR (-4.7% K^{-1}) and a moderated room temperature electrical conductivity and therefore a moderated pixel electrical resistance.

In the next Table 1-9, a state of the art summary of performance characteristics of all non-manganite based uncooled bolometers is presented.

5.3. Comparison

The present efforts in infrared detector researches are directed towards improving the performance of room temperature infrared detectors. This includes elaborating a new sensing material and developing enhanced pixel geometries and thermal isolation. Many thermometer materials have been investigated as uncooled thermal detectors, which have theoretically unlimited spectral band response. The most popular thermometer materials used in fabrication of the micromachined bolometers are vanadium dioxide, VO_2, and amorphous silicon, a-Si. Other material has been studied in the last two decades. We can cite here semiconducting YBCO, SiGe oxide, and manganite oxides.

Table 1-9. Uncooled thermal detectors based on non-manganites materials

Ref.	Composition/ Substrate	Film Area/ Form/ thickness	TCR (%K^{-1})	G (W·K^{-1})	R_m (Ω)/ ρ (Ω·m)	Time constant τ(ms)	ℜv (V·W^{-1})	NEP (W·Hz$^{-1/2}$)	D* (cm·Hz$^{1/2}$ ·W^{-1})
[65]	a-Si/ Si	200 µm²/ planer / 500 nm	-2.8	N/A	10.5M	13.3	35×10^{3} @ 30Hz	8.6×10^{-12} @ 5 V, @ 30 Hz	1.2×10^{8}
[66]	a-Si/ Si	150×150 µm² / sus. µbridge / 700 nm	N/A	N/A	600k	4.76	8.7×10^{3} @ 5 V, @ 30Hz	6.1×10^{-11} @ 5 V, @ 30 Hz	2.5×10^{8}
[67]	a- $Ge_xSi_{1-x}O_y$/ p-Si	40×40 µm² / sus. µbridge / 200 nm	- 4.67	5.88×10^{-8}	320k/ 6.4×10^{-4}	5.18	9890 @ 2 µA, @ 5 Hz	1.27×10^{-9}	3.15×10^{6}
[68]	$Ge_xSi_{1-x}O_y$/ Si	100×100 µm² / sus. µbridge /	- 4.21	3×10^{-6}	640k	1.8	380 @ 6.75V	2.1×10^{-10}	4.8×10^{7}
[69]	$Ge_xSi_{1-x}O_y$	50×50 µm²/ sus. µbridge/	-4.8	1.4×10^{-7}	700k	13	1×10^{5} @ 250Hz	N/A	6.7×10^{8}
[70]	a-SiGe: H/ SiO_2/Si	70×66 µm²/ sus. µbridge / 500 nm	-4.3	N/A	500M	125	7.2×10^{5}	N/A	2.5×10^{9}
[71]	Poly-SiGe/ Si	50×50 µm² / sus. µbridge / 500 nm	- 1.91	N/A	350k	16.6	15×10^{3} @ 5 V, @ 10 Hz	1.9×10^{-11} @ 5 V, @ 30 Hz	4.7×10^{8} @ 5 V, @ 30 Hz
[72]	a-SiGe:H,F/ SiO_2/Si	100×100 µm²	3.7	2×10^{-7}	30M	300-500	1.9×10^{6} @ 0.55 µA	N/A	1.0×10^{5}
[73]	a-Ge:F/ SiO_2/Si	60×60 µm² / sus. µbridge /	5	2×10^{-7}	1000M	100-800	4.2×10^{6}	2.6×10^{-9}	2.6×10^{6}
[74]	VWO_x/ Si	70×70 µm² / sus. µbridge/ 40 nm	- 2.98	1.2×10^{-5}	27k/ 1.1×10^{-3}	0.723	5000 @ 58 µA, @ 12 Hz	5.4×10^{-10} minimal	1.1×10^{7} maximal
[75]	VO_2/ Si	100×10 µm² / sus. µbridge/ 200 nm	- 1.86	N/A	23.2k	11	9000 @ 22 µA, @ 30 Hz	1.7×10^{-11} @ 22 µA, @ 30 Hz	1.9×10^{8} @ 22 µA, @ 30 Hz
[76]	a-YBCO/ SiO_2/Si	100×100 µm²/ planner / 250 nm	3-4	N/A	14M /3.5	5.7	100 @ 10Hz	1.4×10^{-8}	6.95×10^{5}
[19]	YBCO(sc)/ MgO	1×1 mm² / meander / 900 nm	- 3.2	2.3×10^{-5}	1.3M/ 2.1×10^{-2}	5.3	3.4×10^{-3}A/W @ 1 Hz	2.3×10^{-8} @ 1 Hz	3.6×10^{6}
[77]	a-YBCO/ Si	60×60 µm²/ sus. µbridge / 400 nm	-3.4	4×10^{-7}	3.29M	5.68	3.9×10^{4} @ 1 µA @ 11Hz	4.1×10^{-11}	1.1×10^{8}
[15]	Pt/Si	100×75 µm²/ sus. µbridge	0.08	2×10^{-6}	360	0.7	50 @ 750 µA	N/A	1.6×10^{8}
[78]	Ti/Si	50×50 µm²/ sus. µbridge /	0.26	6.3×10^{-7}	N/A	12	1.6×10^{3}	N/A	5×10^{8}

To make in evidence the performance of these uncooled thermal detectors, we will plot their specific detectivity as function of their thermal time response, shown in Figure 1-19.

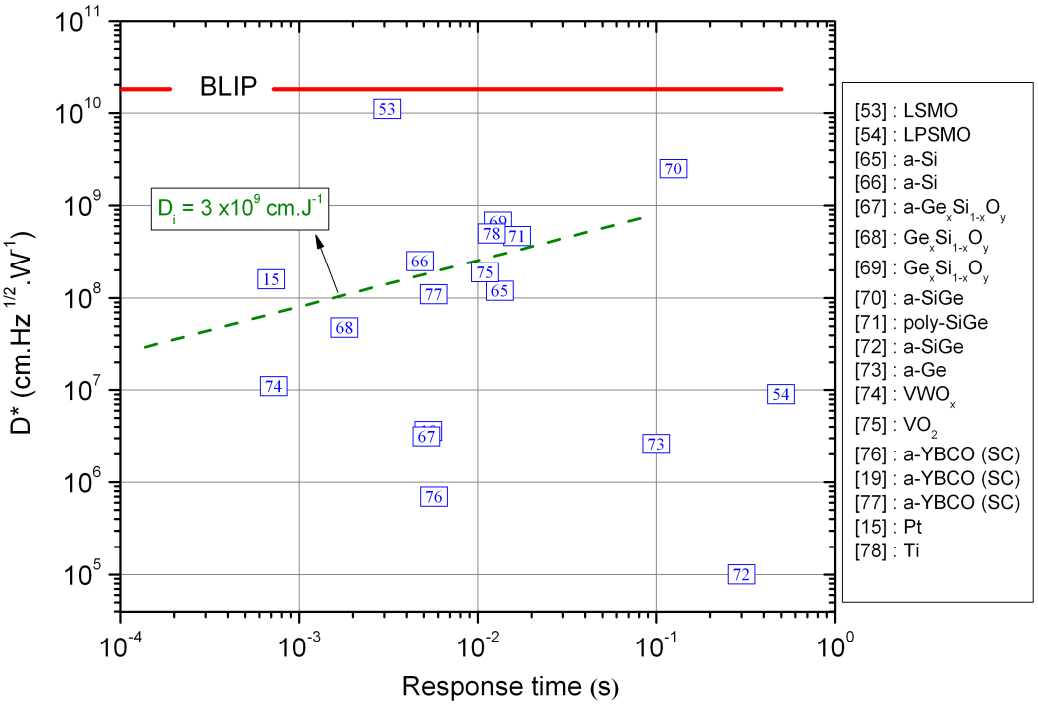

Figure 1-19. Specific detectivity of uncooled bolometers versus response time

The a-SiGe material [70] has proved the maximum D* between the non-manganite materials, but in contrast it has a long response time. In contrast, the metal Pt bolometer [15] presents the shortest response (cf. Table 1-9). In addition, LSMO material [53] shows the highest D* with a value close to that of BLIP detector. This graph shows that these materials have an average D* value of 2×10^{8} cm·Hz$^{1/2}$·W^{-1} and a response time in the range of 1-20 ms. Also, these materials have an average specific detectivity, D_i, value of 3×10^{9} cm·J^{-1}. The main objective of developing a detector is to achieve higher specific detectivity and lower response time. In this thesis, we will explore the performance of LSMO manganite oxide as uncooled infrared thermal detector, because it has been shown that this material is potential candidate for uncooled thermal detector [20][21][22][23].

6. Chapter conclusion

Infrared (IR) detectors are broadly classified into photon detectors and thermal detectors. Photon detectors are fast and more sensitive compared to the thermal detectors. The appearance of uncooled detectors has opened new opportunities for IR detection for both military and commercial applications due to their small size, less power consumption, and they are less expensive. The recent advances in microelectromechanical systems (MEMS) technology allow fabricating sensitive thermal bolometric detectors on thermally isolated hanging membranes. A bolometer employs a characteristic of thermally sensitive layer that changes its resistance according to the change in temperature. Many materials have been used for IR active layer of bolometer, such as metals and semiconductors.

In this chapter we presented the fundamentals of infrared detectors, with introducing the principle of IR radiation and detectors. Then, the thermal detector types and principle of operation have been given. Also, a detailed discussion of bolometers (principle, types, model, and figures of merit) was presented. We also introduced the main properties of the developed used material in this thesis, LSMO. Finally, a state of the art of uncooled bolometers has been exposed.

References for chapter I

[1] A. Rogalski, "Infrared detectors: Status and trends", Progress in Quantum Electronics, vol. 27, no. 2, pp. 59–210, (2003).

[2] J-H Kim Phd thesis, "Micromachined epitaxial golossal magnetoresistors for uncooled uncooled infrared bolometer", Royal Institude of Technology, (2005).

[3] A. Rogalski, "Infrared detectors: 2nd ed.", CRC Press, (2011).

[4] H. Budzier and G. Gerlach, "Thermal infrared sensors: Theory, Optimisation and Practice", John Wiley & Sons Inc., (2011).

[5] P. Kruse, L. McGlauchlin, and R. McQuistan, "Elements of Infrared Technology: Generation, Transmission and Detection", John Wiley & Sons, Inc., (1962).

[6] "Aerospace science and technology dictionnary." http://www.hq.nasa.gov/office/hqlibrary/aerospacedictionary/

[7] P.R. Norton, "Infrared detectors in the next millennium", Proceedings of SPIE 3698, pp. 652-665, (1999).

[8] M. Razeghi, "Current status and future trends of infrared detectors", Opto-Electronics Rev., vol. 6, pp. 155-194, (1998).

[9] A. Rogalski, "History of infrared detectors", Opto-Electronics Rev., Vol. 20, pp. 279-308, (2012).

[10] H. V. Hayes, "A new receiver of radiant energy," Rev. Sci. Instrum., vol. 7, no. 5, pp. 202-204, (1936).

[11] H. A. Zahl and M. J. E. Golay, "Pneumatic heat detector", Rev. Sci. Instrum., vol. 17, no. 11, pp. 511-515, (1946).

[12] M. J. E. Golay, "A pneumatic infrared detector", Rev. Sci. Instrum., vol. 18, no. 5, pp. 357-362, (1947).

[13] R. A. Wood, "Uncooled infrared imaging systems," in Semiconductor and Semimetals, (D. D. Skatrud and P. W. Kruse, eds.), vol. 47, ch. 3, Academic Press, (1997).

[14] A. Giani, F. Mailly, F. Pascal-Delannoy, A. Foucaran, and A. Boyer, "Investigation of Pt/Ti bilayer on SiN_x/Si substrates for thermal sensor applications ", J. Vac. Sci. Technol. A vol. 20, p.112, (2002).

[15] K. C. Liddiard, "Thin Film Resistance Bolometer IR detectors", Infrared Phys., vol. 24, pp. 57-64, (1984).

[16] V. Y. Zerov, Y. V. Kulikov, V. G. Malyarov, I. A. Khrebtov, I. I. Shaganov, and E. B. Shadrin, "Vanadium oxide films with improved characteristics for IR microbolometric matrices", Tech. Phys. Lett. , vol. 27, pp. 378-380, (2001).

[17] A.J. Syllaios, T.R. Schimert, R.W. Gooch, W.L. McCardel, B.A. Ritchey and J.H. Tregilgas, "Amorphous Silicon Microbolometer Technology", Mater. Res. Soc. Symp. Proc. 609, (2000).

[18] A. G. Unil Perera, "Bolometers", Published by InTech, (2012).

[19] V. S. Jagtap, A. Scheuring, M. Longhin, A. J. Kreisler, and A. F. Dégardin, "From Superconducting to Semiconducting YBCO Thin Film Bolometers: Sensitivity and Crosstalk Investigations for Future THz Imagers", IEEE T. Appl. Supercon., vol. 19, (2009).

[20] A. Goyal, M. Rajeswari, R. Shreekala, S. E. Lofland, S. M. Bhagat, T. Boettcher, C. Kwon, and T. Venkatesan, "Material characteristics of perovskite manganese oxide thin films for bolometric applications", Appl. Phys. Lett. Vol. 71, p. 2535, (1997).

[21] L. Méchin, J.-M. Routoure, B. Guillet, F. Yang, S. Flament, and D. Robbes, "Uncooled bolometer response of a low noise $La_{0.7}Sr_{0.3}MnO_3$ thin film" J. Appl. Phys, vol. 87, p. 204103, (2005).

[22] L. Méchin, J.-M. Routoure, S. Mercone, F. Yang, S. Flament, and R. Chakalov, "1/f noise in patterned $La_{0.7}Sr_{0.3}MnO_3$ thin films in the 300–400 K range", J. Appl. Phys, vol. 103, p. 083709, (2008).

[23] F. Yang, L. Méchin, J.-M. Routoure, B. Guillet, and R. A. Chakalov, "Low-noise $La_{0.7}Sr_{0.3}MnO_3$ thermometers for uncooled bolometric applications," J. Appl. Phys, vol. 99, p. 024903, (2006).

[24] S. Wu, "Bruit basse fréquence dans des couches minces $La_{0.7}Sr_{0.3}MnO_3$ gravées: vers la réalisation de microcapteurs performants", Phd thesis, university of Caen Basse-Normandie, (2012).

[25] S. Maine, C. Koechlin, R. Fleurier, R. Haidar, N. Bardou, C. Dupuis, B. Attal-Trétout, P. Mérel, et al. "Mid-infrared detectors based on carbon nanotube films", phys. status solidi C, vol. 7, pp. 2743-2746, (2010).

[26] S. Karanth, M.A. Sumesh, V. Shobha, H. Ganesh Shanbhogue, and C.L. Nagendra, "Infrared detectors based on thin film thermistor of ternary Mn–Ni–Co–O on micro-machined thermal isolation structure", Sensor Actuator A, vol. 153, pp 69-75, (2009).

[27] D. Fobes, E. Vehstedt, J. Peng, G. C. Wang, T. J. Liu et al., "Metal-insulator transition in doped Ca_2RuO_4: bolometric detection", J. Appl. Phys., vol. 111, p. 083709 (2012).

[28] S. Verghese, P. L. Richards, K. Char, and S. A. Sachtjen, "Fabrication of an infrared bolometer with a high Tc superconducting thermometer", IEEE Trans. Magn., vol. 27, pp. 3077-3080, (1991).

[29] P. L. Richards, "Bolometers for infrared and millimeter waves", J. Appl. Phys., vol. 76, p. 1, (1994).

[30] P. W. Kruse, "Physics and application of high temperature superconductors for infrared detectors", Semicond. Sci. Technol., vol. 5, pp. S229-S239, (1990).

[31] J. C. Mather, "Bolometer noise: nonequilibrium theory", Applied Optics, vol. 21, pp. 1125-1129, (1984).

[32] F.N. Hooge, "1/f noise is no surface effect" Physics Letters A, vol. 29, pp. 139-140, (1969).

[33] P. W. Kruse, "The design of uncooled infrared imaging arrays" Proc. SPIE 2746, pp. 34-37, (1996).

[34] P. W. Kruse, "Principles of Uncooled Infrared Focal Plane Arrays", Edited by P.W. Kruse, and D. D. Skatrud, Academic Press, (Semiconductors and Semimetals ; v. 47), pp. 17-40. (1997).

[35] I. A. Khrebtov, "Superconductor Infrared and Submillimeter Radiation Receivers", Sov. J. Opt. Technol., vol. 58, p. 261, (1991).

[36] A. Urushibara, Y. Moritomo, T. Arima, A. Asamitsu, G. Kido and Y. Tokura, "Insulator-metal transition and giant magnetoresistance in $La_{1-x}Sr_xMnO_3$", Phys. Rev. B, vol. 51, p. 14103, (1995).

[37] Y. Okimoto, T. Katsufuji, T. Ishikawa, T. Arima, and Y. Tokura "Variation of electronic structure in $La_{1-x}Sr_xMnO_3$ ($0 \leq x \leq 0.3$) as investigated by optical conductivity spectra", Phys. Rev. B, vol. 55, p. 4206, (1997).

[38] C. M. Sierra, Phd thesis, " New features in solution derived $La_{0.7}Sr_{0.3}MnO_3$ thin films: spontaneous outcropping and nanoscale reversible resistive switching ", University of Autònoma de Barcelona, (2010).

[39] G. H. Jonker, J.H. Vansanten, "Ferromagnetic Compounds of Manganese with Perovskite Structure", Physica, vol. 16, pp. 337–349, (1950).

[40] R. von Helmolt, J. Wecker, B. Holzapfel, L. Schultz, and K. Samwer, "Giant negative magnetoresistance in perovskitelike $La_{2/3}Ba_{1/3}MnO_x$ ferromagnetic films", Phys. Rev. Lett., vol. 71, p. 2331, (1993).

[41] H. Y. Hwang, S-W. Cheong, N. P. Ong, and B. Batlogg, "Spin-Polarized Intergrain Tunneling in $La_{2/3}Sr_{1/3}MnO_3$", Phys. Rev. Lett., vol. 77, p. 2041, (1996).

[42] S. Jin, T.H. Tiefel, M. McCormack, R.A. Fastnacht, R. Ramesh, and L.H. Chen, "Thousandfold change in resistivity in magnetoresistive La-Ca-Mn-O films", Science vol. 264, pp. 413-415, (1994).

[43] Y. Tokura, Y. Tomioka, H. Kuwahara, A. Asamitsu, Y. Morimoto, and M. Kasai, "Origins of colossal magnetoresistance in perovskite-type manganese oxides", J. Appl. Phys. , vol. 79, pp. 5288–5291, (1996).

[44] D. Fadil, S. Wu, P. Perna, B. Renault, M. Saïb, S. Lebargy, J. Gasnier, B. Guillet, J.-M. Routoure, S. Flament, L. Méchin, "Direct observation of magnetization reversal and low field magnetoresistance of epitaxial $La_{0.7}Sr_{0.3}MnO_3/SrTiO_3$ (001) thin films at room temperature", J. Appl. Phys., vol. 112, p. 013906, (2012).

[45] S. Liu, B. Guillet, A. Aryan, C. Adamo, C. Fur, J.-M. Routoure, F. Lemarié, D.G Schlom, L. Méchin, "$La_{0.7}Sr_{0.3}MnO_3$ suspended microbridges for uncooled bolometers made using reactive ion etching of the silicon substrates", *Microelectronic Engineering*, *In Press, Accepted Manuscript*, *201.3*

[46] S. Wu, D. Fadil, S. Liu, A. Aryan, B. Renault, J. –M. Routoure, S. Flament, P. Langlois, L. Méchin, and B. Guillet, "$La_{0,7}Sr_{0,3}MnO_3$ Thin films for magnetic and Temperature Sensors at Room Temperature ", Sensor & Transd. J., vol. 14-1, pp. 253-265, (2012).

[47] A. Hammouche, E. Siebert, and A. Hammou, "Crystallographic, thermal and electrochemical properties of the system $La_{1-x}Sr_xMnO_3$ for high temperature solid electrolyte fuel cells", Mater. Res. Bull., vol. 24, pp. 367-380, (1989).

[48] T. Venkatesan, M. Rajeswari, Z.-W. Dong, S. B. Ogale, and R. Ramesh, "Manganite-based devices: opportunities, bottlenecks and challenges", Phil. Trans. R. Soc. Lond. A, vol. 356, no. 1742, pp. 1661–1680, (1998).

[49] L. M. Wang, J. -H. Lai, J. -L. Wu, Y. -K. Kuo, and C. L. Chang, "Effects of Ru substitution for Mn on $La_{0.7}Sr_{0.3}MnO_3$ perovskites", J. Appl. Phys., vol. 102, p. 023915, (2007).

[50] Y. K. Kuo , R. T. Jiang , L. M. Wang, "Anomalous Behavior in Ru-doped $La_{0.7}Sr_{0.3}MnO_3$ perovskites", Chinese J. of Physics, vol. 43, p. 745, (2005).

[51] M. N.Khlopkin, G. Kh.Panova, A. A. Shikov, V. F. Sinyavskiĭ, and D. A. Shulyatev, "Heat Capacity of $La_{1-x}Sr_xMnO_3$ Single Crystals in Different Magnetic States", Phys. Solid State, vol. 42, p. 114, (2000).

[52] I. El-Kassab, A.M. Ahmed, P. Mandal, K. Barner, A. Kattwinkel, and U. Sondermann, "Heat conductivity of $La_{1-x}Sr_xMnO_3$ surface layers", Physica B, vol. 305, p. 233 (2001).

[53] S. Liu, "Fabrication et caractérisation électrique et thermique de microbolomètres non refroidis suspendus à base de couches minces $La_{0.7}Sr_{0.3}MnO_3$ sur silicium", Phd thesis, university of Caen Basse-Normandie, (2013).

[54] A. Lisauskas, S. I. Khartsev, and A. Grishin, "Tailoring the colossal magnetoresistivity: $La_{0.7}(Pb_{0.63}Sr_{0.37})_{0.3}MnO_3$ thin-film uncooled bolometer ", Appl. Phys. Lett., vol. 77, p. 756 (2000).

[55] K. Hayashi, E. Ohta, H. Wada, H. Higuma, and S. Miyashita, "Fabrication of Bi–La–Sr–Mn–O Uncooled Microbolometer", Jpn. J. Appl. Phys., vol. 40, pp. 5281–5284, (2001).

[56] P. Lobotka, M. Lexmann, S. Gazi, I. Vavra, K. Sedlackova, M. Pripko, and K. Frohlich, "La_xMn0_3 manganite perovskite thin films for bolometric applications", Proc. Of 16th European Conf. on solid state Transducers, pp. 141-143, (2002).

[57] M. Rajeswari, C. H. Chen, A. Goyal, C. Kwon, M. C. Robson, R. Ramesh, and T. Venkatesan, "Low-frequency optical response in epitaxial thin films of $La_{0.67}Ca_{0.33}MnO_3$ exhibiting colossal magnetoresistance", Appl. Phys. Lett., vol. 68, p. 3555, (1996).

[58] M-T. Hong, Y-C. Chen, C-C. Hsu, W-C. Wu, T-C. Chow, and H. Chou, "Optical Detection by a $La_{0.67}Ca_{0.33}MnO_{3-y}$ Thin-Film Microbridge", Jpn. J. App. Phys., vol. 40, pp. 4886-4890, (2001).

[59] J. H. Hao, X. Mao, C. H. Chen, and D. X. Lu, "Room Temperature Bolometric Applications Using Manganese Oxide Thin Films", Int. Journal of Infrared and Millimeter Waves, vol. 20, pp. 2113-2120, (1999).

[60] J. H. Hao, X. T. Zeng, and H. K. Wong, "Optical response of single-crystal (La,Ca)MnO_3 thin films", J. Appl. Phys., vol. 79, pp. 1810-1812, (1996).

[61] R. J. Choudhary, Anjali S. Ogale, S. R. Shinde, S. Hullavarad, S. B. Ogale, and T. Venkatesan, "Evaluation of manganite films on silicon for uncooled bolometric applications", Appl. Phys. Lett., vol. 84, pp. 3846-3848, (2004).

[62] W-B. Song and J. J. Talghader, "Design and characterization of adaptive microbolometers", J. Micromech. Microeng., vol. 16, pp. 1073–1079, (2006).

[63] V. S. Jagtap, A. Scheuring, M. Longhin, A. J. Kreisler, and A. F. Dégardin, "From Superconducting to Semiconducting YBCO Thin Film Bolometers: Sensitivity and Crosstalk Investigations for Future THz Imagers", IEEE T. Appl. Supercon., vol. 19, pp. 287-292, (2006).

[64] A. Mahmood, D. P. Butler, and Z. Çelik-Butler, "Micromachined bolometers on polyimide", Sensor Actuator A, vol. 132, pp. 452–459, (2006).

[65] X-M Liu, H-J Fang, and L-T Liu, "Study on new structure uncooled a-Si microbolometer for infrared detection", Microelectron. J., vol. 38, pp. 735–739, (2007).

[66] T. Ma, Y. Liu, and T. Li, "A (100) direction front-etched membrane structure for a micro-bolometer",J. Micromech. Microeng., vol. 19, p. 129901, (2009).

[67] M. M. Rana and D. P. Butler, "High responsivity a-$Si_xGe_{1-x}O_y$:H Microbolometers," IEEE Sensors J., vol. 7, pp. 1413–1419, (2007).

[68] E. Iborra, M. Clement, L.V. Herrero, and J. Sangrador, "IR uncooled bolometers based on amorphous $Ge_xSi_{1-x}O_y$ on silicon micromachined structures", J. Microelectromech. S., vol. 11, pp. 322–328, (2002).

[69] A.H.Z. Ahmed and R.N. Tait, "Characterization of an amorphous $Ge_xSi_{1-x}O_y$ microbolometer for thermal imaging applications", IEEE T. Electr. Dev., vol. 52, pp. 1900- 1906, (2005).

[70] M. Moreno**,** A. Kosarev, A. Torres and R. Ambrosio, "Fabrication and performance comparison of planar and sandwich structures of micro-bolometers with Ge thermo-sensing layer" , Thin Solid Films, vol. 515, pp. 7607-7610, (2007) .

[71] L. Dong, R. Yue, and L. Liuff, "An uncooled microbolometer infrared detector based on poly-SiGe thermistor", Sensor Actuator A, vol. 105, pp. 286–292, (2003).

[72] M. Garcia, R. Ambrosio, A. Torres, and A. Kosarev, "IR bolometers based on amorphous silicon germanium alloys", J. Non-Cryst. Solids, vol. 338–340, pp. 744–748, (2004).

[73] A. Torres, A. Kosarev, M.L. Garcia Cruz, and R. Ambrosio, "Uncooled micro-bolometer based on amorphous germanium film", J. Non-Cryst. Solids, vol. 329, pp. 179–183, (2003).

[74] N. Chi-Anh, H-J. Shin, K. Kim, Y-H. Han, and S. Moon, "Characterization of uncooled bolometer with vanadium tungsten oxide infrared active layer", Sensor Actuator A, Vol. 123–124, pp. 87-91, (2005).

[75] C. Chen, X. Yi, X. Zhao, and B. Xiong, "Characterizations of VO_2-based uncooled microbolometer linear array", Sensor Actuator A, vol. 90, pp. 212-214, (2001).

[76] A. J. Kreisler, V. S. Jagtap, and A. F. Dégardin, "Infrared Response in the 95 to 300 K Temperature Range of Detectors Based on Oxygen-depleted Y-Ba-Cu-O Thin Films", Physics Procedia, vol. 36, pp. 223-228, (2012).

[77] S. A. Dayeh, D. P. Butler, and Z. Celik-Butler, "Micromachined infrared bolometers on flexible polyimide substrates", Sensor Actuator A, vol. 118, pp. 49–56, (2005).

[78] H.K. Lee, J.B.Yoon, E. Yoon, S.B. Ju, Y.J. Yong, W. Lee and S.G. Kim, "A High Fill-Factor Infrared Bolometer using Micromachined Multilevel Electrothermal Structures", IEEE T. Electr. Dev., vol. 46, pp. 1489-1491, (1999).

CHAPTER II

Design, realizing and characterization of measurement setup

One objective of this thesis was the design and realization of an optical set-up to characterize the LSMO (or other similar material) bolometer samples in terms of radiation detector. This test-stand aims to be flexible, and allows trustful and repeatable measurements over a large range of frequency. In this chapter I will present a detailed explanation of the used measurement setup, including design considerations and background principles.

1. Block diagram and measurement principle

1.1. Block diagram

The overall total measurement system is presented in Figure 2-1. The system consists of four main blocks, which will be described in details in the next paragraphs.

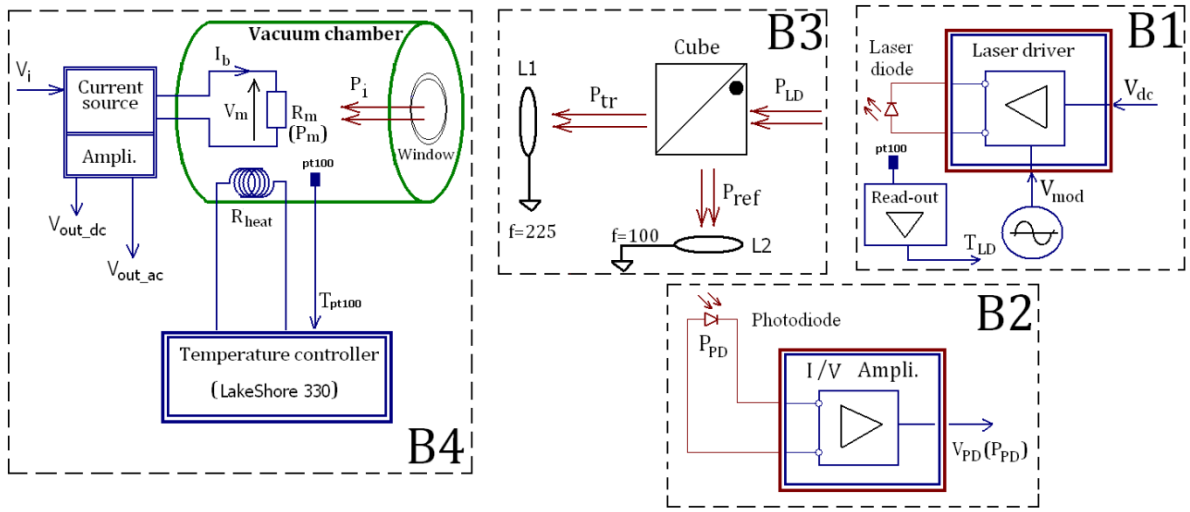

Figure 2-1. Block diagram of the measuring test-stand setup. B1 is laser diode and its driver, B2 is the photodiode and its amplifier power measurement unit, B3 is the optical elements, B4 is the sample installation and control equipment

The first block B1 consists of the radiation source (semiconductor laser diode) and the necessary electronic driver circuit. Its role is to provide a stable modulated power of the laser diode to heat the tested sample. The laser spot will be precisely identified, in order to calculate the received power by the tested sample. This block will be detailed in sections 2 and 3. The block B2 is used to measure simultaneously the radiated power. Thus, it includes a high speed photodiode and current/voltage amplifier. All the optical elements are included in block B3, which consists of beam splitter and convergent lenses. A detailed characterization

of B2 and B3 will be given in section 4. The block B4, detailed in section 5, contains the necessary equipments for installing the tested sample and controlling the temperature of the sample holder. Also, this block includes the homemade readout electronics that is used to measure the electrical resistance of the sample, and also to measure its intrinsic noise. More details on this block will be presented in section 6 of this chapter.

All the equipments of this system are homemade electronic boards, except the temperature controller and the optical elements in the block B3. These homemade electronic boards include: Read-out electronics, sample installation equipments, readout electronics (current source with amplification stage), laser driver, I/V converter.

The tested sample, which electrical resistance is R_m, is glued to a copper plate, having a resistive heating element (R_{heat}), then fixed into a vacuum chamber equipped with an optical window. The chamber is evacuated by a mechanical pump, and no cooling system was used. A temperature controller was used to maintain temperature stability of 15 mK during measurements at fixed temperature. The controller, also, provides the possibility of heating the sample in the range 300-350 K.

1.2. Measurement principle

In order to characterize the performance of bolometer as uncooled radiation thermal detector, we need to measure its optical responsivity to a radiation heating source. So that a semiconductor laser diode (635 nm, 5 mW), in the block B1, is biased to a DC working point (by V_{dc}) and then electronically modulated at different frequencies (by V_{mod}). The output radiated power (P_{LD}) is finally used to optically heat the device, after passing through many optical elements of block B3 (Cube, L1, L2). The laser beam was collimated and passed through a 1:1 beam splitter with one beam reaching a photodiode (P_{PD}) and the other reaching the studied sample (P_i). Thus, by knowing the transmission coefficient of all optical elements, the power of the incident light on the sample (P_i) can be directly obtained by measuring the photodiode output signal (V_{PD}). Moreover, the laser diode spot shape and size has been identified and measured.

The LSMO sample was current biased using a quasi-ideal DC current source, which exhibits very high output impedance and a negligible noise contribution [1]. A standard four-probe technique was used to provide bias current and measure the voltage signal of the LSMO sample (V_m). The output voltage of the sample was read out by a homemade voltage

amplifier, which provides two outputs: one DC voltage measurements, and one AC voltage measurements with amplification and filtering. The dynamic optical response and electrical noise measurements were carried out using a spectrum analyser (HP3562A). The measurement setup is equipped with a laptop computer with GPIB interface to read and store the measured values.

2. Laser Diode Characteristics

2.1. Fundamental of laser diode

The light emitted by a semiconductor diode arises from the recombination of electrons and holes at a p-n junction as current flows through it in the forward direction. An electron from the n-layer conduction band recombines with a hole from the p-layer emitting a photon. This mechanism was first proposed by Watanabe and Nishizawa in 1957 [2] and eventually realized in 1962 with the first homojunction diode laser [3][4]. The detailed theory of the semiconductor laser has been extensively discussed. However, it is useful here to focus on specific features of these devices to understand their role in the work herein.

2.2. Electro-optical characteristics

The most common of the laser diode characteristics is the P-I curve [5], as seen in Figure 2-2(a). It plots the output light power against the drive or forward current applied to the laser. This curve is used to determine the laser's DC operating point (drive current at the rated optical power) and the threshold current I_{th} (current at which lasing begins). This current distinguishes the LED light emitting region A from the laser oscillating region B. The I_{op} current is a current in the forward direction that is required to generate rated light output power P_o. Another important characteristic is the efficiency (γ) expressed in $W \cdot A^{-1}$. This is the increase in light output power per unit of drive current, in the laser oscillating region. As can be seen in Figure 2-2(b), the threshold and the efficiency of the laser are affected by the laser's temperature.

The laser diode driver must maintain a fixed drive current to get a fixed output power, or employ a real time regulation of the output power. Also, the stabilization of laser temperature must be considered and optimized. The detailed design of laser diode driver circuit will be presented in the paragraph 3.2 of this chapter.

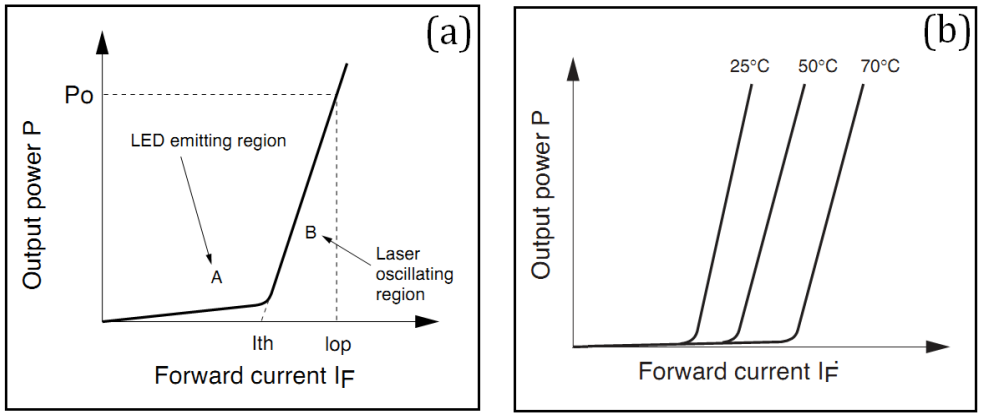

Figure 2-2. A schematic laser diode characteristics: power-current curve (a) and influence of laser temperature (b)

2.3. Spatial characteristics

Another important characteristic of the laser diode is the output light intensity profile. Indeed, laser diodes emit a cone of light, typically elliptical in cross section [5][6], as seen in Figure 2-3(a). The divergence angles of this cone are measured by the full width half maximum light power in the axes perpendicular to (x axis) and parallel to (y axis) the laser's active region [7][8]. To overcome this problematic, one can use collimation optics to get a non divergent parallel beam. The light intensity distribution profile of semiconductor laser diode output is roughly Gaussian in the perpendicular plane [6][7][9], as seen in Figure 2-3(b). If a circular beam profile is required, beam shaping optics can be included in the optical system using prisms or cylindrical lenses.

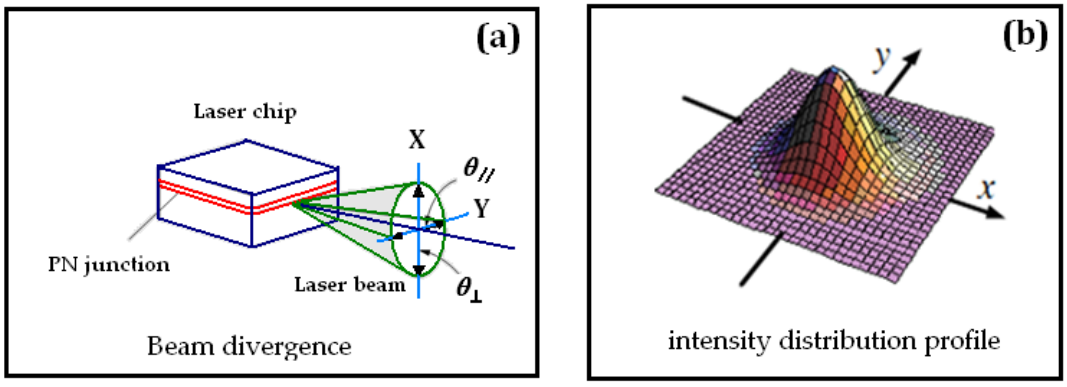

Figure 2-3. Laser beam divergence (a) and intensity distribution profile (b);adapted from[6]

The Gaussian laser beam has an intensity or irradiance (defined as the power incident on a surface, expressed in $W \cdot m^{-2}$) distribution, as a function of the Cartesian coordinates (x and y) measured from the beam center perpendicular to the axis of propagation (z axis), given by [9][11]:

$$E(x,y) = \frac{2P_{tot}}{\pi w^2} \times \exp\left(-\frac{2x^2 + 2y^2}{w^2}\right) \qquad \text{(II- 1)}$$

where P_{tot} is the total power of the laser beam and w is a measure of the beam width where the irradiance drop to $1/e^2$ of its maximal value.

2.4. Laser diode spot size

Knowledge of beam profile parameters, such as beam diameter, shape, and intensity distribution, is essential for the effective use of lasers in many scientific and industrial applications. The beam diameter, so the spot size, is the most important basic parameter of the laser beam profile to quantify the radiated power. Thus, a correct measurement of the laser beam profile, and so on the beam diameter, is essential for estimating the incident laser power on the tested sample, especially for samples that are smaller than the laser spot size.

2.4.1. Beam profile estimation methods

Many beam profilers, with different techniques, are commercially available for beam profile measurement. There are four main types of spatial beam-profiling instrumentation: camera-based systems, pinhole scanners, knife-edge scanners, and slit scanners [9][11][12][13][15]. Other techniques have been developed recently, like the photoacoustic technique [14]. Each method has specific advantages and disadvantages and may result in slightly different measurements. In addition, each method has its own speed and accuracy characteristics. The criteria for selecting the best suited measurement technique depend on the nature of the laser source and the requirements for the measurements.

a) Camera-Based method

Cameras use a two dimensional array of square or rectangular pixels as the imaging device. The intensity distribution of a laser source is thus recorded pixel by pixel. The main

advantage of such method is that it can detect and display any profile structure, and it can be used with both continuous wave (CW) and pulsed lasers [15].

The main disadvantage of this method is that the measurement resolution is limited by pixel size; therefore it is not useful for measuring very small beams. The pixel size depends on the camera technology (minimum of about 5µm). Indeed, the minimum beam size for these instruments will be typically on the order of 50 µm to 60 µm. Although silicon CCDs (Charge Coupled Device) arrays are quite inexpensive, their spectral response is restricted to the visible range. For higher wavelength, it is necessary to use InGaAs arrays. These are very costly and have fairly large pixel sizes (>30 µm), which limit their spatial resolution. Another disadvantage of camera-based method is its low saturation and damage threshold levels, thus, the use of attenuation element are often required.

b) Scanning Based methods: Knife-edge, Slit, and Pinhole method [9][11][15][16].

Knife-edge, slit, and pinhole scanners generate a profile by mechanically moving a knife-edge or an aperture (slit or pinhole) across the beam in a plane orthogonal to the optical propagation axis. The light passing through is measured by a detector and correlated with the position of the aperture as it crosses the beam. Unlike camera based method, scanners measure only one or two dimensions at a time. Consequently, three dimensional representations generated by these systems are calculated, not measured. The pinhole/knife-edge methods are accurate techniques and have a resolution closer to 1 µm, but they are time-consuming and difficult and do not operate in real time for pulsed lasers with a pulse repetition frequency of less than 100 kHz [13][14]. Thus, typically, these methods can only be used with CW lasers.

2.4.2. Beam diameter definitions

Optical beams do not actually have sharp physical edges. Hence, the common methodology is to consider the beam diameter that is made between two opposite points at which the intensity equals a specified fraction of the beam's peak intensity [17]. When beams are Gaussian, or approximately Gaussian, the common value of this measurement is at the $1/e^2$ diameter. This is the point at which the beam intensity has fallen to $1/e^2$ (13.5%) of its peak value when measured in a plane orthogonal to the optical axis. Another common measurement is at the full-width-half maximum (referred to as FWHM) level, where the

intensity drops to one half of its maximum value (see Figure 2-4). The beam diameter measurement, by either method, allows one to determine other important features of the spatial irradiance pattern of the beam.

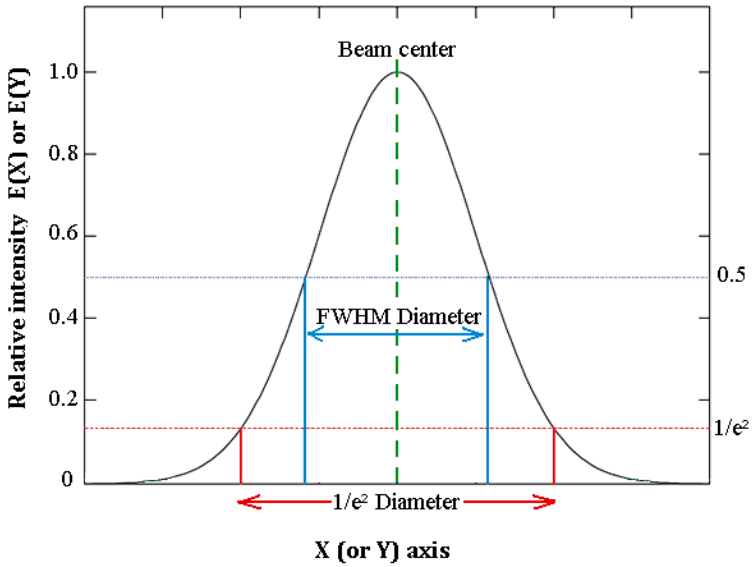

Figure 2-4. One dimension diagram of a Gaussian laser beam showing FWHM and 1/e² diameter

For a Gaussian beam, the relationship between $1/e^2$ diameter ($D_{1/e^2} = 2w$) and the FWHM diameter (D_{FWHM}) can be deduced from equation (II- 1), and given by,

$$D_{1/e^2} = 2w = \frac{\sqrt{2}\, D_{FWHM}}{\sqrt{\ln 2}} = 1.699 \times D_{FWHM} \qquad \text{(II- 2)}$$

A more recent definition of beam width or diameter is called the second moment [18]. Recent ISO standards have defined a second moment beam width, abbreviated D4σ, which, for many cases, gives the most realistic measure of the actual beam width. D4σ is shorthand for the diameter that is 4 times σ, where σ is the standard deviation of the intensity distribution. The D4σ is the ISO international standard definition for beam width. For an ideal single-mode Gaussian beam, the D4σ and $1/e^2$ width measurements would give the same value.[16][18][19][20].

3. Radiation source and driver

I will explain in this section the detailed design and functionality principles of our laser diode driver circuit. Also, the electro-optical and special characteristics of the used laser diode as radiation heating source will be given. Finally, I will present the estimation method of the received power by the studied sample.

3.1. Laser diode driver: theory and principle

The aim of this paragraph is to present a conceptual approach to the design of a basic semiconductor laser diode driver. Since the laser output power depends on both the diode junction temperature and drive current, stable laser operation requires that these quantities be precisely regulated. Basically, there are two fundamental methods, ACC and APC, which can be used to control the operation of laser diode [6][21][22].

3.1.1. Automatic Current Control (ACC)

A laser diode is a current-driven device, and the most fundamental method for operating a laser diode is in a constant current mode using Automatic Current Control (ACC) method. This approach maintains a precise and constant current through the laser diode regardless of impedance changes in the device or other external factors such as variations in the power supplied to the driver itself.

One drawback to constant current operation is that the output power of the laser diode changes inversely to its operating temperature. Therefore, ACC works best in conjunction with some sort of temperature control on the laser diode. An advantage of constant current operation is that unlike Automated Power Control (APC) mode, the laser diode is not inside the control loop, making modulation and pulsing of the laser's output power much easier.

3.1.2. Automatic Power Control (APC)

As previously mentioned, ACC mode has a limitation in the fact that laser diodes are susceptible to changes in operating temperature. This can be overcome by operating the laser diode in constant power mode using APC method. It makes use of a current provided by a photodiode, which is directly proportional to the output power of the laser diode. The photodiode can either be external to the laser diode or integrated into the rear facet of the

device. When operating in APC mode, the photodiode current becomes a feedback signal to the current source, thereby placing the laser diode inside of the control loop. Instead of regulating the laser diode current, the system regulates the photodiode current and indirectly regulates the output power of the laser diode.

A significant drawback to APC driver is that it needs a means to limit the current through the laser diode, which could complicate the driver. Another drawback is, in cases such as simply forgetting to connect the photodiode, that it would cause an open loop situation that would be catastrophic to the laser diode.

Finally, choosing one method or the other depends strongly on the application itself, and the final implementation of the driver. In our case, I did use the ACC mode to get a simple driver circuit. Using the real time measurement of radiated power by a photodiode (cf. section 4), we can overcome the problem of the operating temperature of laser diode.

3.2. Laser diode driver: design and characterization

3.2.1. The desired functionality

The primary function of the wanted laser driver is to provide appropriate currents for bias and modulation of the laser diode (Figure 2-5). The bias current (I_{dc}) is a constant current that pushes the laser diode operating range beyond its threshold value (I_{th}) and into the laser emitting region. In contrast, the modulation current (I_{mod}) is an alternating current that modulates the output laser power (P) in the required frequency rang. Thus, the driver design has to achieve the functionality presented in Figure 2-5.

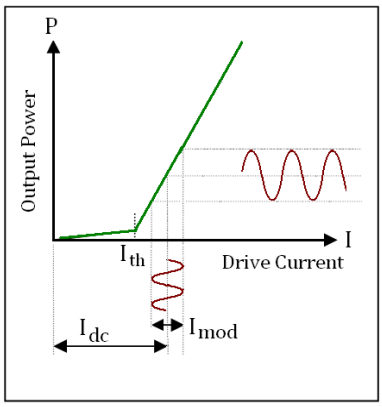

Figure 2-5. The desired functionality of the laser driver

3.2.2. The basic driver design

The objective of this paragraph is to describe the circuit design that has been used to drive the continuous wave laser diode. The basic driver circuit is shown in Figure 2-6. A detailed electronic circuit is given in appendix B. We make the choice of ACC mode to drive the laser diode because we want to make the modulation of the laser's output power much easier. For the drawback of this mode related to temperature, I have analyzed this parameter (cf. Figure 2-9 and related discussion), and a precaution will be considered to overcome it.

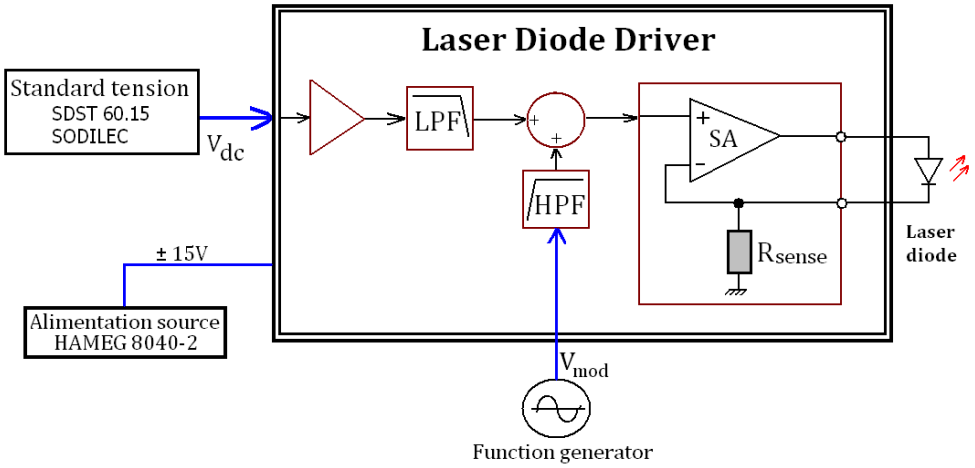

Figure 2-6. Basic representation of laser diode driver electronic circuit

The circuit is a voltage-to-current converter configuration whose objective is to provide a regulated current (bias and modulated) to the laser diode. This regulator consists of operational amplifier SA and current sensing resistor R_{sense} of 50 Ω. The SA amplifier (LT1206) can provide a maximum current of 250 mA with a very high slew rate value of 900 $V \cdot \mu s^{-1}$. It has a nominal bandwidth of 60 MHz, which will be limited to about 10 MHz for the used configuration.

The output is DC biased using a non-inverting input at a DC drive current value of V_{dc}/R_{sense}. This is true since the dynamic resistance of the laser diode is low, about few ohms, compared to R_{sense}. The V_{dc} is a regulated voltage coming from specialized standard voltage source. A Low Pass Filter (LPF) with about 1 Hz cutoff frequency has been used to reject the unwanted perturbations in the V_{dc} input. The modulation input (V_{mod}) is coupled to the non-inverting input via the High Pass Filter (HPF) with cutoff frequency of about 1 Hz.

The characterization of this driver as current regulation will be presented later in Figure 2-9. Also, the dynamic behavior will be analyzed later in Figure 2-16 and its related discussions.

3.3. Laser diode characterization

3.3.1. Electro-optical characteristics

As a radiation source used to heat the studied samples, we selected a red semiconductor continuous wave laser diode referenced as ADL-63058TL (635 nm, 5 mW) from Arima Lasers Company. In order to optimize the use and functionality of this radiation source, we need to characterize its electro-optical and spatial properties. So, I will employ the measuring schema seen in Figure 2-7. Here I used the homemade laser driver (described in paragraph 3.2) to develop a fixed current that drives the laser diode. This current will be changed by varying the input voltage V_{dc}, and measures using the V_I voltage. The output power of laser light (relative to V_P) will be measured using the photodiode PD300 and a watt meter NOVA II. The PD300 size is 10×10 mm² with sensitivity range from 500 pW to 300 mW into the wavelength range 350-1100 nm. To study the temperature stabilization of laser diode, a Pt100 sensor was glued on the laser diode box by using silver paste. This temperature will be acquired by homemade read-out electronics, as a function of V_T voltage. This is a ¼ DC Wheatstone bridge circuit with three-wire configuration for connecting the Pt100. Also, I did use a type K thermocouple (positioned in the area next to the laser source) with a dedicated read-out (referenced as TA-DT-9610Y) for measuring the ambient temperature. A data logger Yokogawa MV100 has been employed to store all measured data during measurement time, with acquisition speed equals to 5 samples per second. To eliminate the variations in outdoor lighting, an opaque tube has been used in face of the photodiode, so reducing the solid angle.

I apply a voltage V_{dc} step by step and wait each time to stabilize the system, and then save the instantaneous values of the radiated laser power (equals $0.6 \times V_P$ for 3 mW measurement range, and 5 volt analog output range of wattmeter), the control voltage (V_{dc}), the laser drive current (equals to V_I/R_{sense}), and the temperature of the metal box of the diode laser (equals $10.7 \times V_T + 25.85$) as function of time.

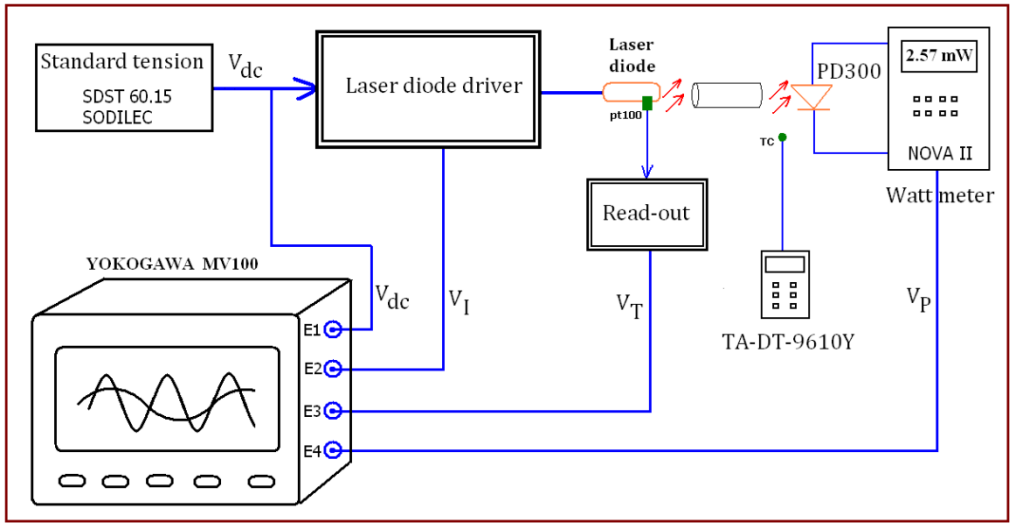

Figure 2-7. Laser diode characterization measurement setup

The Figure 2-8 shows the radiated laser power as a function of laser drive current. It presents the measured characteristic values at 21 °C which are ideally coherent with the nominal values given in the datasheet at 25 °C. Using this graph we can identify the working point, so on the dc power, of the laser diode.

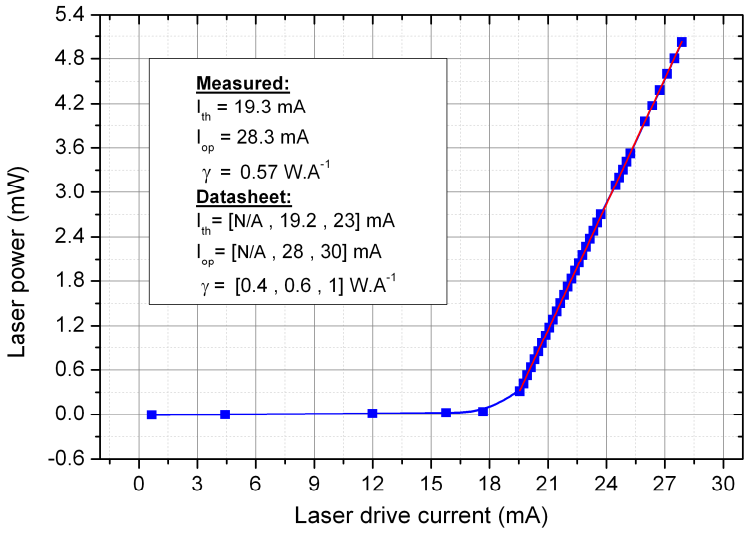

Figure 2-8. The measured laser diode power versus laser drive current at 21 °C. The legend shows the measured and datasheet characteristics

Another important characterization is the stabilization of laser power during the time and as function of laser box temperature. To achieve that, we apply at starting time (t=0 s) a

sufficient V_{dc} voltage in order to get an output laser power equals 5 mW. In the same time I start saving the instantaneous values of laser power (by V_P), laser drive current (by V_I), and the laser box temperature (by V_T) as seen in Figure 2-9.

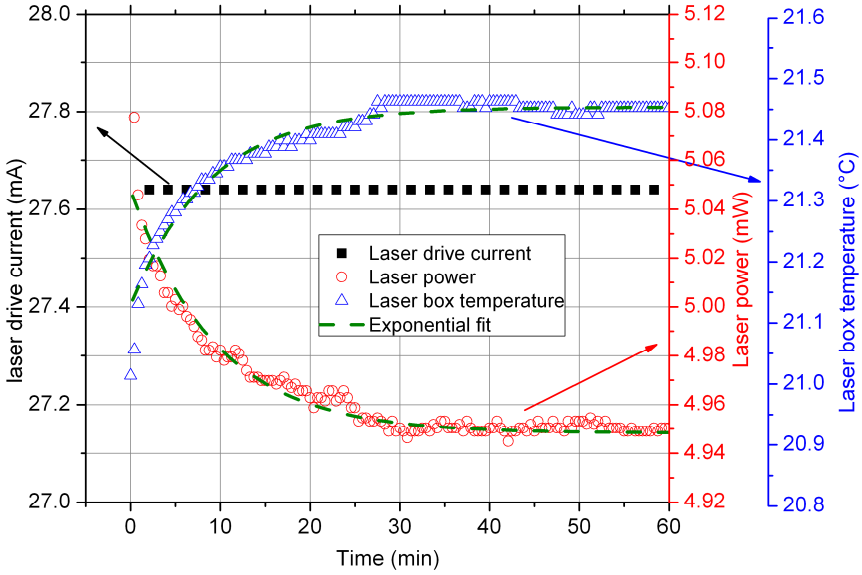

Figure 2-9. The measured power, temperature, and current of the laser diode versus time (100 skipped data points was used for clarity)

From Figure 2-9 we note that the used laser driver (which will be explained later) maintains a very good stability of the laser drive current, so the variation of laser power comes from the variation of temperature (self heating). The operating current equals to 27.6 mA, knowing that the typical nominal value is 28 mA at 25°C.

The laser power shows an exponential decay (Figure 2-9) from its initial value (5.14 mW), with a first order time constant equals to 9.4 min by using the exponential fitting. In contrast, the laser temperature shows an exponential grow from its initial value (21.0 °C) with a first order time constant equals to 8.8 min by using the exponential fitting. Both power and temperature have almost the same time constant, so their variations are strongly related. The laser power stabilizes after about 30 min to a value of about 4.95 mW. Thus, the power drop equals ΔP = 180 µW, so a total power drop of about 3.5%. This drop is in the range of nominal maximum drop 10%.

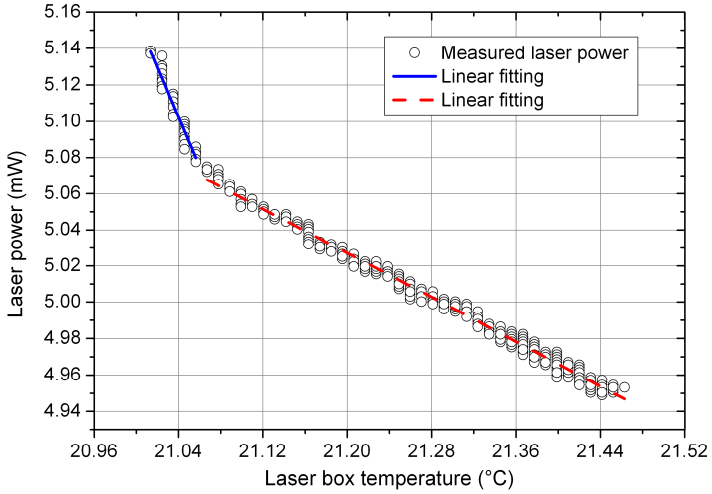

Figure 2-10. Laser diode power versus laser box temperature

As seen in Figure 2-10, we have two linear relations between power and temperature of the laser diode. The solid line, with a higher slope, presents indeed the self heating effect and is related to the thermalization of the laser box temperature with the ambient temperature. The duration of this regime is about 20 s, which was evaluated using the power and temperature measurements as function of time. The dash line presents the variation of laser power with the ambient temperature, with a rate of -305 µW·(°C)$^{-1}$. It is large dependence, but knowing that the duration of an AC optical responsivity measurement takes practically about 1.5 min, this means about 3 µW of DC radiated power variation during this time. This is true by maintaining the same environment conditions, so the same rate of temperature variation. Anyway, this drawback is resolved by a real time measurement of radiated laser power (so on the sample received power) by using a high speed photodiode (cf. paragraph 4.1).

As a result, our laser driver will not incorporate a temperature controller to regulate the laser temperature, which is usually done by employing a Peltier element. This decision has been made to simplify the driver, knowing that this regulation is not needed to achieve our measurement of optical responsivity of LSMO samples.

3.3.2. Spatial characterization

In order to quantify the incident laser power on the studied sample, we need to identify the beam profile and irradiance (or intensity) distribution of the used laser diode. Depending on the availability, advantage, and disadvantage of the known methods to identify the profile

of the laser beam, I chose to use a CCD camera, which gives a true 2D image of the beam. The CCD array sensor can just accept very small power, in order to avoid saturation. This means that it is necessary to use external attenuators to control the amount of light hitting the array.

To identify the laser diode profile, and then estimate the beam diameter and surface, I did employ the measurement setup seen in Figure 2-11. Two polarizers were used to attenuate the laser beam intensity to not saturate the camera imager. Also, I removed the camera lens to get the real size of the spot. Also, a plastic tube has been used in front of the the camera to remove the outdoor lighting. The spot image was captured by a Hauppauge 42019 adapter and special software installed on the laptop. The used camera (Watec 221S) has a number of effective pixels equals 752×582 pixels, and a pixel size equals 8.6×8.3 µm².

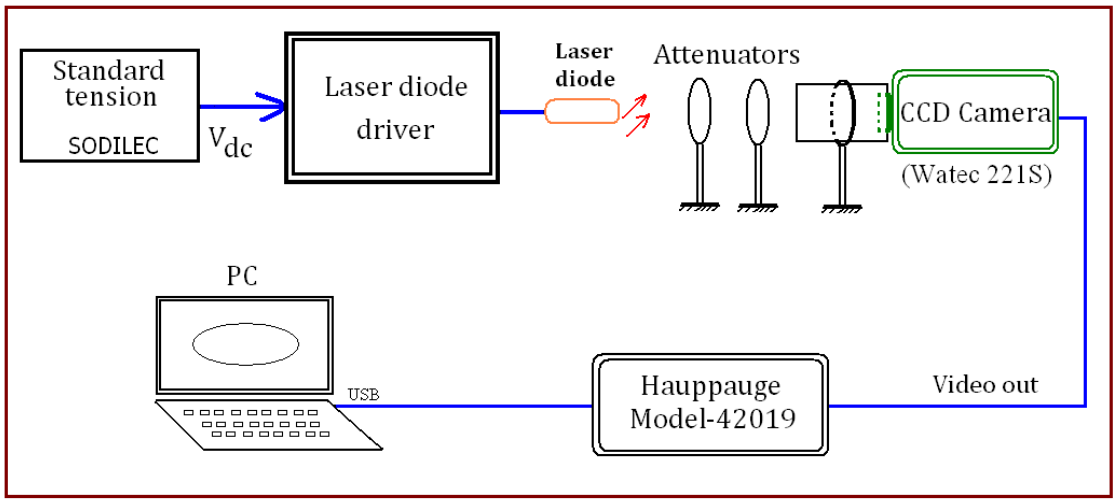

Figure 2-11. Measurement setup for laser diode beam profile

First, I fix the laser current in the laser operation domain. Then, the attenuators are adjusted to get an image of the laser spot without saturation (without white color zones). Now, the image is saved as a jpg file format. Using the image processing software, ImageJ, we can extract the gray scale intensity level (8 bits, thus 0-255) along both X and Y spot axes. Therefore, using Origin software, we plot the curves of variation of the intensity according to X and Y spot axes. We can now estimate the diameter (per X and Y axis) of the laser spot using a Gaussian fitting, and then calculate its surface as an ellipse (see Figure 2-12).

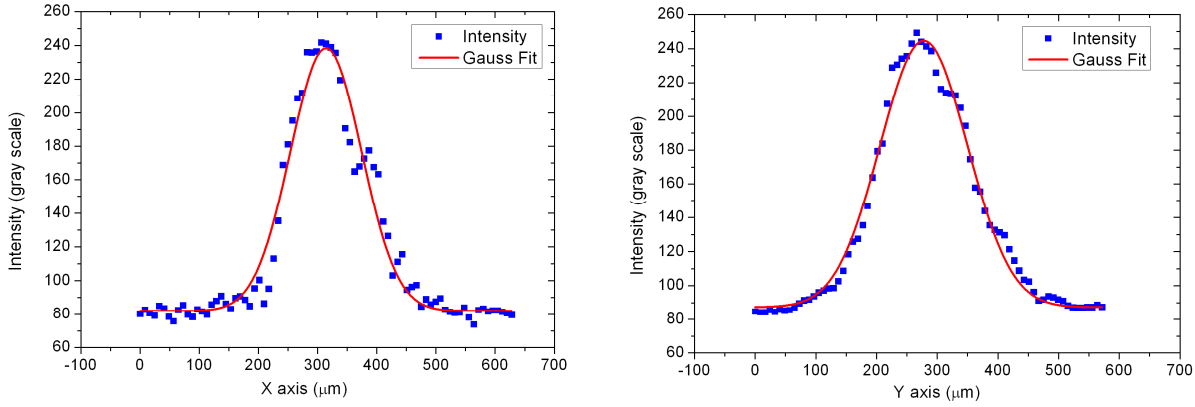

Figure 2-12. Intensity measurement following the X and Y axis of the spot of LD-1 laser diode

The background intensity is not ideally black, which is clear also in the spot photo, so we got an intensity of about 80 in gray scale gradient. Table 2-1 resumes the results for the used laser diodes. Indeed, more than one laser diode has been used because of burnouts during the manipulations. The FWHM diameter estimation was obtained from Gaussian fitting, and the $1/e^2$ diameter (equals D4σ diameter for Gaussian beam) estimation was calculated using equation (II- 2). The surface calculation is based on that the spots have almost an elliptical form, thus its surface equals to $(\pi/4)\times XY$.

Table 2-1 Diameter and surface estimation of used laser diodes

	FWHM diameter (D_{FWHM})			$1/e^2$ diameter (D_{1/e^2})		
	X (μm)	Y (μm)	Surface (10^3 μm²)	X (μm)	Y (μm)	Surface (10^3 μm²)
LD-0	182	267	38.2	310	454	110.5
LD-1	152	176	21.0	258	300	60.8
LD-2	125	105	10.3	214	180	30.3
LD-3	167	138	18.1	290	236	53.8

Indeed, I have many samples with different surfaces, thus knowing the laser spot surface is needed to calculate the power received by the sample. At first glance, I think to use the ratio between sample surface and laser spot surface. The surface of spot can be calculated by considering the elliptical form of the spot and the estimation of its diameter over the two axes X, Y.

Practically, and during measurements, I adjust the fine position of the laser spot in order to have a maximum response of the sample. This means that the spot center is coincident with that of the sample. In fact, using the surface ratio method will results in over estimation of the received power for the small area samples (like 50×50 µm²) because it will receive the portion of spot with the higher intensity, as shown in Figure 2-13. Therefore, the bigger area sample (like 200×200 µm²) will be under-estimated for the received power. Thus, using this method is correct when the spot intensity is uniform. This leads us to think about another correct estimation of the power received by the sample, which will be explained in the next paragraph.

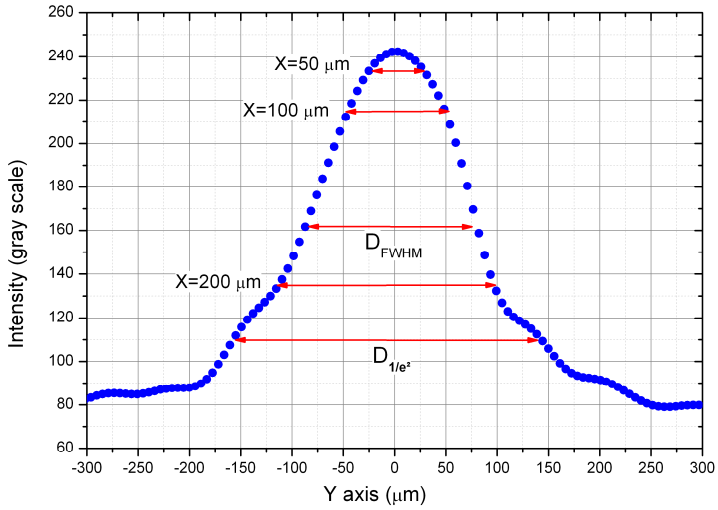

Figure 2-13. Comparison for interpolated received intensity according to sample size (50, 100, 200 µm) over the Y axis (one dimension) of LD-1 laser diode

3.4. Estimation of received power by the studied samples

This estimation is based on the calculus of the ratio between the incident laser power (P_i) and the power received by the studied sample (P_m). The total power calculated by the integration of the laser diode intensity profile equation, and the received power calculated by the integration of intensity equation in the interval defined by the sample size.

We assume a beam propagating in the z-direction with a Gaussian intensity profile given by:

$$E(x,y) = E_0 \exp\left(-\frac{2x^2}{w_x^2}\right) \exp\left(-\frac{2y^2}{w_y^2}\right) \qquad \text{(II- 3)}$$

where w_x and w_y are the $1/e^2$ radius of the beam in the x and y directions respectively. E_0 is the peak intensity expressed in $W \cdot m^{-2}$.

The total power in the beam is given by:

$$P_i = E_0 \int_{-\infty}^{+\infty} \exp\left(-\frac{2x^2}{w_x^2}\right) dx \int_{-\infty}^{+\infty} \exp\left(-\frac{2y^2}{w_y^2}\right) dy = \frac{\pi}{2} E_0 w_x w_y \qquad \text{(II- 4)}$$

If the laser diode spot size is bigger than that of the studied sample, then we need to calculate the portion of power that is received by the sample (P_m). We assume that the studied sample has a rectangular form of dimension 2a×2b. We will consider that the laser beam passes through a rectangular aperture with the same dimension as the sample. Therefore, the power received by the sample, P_m, is given by the equation (II-5):

$$P_m = E_0 \int_{-a}^{+a} \exp\left(-\frac{2x^2}{w_x^2}\right) \int_{-b}^{+b} \exp\left(-\frac{2y^2}{w_y^2}\right) dx\, dy \qquad \text{(II- 5)}$$

Since this integral cannot be solved in closed form, the Error function can be used, which has tabulated values available in books of mathematical tables and on various web sites. The error function is defined as follows:

$$\text{erf}(t) = \frac{2}{\sqrt{\pi}} \int_0^t \exp\left(-t^2\right) dt \qquad \text{(II- 6)}$$

and has the properties that:

$\text{erf}(+\infty) = 1$ and $\text{erf}(-t) = -\text{erf}(t)$

To calculate P_m we have to cast the integral of equation (II- 5) in a standard form. Making the substitutions $u^2 = 2x^2/w_x^2$, $v^2 = 2y^2/w_y^2$ so that $dx = w_x du/\sqrt{2}$, $dy = w_y dv/\sqrt{2}$ and making the necessary change to the limits of the integral leads to:

$$P_m = E_0 \frac{w_x w_y}{2} \int_{-\frac{\sqrt{2}a}{w_x}}^{+\frac{\sqrt{2}a}{w_x}} \exp\left(-u^2\right) \int_{-\frac{\sqrt{2}b}{w_y}}^{+\frac{\sqrt{2}b}{w_y}} \exp\left(-v^2\right) du\, dv \qquad \text{(II- 7)}$$

Using the standard definition and properties of the Error function listed in equation (II- 6), and the symmetry and additive properties of the integral, we get the final result:

$$P_m = P_i \ \mathrm{erf}\left(\frac{\sqrt{2}\,a}{w_x}\right) \mathrm{erf}\left(\frac{\sqrt{2}\,b}{w_y}\right) \qquad \text{(II- 8)}$$

Therefore, this relation provides the possibility to practically calculate the power received by a sample, P_m, of dimensions 2a×2b by knowing the total incident power, P_i, and the radius of the laser spot following the X axis (w_x) and the Y axis (w_y).

Actually, the studied samples have a meander shape (cf. section 8). Hence, the portion of the received power that is laid between meander strips has to be considered, therefore introducing the concept of fill factor. The fill factor is defined as the ratio of the light sensitive area to the total photosite area. Finally, we can calculate the portion of total laser power that is absorbed by a sample of rectangular form with dimensions 2a×2b, which is given by:

$$\frac{P_i}{P_m} = \frac{\text{Fill factor}}{\mathrm{erf}\left(\frac{\sqrt{2}\,a}{w_x}\right) \mathrm{erf}\left(\frac{\sqrt{2}\,b}{w_y}\right)} = F_t \qquad \text{(II- 9)}$$

This way, the real received power by the studied sample can be directly deduced from equation (II- 9). Values of F_t for all the studied samples will be given later in Table 2-5, Table 2-6, and Table 2-7.

4. Measurement of radiated power

4.1. Photodiode and driver

I employ a high speed Si photodiode (Hamamatsu S10784). This photodiode provides high sensitivity (0.45 $A \cdot W^{-1}$ Typ. at 650 nm) with large response band (300 MHz Typ. at 650 nm). Also, I elaborated a homemade Current-to-Voltage (I/V) amplifier (cf. Appendix B) to simultaneously measure the radiated power of the laser diode, then estimate the incident power on the studied sample.

To characterize the photodiode with the I/V amplifier in DC and AC mode, I will employ the setup seen in Figure 2-14. A convergent L1 lens (f = 100 mm) has been used to focus the laser spot over the active surface of the photodiode, and therefore to measure the

total radiated power of the laser diode (P_{LD}). The P_{LD} was measured simultaneously by the photodiode PD300 and a wattmeter (NOVA II) after the lens to eliminate its attenuation.

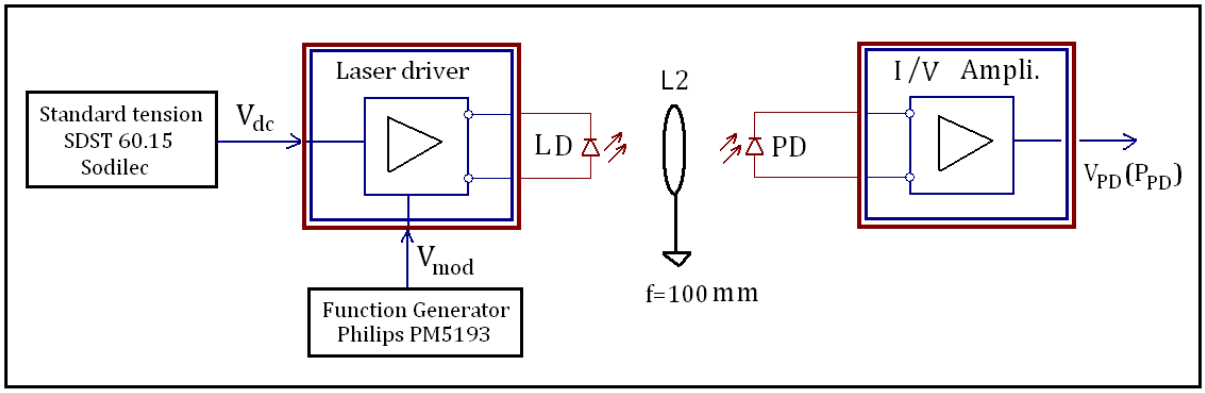

Figure 2-14. Characterization setup of the photodiode

The tension V_{mod} is a sinusoidal voltage of fixed amplitude and variable frequency, and V_{PD} is the output voltage of the I/V converter which is proportional to the power measured by the photodiode, then to that radiated by the laser diode (P_{LD}). I have to mention here that with the used type of operational amplifier, the I/V converter has a band-pass response of 20 MHz.

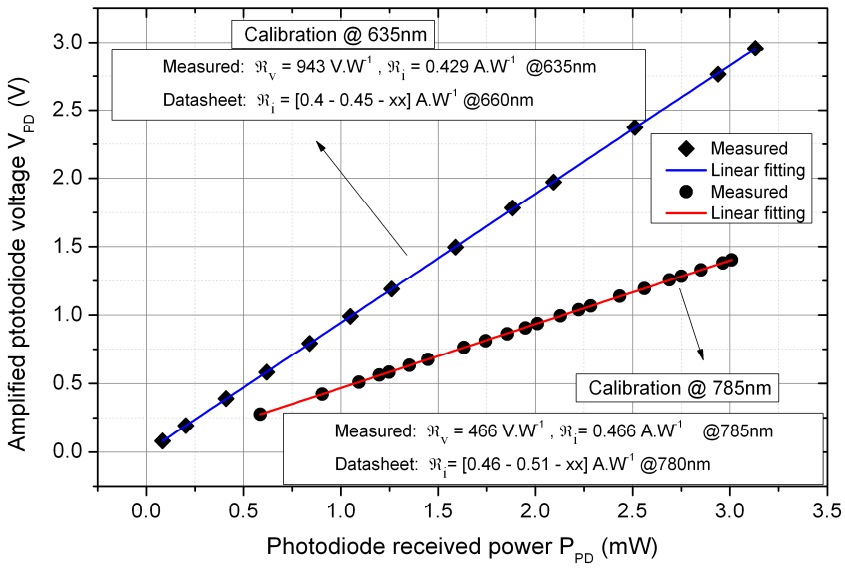

Figure 2-15. Static calibration of S10784 photodiode with I/V Amplifier at 635 nm and 785 nm wavelength. The legends show measured and datasheet characteristics

The Figure 2-15 presents the static calibration of this photodiode at 635 nm and 785 nm laser diode wave length. It shows a linear relationship between P_{PD} and V_{PD}, with a slope value close to the typical manufacturer value for both wavelengths. Indeed, $\Re_v$ was calculated from the measured $\Re_i$ and using the feedback resistance value (2.2 kΩ for measurement at 635 nm, and 1 kΩ for measurement at 785 nm) of I/V amplifier (cf. Appendix B). The relation (II- 10) mentions the overall responsivity of the photodiode and the I/V amplifier. This relation is essential for the estimation of radiated laser power, as we will see later.

$$V_{PD} = (943 \pm 1) P_{PD}\ [V \cdot W^{-1}] \quad @\ 635\ nm \tag{II- 10}$$

Another important characterization is to find out the frequency response of the photodiode with I/V amplifier. So, I used a function generator to get a modulated laser power at different frequencies. This way we can plot the V_{PD}/V_{mod} as function of laser modulation frequency (see Figure 2-16). This dynamic response shows a pass-band behavior with low pass frequency of f_L=0.7 Hz and high pass frequency of f_H=2.6 MHz. The low pass frequency is related to the high pass filter in the laser driver. Therefore, in the studied frequency range, from 1 Hz to 100 kHz (cf. chapter III), the photodiode and its amplifier stage do not present any limitation for the frequency response.

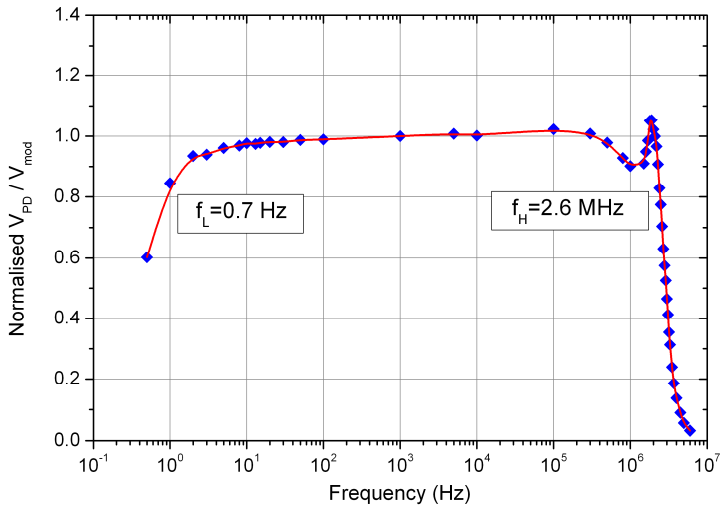

Figure 2-16. Dynamic characterization of the S10784 photodiode with I/V Amplifier

4.2. Characterization of optical elements

To calculate the overall of the incident power on the studied sample, we need to measure the transmission rate of the used optical elements (B3 in the block diagram). I have used two convergent lenses: L1 with focal distance 225mm and L2 with focal distance 100 mm, used to focalize the laser beam on the studied sample and on the photodiode, respectively. The glass window of the vacuum chamber has been employed to pass the laser beam inside the vacuum chamber and hit the studied sample.

The beam splitter (cube, plate, or pellicle type) separates an incoming beam of light into two separate beams: a transmitted beam and a reflected beam [8]. The beam splitting surface must be mounted at a 45° angle to the incoming beam, as seen in Figure 2-17. Consequently, the transmitted beam is parallel to the incoming beam and the reflected beam is orthogonal to it. The used beam splitter is a cube type with 50/50 nominal splitting percentage. This rate has to be identified practically by measurements.

To estimate the transmission rate for all elaborated optical elements, I measured the power before (incident power) and after each one by using the photodiode PD300 and the wattmeter NOVA II. Many measurement data have been done for different values of radiated laser power, and an average value with standard deviation has then been extracted. The measured transmission and reflection rates can be seen in Figure 2-17(b).

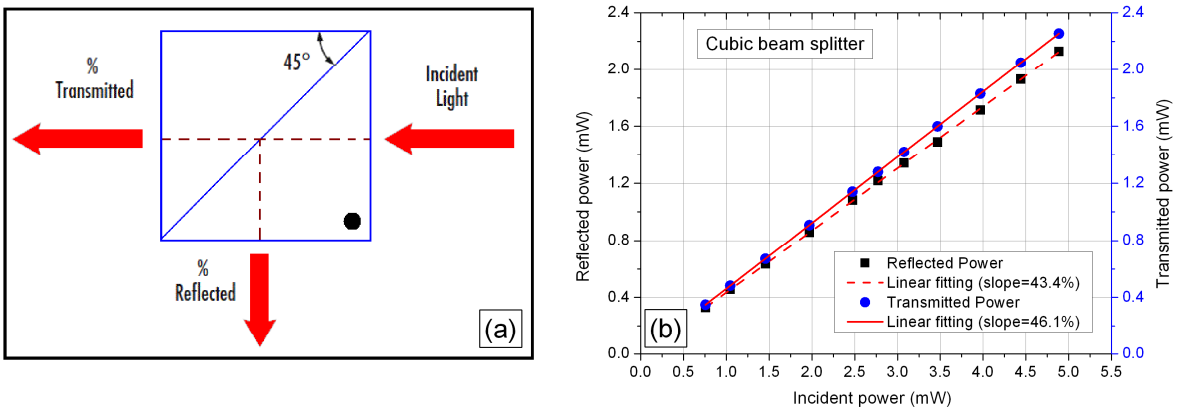

Figure 2-17. Cubic beam splitter (a) and its characterization at 635 nm (b)

We note, for the cubic beam splitter, that there is about 10.5% of the incident power absorbed by the cube, since the total sum of passed and reflected ratios equals to 89.5%.

The measured data for transmission rates for the two lenses (L1, L2) and vacuum chamber window is given in Figure 2-18.

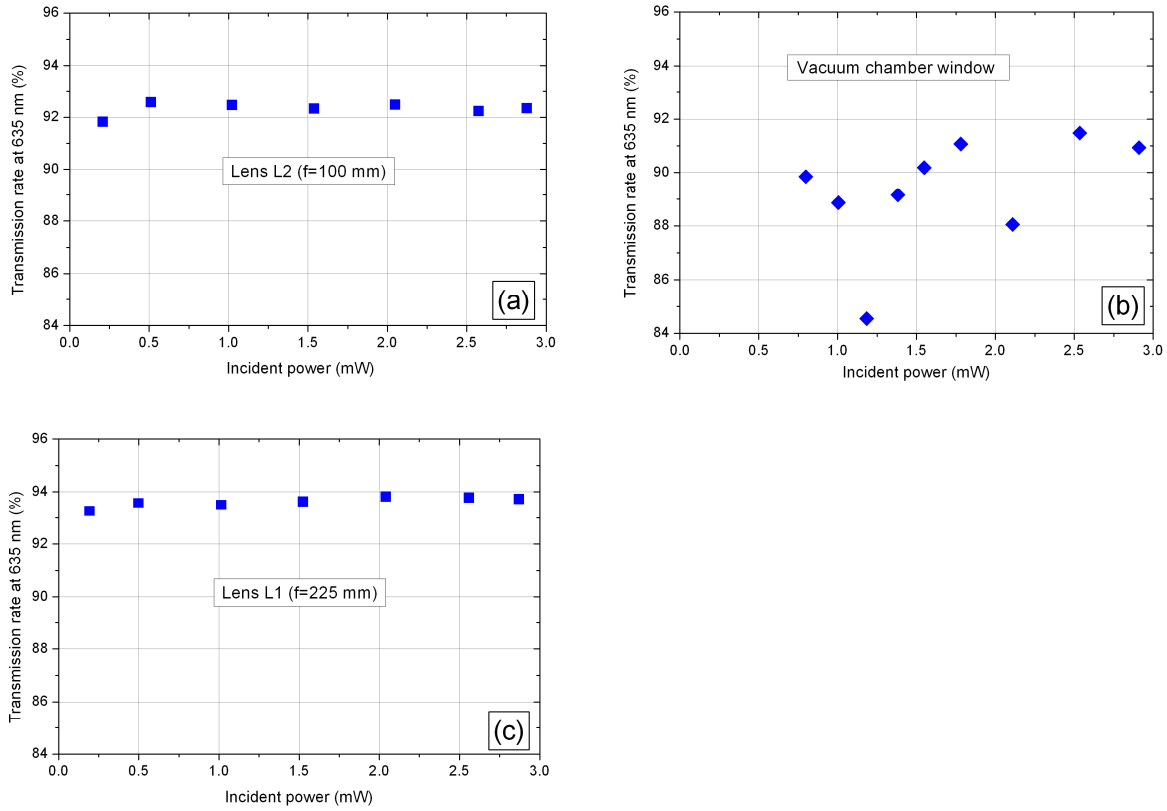

Figure 2-18. The measured transmission rates for L2 lens (a), the vacuum chamber window (b), and L1 lens (c) at 635 nm wavelength

Table 2-2 summarizes the measured average transmission rate values for all the used optical elements at 635 nm wavelength.

Table 2-4 : Transmission rates at 635nm of the optical elements

Element	Transmission rate (%)	Standard deviation (%)
Lens L2	TR_{f100} = 92.33	0.25
Lens L1	TR_{f225} = 93.61	0.19
Vacuum chamber window	TR_{win} = 89.35	2.12
Cube_ transmitted	$TR_{C\text{-}tr}$ = 46.13	0.01
Cube_ reflected	$TR_{C\text{-}rf}$ = 43.38	0.02

The dispersion of transmission rate of the window (therefore the standard deviation) is higher than that of the other optical elements. This is due to measurement sensibility to perpendicularity of the window with the laser propagation axe.

5. Sample installation and equipments

The studied sample has to be studied in vacuum condition with the possibility of temperature regulation of the sample. So, we need a vacuum chamber with temperature regulation of the sample. These equipments, of course, have to provide the suitable connectivity with the exterior electronics. In this section I will explain the sample installation equipments required to get the sample ready for optical characterization.

5.1. Overall setup: holder, connections

The sample was glued to a copper plate, which is a part of the sample holder (see Figure 2-19), by using the silver paste material. This sample holder consists of two copper plates with an epoxy layer between them [23]. A heating element, which is a Constantan wire (diameter of 0.2 mm, electrical resistance of 15.6 $\Omega \cdot m^{-1}$), is twisted then rolled over the upper copper plate. An epoxy disk with connection pads is glued on the upper plate. Ultrasonic bonding with aluminum wire, of diameter 50 µm, was used to connect the four gold pads of the sample (Bias current: I+, I- ; Output voltage: V+, V-) with the pads on as epoxy disk, hence providing the connectivity with the exterior of the chamber.

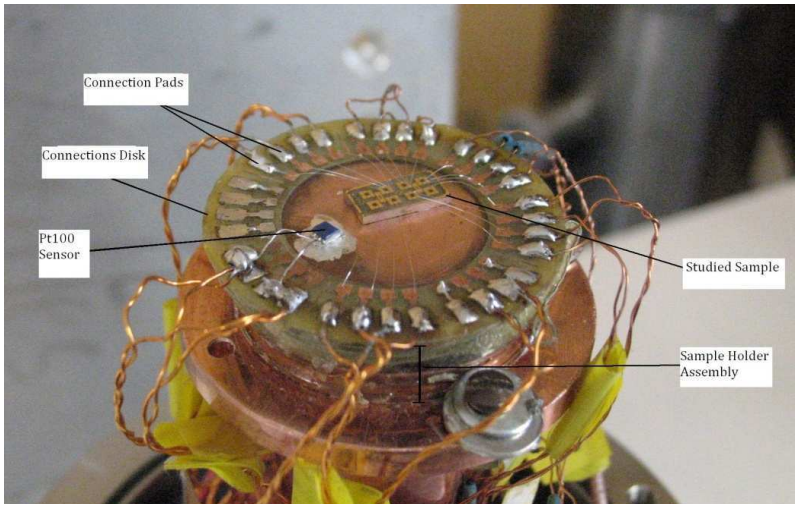

Figure 2-19. A photo of a tested sample glued on the sample holder. The Pt100 sensor glued next to the sample. Connections made by pads of epoxy disk

Then, the sample holder is fixed with the cold head (a copper stem) by the silver past and screws. The connection wires pass inside the chamber and tubes to make connection between sample pads and connection jacks (see Figure 2-20). A temperature controller was used to maintain temperature stability during measurements at fixed temperature. The controller, also, provides the possibility of heating the sample by using the heating element and Pt100 sensor. I will characterize this temperature controller in the next paragraph.

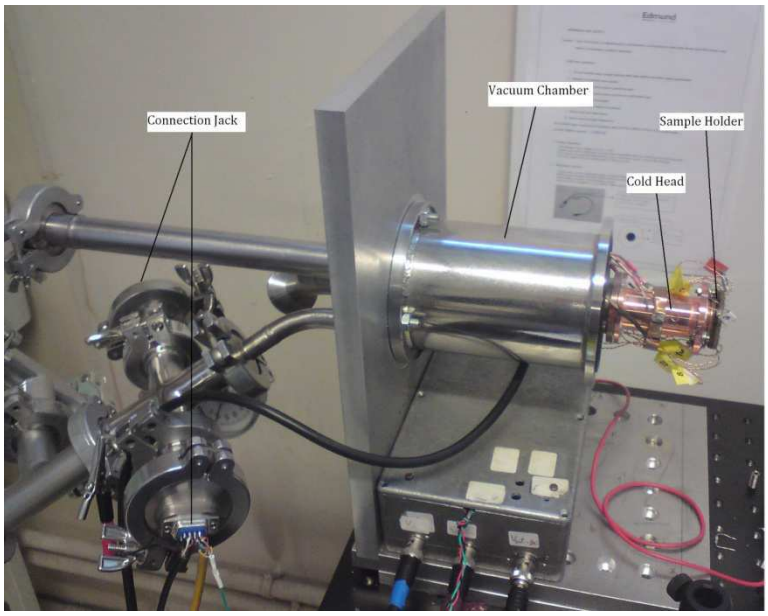

Figure 2-20. A photo of the vacuum chamber assembly showing the connection jacks with the external equipments

5.2. Temperature controller

I did use the temperature regulator, LakeShore 330, to regulate the temperature of the studied sample in the range 300-350 K. To achieve this regulation, a Pt100 temperature sensor has been glued beside the sample (see Figure 2-19), and a heating element (Constantan wire of about 30 Ω) was rolled over the sample holder copper plate. The LakeShore 330 provides three levels of heating power: Low (0.3 W/ 30 Ω), Medium (3 W/ 30 Ω), High (30 W/ 30 Ω). The Medium level will be used because the low level is too slow and need a lot of time, and the high level may burn the wire of the heating element due to overheating. This instrument is equipped with an integrated PID controller with control stability of ±15 mK. It will be used to heat and regulate the temperature of the sample at a fixed temperature where the sample will be optically characterized. Hence, an accurate measurement of this temperature is required. To achieve this purpose, I will try next to explore the accuracy of measurement readings. The

temperature, coming up from the electrical resistance value of Pt100 sensor, can be read by the IEEE-488 interface integrated in the regulator. We can also read this electrical resistance by a precision $6^{1/2}$ digits voltmeter (HP34401A). The Pt100 sensor is biased by the measured 1.0018 mA current source of the LakeShore temperature controller.

Finaly, we note that we have an average deviation of 0.312±0.044 K between the temperature measured by the LakeShore regulator and that measured by the voltmeter. Hence, all measurement of temperature will be done using the direct measurement of the Pt100 sensor by this voltmeter. To achieve this measurement we will use the resolution of the standard second order relation model (Callendar-Van Dusen model) of Pt100 resistance as function of temperature, as seen in equation (II- 2). It's clear that the displayed temperature has a 0.1 K resolution, so this will be used as indicator only.

$$R(T) = R_0[1 + A(T - T_0) + B(T - T_0)^2] \qquad \text{(II- 11)}$$

where R_0 = 100 Ω (the electrical resistance at T_0=0 °C), A = 3.9083×10^{-3} K^{-1}, B = -5.775×10^{-7} K^{-2}.

Figure 2-21 shows the measured electrical resistance of G455_L300W100 sample and of Pt100 sensor during regulating period of temperature at 319.6 K. Here, we need about one hour to get stable temperature, so this will be considered during all measurements. Also, the electrical resistance of the sample still changes even after temperature stabilization. This comes up from the higher temperature sensitivity of the sample, which is about 83 $\Omega\cdot K^{-1}$ (cf. section 1 of chapter III) in comparison with 0.4 $\Omega\cdot K^{-1}$ of the Pt100 sensor. Indeed, this will not draw back the AC optical responsivity measurements, since that change the offset of the AC measured values. Practically, I begin measurements at least one hour after starting temperature regulation. In addition, the AC optical responsivity measurement is practically achieved in relatively low time of about 1.5 min (cf. paragraph 1.3 of chapter III).

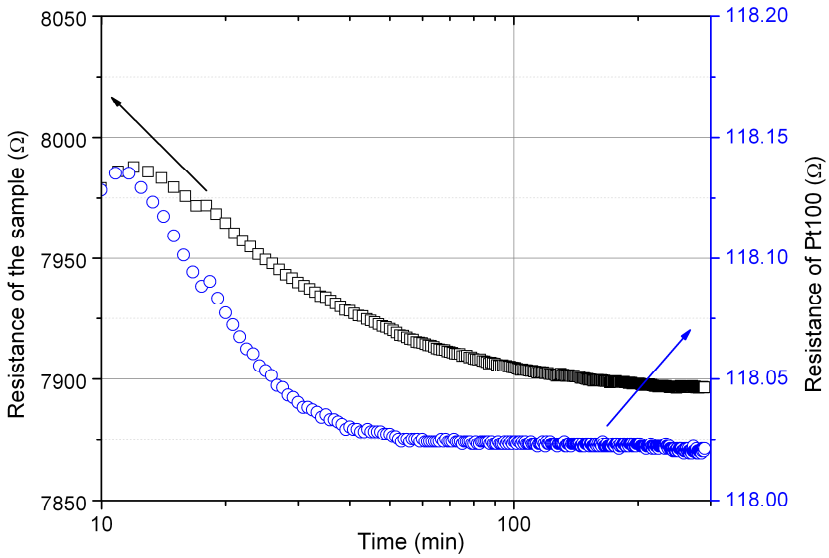

Figure 2-21. The electrical resistance of the sample G455_L300W100 and the Pt100 sensor versus time during temperature stabilization at 319.6 K

6. Readout electronics: design & characterization

To measure the optical responsivity and the noise, and then estimate the figures of merit that characterize our samples as bolometer radiation detector, we need to elaborate readout electronics. In principle, the bolometer is a variable electrical resistance element as function of temperature. When the laser hits this element its temperature increases, and then its electrical resistance changes. So, to estimate the variation of temperature we have to measure the variation of its electrical resistance.

6.1. Overall block diagram

The objective of this electronic bench is to provide a low noise bias current to measure the electrical resistance of the studied samples. I will try in the following to analyze its performance and describe its features. The following Figure 2-22 shows the block diagram of the used homemade readout electronics.

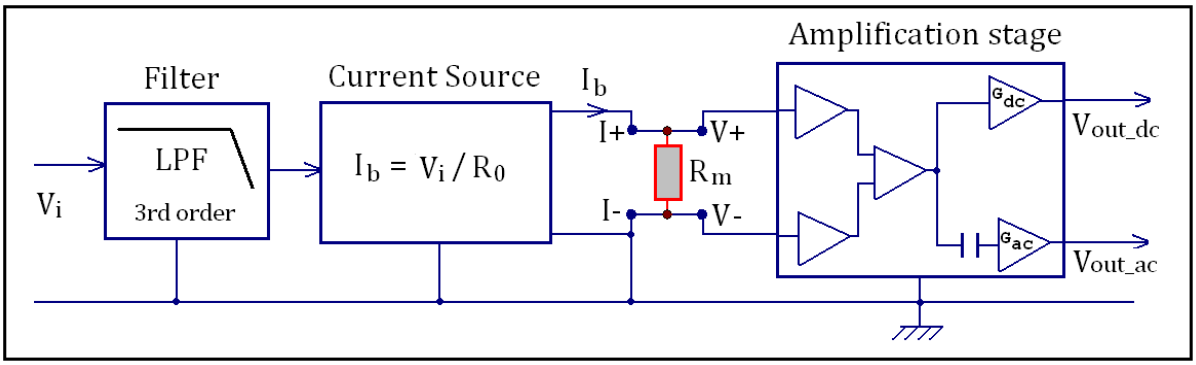

Figure 2-22. The block diagram of the homemade readout electronics

As we can see in the block diagram, the homemade readout electronics consists of 3rd order low pass filter, current source, and amplification stage. The current source is a quasi-ideal DC current source which exhibits a very high output impedance and a negligible noise contribution [1]. It will be used to bias the studied sample (R_m) by stable current (I_b). Finally, an amplification stage is used to measure the output voltage of the sample (V_+ - V_-). In the next paragraphs I will describe the design and characterization of each of these stages.

6.2. Characterization of the filtering stage

First, I will start by characterize the filtering stage, which has an objective to purify the input voltage (V_i) of all unwanted perturbations. This filter has been designed as 3rd order Tchebytcheff filter of cutoff frequency of 350 mHz and DC gain equals to 2, and -30 dB attenuation at 1 Hz. The Figure 2-23 shows the measured frequency response of this filter.

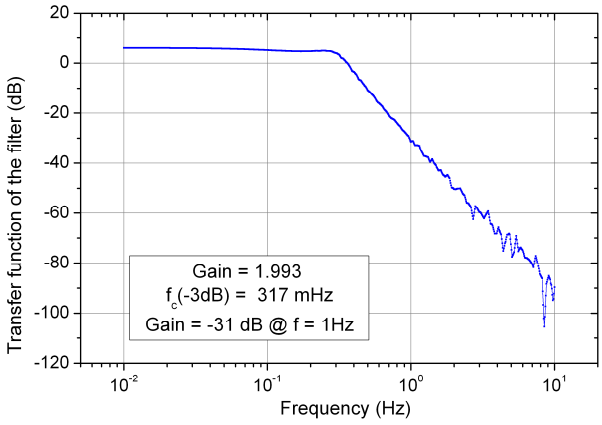

Figure 2-23. The transfer function and the characteristics of the 3rd order low-pass filter

This filter shows practically a DC gain of 1.993 and a gain of -31 dB at frequency 1 Hz. The -3dB cutoff frequency is 317 mHz, therefore we obtain a reasonable response time for the DC measurement. These specifications agree well with those of the theoretical design.

6.3. Characterization of Amplification stage

6.3.1. DC output

The amplification stage has two independent outputs: continuous (V_{out_dc}) and alternative (V_{out_ac}), so we can characterize each one separately. To measure the gain of the DC output, I used a metallic film 10 kΩ resistance exhibiting a low temperature coefficient of 50 ppm·(°C)$^{-1}$ instead of the sample electrical resistance R_m. Then I changed the input voltage V_i to get many values of bias current (cf. paragraph 6.4 of this chapter). By measuring the voltage drops on R_m terminals (V_+ - V_-) and the DC output voltage (V_{out_dc}) by two HP34401A voltmeters, we can calculate the average gain of the DC output (see Figure 2-24).

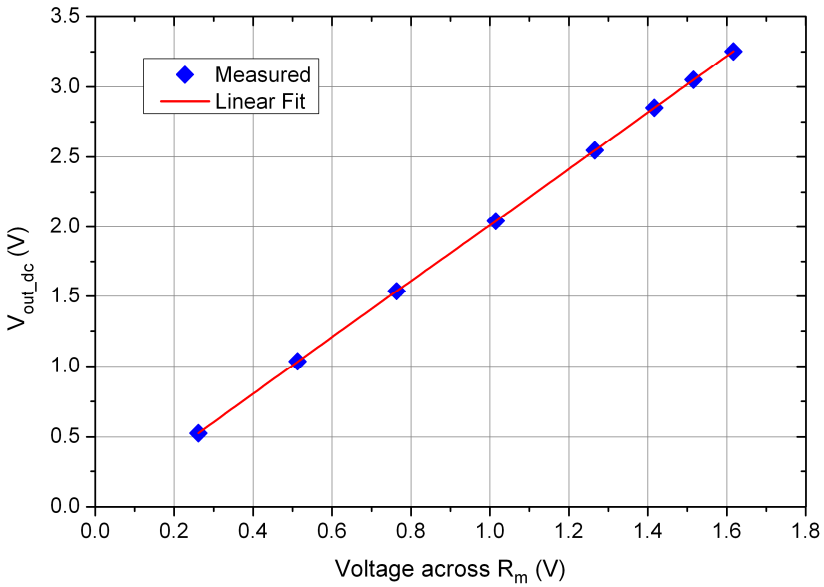

Figure 2-24. The measured gain of the DC output (V_{out_dc}) of the amplification stage

The design theoretical DC gain value equals to 2, and I obtained a practical measured value equals to G_{dc} = 2.01. This gain will be used in all measurements of sample resistance (R_m) or sample voltage (V_m).

6.3.2. AC output

To measure the frequency response of the amplifier stage and estimate its transfer function, we apply a sinusoidal signal (as simulated sample voltage V_m) between V+ and V- terminals, and then we plot V_{out_ac}/V_m (as seen in Figure 2-25). The AC output (V_{out_ac}) is used to measure the frequency response of the optical responsivity and the electrical noise of the studied sample, and then calculate the other figures of merit like NEP and D*.

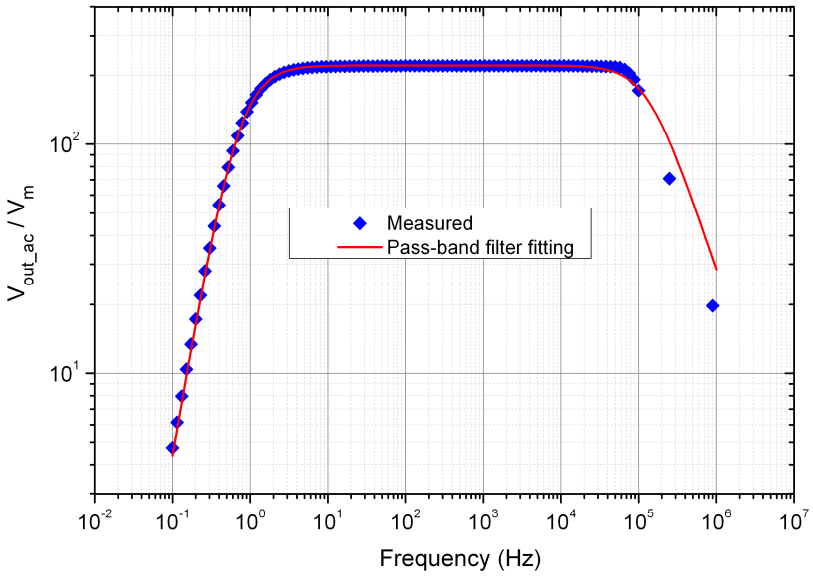

Figure 2-25. The measured and fitted transfer function of AC output (V_{out_ac} output) of the amplification stage

The transfer function of the AC output is that of a pass band filter; one filter is a 2nd order pass high and another is a 1st order pass low filter, as presented in equation (II- 12). Using the non linear fitting in Origin software, we can estimate the three constants (A1, A2, A3) of the mathematical model.

$$\frac{V_{out\_ac}}{V_m} = \frac{A1}{1+\left(\frac{f}{A2}\right)^2} \times \frac{\left(\frac{f}{A3}\right)^2}{1+\left(\frac{f}{A3}\right)^2} \qquad \text{(II- 12)}$$

Where A1 = G_{ac} = 221.4 ± 0.2

A2 = (130.6 ± 1.5)×10^{+3} Hz

A3 = (705 ± 4)×10^{-3} Hz

This equation presents a very good fitting for the real transfer function, with 0.995 of Mean Squared Error value. Indeed, the frequency range where studied samples will be characterized is 1 Hz-100 kHz, so the deviation noticed at frequencies higher than 100 kHz will be neglected.

6.3.3. Noise of AC output

In order to measure the intrinsic noise of each sample, we need to measure the noise level of the amplification stage itself. By connecting the AC output (V_{out_ac}) with the spectrum analyzer (HP3562A) and short-circuit the two differential inputs (V+ and V-) with the ground, we can measure the noise spectral density of the amplification stage. The graph seen in Figure 2-26 shows the noise spectral density $S_v(f)$ observed from 1 Hz to 100 kHz.

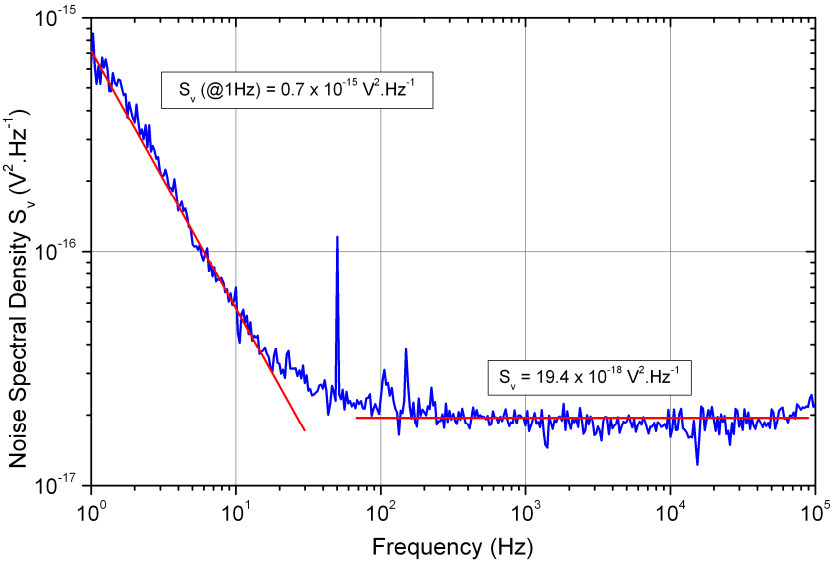

Figure 2-26. The noise spectral density of the AC output (V_{out_ac}) of the amplification stage

The amplification stage shows a low noise level, with a white noise equals to 19.4×10^{-18} $V^2 \cdot Hz^{-1}$, and low frequency noise equals to 7×10^{-16} $V^2 \cdot Hz^{-1}$ at 1 Hz. Therefore, we can measure the noise level of any sample that have a noise level higher than this value.

6.4. Current source: Noise measurement

This is a quasi ideal DC current source dedicated to 4 terminals noise measurements [1]. It shows an output impedance, Z_s, value of 3 MΩ (for R_0=1 kΩ) with maximum output

current of 1.5 mA, with low noise contribution, i_{ns}^2, of the order of 10^{-23} $A^2 \cdot Hz^{-1}$. The output current I_b is controlled by the value of the input voltage V_i and the electrical resistance R_0 ($I_b = V_i / R_0$). To maintain high output impedance, one design condition should be respected; it is that R_m is negligible in comparison with R_0 [24]. Another design parameter is that the small signal output impedance is at least one thousand time the electrical resistance R_0 at frequencies up to one kHz. Next I will present the noise characterization of the current source, because it's the more critical characteristic of this electronics. A detailed noise measurement will then be described.

Figure 2-27 shows a schematic representation of all noise sources, which influence the sample noise measurement, using 4 terminals technique in the overall readout electronics.

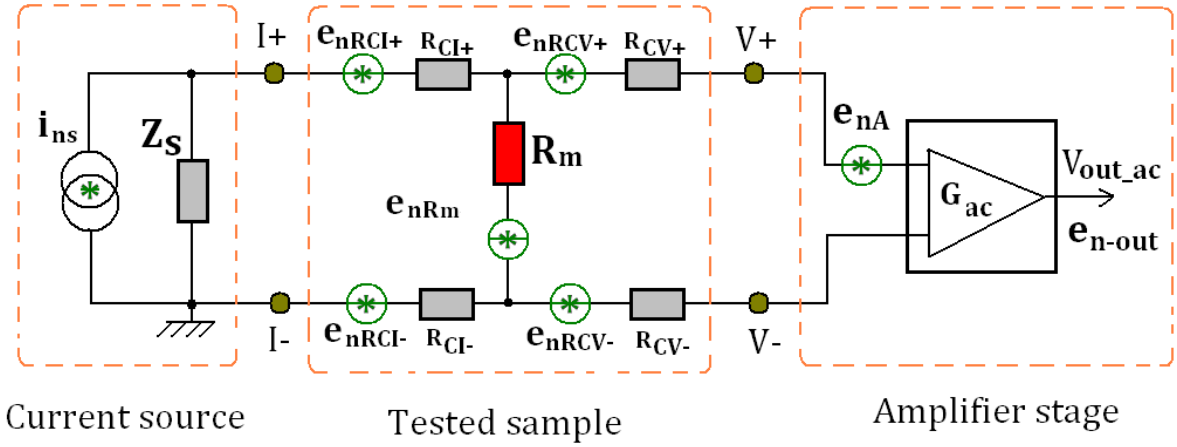

Figure 2-27. Schematic representation of all noise sources in the readout electronics using 4 terminals technique

The noise measurements can be performed in the same configuration as electrical resistance measurements, if the voltage fluctuations between the voltage pads V+ and V- are amplified by a differential voltage amplifier (Figure 2-27). The voltage noise spectral density e_{n-in}^2 can then be calculated by measuring the output noise spectral density e_{n-out}^2 by using a spectrum analyzer connected at the amplifier stage output, as given in equation (II-13). We will consider that the amplifier has a very high input impedance (by choosing a JFET based operational amplifiers) so that its current noise can be neglected.

Using Figure 2-27, and if G_{ac} is constant over all the measuring frequency range (cf. Figure 2-26) and $Z_{eq} = Z_S + R_{CI} + R_m$, we can write:

$$e_{n-in}^2 = \frac{e_{n-out}^2}{G_{ac}^2} = e_{nRCV}^2 + e_{nA}^2 + i_{ns}^2 \frac{|Z_s|^2 . R_m^2}{|Z_{eq}|^2} + e_{nRm}^2 \frac{|R_{CI} + Z_s|^2}{|Z_{eq}|^2} + e_{nRCI}^2 \frac{R_m^2}{|Z_{eq}|^2} \quad \text{(II-13)}$$

Where:

- $e_{nRCI}^2 = e_{nRCI+}^2 + e_{nRCI-}^2$: The voltage noise spectral density of the current contact resistance $R_{CI} = R_{CI+} + R_{CI-}$ (the electrical resistance of current pads takes place between Gold-LSMO connection; see section 8 of this chapter)
- $e_{nRCV}^2 = e_{nRCV+}^2 + e_{nRCV-}^2$: The voltage noise spectral density of the voltage contact resistance $R_{CV} = R_{CV+} + R_{CV-}$ (the electrical resistance of voltage pads takes place between Gold-LSMO connection; see section 8 of this chapter)
- e_{nRm}^2 : The voltage noise spectral density of the studied sample (R_m)
- e_{nA}^2 : The voltage noise spectral density of the amplification stage
- i_{ns}^2: The current noise spectral density of the current source

Following the design conditions of the current source [1], we have:

$Z_S >> R_m \Rightarrow Z_{eq} >> R_m$ and $Z_S >> R_{CI}$, then we got the next relation,

$$e_{n-in}^2 = \frac{e_{n-out}^2}{G_{ac}^2} = e_{nRCV}^2 + e_{nA}^2 + i_{ns}^2 R_m^2 + e_{nRm}^2 \quad \text{(II-14)}$$

From the equation (II-14), and to estimate the intrinsic noise of the sample (e_{nRm}^2) we need to evaluate the noise of the current source (i_{ns}^2), as we will see next. In practice, the voltage contact noise (e_{nRCV}^2) can be estimated when no DC current follows into the device and can be subtracted from all the measurement performed when a DC current is applied.

The noise of the current source is due to the thermal noise of its resistances and to the equivalent voltage noise of the two operational amplifiers, which all make up the circuit of the source. The measured current noise spectral density (i_{ns}^2) of the current source is plotted in Figure 2-28 for three values of R_0=R_m. For simplify the calculation, we will assume that the voltage contact noise is neglected.

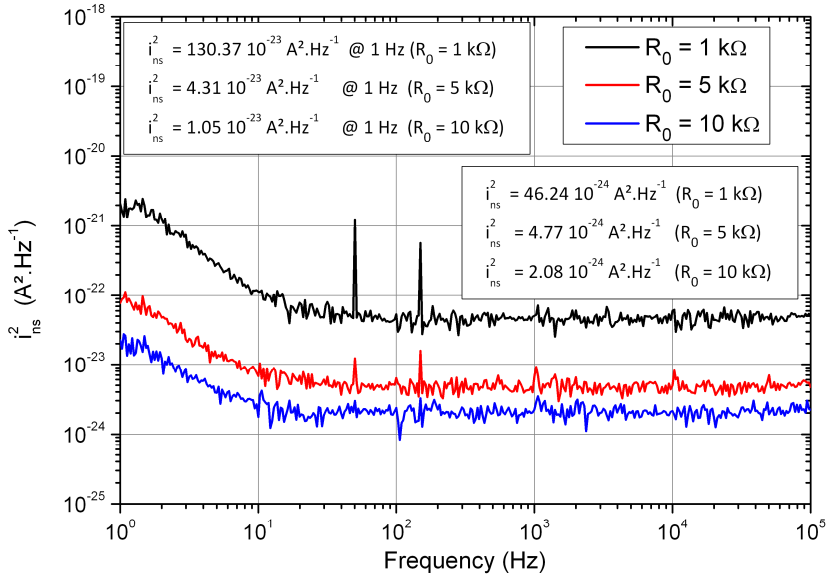

Figure 2-28. The measured current noise spectral density of the current source for three value of R_0=R_m

The measured current noise shows a white noise level, as indicated in the Figure 2-28, and a low frequency noise which is due to the operational amplifier of the source. The value of this noise decreases, eventually, for higher value of R_0. To estimate the noise of the studied sample for any value of R_0 we will use the relation that modelizes the current white noise spectral density, as seen in equation (II- 15). This model propose that the current white noise equals the sum of white noise issues from R_0 and the white noise related to other electrical resistances and operational amplifiers in the current source.

$$i_{ns}^2 = \frac{4k_B\,T\,R_0 + Ct1}{R_0^2} \qquad \text{(II- 15)}$$

At low frequency, the only noise source will be issued from the operational amplifiers, and the model is presented in equation (II- 16).

$$i_{ns}^2 = \frac{Ct2}{R_0^2} \qquad \text{(II- 16)}$$

Using the measured data for the three values of R_0, as indicated in Figure 2-28, and the fitting of equation (II- 15), we can estimate the value of Ct1= 29.7 ×10^{-18} V^2·Hz^{-1} (see Figure 2-29(a)). Using the same methodology, we can also estimate the value of Ct2 = 1.3 ×10^{-15}

$V^2 \cdot Hz^{-1}$ at 1Hz (see Figure 2-29(b)). The value of Ct2 is as the expected value of 2×10^{-15} $V^2 \cdot Hz^{-1}$ due to the noise of the used type of operational amplifiers. This way, and whatever is the value of R_0, we can calculate the white noise and the low frequency noise (at 1 Hz) of the current source.

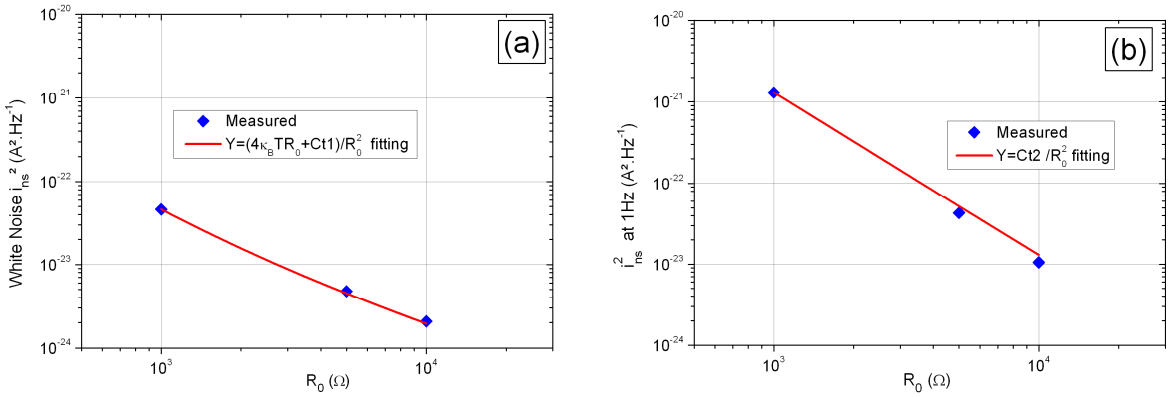

Figure 2-29. Estimation of current noise spectral density of the current source (a) white noise (b) low frequency noise

Finally, I could characterize the noise of all parts of the readout electronics. Indeed, the current source and the amplifier stage present very low noise contributions. This will provide the possibility of measure the intrinsic noise of the tested sample.

6.5. Overall characteristics of the readout electronics

I will try in this paragraph to summarize the main characteristics of the readout electronics. It was designed to provide a low noise current source to measure the electrical resistance of the studied sample. In addition, it provides the possibility of achieving noise measurement of the samples. The device measured characteristics are:

- Providing a maximum of 5 V across the studied sample resistance R_m, thus a maximum bias current value of $5/R_m$, with respect to stabilization condition of current source ($R_0 \geq 2R_m$).
- The measured current source noise exhibits a white noise level and a low frequency noise. The value of these noises can be calculated using the models:

  i_{ns}^2 (white noise region) = $(4k_BTR_0 + 29.7\times10^{-18})/R_0^2$

  i_{ns}^2 (1/f noise region) = $(1.3\times10^{-15})/R_0^2$

- The gain value of the DC output (V_{out_dc}) equals to G_{dc} = 2.01.

- The transfer function of the AC output (V_{out_ac}) is that of a pass band filter. The 2nd order high pass cutoff frequency equals 0.7 Hz, and the 1st order low pass filter equals 131 kHz. The gain value equals to $G_{ac} = 221.4 \pm 0.2$
- The AC output has a white noise value equals to 19.4×10^{-18} $V^2\cdot Hz^{-1}$, and low frequency noise equals to 7×10^{-16} $V^2\cdot Hz^{-1}$ at 1 Hz.

Therefore, the white noise and the low frequency noise (at 1 Hz) of the current source can be estimated for any value of R_0.

7. Summary of measurement setup

7.1. The overall optical responsivity measurement

I will describe in this paragraph the overall estimation of the incident power on the tested sample, using the characterization of all the participated elements in the optical axis (optical elements) and the characterization of all electronics (readout electronics, laser diode driver) and measurement devices (photodiode).

Indeed, we are looking to find out the relation related the incident power on the tested sample (P_m) and the output voltage measured between sample terminals (V_m). Therefore, we can calculate the optical responsivity ($\Re_v$) of the sample which equals V_m/P_m.

Referring to the total block diagram of measurement setup, shown in Figure 2-1, we can illustrate the equation that relates all the measurement parameters as follow:

$$\frac{V_{out\_ac}}{V_{PD}} = \frac{V_{out\_ac}}{V_m} \times \frac{V_m}{P_m} \times \frac{P_m}{P_i} \times \frac{P_i}{P_{PD}} \times \frac{P_{PD}}{V_{PD}} \qquad \text{(II- 17)}$$

To calculate the optical responsivity, $\Re_v = V_m/P_m$, we need to identify the other quotients. First, the relation between V_{PD} and P_{PD} has been identified by equation (II- 10). Also, the quotient V_{out_ac} / V_m is already given by equation (II- 12), and the ratio P_m/P_i has been calculated in equation (II- 9). Referring to Table 2-4, we can write:

$$\frac{P_i}{P_{PD}} = \frac{TR_{win} \times TR_{f225} \times TR_{C-tr} \times P_{LD}}{TR_{f100} \times TR_{C-tr} \times P_{LD}} = (96.33 \pm 2.80)\ \% \qquad \text{(II- 18)}$$

The uncertainty was calculated using the uncertainty propagation law.

Finally, the optical responsivity writes as,

$$\Re_v(\omega) = \frac{V_m}{P_m}(\omega) = \left(\frac{V_{out\_ac}}{V_{PD}}\right) \times \frac{\left(\frac{P_i}{P_m}\right)}{\left(\frac{V_{out\_ac}}{V_m}\right) \times \left(\frac{P_i}{P_{PD}}\right) \times \left(\frac{P_{PD}}{V_{PD}}\right)}(\omega) \qquad \text{(II- 19)}$$

Thus, to calculate the optical responsivity we need just to measure the ratio V_{out_ac} / V_{PD}. This can be done easily by using the signal analyzer HP3562A (connecting V_{PD} to the first channel input, and connecting V_{out_ac} to the second channel input) in transfer function mode.

7.2. The overall characteristics of the measurement setup

I will summarize in this paragraph the main characteristics of the realized measurement setup, except the readout electronics which was given in paragraph 6.5.

- Provide DC drive current I_{dc} (200 mA maximum) to operate the laser diode in the emitting region (V_{dc} = 1.2 V ⇔ I_{dc} = 24 mA).
- Provide AC bias current I_{mod} to modulate the output laser power in the required frequency range (I_{mod} = ± 3mA ⇔ P_{mod} = ±1.8 mW).
- Operate the laser diode in a constant current mode using Automatic Current Control (ACC) method (P_{dc} = 2.7 mW).
- Overall pass-band behavior of the laser driver with low pass frequency 0.7 Hz and high pass frequency 2.6 MHz.
- The laser power stabilizes after about 30 min, with a total power drop of about 3.5% of the initial value.
- Real time measurement of laser radiated power using high speed photodiode with voltage responsivity $\Re_v$ = 943 ± 1 V·W^{-1} @ 635 nm
- Temperature regulation of the studied sample in the range 300-350 K, with stability of ±15 mK.
- Estimation of laser spot size by CCD camera, with minimal resolution of about 8 µm. The maximum measurable spot size is 6.4×4.8 mm², and minimum size about 80×80 µm² (about 10 times the pixel size).
- Usable in the visible wavelength, with the possibility to extended to IR range by using adaptable optical elements.

8. List of tested samples

I will present in this section the design mask and fabricated tested samples in this thesis. First we used a plastic mask, called mask-A, which has an optical resolution of 15 µm. Then, and to have a better optical resolution a glass/chromium mask, called mask-B, was designed. It has an optical resolution of 2 µm and was fabricated by PhotoData Company. Actually, samples patterning was done by Cedric Fur, a GREYC technician, in the clean room in GREYC. More Details on film deposition and patterning will be given in Appendix A.

8.1. Mask-A design

The mask-A design is based on fixed length (L) and strips width (W), and variable number of strips (n). This way we will get a variable width (L'), as we can see in Figure 2-30. The parameter d presents the distance between two successive strips, which is about 15 µm.

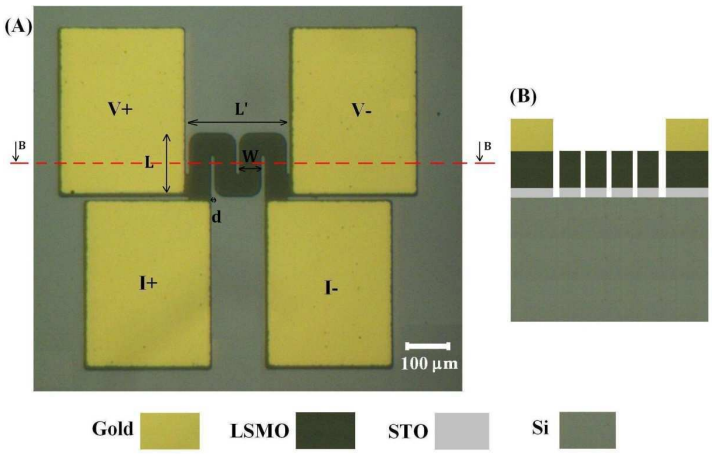

Figure 2-30. (A) Optical photography of the mask-A CA656-7(L150W50) sample with the measurement current (I+, I-) and voltage (V+, V-) probes. (B) Schematic cross-section of the sample.

The Table 2-5 shows all the tested samples fabricated using this mask (deposition and patterning was done by C. Fur). It shows the geometrical dimensions for each sample, with their fill factors. In addition, it presents the corresponding beam radius (w_x, w_y) of the laser diode used during the optical characterization, with the correction factor (F_t) of received power by each sample (cf. paragraph 3.4). I used a notation that contains the main information about sample's dimensions. For example, the notation of the sample L150W50 means that it has length of 150 µm and strips width of 50 µm.

Table 2-5 Tested samples fabricated with the mask-A

	Geometry	L × L' (µm×µm)	W (µm)	n	Thickness Film/sub. (nm/µm)	w_x (µm)	w_y (µm)	Fill Factor (%)	F_t
CA656-7 LSMO/STO/Si	**L150W50**	150 × 230	50	4	100/300	155	227	91	**1.208**
	L250W50	250 × 350	50	6	100/300	155	227	89	**1.133**
	L320W20	320 × 110	20	4	100/300	155	227	74	**2.013**
	L400W100	400 × 650	100	6	100/300	155	227	94	**1.061**
G455 LSMO/STO	**L220W20**	220 × 110	20	4	100/1000	885	296	75	**6.432**
	L300W100	300 × 870	100	8	100/1000	885	296	95	**2.104**

I have to mention here that the film thickness (t_f) for all these samples is 100 nm, and the substrate thickness was 300 µm for LSMO/STO/Si samples and 1 mm for LSMO/STO samples.

8.2. Mask-B design

The mask-B was mainly optimized to minimize the measured noise of the sample. It has been proven that this noise is in relation with current pad form, and with the relative positioning of voltage and current pads from each other [25]. The mask design is based on equal fixed length and width (L = L'), and variable number of strips (n). This way we will get a variable width of strips (W), as we can see in Figure 2-31. The parameter "d" presents the distance between two strips, which is about 2 µm.

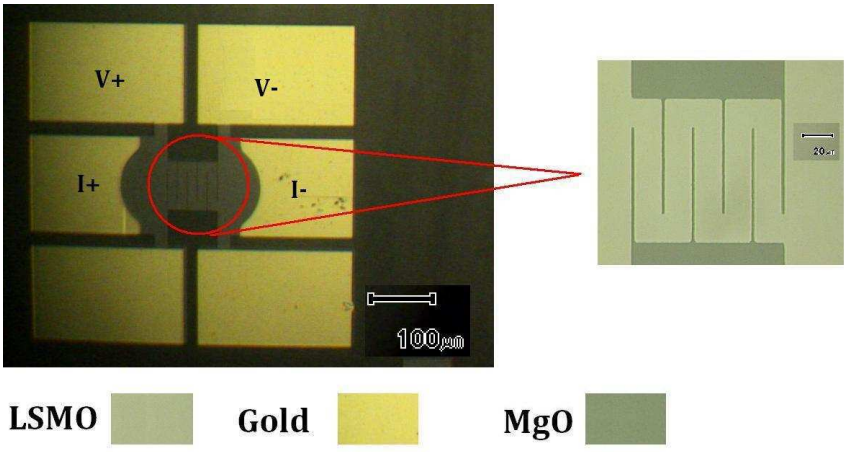

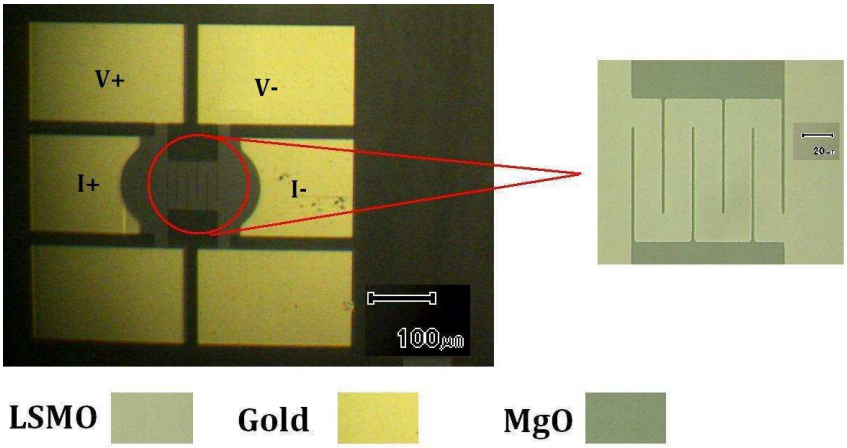

Figure 2-31. Optical photography of the mask-B G623-L100M5 sample with the measurement current (I+, I-) and voltage (V+, V-) probes

Table 2-6 : Tested samples fabricated with the mask-B

	Geometry	L × L (µm×µm)	W (µm)	n	Thickness Film/sub. (nm/µm)	w_x (µm)	w_y (µm)	Fill Factor (%)	F_t
G568 LSMO/STO	**L50M7**	50×50	5	7	75/1000	129	150	77	**4.927**
	L100M5	100×100	18.4	5	75/1000	129	150	93	**1.489**
	L100M7	100×100	12.6	7	75/1000	129	150	90	**1.553**
	L100CR	100×100	100	0	75/1000	129	150	100	**1.392**
	L200M7	200×200	27	7	75/1000	129	150	95	**1.064**
G623 LSMO/MgO	**L50M5**	50×50	8	5	75/1000	145	118	86	**3.907**
	L50M7	50×50	5	7	75/1000	145	118	77	**4.436**
	L100M5	100×100	18.4	5	75/1000	145	118	93	**1.413**
	L200M5	200×200	38	5	75/1000	145	118	96	**1.041**
G621 LSMO/STO/Si	**L50M5**	50×50	8	5	75/300	107	90	86	**2.506**
	L100M5	100×100	18.4	5	75/300	107	90	93	**1.171**
	L200M5	200×200	38	5	75/300	107	90	97	**1.034**
CA660-8 LSMO/STO/Si	**L50M5**	50×50	8	5	75/300	107	90	86	**2.506**
	L100M3	100×100	32	3	75/300	107	90	97	**1.128**
	L100M5	100×100	18.4	5	75/300	107	90	93	**1.171**

The Table 2-6 shows all the tested samples fabricated (deposition and patterning was done by C. Fur) using mask-B. It shows the geometrical dimensions for each sample, with their fill factors. In addition, it presents the corresponding beam radius (w_x, w_y) of the laser

diode used during the optical characterization, with the correction factor (F_t) of received power by each sample (cf. paragraph 3.4).

I used a notation that contains the main information about sample's dimensions. For example, the notation of the sample L100M5 means that it has a meander shape with length and width equals to 100 µm and number of strips equals 5. The notation L100CR was used for square sample with length and width equals to 100 µm. I have to mention here that the film thickness (t_f) for all these samples is 75 nm, and the substrate thickness was 300 µm for LSMO/STO/Si samples and 1 mm for LSMO/STO and LSMO/MgO samples.

8.3. Suspended-structure samples mask

A suspended structure mask was used during another research study done by S. Liu [25]. This mask was used to fabricate microbridge LSMO samples on STO buffered Si substrate. The suspended microbridge is of length (L), width (W), and thickness (t_f) as we can see in Figure 2-32(a). Indeed, I had tested two samples of length 50 µm and 100 µm and width 4 µm. Figure 2-32(b) shows a representative 3D form of the microbridge.

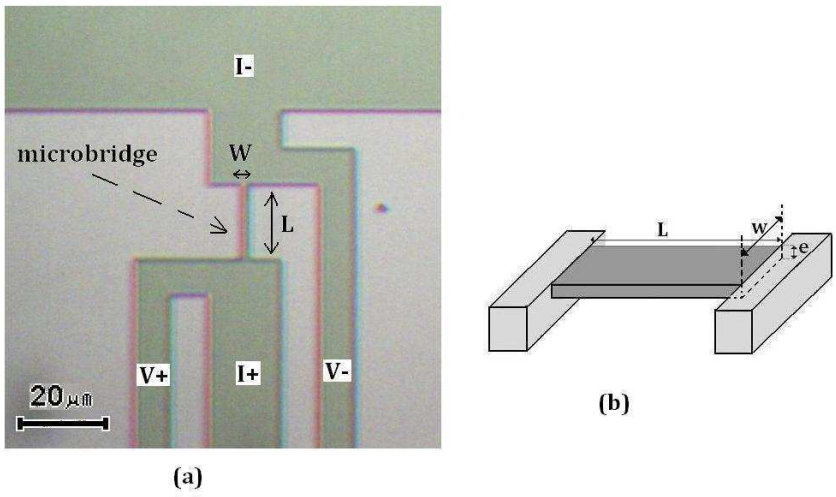

Figure 2-32. (a) Optical photography of the suspended-structure mask with the measurement current (I+, I-) and voltage (V+, V-) probes. (b) Representative 3D form of suspended sample.

The Table 2-7 shows all the samples fabricated (by S. Liu [25]) using this mask and tested by my setup. It shows the geometrical dimensions for each sample, with their fill factors. In addition, it presents the corresponding beam radius (w_x, w_y) of the laser diode used during the optical characterization, with the correction factor (F_t) of received power by each

sample (cf. paragraph 3.4). I used a notation that contains the main information about sample's dimensions. For example, the notation of the sample L50W4 means that it has length of 50 µm and width of 4 µm.

Table 2-7 : Tested samples fabricated with the suspended mask

	Geometry	L × L (µm×µm)	W (µm)	n	Thickness Film/sub. (nm/µm)	w_x (µm)	w_y (µm)	Fill Factor (%)	F_t
CA660-22 LSMO/STO/Si	**L50W4**	50×4	4	1	75/300	155	227	100	**73.923**
	L100W4	100×4	4	1	75/300	155	227	100	**44.293**

9. Chapter conclusion

This chapter is devoted to present a detailed description of the measurement setup, including the design considerations and background principles. The design objectives were to achieve trustful and repeatable measurements over a large range of frequency, with the flexibility of manipulation. This setup has been used during the thesis to characterize the LSMO bolometer samples as thermal radiation detector. This includes the measurement of the optical responsivity and the noise for each sample. Therefore, the other figures of merit (NEP, D*) can be estimated.

The measurement setup is divided into four main blocks. The first block B1 consists of the semiconductor laser diode and the necessary electronic driver circuit. Its role is to provide a stable modulated power of the laser diode to heat the tested sample. The block B2 is used to measure simultaneously the laser diode radiated power using a high speed photodiode and current/voltage amplifier. The block B3 contains all the necessary optical elements (beam splitter and convergent lenses) needed to drive the radiated beam. The block B4 contains the equipments for installing the tested sample and controlling the temperature of its holder. Also, it includes the necessary readout electronics. Most of our used equipments are homemade electronic boards, except the temperature controller and the optical elements.

In order to measure the optical responsivity of LSMO sample a laser beam is used to optically heat the device, after passing through many optical elements. Thus, the transmission coefficient of all optical elements has been measured. The power of the incident light on the sample can be directly obtained by measuring the photodiode output signal. Moreover, the laser diode spot shape and size has been identified and measured. In addition, the power really

received by all studied samples, which is related to laser spot size and sample size, has been estimated.

The LSMO sample was current biased using a quasi-ideal DC current source, which exhibits very high output impedance and a negligible noise contribution. A standard four-probe technique was used to provide the bias current and measure the output voltage signal of the LSMO sample. This voltage was read out by a homemade voltage amplifier, which provides two outputs: one DC voltage measurements, and one AC voltage measurements with amplification and filtering. The AC output is also used to measure the noise of the samples. The characteristics of the current source and the amplification stage have been explored in details. These characteristics show a good consistence with the intended ones.

At the end of this chapter I provide a detailed list of all the tested samples, including samples fabricated using the mask-A and mask-B. The detailed used deposition technique, and characterisation of unpatterned deposited LSMO films on different substrates will be given in appendix A.

Finally, I could design, realize, characterise a measurement setup that can be used to achieve the optical characterisation of LSMO samples as uncooled radiation detector. Indeed, this setup can be used for any other thermosensible material. This was one objective of this thesis that was achieved.

References for Chapter II

[1] J.-M. Routoure, D. Fadil, S. Flament, and L. Méchin, “A low-noise high output impedance DC current source”, AIP Conference Proceedings, vol. 922, pp. 419–424, (2007).

[2] Y. Watanabe and W. Nishizawa, “Semiconductor MASER”, Japanese Patent no.273217, (1957).

[3] R.N. Hall, G.E. Fenner, J.D. Kingsley, T.J. Soltys, and R.O. Carlson, “Coherent light emission from GaAs p-n junctions”, Phys. Rev. Lett., vol 9, pp. 366-368, (1962).

[4] M.I. Nathan, W.P. Dumke, G. Burns, J.F.H. Dill, and G. Lasher, "Stimulated emission of radiation from GaAs p-n junctions", Appl. Phys. Lett., vol 1, pp. 62-64, (1962).

[5] ILX Lightwave Application note, "An Overview of Laser Diode Characteristics", http://assets.newport.com/webDocuments-EN/images/AN05_Laser_Diode_Overview_IX.pdf.

[6] Sanyo Electric Co., products catalogue, "Laser Diodes", http://www.laser029.com/english/UpLoadFile/2009917915750974.pdf, (2007).

[7] CVI Melles Griot, Technical Guide, "Fundamental of beam profileing and beam measurement", https://www.cvimellesgriot.com/products/Documents/TechnicalGuide/Beam_Profiling_and_Beam_Measurement.pdf.

[8] CVI Melles Griot, Technical Guide, "Beamsplitters", https://www.cvimellesgriot.com/products/Documents/Catalog/Beamsplitters_Introduction.pdf.

[9] R. E. Ficher, B. T-Galeb, and P. R. Yoder, " Optical System Design", 2nd edition, Mc Graw Hill, pp. 199-208, (2008).

[10] A. Sakaki, F. Yamada and T. Masui, "A Simple and Accurate Measuring Technique of the Spot Size of Gaussian Laster Beams", Jpn. J. Appl. Phys., vol. 17, pp.1163-1164, (1978)

[11] W. J. Marshall, "Two methods for measuring laser beam diameter", J. Laser Appl. vol. 22, p. 132 (2010).

[12] Y. A. Alsultanny, "Laser Beam Analysis Using Image Processing", J. Comput. Sci., vol. 2, pp. 109-113, (2006).

[13] N. S. Nishioka, D. P. Bua, and T. F. Deutsch, "Measurement of laser-beam profile by using a video camera", Laser Med. Sci., vol. 2, pp. 21-23, (1987).

[14] S. Mallidi and S. Emelianov, "Photoacoustic technique to measure beam profile of pulsed laser systems", Rev. Sci. Instrum. vol. 80, p. 054901, (2009).

[15] Coherent Company, Technical Guide, "Understand Different Laser Beam Profiling Technologies Available", http://www.coherent.com/downloads/UnderstandingLaserBeamProfilingTechnologies.pdf.

[16] D. Wright, P. Greve, J. Fleischer, and L. Austin, "Laser beam width, divergence, and propagation factor- an international standardization approch", Opt. Quant. Electron., vol. 24, pp. S993-S1000, (1992).

[17] Photon Inc., Technical guide "Beam profilers", http://www.bfioptilas.com/html_files/country/germany_eastern_europe/tm/NL3/BeamProfiling.pdf

[18] F. M. Dickey and S. C. Holswade, "Laser Beam Shaping: Theory and Techniques", Marcel Dekker Inc., pp. 395-400, (2000).

[19] ISO/11146-1:2005(E), "Lasers and laser-related equipment — Test methods for laser beam widths, divergence angles and beam propagation ratios — Part 1: Stigmatic and simple astigmatic beams."

[20] ISO/11146-2:2005(E), "Lasers and laser-related equipment — Test methods for laser beam widths, divergence angles and beam propagation ratios — Part 2: General astigmatic beams."

[21] C. E. Webb and J. D-C Jones, "Handbook of Laser Technology and Applications_ Volume II: Laser Design and Laser Systems", IOP Pub. Ltd, pp. 1211-1216, (2004).

[22] K. G. Libbrecht, and J. L. Hall, "A low-noise high-speed diode laser current controller", Rev. Sci. Instrum. vol. 64, p. 2133, (1993).

[23] B. Guillet, D. Robbes, and L. Méchin, "YBCO transition edge sensors used for very low noise thermal control", IEEE Trans. Appl. Supercond., vol. 13, pp. 657-660, (2003).

[24] S. Wu, "Bruit basse fréquence dans des couches minces $La_{0.7}Sr_{0.3}MnO_3$ gravées: vers la réalisation de microcapteurs performants", Phd thesis, university of Caen Basse-Normandie, (2012).

[25] S. Liu, "Fabrication et caractérisation électrique et thermique de microbolomètres non refroidis suspendus à base de couches minces $La_{0.7}Sr_{0.3}MnO_3$ sur silicium", Phd thesis, university of Caen Basse-Normandie, (2013).

CHAPTER III

Experimental results and analysis

In this chapter I will present the measurement results achieved to characterize the performance of LSMO bolometer samples. Then, the proposed thermal model will be detailed to understand LSMO film on substrate frequency response. Finally, a detailed measurement analysis will be presented to optimize the pixel geometry.

1. Bolometric characterization and measurement results

The bolometer is a resistor sensitive to temperature change, and its operation is based on the temperature increase of the thermo-sensing film by the absorption of the incident IR radiation. The change in temperature causes a change in its electrical resistance, which is measured by an external circuit. Thus, it is necessary to characterize the electrical resistance of the bolometer material as function of temperature, and then estimate its Temperature Coefficient of Resistance, or TCR (cf. equation I-10). Another important parameter is the thermal conductance of the bolometer material, which influences its optical responsivity and response time. To characterize the performance of a bolometer as an uncooled radiation thermal detector, its optical responsivity to a radiation heating source has to be measured, and then identify its bolometric (thermal) origin. In addition, noise measurement of bolometer is one of the important characteristics for sensor application since the noise level determines its performance.

In this section we will explain the practical method used to characterize a thin film bolometer deposited on a substrate. This method intends to explore thermal and electrical parameters needed to qualify the performance of the bolometer by identifying the figures of merit (cf. paragraph 3.5 of chapter I).

1.1. Meander pixel geometry

In general, the meander geometry is used to have higher electrical resistance comparing with square geometry having the same surface. One preliminary advantage of getting higher electrical resistance is achieving higher optical responsivity (cf. paragraph 3.5.1 of chapter I). We will assume a pixel of meander geometry with overall surface L×L, a line width “W”, thickness t_f, and a lines spacing “d” (see Figure 3-1). The I+ and I- are the two

current pads which indicate the current flow direction, and V+ and V- are the measuring voltage pads.

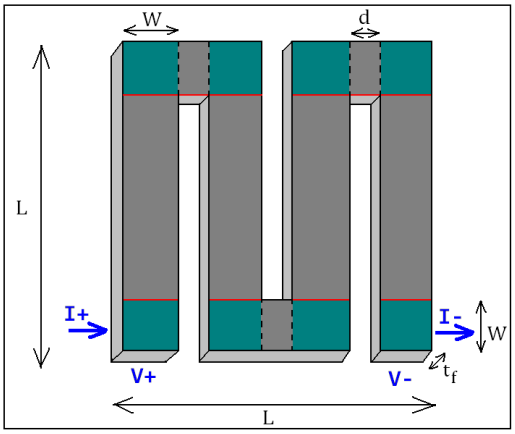

Figure 3-1. Presentation of the meander geometry structure with 4 strips (length L, width L, thickness t_f, strips width W, and strips spacing d) and the current and voltage pads (I+, I- and V+, V- respectively)

The basic relation that should give the electrical resistance of a homogeneous conducting line, at a given temperature, depends on the material properties and the dimensions:

$$R = \frac{\rho}{t_f}\frac{\ell}{W} \qquad \text{(III- 1)}$$

where ρ is the electrical resistivity of the line conductor material (in Ω·m), ℓ is the line length (in m), and $W \times t_f$ is the cross section of the line conductor (in m^2).

In fact, for a meander form resistor, the current tends to crowd at each of the corners, i.e. more current flows nearer to the inner corner than at the outer corner. As a result, the measured resistance tends to be lower than the value calculated using the sheet electrical resistance and the number of squares (where W=l). To estimate the electrical resistance, the squares at the corners of the meander pattern are rated by 0.56 value [1][2]. As a consequence, the total electrical resistance of the meander form is given as follows (where "n" is the number of strips),

$$R = \frac{\rho}{t_f} \times \left[\frac{n(L-2W) + (n-1)d}{W} + 0.56 \times (2n)\right] \qquad \text{(III- 2)}$$

Using the relation L = nW + (n-1)d, we can eliminate the parameter W. Then, the electrical resistance value will be given as follows,

$$R = \frac{\rho}{t_f} \times n \times \left[\frac{L(n-2) + 3(n-1)d}{L-(n-1)d} + 1.12\right] \qquad \text{(III- 3)}$$

The last equation shows the relation that links the electrical resistance of a pixel having meander geometry with the parameter of this geometry (L, n, d, t_f), and with the electrical resistivity (ρ) of the material. Once the electrical resistance is measured, the electrical resistivity can then be calculated by using this equation.

I will show next the measurement process that was used to achieve the bolometric characterization of the studied samples, and then the obtained results will be presented. More detailed analysis concerning the optimization of the main figures of merit of a thermal detector ($\Re_v$, τ_{eff}, NEP, and D^*) depending on pixel detector geometry and the substrate material will be presented later in section 3 of this chapter.

1.2. Electrical characterization

The electrical characterization step includes the measurement of electrical resistance of thin film bolometer material as a function of temperature, therefore extracts the value of the TCR and of the electrical resistivity. Then, we will explain the method used to measure the thermal conductance of a thin-film-on-substrate bolometer, which represents the most important thermal parameter of a bolometer.

1.2.1. Measurement of TCR

The electrical resistance versus temperature (R-T) data of the LSMO thin film sample is measured using a standard four-terminal technique in vacuum condition of about 10^{-3} mbar. This method uses separate pairs of current-carrying and voltage-sensing electrodes. The key advantage of the four-terminal technique is that the separation of current and voltage electrodes eliminates the impedance contribution of the wiring and contact resistances. The R-T data can then be fitted with a smooth polynomial equation and then the dR/dT and TCR data can be calculated and plotted. Figure 3-2, Figure 3-3, Figure 3-4, Figure 3-5, Figure 3-6, and Figure 3-7 show the measured ρ, dR/dT, and TCR versus temperature for all the studied samples.

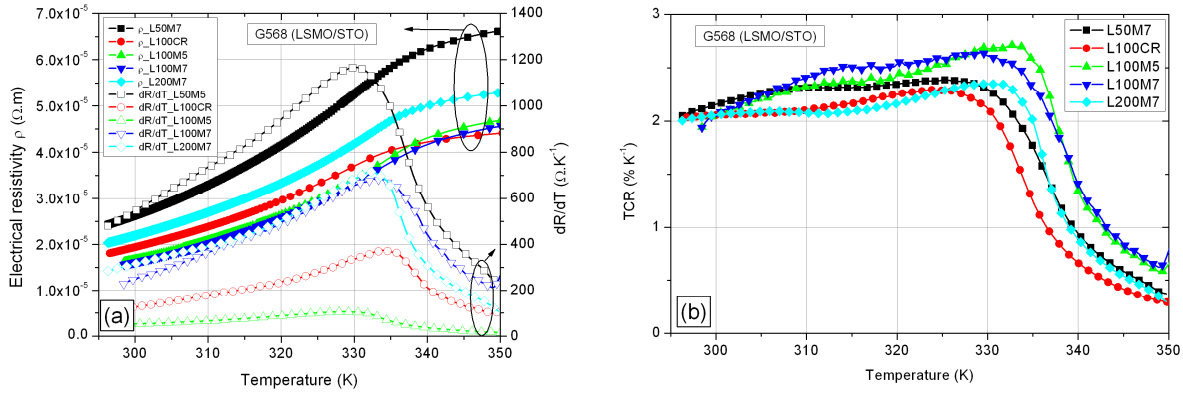

Figure 3-2. Electrical resistivity and dR/dT (a) and TCR (b) versus temperature of LSMO/STO (G568) samples

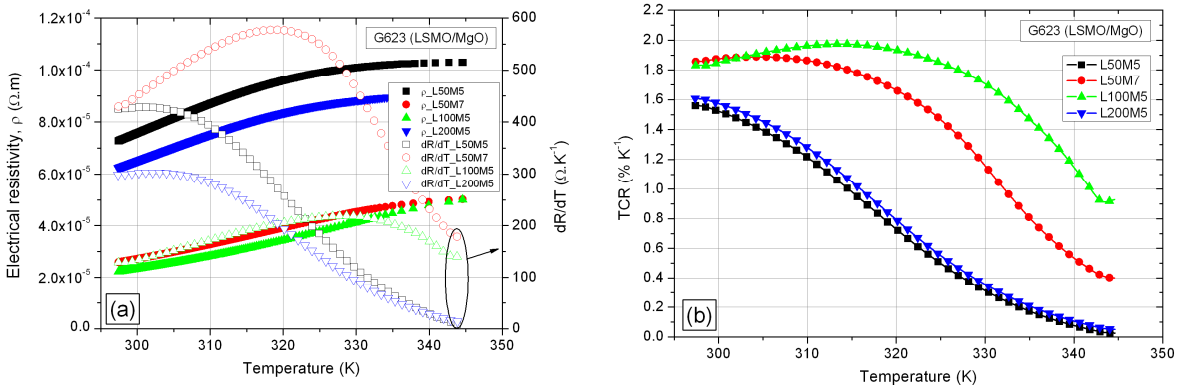

Figure 3-3. Electrical resistivity and dR/dT (a) and TCR (b) versus temperature of LSMO/MgO (G623) samples

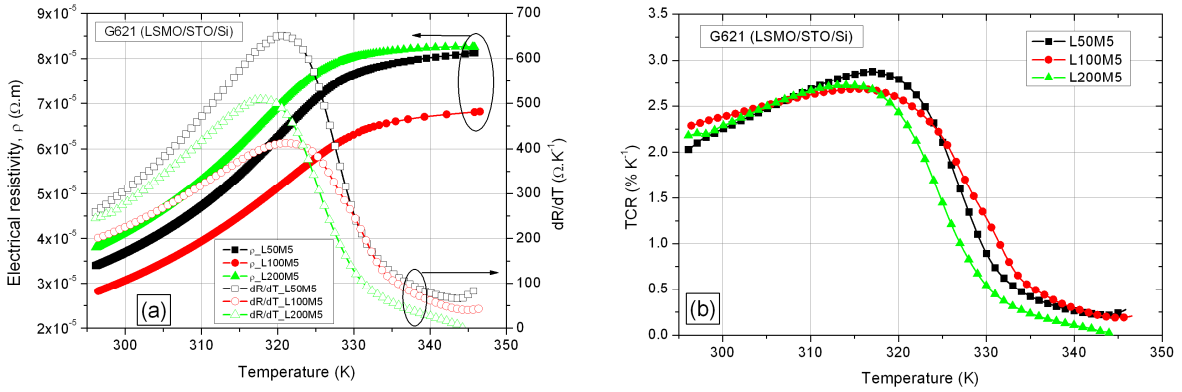

Figure 3-4. Electrical resistivity and dR/dT (a) and TCR (b) versus temperature of LSMO/STO/Si (G621) samples

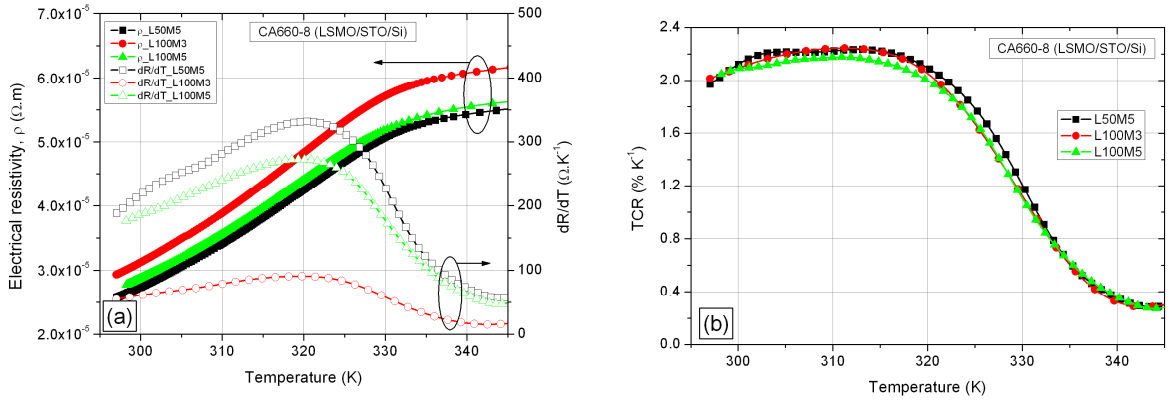

Figure 3-5. Electrical resistivity and dR/dT (a) and TCR (b) versus temperature of LSMO/STO/Si (CA660-8) samples

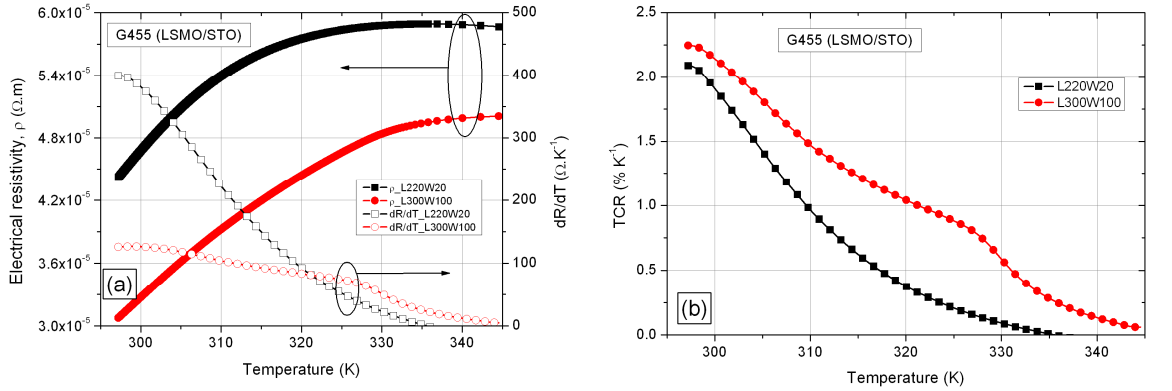

Figure 3-6. Electrical resistivity and dR/dT (a) and TCR (b) versus temperature of LSMO/STO (G455) samples

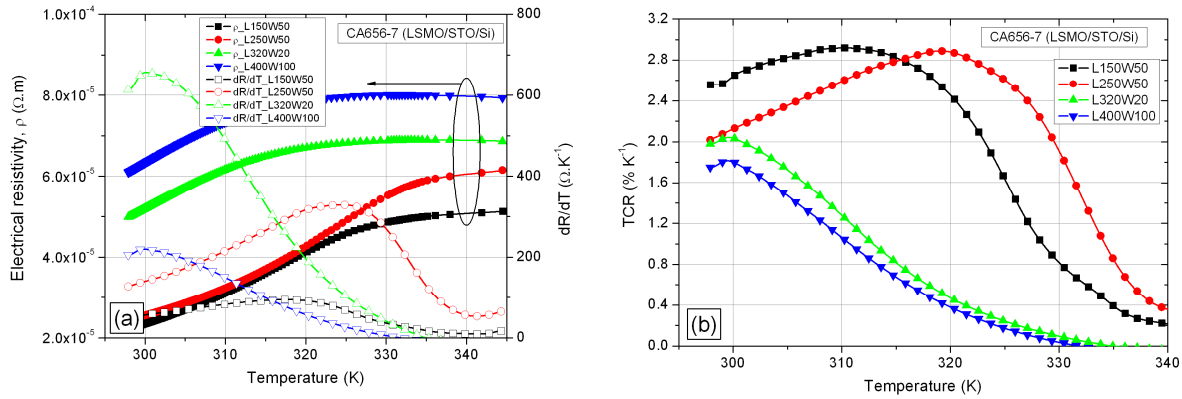

Figure 3-7. Electrical resistivity and dR/dT (a) and TCR (b) versus temperature of LSMO/STO/Si (CA656-7) samples

By knowing the thin film geometry (cf. equation (III- 3)), we can plot the variation of electrical resistivity as a function of temperature. This way, we can calculate the electrical resistivity (ρ) at room temperature, which has a nominal value of 2×10^{-5} Ω·m at 300 K for LSMO thin films [3]. Samples show electrical resistivity value changes in the range of 1.6–7.6 $\times10^{-5}$ Ω·m at 300 K. Indeed, most of the measured ρ values of the studied samples are close to nominal one. But few samples show higher electrical resistivity values. This could be related to the quality of the film, or to the non uniformity of film thickness all over the sample surface.

Based on R-T measurements, Table 3-1 summarizes all the measured and calculated values of $(dR/dT)_{max}$, the optimal working temperature (T_{opt}), the TCR at T_{opt}, the maximum TCR values (TCR_{max}), and the electrical resistivity (ρ) at 300K for all the studied samples. The temperature T_m presents the temperature where TCR_{max} occurs. The last column of this table presents the lattice mismatch (δ) between LSMO film and the substrate (cf. Appendix A).

The maximum TCR values obtained are in the same order of magnitude of that reported in literature. The typical value for the LSMO material is of the order of 2 % K^{-1} [3][5]. The measured TCR values for all the studied samples are in the range 1.6% - 3.0% K^{-1} for the studied temperature range. More detailed analysis of TCR values in respect to resistivity and lattice mismatch will be given next in paragraph 1.2.2.

Another important parameter to extract from R-T measurements is called the optimal working temperature (T_{opt}). It presents the value of temperature where we have the maximum of dR/dT. So, in order to get maximum responsivity (cf. paragraph 3.5 of chapter I), the sample should be optically characterized at T_{opt}. As we can see in these last figures, the optimal temperature is not the same for all samples. For example, in Figure 3-2(a), the maximum dR/dT value equals 1168 $\Omega\cdot K^{-1}$ at 330 K for the sample G568-L50M5, so this sample has to be optically characterized at this optimal temperature (and not at the temperature where TCR is maximal).

Table 3-1 The measured values issued from the R-T measurement for all the studied samples on different substrates, with the lattice mismatch δ between film and substrate

	Geometry	Area (μm^2)	ρ @300K ($10^{-5}\Omega m$)	T_{opt} (K)	$(dR/dT)_{max}$ ($\Omega \cdot K^{-1}$)	TCR at T_{opt} ($\%K^{-1}$)	TCR_{max} ($\%K^{-1}$)	T_m (K)	δ (%)
G568 LSMO/STO	**L50M7**	50×50	2.6	330	1168	2.3	2.4	325	0.82
	L100M5	100×100	1.7	334	374	2.7	2.7	333	0.82
	L100M7	100×100	1.6	334	685	2.5	2.7	329	0.82
	L100CR	100×100	3.8	330	105	2.1	2.3	325	0.82
	L200M7	200×200	2.2	330	716	2.3	2.4	331	0.82
G623 LSMO/MgO	**L50M5**	50×50	7.6	301	429	1.5	1.6	298	8.14
	L50M7	50×50	2.6	319	577	1.7	1.9	305	8.14
	L100M5	100×100	2.3	328	219	1.8	2.0	314	8.14
	L200M5	200×200	6.5	302	303	1.5	1.6	298	8.14
G621 LSMO/STO/Si	**L50M5**	50×50	3.7	320	650	2.8	2.9	317	0.54
	L100M5	100×100	3.1	321	412	2.5	2.7	317	0.54
	L200M5	200×200	4.1	318	508	2.6	2.7	315	0.54
CA660-8 LSMO/STO/Si	**L50M5**	50×50	2.8	320	318	2.0	2.2	313	0.54
	L100M3	100×100	3.1	320	91	2.1	2.2	313	0.54
	L100M5	100×100	2.9	320	373	2.0	2.2	312	0.54
CA656-7 LSMO/STO/Si	**L150W50**	150×230	2.4	318	94	2.6	2.9	311	0.54
	L250W50	250×350	2.5	324	328	2.7	2.9	319	0.54
	L320W20	320×110	5.2	300	657	2.0	2.1	299	0.54
	L400W100	400×650	6.3	300	219	1.8	1.8	299	0.54
G455 LSMO/STO	**L220W20**	220×120	4.7	300	399	2.1	2.1	298	0.82
	L300W100	300×870	3.3	300	127	2.2	2.2	298	0.82

1.2.2. Effect of substrate material on TCR

Among the parameters that can influence the TCR value is the substrate material and film thickness. For manganites, just a few studies have been done to investigate the relation between the substrate material and the TCR of bolometer material, which is one of the most important parameter of a bolometer. It has been proved that lattice mismatch causes bi- or uni-axial strain that affects structural, electrical and magnetic properties of manganese oxides thin films [6]. Therefore, to obtain high performance of manganite films one should control the strain induced from substrate.

Daoudi *et al* [7] have discussed the effect of substrate on the electrical properties of $La_{0.7}Ca_{0.3}MnO_3$ films on LSAT ($[LaAlO_3]_{0.3}$-$[SrAlTaO_6]_{0.7}$) and STO substrates. They had achieved a TCR value of 22% K^{-1} @248 K and 10% K^{-1} @230K for lattice mismatch value of 0.2% and 1.12% between LCMO film and LSAT and STO substrate, respectively. Kim *et al* showed that $La0_{.75}Sr_{0.25}MnO_3$ films on $Si_{0.8}Ge_{0.2}$/Si and $Si_{0.99}C_{0.01}$/Si have higher electrical resistivity and low TCR values compared to Si sample due to excessive compressive and tensile strain, respectively [8]. Also, they demonstrated that TCR is inversely proportional to electrical resistivity.

Based on Table 3-1, we can notice that the difference in the TCR values is related to the strain induced by the lattice mismatch between LSMO film and the different substrates. The relation between TCR_{max} of LSMO film and the lattice mismatch (δ) between film and substrate is investigated in Figure 3-8. The electrical resistivity of bulk LSMO material is about $2\times10^{-5}\Omega\cdot m$ [3].

Figure 3-8 reveals that we obtained higher TCR_{max} value for lower value of δ. This way, to enhance the responsivity and NEP, it is better to choose a substrate that has lower δ with the film as in the case of the STO substrate. In addition, we have to pay attention here to the thermal properties of the substrate materials, in terms of response time of the detector. So, to achieve a faster response a substrate of higher thermal conductivity (κ) will be needed (cf. Table 3-4 in page 124). This is the case of STO-buffered Si substrate, where we minimize the lattice mismatch between LSMO film and Si substrate by using a STO buffer layer, knowing that Si thermal conductivity is higher than that of STO. Furthermore, this can be one perspective to add STO buffer layer in the case of MgO substrate in order to lower the mismatch δ.

The maximum TCR value for LSMO samples is close to 3% K^{-1} near room temperature. This value is fairly close to that reported for semiconducting YBCO and vanadium oxides, but it is still lower than that of amorphous semiconductor compositions (cf. Table 1-9 of chapter I).

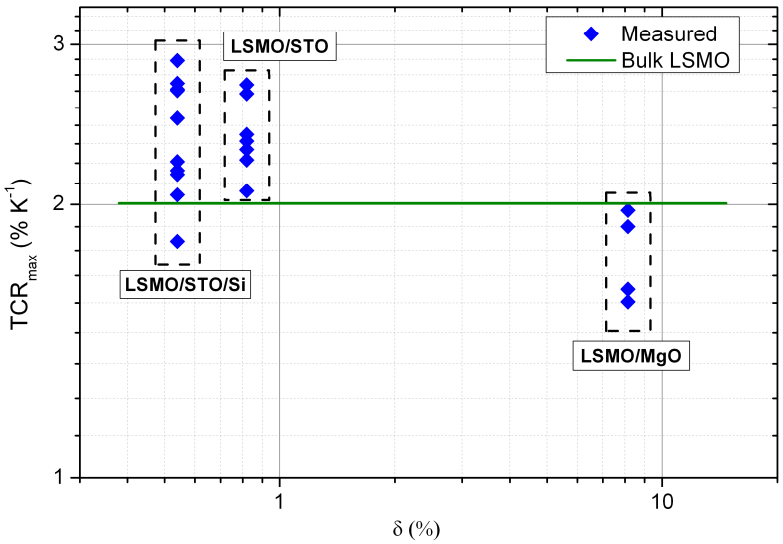

Figure 3-8. The measured TCR_{max} versus lattice mismatch for LSMO film on different substrate materials

Figure 3-9 shows that TCR_{max} value of the LSMO film decreases as the electrical resistivity ρ increases with a linear behavior. This tendency is consistent with the good quality of the film, in terms of epitaxial structure. This tendency has been also reported by Prasad *et al* for $La_{0.88}Sr_{0.12}MnO_3$ thin films grown on $SrTiO_3$ substrate [9]. We have a data dispersion of about 10%. This could be related to the film quality, especially for G621 (cf. appendix A) and to TCR and ρ estimation procedures. This also could be related to the lattice mismatch between film and substrate, which has the higher value for G623 sample.

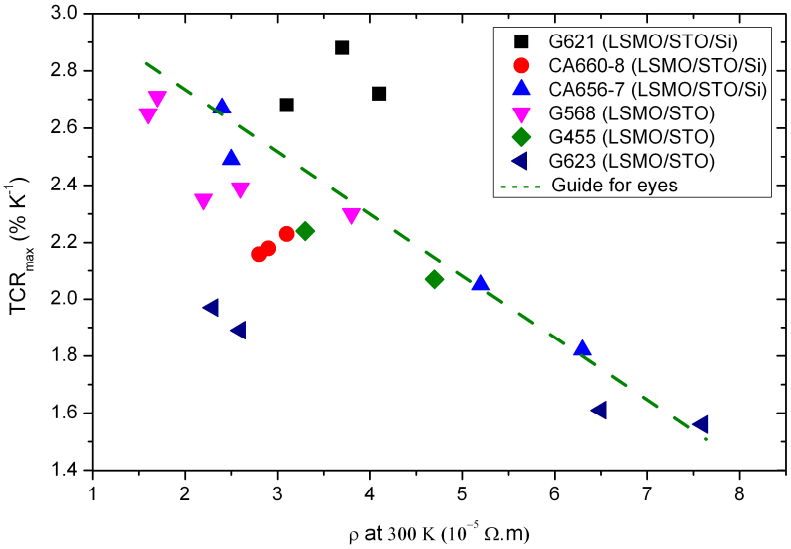

Figure 3-9. The measured TCR_{max} versus electrical resistivity for LSMO film on different substrate material

Another discussion can be made on the effect of film thickness on the value of TCR_{max} and T_m (temperature where we have maximum of TCR). To clarify this relation, we will compare samples LSMO/STO/Si that were made under the same fabrication conditions (MBE) and technology (CA660-8 and CA656-7) and that exhibit close electrical resistivity (see in Figure 3-10). Also, we will use measurement data issued from other thesis results achieved on same samples technology in our laboratory [10]. We can notice that TCR_{max} increases by changing the film thickness from 10 nm to 100 nm (cf. Figure 3-10(a)), and so does the T_m (cf. Figure 3-10(b)). This result is consistent with that achieved by Prasad *et al* [9] for $La_{0.88}Sr_{0.12}MnO_3$ thin film, and Neff *et al* [11] for YBa_2CuO_{7-x} thin film.

Tsuchiya *et al* [12] investigated the TCR value of $La0_{.8}Sr_{0.2}MnO_3$ film by changing the film thickness. They found out that the film with a thickness of 80 nm shows a maximum TCR of ~ 2.4% at 290 K, which is higher than that of 40 nm film (~ 1.3%). The film with a thickness of 120 nm indicates lower TCR than that of the film with the 80-nm thickness. This phenomenon could be caused by the insufficient crystal growth of the films.

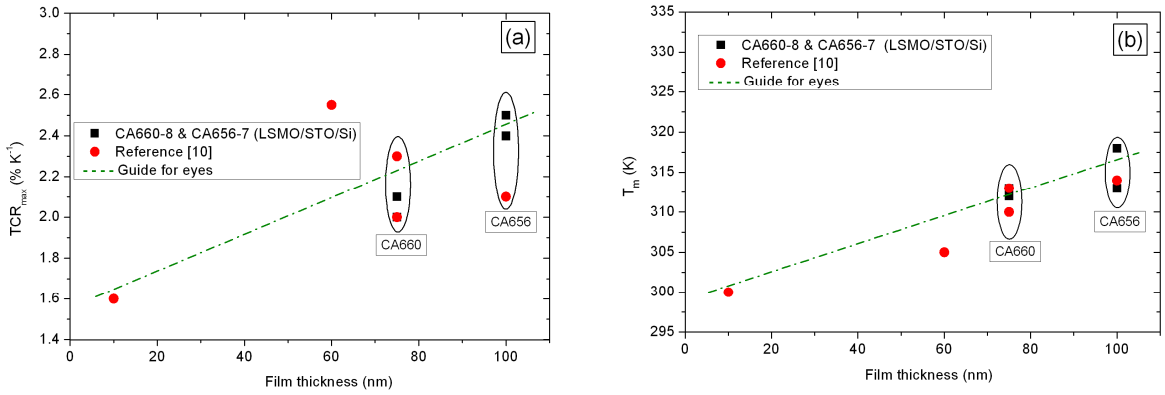

Figure 3-10. The measured TCR_{max} (a) and T_m (b) versus film thickness for LSMO film on Si substrate

1.2.3. Measurement of thermal conductance

In this paragraph we describe the procedure performed in order to obtain the voltage-current (V-I) characteristics of thin film bolometer, and then using this measurement with R-T data to determine the thermal conductance of bolometer.

In order to obtain the V-I characteristics, the standard four-terminal technique will be used. The V-I measurements was achieved by elaborating the precision parameter analyzer HP4156B. We apply a sweep varying bias current (I_b) on the film (using the two current pads: I+, I-) and measure the voltage (V_m) across it (using the two voltage pads: V+, V-). The bias current must be scanned by round trip in both directions (positive and negative) to ensure the absence of hysteresis act and the ohmic performance. This measurement has to be done at the optimal temperature (T_{opt}) which presents the regulated temperature of the sample holder. Also, the sample is fixed inside vacuum chamber to eliminate the heat exchange by convection. The electrical resistance of the film R_m can be calculated according to the equation $R_m=V_m/I_b$ and then plotted. Then, a second order polynomial fit has been used to model the variation of R_m as function of I_b, as seen in Figure 3-11. The noisy values at small currents have been omitted.

The film electrical resistance R_m is not constant and increases nonlinearly as function of bias current. This behavior is coming from Joule self-heating effect. As a result, this heating will raise the temperature of the film and then increases the value of R_m, which is in agreement with R-T characteristics (see Figure 3-7(a)). For each point of V-I data we can

calculate the electrical power dissipated in the film resistance by $P_J=V\times I_b$. The temperature of film can be calculated by fitting R-T data in the vicinity of T_{opt} using the linear approximation ($R_m=aT+b$). This way, we can deduce the temperature of the film T as function of its electrical resistance, R_m. Finally, by plotting P_J as function of T, we can estimate the thermal conductance of the film by $G=dP_J/dT$ (cf. paragraph 3.4 of chapter I), as seen in Figure 3-12.

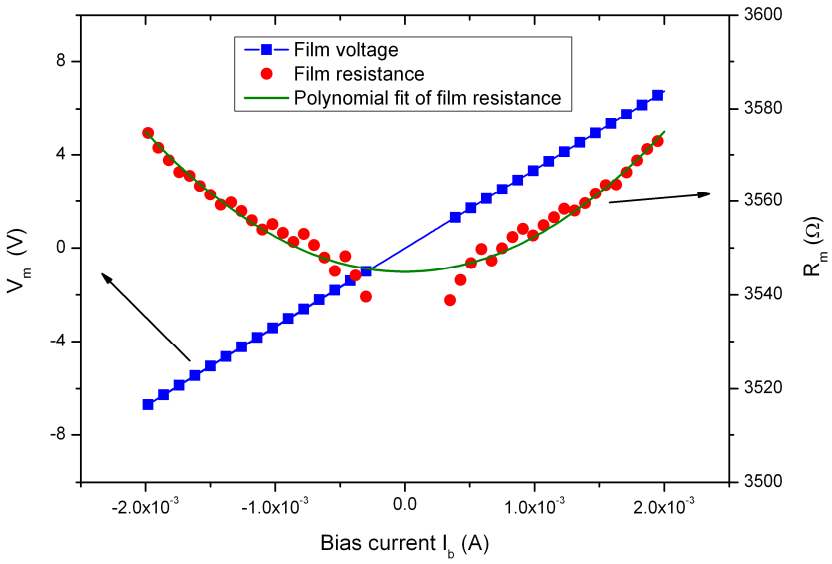

Figure 3-11. Voltage-Current measured data and the deduced electrical resistance at T_{opt} (318 K) and vacuum condition (0.1 Pa) for CA656-7_L150W50 sample

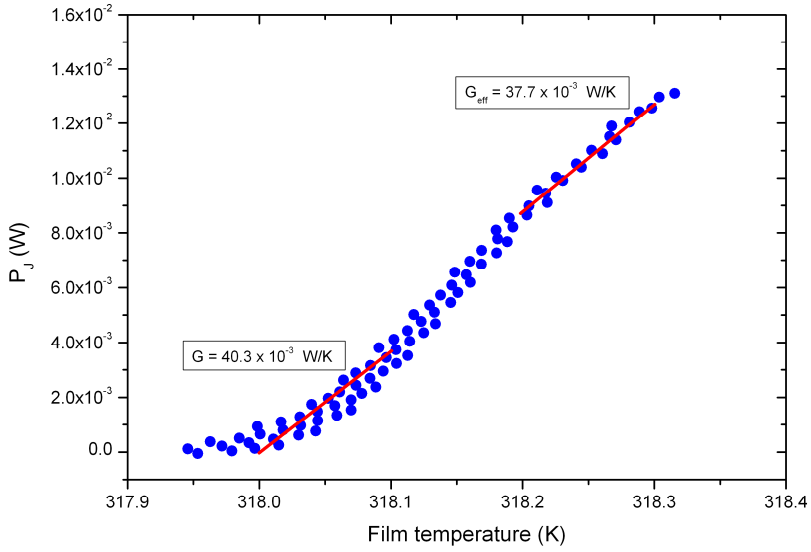

Figure 3-12. Electrical dissipated power versus film temperature at T_{opt} (318 K) and vacuum condition (0.1 Pa) for CA656-7_L150W50 sample

From the slope at the origin (at T_{opt}), one can estimate the geometrical thermal conductance (G) of the film-on-substrate structure. The slope estimation can be done for fixed ΔP_J or ΔT range. On the other side, the slope at other temperature values represents the effective thermal conductance of the film, which is given by the following equation: $G_{eff} = G - I_b^2 \times dR/dT$ (cf. paragraph 3.4 of chapter I). Thus, the effective thermal conductance depends on the bias current, and $G_{eff} < G$ for non-zero bias current.

The measured values of thermal conductance for all square samples will be given later in Table 3-7, and for rectangular samples in Table 3-9. The estimation of G was done at the origin (T_{opt}, 0) for a fixed range of temperature variation 0.1 K. Due to the non linearity of the measured G versus T, estimated value of G could be somewhat changed following the used method. Thus, using the same method for all sample measurements tends to the same order of uncertainty. A linear interpolation has been performed between the point (T_{opt}, 0) and (T_{opt}+0.1 K, P_J). The standard deviation has been used to estimate the uncertainties reported in Table 3-7.

1.3. Optical characterization

In order to characterize the performance of our bolometer as an uncooled radiation thermal detector, we need to measure its optical responsivity to a radiation heating source. Thus, we measure the optical responsivity of the film using an electronically modulated semiconductor laser diode, and then we try to identify its bolometric (thermal) origin.

In this section I will present mainly the method used to characterize the film in terms of optical responsivity and response time, according to the basic bolometer model (cf. paragraph 3.4 of chapter I).

1.3.1. Optical responsivity and frequency response

The calculation of the optical responsivity can be achieved (as explained earlier in paragraph 7.1 of chapter II and the equation II-19) by measuring the ratio V_{out_ac} / V_{PD} using the signal analyzer HP3562A.

The dependence of the optical responsivity as a function of the laser power modulation frequency at different bias currents ($I_b<I_{opt}$) for G568 (LSMO/STO), G623

(LSMO/MgO), and G455 (LSMO/STO) samples are shown in Figure 3-13(a), Figure 3-13(b), and Figure 3-13(c), respectively. We note that at 1 Hz and 80 µA bias current we get an optical voltage responsivity of 10 $V \cdot W^{-1}$ for L100M5(LSMO/STO) sample, and of 1.3 $V \cdot W^{-1}$ for L100M5(LSMO/MgO) sample. This comes up from that the thermal conductivity of STO material is about 5 times lower than that of MgO material (cf. Table 3-4). More detailed analysis on the role of substrate material will be given later in paragraph 3.2.3 of this chapter.

In general, we observe a low-pass behavior for all the samples, but the tendency is different following the sample surface. In addition, the cut-off frequency ($1/(2\pi\tau_{-3dB})$) depends on the sample surface and substrate material. In the first two decades the optical responsivity is almost constant for small samples, but it's not true for big ones. Therefore, the basic model (cf. paragraph 3.4 of chapter I) cannot be used to identify this behavior. Hence, another detailed thermal model of thin-film-on-substrate structure should be developed to understand this behavior. This model will be presented in details in section 2 of this chapter. Also, the role of sample's surface on the performance of bolometer will be detailed in paragraph 3.2.1 of this chapter.

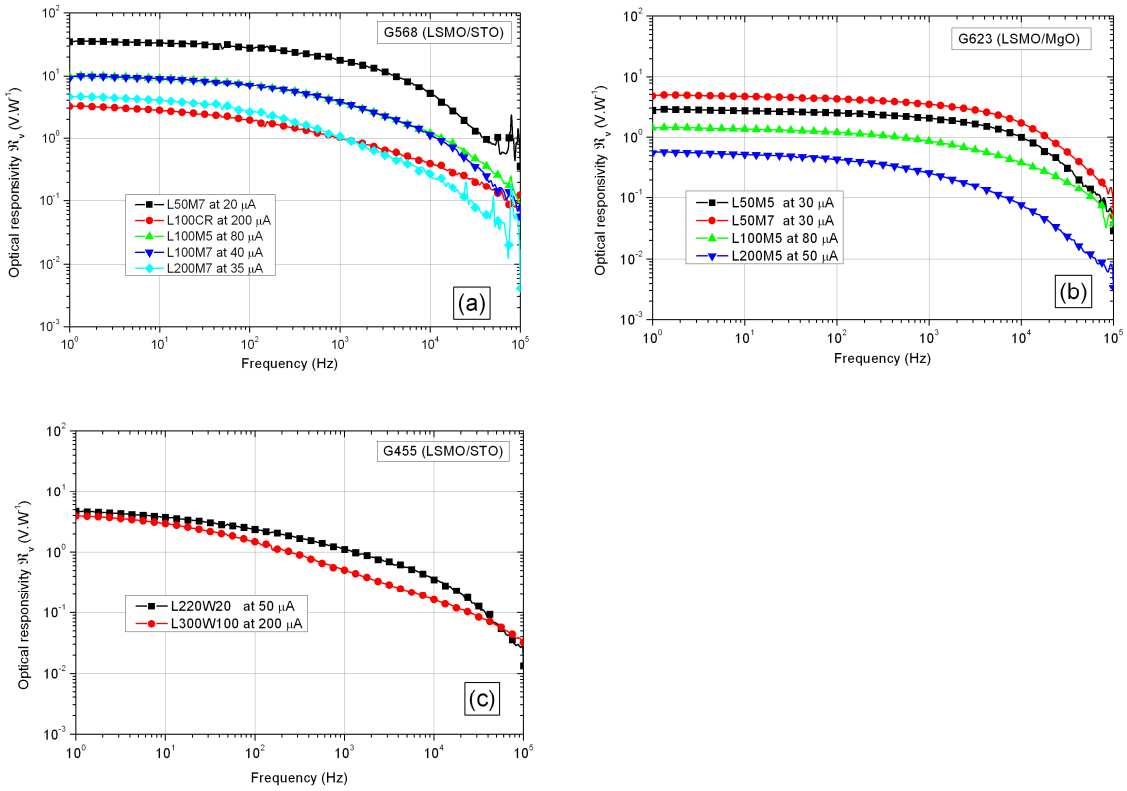

Figure 3-13. Optical responsivity at T_{opt} versus laser modulation frequency at different bias currents for (a) G568 sample (a), G623 sample (b), and G455 sample (c)

The dependence of the optical responsivity as a function of the laser power modulation frequency at different bias currents for LSMO/STO/Si samples CA660-8_L50M5, G621_L200M5, CA656-7_L150W50 is shown in Figure 3-14(a), Figure 3-14(b), and Figure 3-14(c) respectively.

We do not observe the low-pass behavior for all LSMO/STO/Si samples. Indeed, a non-bolometrical contribution is identified at high frequency (more that 100 Hz). Therefore, it is not possible to calculate the cut-off frequency ($1/(2\pi\tau_{-3dB})$) for these samples using the measured frequency response. Indeed, we get a high-pass behavior for zero bias current at high frequency. The increasing optical responsivity at higher frequencies could be related to the contribution of photo-induced effects in LSMO or in the LSMO/STO/Si heterostructure [6]-[15], or to the pyroelectric effect in the LSMO/STO/Si heterostructure, as reported by Kreisler *et al.* for YBCO material [16]. Moreover, this behavior is not observed for suspended structure (cf. Figure 3-49) where film and substrate are not in contact. Further studies should be done to characterize this non-bolometric component, as one perspective of this work.

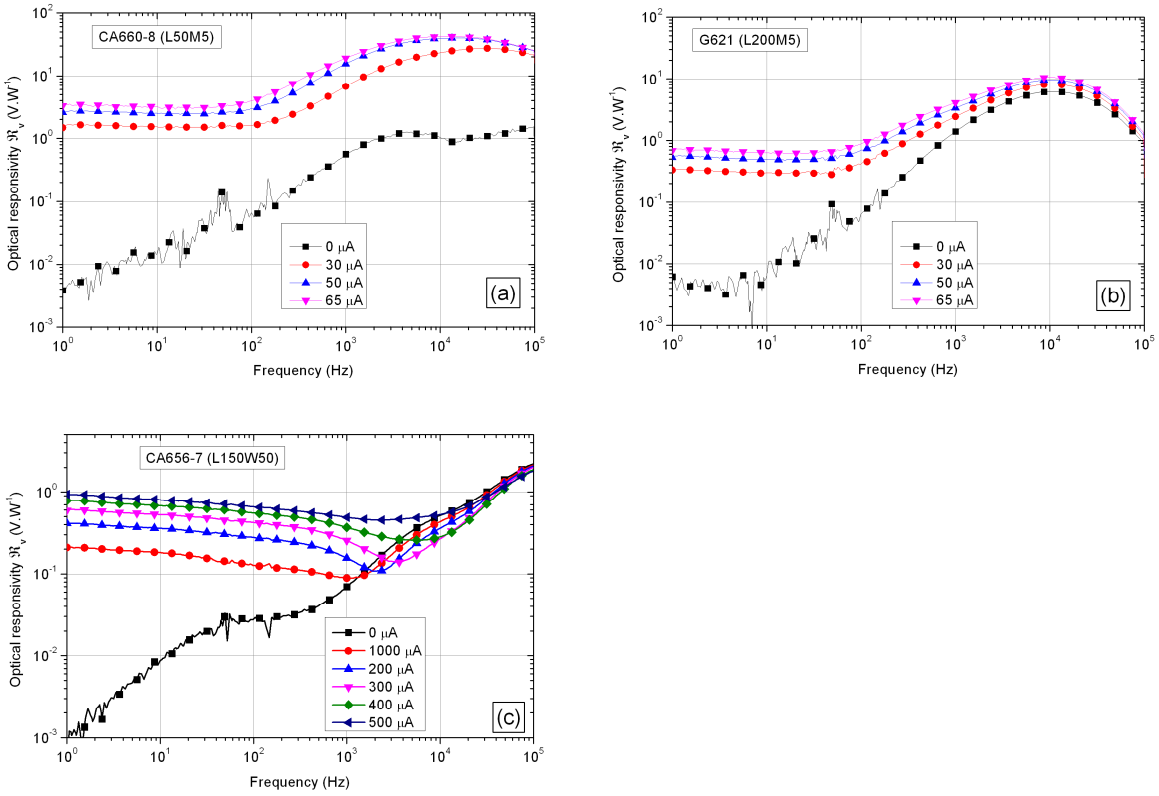

Figure 3-14. Optical responsivity at T_{opt} versus laser modulation frequency at different bias currents for G621_L200M5 (a), G621_L50M5 (b), and CA656-7_L150W50 (c) LSMO/STO/Si samples

The small sample (CA660-8_L50M5) has a higher optical responsivity in comparison with the big one (G621_L200M5). Indeed, the thermal conductance is proportional to the sample surface for the same substrate material. More detailed analysis on the role of sample surface will be given later in paragraph 3.2.1 of this chapter. In general, LSMO based bolometers show moderate responsivity. It is of the same order of that for other manganite oxides, but is still lower than that of other bolometer materials (cf. tables I-8 and I-9 of chapter I), because they have suspended structure (so with a lower thermal conductance). Indeed, the main advantage of LSMO material as bolometer is that it has a low 1/f noise level, as we will see later in this chapter.

1.3.2. Linearity of optical voltage responsivity

In order to achieve an agreement with basic bolometer model (cf. Equation I-21) we need to prove the linearity relationship between the optical voltage responsivity ($\Re_v$) and both bias current (I_b) and received radiation power by the sample (P_m). From the $\Re_v$ measurements at different bias currents, one can estimate the linearity of bolometer responsivity. Taking the value of $\Re_v$ in the frequency range where it is constant (at 1 Hz) and quite equal to $\Re_v(0)$, one can plot $\Re_v$(1Hz) versus I_b as shown in Figure 3-15 (cf. equation (I-21). As we can see in this graph, a very good linear relation between $\Re_v$(1Hz) and I_b is obtained for CA660-7_L150W50 (LSMO/STO/Si) sample. Indeed, this linearity has been checked for all the studied samples, thus validating the basic model of the bolometer.

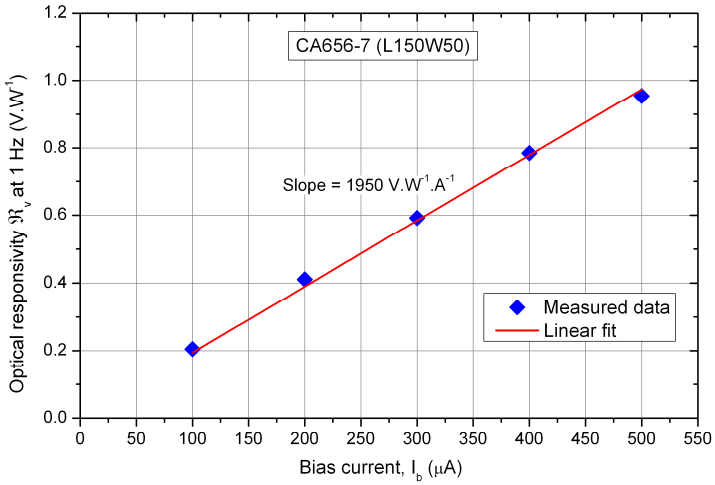

Figure 3-15. The optical responsivity at 1 Hz and T_{opt} (318 K) versus the bias current for CA656-7_L150W50(LSMO/STO/Si) sample extracted from Figure 3-14(c) measurements

Using the slope of this measured data we can estimate the ratio η/G for small bias current (cf. paragraph 3.4 and equation I-21 of chapter I). Using the estimated value of G for this sample (cf. Figure 3-12) which equals to 40.3×10^{-3} $W\cdot K^{-1}$, we can estimate the value of the absorption coefficient η of about 84% for LSMO material.

Also, the linearity of sample's output voltage (V_m) versus the power received by the sample (P_m) must be checked (cf. Equation I-21). So, we measure the output voltage of the sample at fixed temperature (T_{opt}) and at fixed bias current (I_b), for each sample, as function of the laser power received by the sample. Figure 3-16 shows that the sample's output voltage increases linearly with increasing the incident radiated power at a given bias current for each sample, thus, validating the basic model of the bolometer. The slope values are consistent with optical responsivity measured earlier, as seen in Figure 3-13 and Figure 3-14.

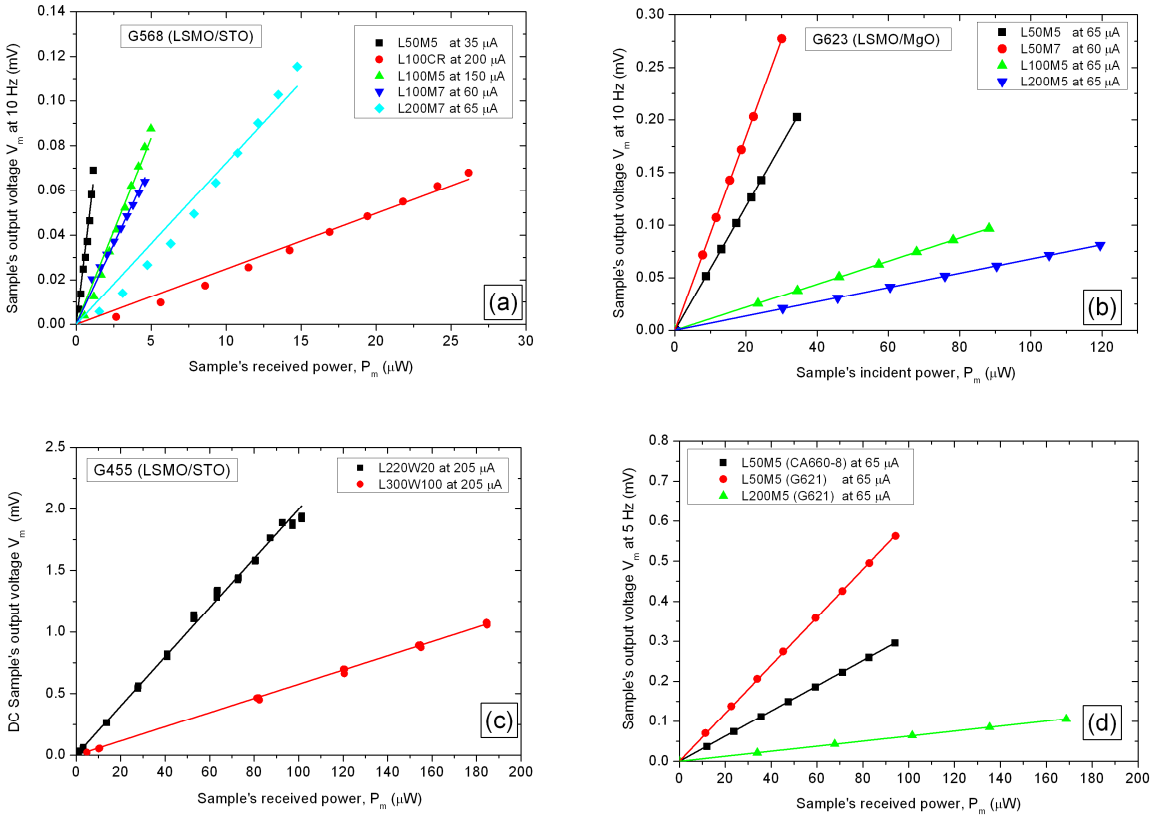

Figure 3-16. The output voltage (V_m) versus the received power (P_m) at T_{opt} for (a) G568(LSMO/STO) samples at modulation frequency 10 Hz, (b) G623 (LSMO/MgO) samples at modulation frequency 10 Hz, (c) G455 (LSMO/STO) samples at DC, and (d) G621 and CA660-8 (LSMO/STO/Si) samples at modulation frequency 5 Hz. The lines are guides for the eyes

1.3.3. Bolometric behavior identification

In order to identify whether the optical responsivity is bolometric (thermal) or has another origin, we need to perform a comparison between the optical voltage responsivity $\Re_V$(1Hz) and dR/dT deduced from R-T measurements (cf. paragraph 1.2.1) as functions of the temperature. These two quantities are plotted in Figure 3-17, Figure 3-18, and Figure 3-19. For the presented results, we notice that the dependence of $\Re_V$ on the temperature follows well the variation of dR/dT versus temperature, and they reach a maximum value at the same temperature. This suggests that the major component of the response at 1 Hz is bolometric for all these samples.

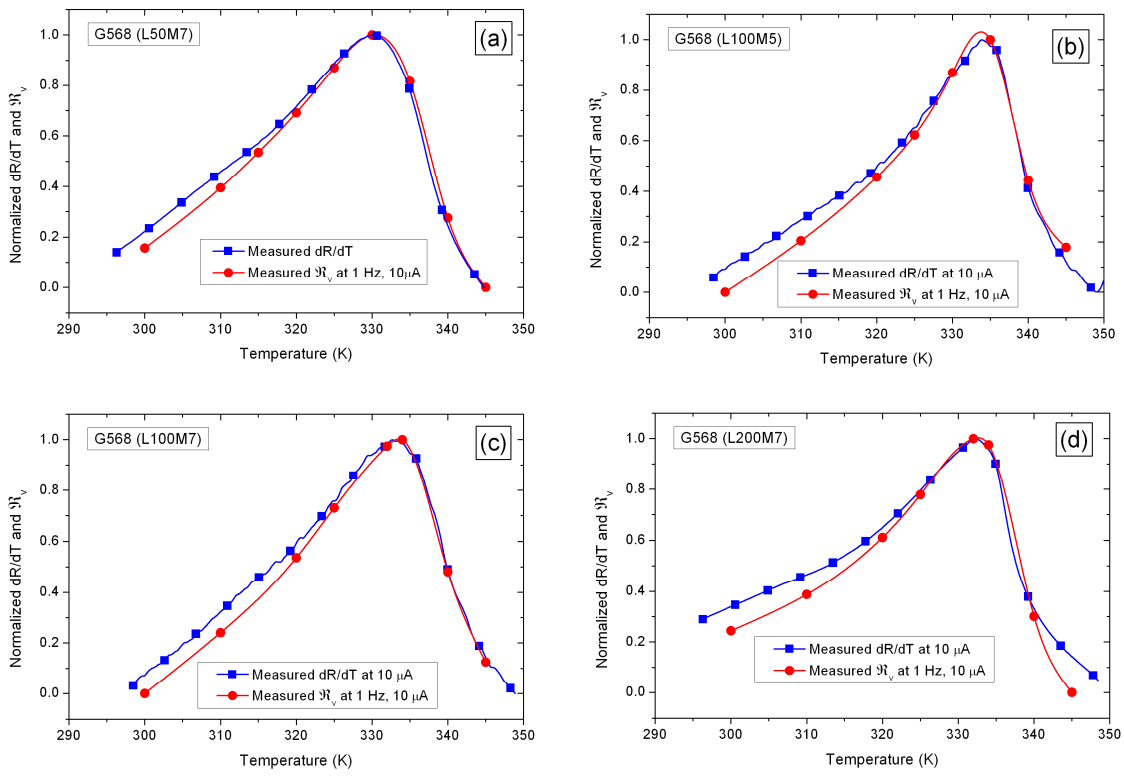

Figure 3-17. The normalized optical responsivity (at 10 μA and frequency 1 Hz) and dR/dT (measured at 10 μA) versus temperature curves for G568 (LSMO/STO) samples

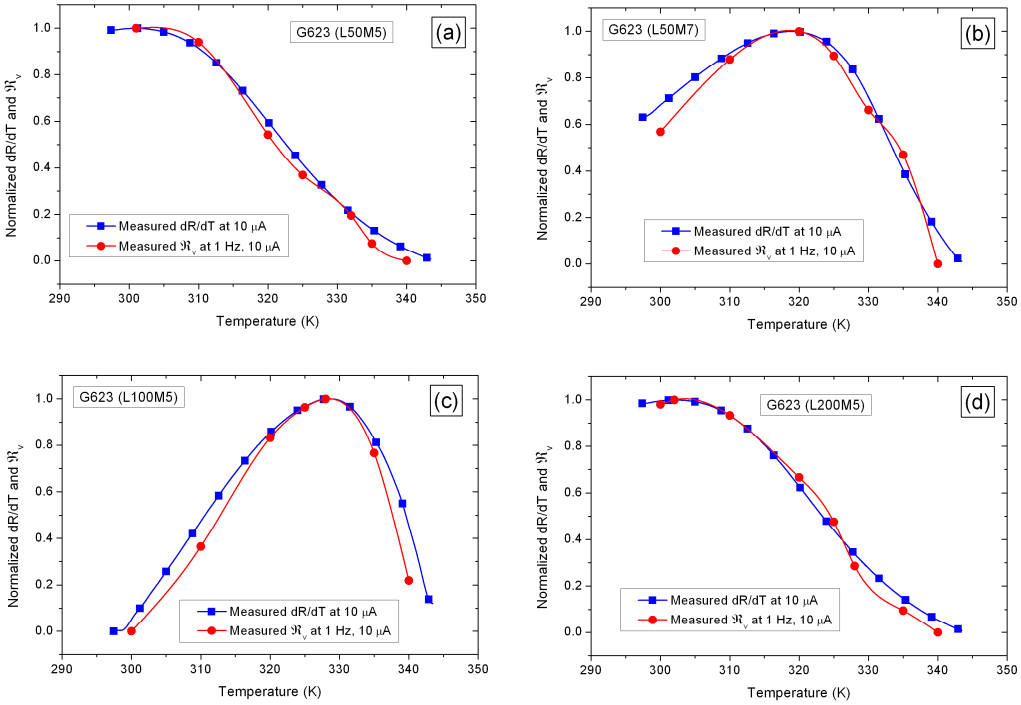

Figure 3-18. The normalized optical responsivity (at 10 μA and frequency 1 Hz) and dR/dT (measured at 10 μA) versus temperature curves for G623 (LSMO/MgO) samples

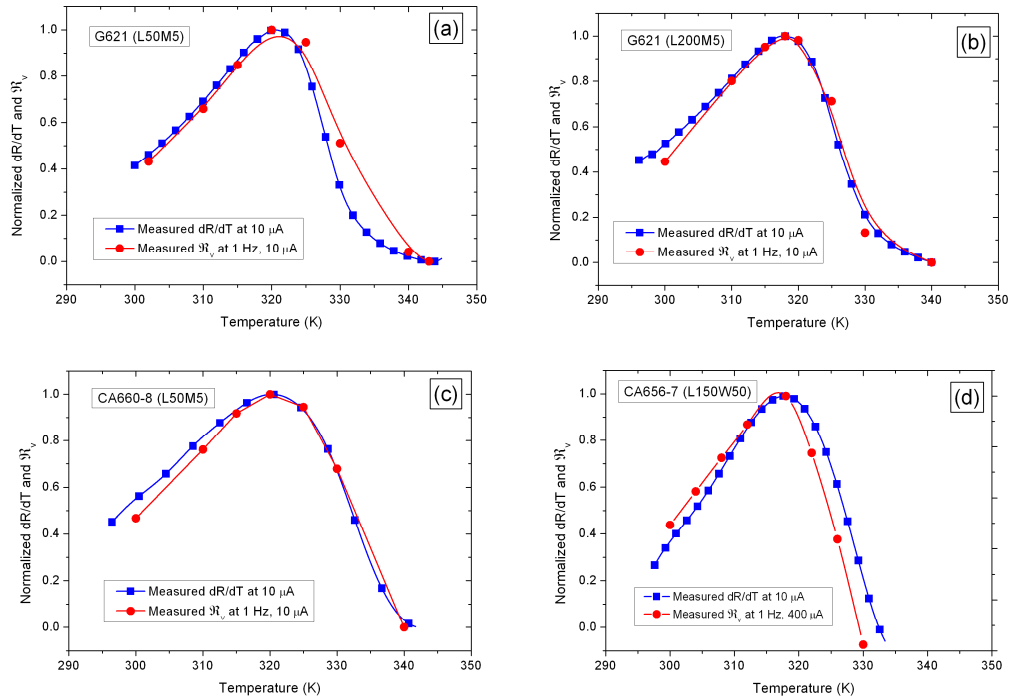

Figure 3-19. The normalized optical responsivity (at bias current 10 μA and 1 Hz) and dR/dT (measured at 10 μA) versus temperature curves for G621_L50M5 sample (a), G621_L200M5 sample (b), CA660-8_L50M5 sample (c), and CA656-7_L150W50 sample

1.4. Noise measurement and NEP & D* estimation

We have measured the voltage noise spectral density (S_v) of the sample for different values of the bias current and at T_{opt} for all the studied samples. Figure 3-20 shows measurement results for four different samples. Actually, this figure presents one geometry of each sample having the same surface (200×200 μm^2) when possible. There are two components in the noise spectra: white noise (at medium frequency), and excess noise (at low frequency) parameterized by Hooge's relation given in equation (I-26). As expected, the white noise level does not depend on the bias current on the contrary of 1/f noise. The frequency where 1/f noise becomes non negligible depends on different experimental and material properties, such as the applied current, the voltage contact resistance, and the intrinsic 1/f noise level (α_H/n described later).

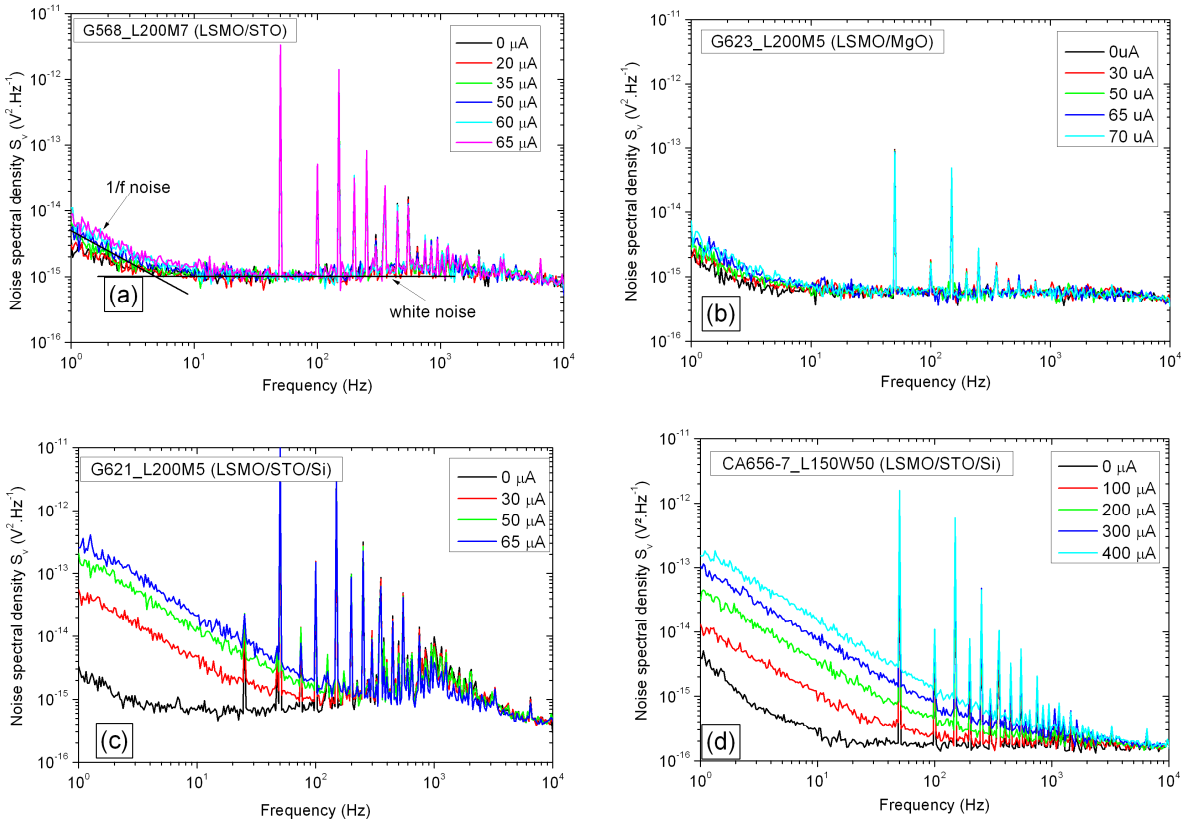

Figure 3-20. The measured noise spectral density at different bias currents (I_b) for G568_L200M7 at T_{opt} =332 K and at R_0=50 kΩ (a), G623_L200M5 at T_{opt} =303 K and at R_0=50 kΩ (b), G621_L200M5 at T_{opt} =320 K and at R_0=50 kΩ (c), CA656-7_L150W50 at T_{opt} =318 K and at R_0=10 kΩ (d)

1.4.1. White noise

The total measured voltage noise spectral density writes as in equation (II-14) of chapter II. This way, and after having performed the characterization of the readout electronics, that has been done in chapter II (cf. section 7 in chapter II), we can identify the value of all parameters involved in equation (II-14). Using the estimation of sample's white noise at medium frequency ($4k_BTR_m$) and the total measured noise spectral density at the input of the amplifier, one can calculate the noise spectral density of voltage contact ($4k_BTR_{CV}$), thus estimate the voltage contact resistance R_{CV}. For example, R_{CV} equals to 5.5 kΩ, 1.3 kΩ, 8.6 kΩ, and 2.6 kΩ in the sample G568_L200M7, G623_L200M5, G621_L200M5, and CA656-7_L150W50 respectively. The value of R_{CV} is mainly related to the design of the mask: a long path between the meander and voltage contact leads obviously to high values of voltage contact resistance (cf. the masks design section 8 of chapter II).

1.4.2. Excess noise estimation

The excess (or 1/f) noise increases with bias current, as seen in Figure 3-20. We calculate $[S_v(I_b)-S_v(0)]\times f$ to estimate 1/f noise at 1 Hz for each value of bias current, assuming an error bar equals to ±10% [17]. The subtraction S_v (at I_b) - S_v (at I_b=0) is used to eliminate the contribution of instrumentation noise from the measurements. The relation of Hooge (cf. equation I-26 of chapter I) gives an empirical model of the voltage noise spectral density ($S_v^{1/f}$) of the 1/f noise as a function of the frequency f.

We have then to verify the quadratic dependence to voltage of the 1/f noise, thus verify the agreement of our estimation with the relation of Hooge. To do this we plot the estimated 1/f noise at each current versus the measured voltage across the sample $V_m(I_b)$-$V_m(0)$ and check that these points fit well with a line of slope 2, as shown in Figure 3-21.

To estimate the 1/f noise at any bias current we need to estimate the value of normalized Hooge parameter (α_H/n). This is an important parameter that we will use later in this chapter to estimate the optimal NEP (NEP at the optimal bias current) for our samples. Using the intersection of the line of slope 2 with the vertical coordinate, we can estimate the value of α_H/n. For example, α_H/n equals to 1.4×10^{-29} m^3 in the sample G455_L220W20 (LSMO/STO), 2.7×10^{-30} m^3 in the sample G568_L200M7 (LSMO/STO). Indeed, L200M7 shows α_H/n value 5 times lower than that of L220W20 while they are both deposited on STO substrate. Furthermore, L200M7 has 7 strips with an effective surface of 38.1×10^{-9} m^2, and

L220W20 has 4 strips with an effective surface of 18.2×10^{-9} m². Getting lower value of 1/f noise level is mainly related to the mask design (cf. paragraph 8 of chapter II) where B-mask was optimized to reduce the noise.

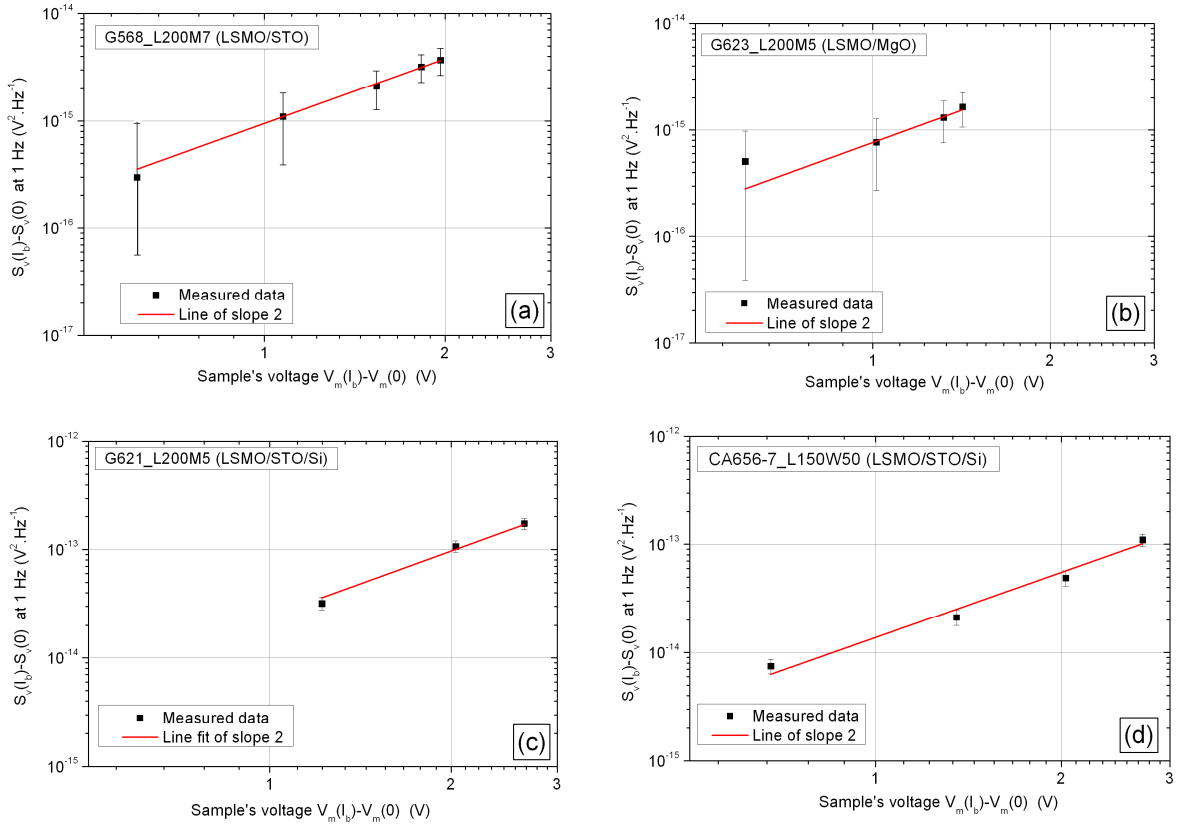

Figure 3-21. Voltage noise spectral density versus sample's voltage for G568_L200M7 at T_{opt} =332 K and at R_0=50 kΩ (a), G623_L200M5 at T_{opt} =303 K and at R_0=50 kΩ (b), G621_L200M5 at T_{opt} =320 K and at R_0=50 kΩ (c), CA656-7_L150W50 at T_{opt} =318 K and at R_0=10 kΩ (d)

In addition, the estimated values of 1/f noise level α_H/n equals to 2.1×10^{-30} m³, 7.2×10^{-29} m³, and 4.5×10^{-29} m³ for the sample G623_L200M5 (LSMO/MgO), G621_L200M5 (LSMO/STO/Si), and CA656-7_L150W50 (LSMO/STO/Si) respectively. In general, α_H/n value for film of STO/Si substrate is higher more than one order of magnitude in comparison with that for LSMO film on STO or MgO substrate. Thus, this parameter depends on the type of substrate.

1.4.3. Evaluation of NEP and D*

Using the values of the measured optical responsivity and noise we can estimate the values of NEP and D* as function of frequency at T_{opt} as given in equations I-4 and I-5 of chapter I as displayed in Figure 3-22. Actually, to compare the performance of different detectors, the values of NEP and D* are given at a fixed frequency (usually 30 Hz). Due to the non-bolometric effect observed in LSMO/STO/Si samples, the presented graph of these samples is still limited to frequency about 1 kHz (cf. Figure 3-22(c) and Figure 3-22(d)).

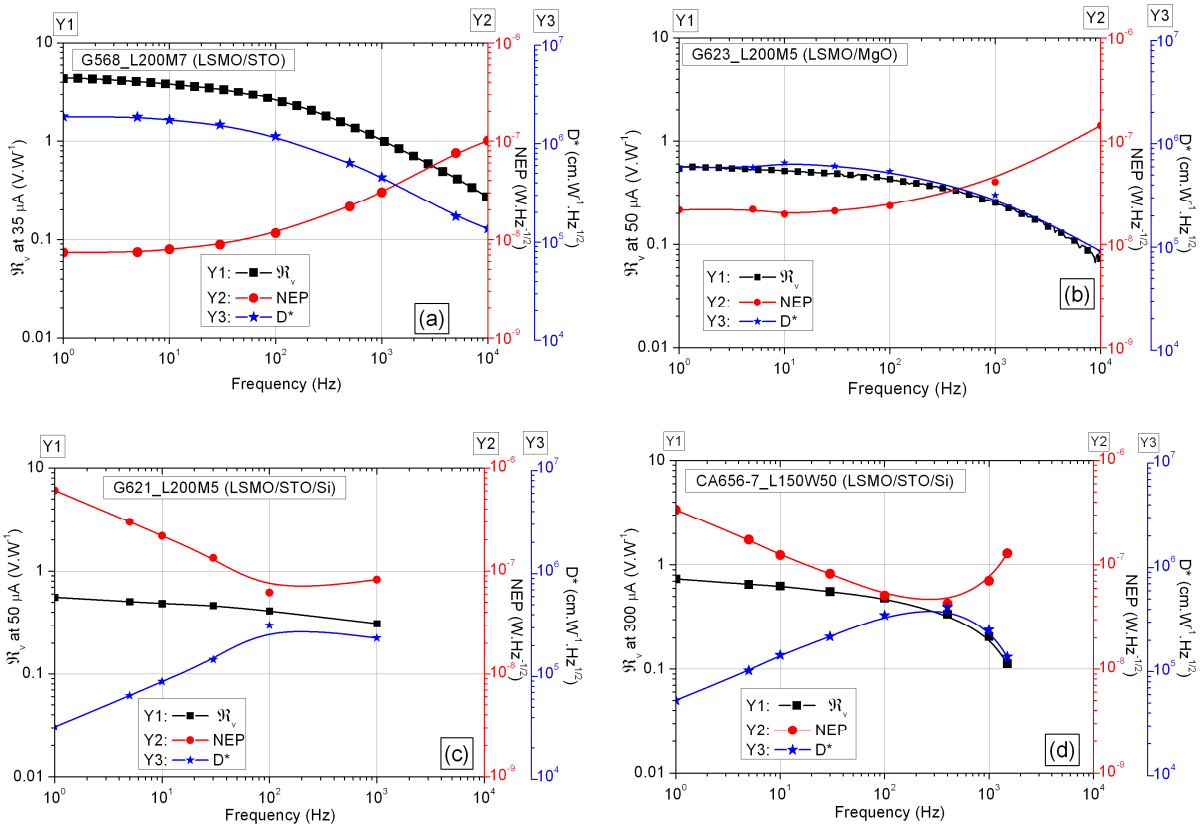

Figure 3-22. The measured $\Re_v$, NEP and D versus the modulation frequency for G568_L200M7 at T_{opt} =332 K and at R_0=50 kΩ (a), G623_L200M5 at T_{opt} =303 K and at R_0=50 kΩ (b), G621_L200M5 at T_{opt} =320 K and at R_0=50 kΩ (c), CA656-7_L150W50 at T_{opt} =318 K and at R_0=10 kΩ (d)*

The higher optical responsivity is achieved by LSMO/STO sample (G568_L200M7) with a value of 4.8 $V \cdot W^{-1}$ at 1 Hz and at 35 µA bias current. The value of response time estimated at -3dB (τ_{-3dB}) equals to 3.6 ms, 0.97 ms, 0.19 ms, 0.18 ms for G568_L200M7, G623_L200M5, G621_L200M5, and CA656-7_L150W50 respectively. The faster response is achieved by LSMO films on STO/Si substrate, this because this substrate has the higher

thermal conductivity (cf. Table 3-4). The minimum measured NEP value is 8.9×10^{-9} W·Hz$^{-1/2}$ and maximum D* value is 1.6×10^{6} cm·W^{-1}·Hz$^{1/2}$ at 30 Hz, achieved by G568_L200M5 (LSMO/STO). Then, STO substrate is the best choice to achieve higher specific detectivity, but STO/Si substrate is the best choice to achieve faster response.

Actually, all samples have been characterized at a bias current I_b lower than the optimal bias current I_{opt} due to the readout electronics limitation. Therefore, these results do not present the best performance. To get the optimum performance of such sample, it should be characterized at the optimal bias current, where we reach the maximum optical responsivity. Therefore, the performance of the samples at I_{opt} will be estimated by extrapolation based on performance measured at I_b, as we will see in section 3 of this chapter.

2. Thermal model of "thin film on substrate" bolometers

We will try in this section to propose a thermal model for the thin-film-on-substrate structure. It helps to understand and characterize the heat diffusion into the substrate. This model is based on heat conduction from film to substrate, with neglecting the radiative and convective leakage knowing that practical sample characterization is done at vacuum condition. Heat conduction

Whenever a temperature gradient exists in a solid medium, heat will flow from the higher temperature to the lower temperature region. The Fourier's Law (1822) of thermal conduction shows that "the rate at which heat is transferred by conduction, q, is proportional to the temperature gradient times the area A through which heat is transferred" [17][19]. In an homogeneous medium, this can be written as,

$$q = -\kappa A \frac{dT(x)}{dx} \qquad \text{(III-4)}$$

where κ is the material thermal conductivity expressed in W·m^{-1}·K^{-1} in the International System of Units (abbreviated as SI). In this relation, T(x) is the local temperature and x is the distance in the direction of heat flow.

The thermal conductivity is a material property that indicates the amount of heat that will flow per unit time across a unit area when the temperature gradient is unity.

For the simple case of steady-state one-dimensional heat flow through a plane wall (see Figure 3-23), with dissimilar temperatures on both sides and no internal heat generation, the heat flow does not vary with time and the cross-sectional area along the heat flow path is uniform. By integration of Equation (III-4) we can find that,

$$\frac{q}{A}\int_0^L dx = -\int_{T1}^{T2} \kappa \, dT \quad \Rightarrow \quad q = \frac{T1-T2}{L/(A\kappa)} \qquad \text{(III- 5)}$$

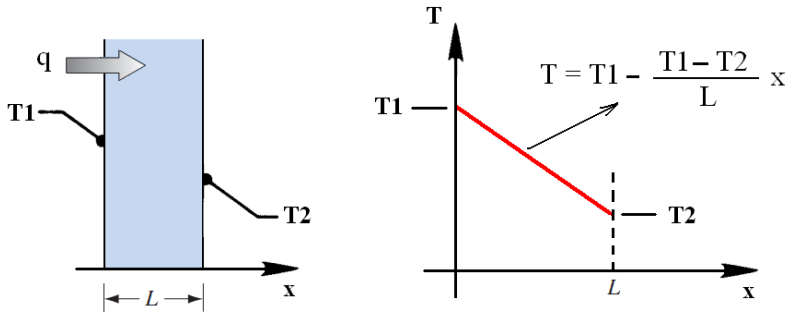

Figure 3-23. Heat conduction through a wall; adapted from [19]

The quantity L/(Aκ) is equivalent to a thermal resistance (expressed in $K \cdot W^{-1}$) that the wall shows to the flow of heat by conduction. This way, we can represent heat flow through a wall by perfect analogy with an electric circuit, which will be explained in paragraph 2.3.

2.2. The heat diffusion equation

A major goal in a thermal conduction analysis is to determine the temperature distribution, which represents how temperature varies with the position in the medium. Once this distribution is known, the conduction heat flow at any point in the medium or on its surface may be computed from Fourier's law.

The general three dimensions heat diffusion equation for incompressible homogeneous materials is [19][20],

$$\kappa \nabla^2 T + q'' = \rho_v c_p \frac{\partial T}{\partial t} \qquad \text{(III- 6)}$$

where t is the time and q″ is the volumetric heat generation (expressed in $W \cdot m^{-3}$).

The term $\nabla^2 T = \nabla . \nabla T$ is called the Laplacian, and is defined in Cartesian coordinates as,

$$\nabla^2 T = \frac{\partial^2 T}{\partial x^2} + \frac{\partial^2 T}{\partial y^2} + \frac{\partial^2 T}{\partial z^2}$$

With no internal heat generation, Equation (III- 6) becomes,

$$\nabla^2 T = \frac{1}{D} \frac{\partial T}{\partial t} \qquad \text{(III- 7)}$$

Where D is the thermal diffusivity of the material, and describes the rate at which heat diffuses through a material. The thermal diffusivity D presents an important property in heat transfer analysis, and has units of $m^2 \cdot s^{-1}$.

$$\boxed{D = \frac{\kappa}{c_p . \rho_v}} \qquad \text{(III- 8)}$$

The product $c_p.\rho_v$ (expressed by $J \cdot K^{-1} \cdot m^{-3}$) is commonly called the volumetric heat capacity [20]. It measures the ability of a material to store thermal energy. Furthermore, as we can see from its definition, D measures the ability of a material to conduct thermal energy relative to its ability to store thermal energy. It increases with increasing thermal conductivity since heat will able to conduct across the material quickly, and it decreases with increasing thermal capacity because heat is preferentially stored as internal energy within the material instead of being conducted through it.

2.3. The overall model of the studied samples

In order to understand the relation between the optical responsivity as function of frequency and the thermal parameters of the bolometer (film and substrate), we need some kind of thermal model that can predict the effect of these different parameters related to the bolometer. With the aim of describing the thermal model, we can make an analogy between thermal and electrical parameters as given in Table 3-2.

Table 3-2 Analogy between thermal and electrical parameters; adapted from [21]

Thermal parameter	*Electrical Analog*
Heat energy (J)	Charge (C)
Heat flow (W)	Current (A)
Temperature (K)	Voltage (V)
Thermal impedance ($K \cdot W^{-1}$)	Electrical impedance ($V \cdot A^{-1}$, Ω)
Thermal conductance ($W \cdot K^{-1}$)	Electrical conductance ($A \cdot V^{-1}$, Ω^{-1})
Heat capacity ($J \cdot K^{-1}$)	Electrical capacitance ($C \cdot V^{-1}$)

According to this electro-thermal analogy, we can establish a one-dimensional thermal model to describe our "thin film on substrate" samples, as seen in Figure 3-24. Indeed, this thermal model is similar to that proposed by Bozbey [21].

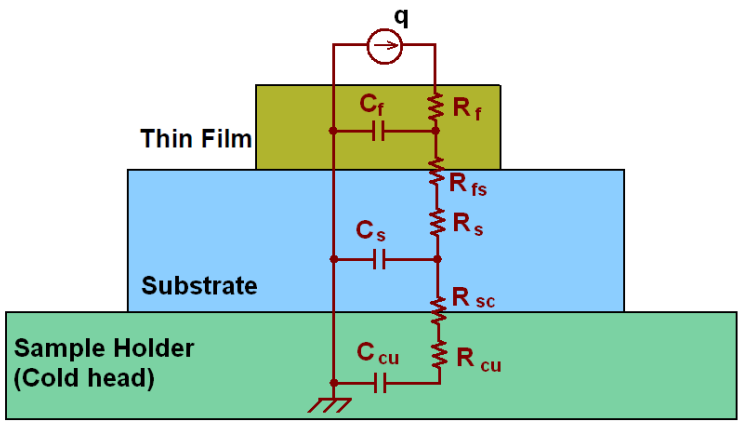

Figure 3-24. Electrical analog of the one dimension thermal model for a bolometer consisting of thin film on substrate glued on a sample holder

In this model we have:

q is the absorbed radiated heat flow at the surface of the sample,

R_f and C_f are the thermal resistance and the heat capacity of the film material

R_s and C_s are the thermal resistance and the heat capacity of the substrate material

R_{cu} and C_{cu} are the thermal resistance and the heat capacity of the sample holder (thermostat)

R_{fs} is the thermal boundary resistance at the film-substrate interface

R_{sc} is the thermal boundary resistance at the substrate- sample holder interface,

This way we can illustrate the electrical equivalent circuit, as seen in Figure 3-25.

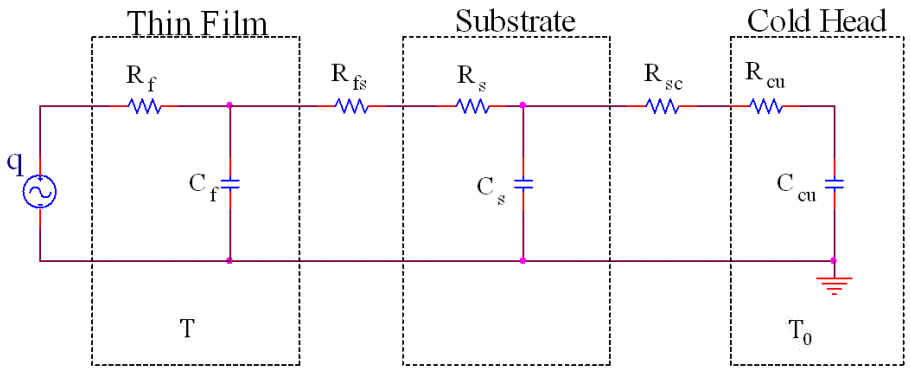

Figure 3-25. Circuit analog of the one dimension thermal model

This thermal model shows that two interfaces have to be considered in this configuration, the film/substrate interface and the substrate/cold-head interface. These interfaces are described by a thermal boundary resistance, which will be described in the next paragraph.

Therefore, the total steady state thermal conductance of this structure in can be given as follows,

$$\frac{1}{G_{tot}} = \frac{1}{G_f} + \frac{R_{fs}}{A_f} + \frac{1}{G_s} + \frac{R_{sc}}{A_f} \qquad \text{(III- 9)}$$

where $G_f = 1/R_f$ is the thermal conductance of the film, and $G_s = 1/R_s$ is the thermal conductance of the substrate.

We have to mention here that the sample holder presents a large volume compared to both film and substrate. Also, due to the thermal properties of copper (see Table 3-4), the sample holder could be considered as isothermal mass at fixed temperature T_0. Then, the response will be mainly influenced by thermal parameter of film (R_f, C_f) and substrate material (R_s, C_s), and by the thermal boundary resistance at the film-substrate interface (R_{fs}).

2.4. Thermal boundary resistance

2.4.1. Conceptual Background

When two different conducting surfaces are placed in contact as shown in Figure 3-26, a thermal resistance is present at the interface of the solids. The interface resistance, frequently called the thermal contact resistance or thermal boundary resistance, develops when two materials will not fit tightly together and a thin layer of fluid is trapped between them. The interface resistance is primarily a function of surface roughness, the pressure holding the two surfaces in contact, the interface fluid, the interface temperature and the materials that are in contact [18]-[20].

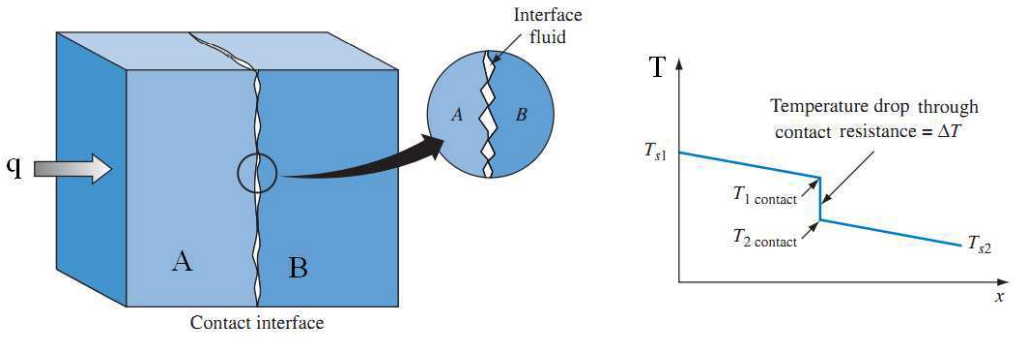

Figure 3-26. Contact schematic diagram and temperature profile between two solids [18]

If the heat flux through two solid surfaces in contact is q/A and the temperature difference across the interface of area A between the two solids is ΔT, then the interface resistance R_{bd} is defined by [22],

$$R_{bd} = \frac{1}{h_c} = \frac{\Delta T}{(q/A)} \qquad \text{(III- 10)}$$

where h_c is the surface interface thermal conductance (expressed in $W \cdot K^{-1} \cdot m^{-2}$). This way, the unit of interface thermal resistance R_{bd} is $m^2 \cdot K \cdot W^1$.

For imperfect thermal contact, a temperature difference occurs at the interface, as shown in Figure 3-26. The interface formed due to the joining of two solids (like film and substrate) is represented in different ways as seen in Figure 3-27. In general, practical situations appear as in Figure 3-27(b, c). To measure the interface thermal resistance R_{bd}, the

contact area at the interface needs to be determined. A larger area provides a greater path for heat transfer and thus reduces the interface resistance [22]. The actual value of R_{bd} depends on the surface quality of the interfaces, as well as the specific details of the deposition [22].

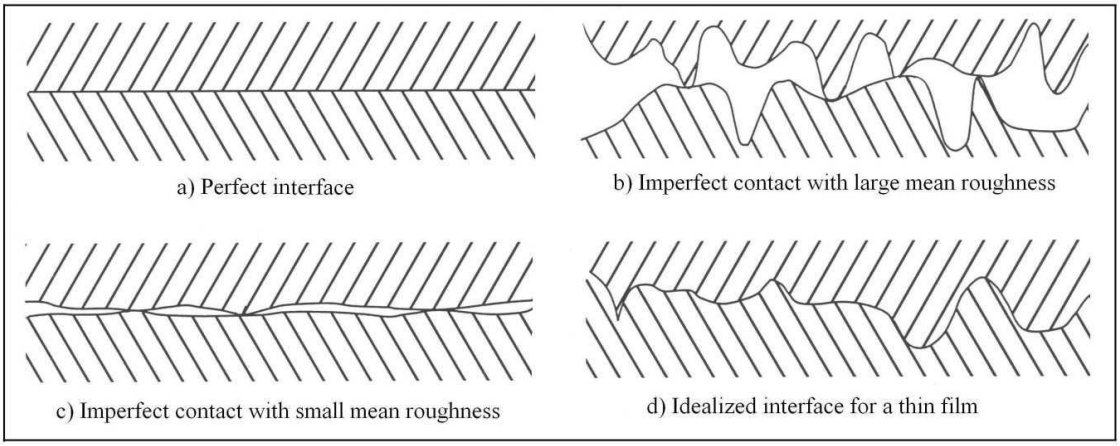

Figure 3-27. Schematic presentation of different types of film/substrate interfaces [23]

2.4.2. Literature data of thermal boundary resistance

The thermal boundary resistance between the thin film and the substrate (denoted as R_{fs}) can strongly affect the thermal design of bolometric thermal detectors. The time constant and the frequency response of LSMO thin film deposited on substrate both depend on R_{fs}. Therefore, this thermal boundary resistance is one of the key parameters for the design of radiation detectors [23].

The film/substrate interface and its corresponding thermal boundary resistance, R_{fs}, has been studied by Nahum *et al.* [22] and Kelkar *et al.* [23] as well as many others. Nahum has performed direct measurements on the thermal boundary resistance between epitaxial films of $YBa_2Cu_3O_{7-\delta}$ (YBCO) deposited on a variety of substrates with and without buffer layers. They showed that the measured R_{fs} does not continue to decrease as T^{-3} (as proposed by the acoustic mismatch model, AMM, which estimate the thermal boundary resistance) and becomes constant for temperature higher than 100K. Also, his measurements indicate that R_{fs} is weakly dependent on temperature, and reach a value of $0.8\text{-}1.4\times10^{-7}$ $m^2\cdot K\cdot W^1$ between 90 and 200 K. Kelkar has studied the thermal boundary resistance between EBCO (Er-Ba-Cu-O) films on MgO and $SrTiO_3$ (STO) substrates. He states that the boundary resistance shows a decreasing trend with increasing heat flux and interfacial temperature drop.

No value for R_{fs} between LSMO and STO, MgO or Si substrates has been reported yet to my knowledge, even by direct measurements or by estimation. In contrast, many values of R_{fs} at room temperature have been reported for YBCO on MgO substrates [23][24][25][26], YBCO on STO substrate [26][27]. For manganese oxides, some values have been reported, like for LPSMO ($La_{0.7}(Pb_{0.7}Sr_{0.3})_{0.3}MnO_3$) on STO and LAO ($LaAlO_3$) substrates [28], and LCMO ($La_{0.65}Ca_{0.35}MnO_3$) on STO substrate [30]. A summary is given in Table 3-3.

Table 3-3 Thermal boundary resistance from literature at 300 K

Ref.	**Film/interlayer**	**Substrate**	**R_{fs} ($m^2 \cdot K \cdot W^1$)**	**Measurement method**	**R_{sc} ($m^2 \cdot K \cdot W^1$)**
[22][24]	Epitaxial $YBa_2Cu_3O_{7-\delta}$	MgO	2.5×10^{-7}	Optical-transient grating	N/A
[25]	Epitaxial $YBa_2Cu_3O_{7-\delta}$	MgO	0.5×10^{-7}	Optical-transient grating	N/A
[26]	Epitaxial $YBa_2Cu_3O_{7-\delta}$	MgO	1×10^{-7}	Optical-transient grating	N/A
[26]	Epitaxial $YBa_2Cu_3O_{7-\delta}$	$SrTiO_3$	$\leq 1 \times 10^{-7}$	Optical-transient grating	N/A
[27]	Epitaxial $YBa_2Cu_3O_{7-\delta}$	$SrTiO_3$	0.5×10^{-7}	thermoelectric effect	N/A
[28]	$La_{0.7}(Pb_{0.7}Sr_{0.3})_{0.3}MnO_3$	$SrTiO_3$	1×10^{-7}	Pulsed microwave	2×10^{-3}
[28]	$La_{0.7}(Pb_{0.7}Sr_{0.3})_{0.3}MnO_3$	$LaAlO_3$	1×10^{-5}	Pulsed microwave	N/A
[29]	$(Fe_{0.5}Co_{0.5})_{0.4}Cu_{0.6}$ / 50nm SiO_2	Si	2.5×10^{-5}	Pulsed microwave	1.43×10^{-3}
[30]	$La_{0.65}Ca_{0.35}MnO_3$ / 400nm $YBa_2Cu_3O_7$	$SrTiO_3$	$\leq 10^{-6}$	Pulsed microwave	8.3×10^{-3}
[31]	Semiconductor $YBa_2Cu_3O_{6+\delta}$	MgO	2×10^{-7}	N/A	7.7×10^{-4}

According to these literature data, the minimal R_{fs} values are in the order of magnitude of 10^{-7} $m^2 \cdot K \cdot W^1$. This value corresponds to perfect epitaxial film in the YBCO/MgO and YBCO/$SrTiO_3$ structures with the minimal lattice mismatch between film and substrate [29][30]. The maximal values of 10^{-3}–10^{-2} $m^2 \cdot K \cdot W^1$ were estimated by Kelkar *et al.* [23] for EBCO/MgO and EBCO/$SrTiO_3$ structures at 19 K. The thermal boundary resistance shows a wide range of variation, of about five orders of magnitude, in various kinds of materials.

The large value of R_{fs} in FeCoCu/SiO_2/Si arrangement could be related to the possible effect of a grain structure on the thermal boundary resistance of the film–substrate interface

[29]. It should be noted that this increase in R_{fs} cannot be related to the presence of the oxide interlayer (SiO_2) with a regular structure. This interpretation has also been reported too in [30] where they have almost the same value for R_{fs} for LCMO film on STO substrate with and without the non-conducting $YBa_2Cu_3O_7$ interlayer.

To analyze the optical response of LSMO thin film on substrate bolometer, we will need to estimate the value of thermal boundary resistance, as we will see later in this chapter.

2.5. Thermal properties of materials

To perform a thermal modeling and analysis of a thin-film-on-substrate bolometer, the thermophysical properties of the film and substrate materials need to be known. Table 3-4 presents the thermal properties of the different materials that were used in our samples. In this table we explore the reported value of: the thermal conductivity κ, the specific heat capacity c_p, the density ρ_v and the thermal diffusivity D, for the LSMO film and the substrate materials (STO, MgO, Si), as well as Gold and Copper.

Table 3-4 Thermal properties of used materials at 300 K

	κ ($W \cdot m^{-1} \cdot K^{-1}$)	**c_p ($J \cdot kg^{-1} \cdot K^{-1}$)**	**ρ_v ($kg \cdot m^{-3}$)**	**D ($10^{-6}\ m^2 \cdot s^{-1}$)**
STO	11.2 [32], 10.3 [34] 10.9 [35], 11.1 [36], 11.0 [37]	544 [33] 537 [38][39]	5170 [39] 5118 [54]	4.01 [39] 3.92 (calculated)
MgO	51 [43]	923 [40], 929 [44] 927 [46], 898 [47]	3600 [41]	15.87 [45] 15.41 (calculated)
Si	156 [48]	703 [40]	2330 [32]	86 [49] 95 (calculated)
Cu	398 [42]	381 [40]	8960 [41]	117 (calculated)
Au	315 [42]	129 [40]	1930 [41]	1265 (calculated)
LSMO	2.46 [50], 2.47 [51]	568 [50][52]	6600 [53]	0.66 (calculated)

Many remarks of the values presented in this table need to be commented. The thermal conductivity of STO substrate material is five times smaller than that of MgO, but they have close volumetric thermal capacity, $c_p \times \rho_v$. Also, Si shows the highest thermal conductivity

(about 3 times higher than that for MgO) and the lowest volumetric thermal capacity (about half that for MgO). The calculated value for D mentioned in this table has been obtained using the mean value of the reported κ, c_p, ρ_v values.

Knowing the above properties of these substrate materials, one can choose one of these substrates (or other) to achieve optimum design of thermal detector figures of merit depending on the application purpose (sensitive or fast detector). To predict the heat flow into the substrate material as a function of the modulation frequency, we can use a simple one-dimensional model. This model is based on what is called "the thermal diffusion length" L_P, defined by the following equation,

$$L_P = \sqrt{\frac{D}{\pi f}} \qquad \text{(III- 11)}$$

Indeed, L_P indicates the characteristics penetration depth of the temperature variation into the substrate, and it depends of the modulation frequency f. Figure 3-28 illustrates the variation of L_p as a function of the frequency for different substrate materials and for LSMO film. The f_L presents the knee frequency defined later in equation (III- 14).

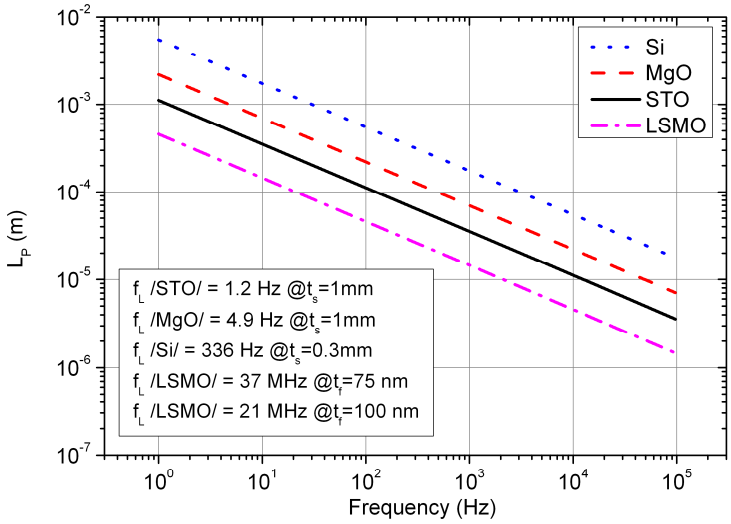

Figure 3-28. Thermal diffusion length, L_p, for LSMO film and substrate materials as a function of modulation frequency at 300 K

We can notice that the thermal diffusion length (L_p) for LSMO film is bigger than the film thickness (t_f), which equals 75 nm and 100 nm, within the studied frequencies range.

This means that the AC heat flow passes completely through the film and reaches the substrate. Therefore, the film can be considered as an isothermal layer. For frequencies higher than f_L (given in the graph legend, and defined later in equation (III- 14)), L_p is less than substrate thickness (t_s), therefore, the AC heat flow into the substrate will not reach the substrate/Holder interface. Hence, the influence of the thermal boundary resistance at the substrate-sample holder interface, R_{sc}, will be ignored.

Considering the thermal diffusion length, L_p, as the effective length for heat flow into the substrate, the corresponding thermal conductance of the substrate, G_s, can be found from [55][56] as one approximation:

$$G_s = \chi \kappa_s (A_f/L_p) \qquad \text{(III- 12)}$$

where, κ_s is the thermal conductivity of the substrate material, A_f is the film surface, and χ is a correction factor for the above approximation of the length of the heat flow. Substituting the expression of L_P from equation (III- 11) in equation (III- 12), we have:

$$G_s = \chi A_f \sqrt{c_s \kappa_s \pi f} \qquad \text{(III- 13)}$$

where, $c_s = c_p \rho_v$ is the volumetric thermal capacity of the substrate material. Thus G_s will be a function of frequency and scales as $f^{0.5}$, therefore increases with the frequency.

In addition, one can find the modulation frequency at which the substrate thickness, t_s, is equal to the thermal diffusion length, L_p. This frequency is so-called the knee frequency, f_L, which is dependent on the substrate material and its thickness. It is given by [55]:

$$f_L = \sqrt{\frac{D}{\pi t_s^2}} \qquad \text{(III- 14)}$$

For frequencies less than f_L (where $L_p > t_s$) G_s remains constant and independent of frequency, and so does the optical response. For frequencies higher than f_L the thermal conductance G_s will depend on frequency. A detailed analysis of the heat diffusion from film into substrate will be presented in the next paragraph.

2.6. Heat diffusion into the substrate

In order to understand the optical response of LSMO thin films on substrate we need to use a model that analyses how the heat diffuses into the substrate, taking into account the film-substrate interface. We will model the contact between the film and the substrate as an hemisphere of radius a, as shown in Figure 3-29. So, the heat flux is radial into the substrate. The area $A_f = 2\pi a^2$ is set equal to the surface of the film, as also proposed in [57][58].

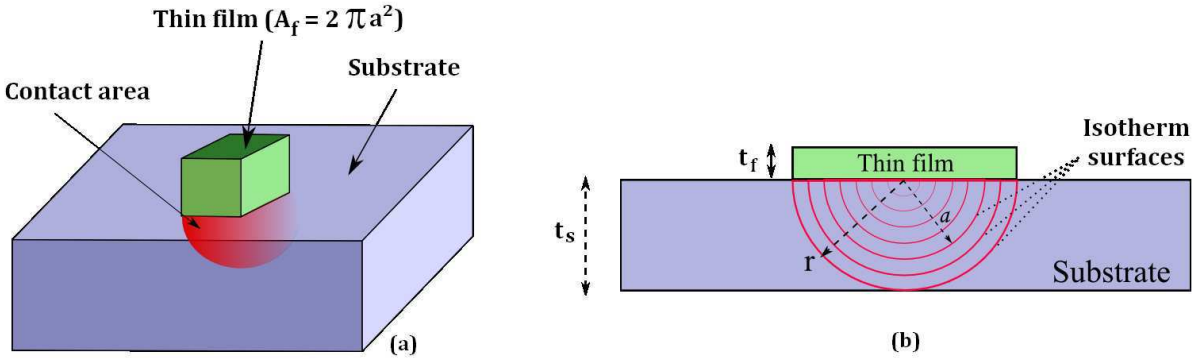

Figure 3-29. Schematic diagram of the film-substrate contact model in 3D (a) and a cross section (b)

In spherical coordinates (r,θ,φ) as seen in Figure 3-30, the temperature gradient writes as:

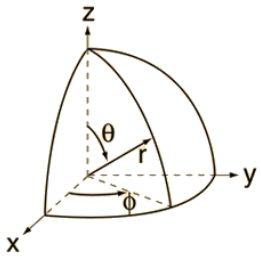

Figure 3-30. The spherical coordinate system (r,θ,ϕ)

$$\nabla^2 T = \frac{1}{r^2}\frac{\partial}{\partial r}\left(r^2\frac{\partial T}{\partial r}\right) + \frac{1}{r^2 \mathrm{Sin}\theta}\frac{\partial}{\partial r}\left(\mathrm{Sin}\theta\frac{\partial T}{\partial \theta}\right) + \frac{1}{r^2 \mathrm{Sin}\theta}\left(\frac{\partial^2 T}{\partial \phi^2}\right) \qquad \text{(III- 15)}$$

In this model the heat flow is radial, so the temperature depends only on the hemisphere radius (r) and is independent of ϕ and θ. This way, the three dimensional heat diffusion equation (III- 7) becomes,

$$\frac{\partial^2 T}{\partial r^2} + \frac{2}{r}\frac{\partial T}{\partial r} = \frac{c_p \rho_v}{\kappa}\frac{\partial T}{\partial t} \qquad \text{(III- 16)}$$

So, in the frequency domain:

$$\frac{\partial^2 T}{\partial r^2} + \frac{2}{r}\frac{\partial T}{\partial r} = \frac{c_p \rho_v}{\kappa}(2\pi j f)T \qquad \text{(III- 17)}$$

The last relation is a 2nd order differential equation with variable coefficients. The solution of this equation which gives the temperature distribution in the substrate is [58]:

$$T(r) = T_0 + \Delta T \,.\left(\frac{a}{r}\right).\exp\left[\frac{a-r}{L_p}\right].\exp\left[j(2\pi ft - \frac{r}{L_p})\right] \qquad \text{(III- 18)}$$

The thermal conductance of the substrate G_s can be written as [57][58],

$$G_s(f) = \kappa_s(\Delta T)^{-1}\left|\int_s \nabla T.\, ds\right| \qquad \text{(III- 19)}$$

Where κ_s is the thermal conductivity of the substrate, T is the position-dependent temperature in the substrate, ΔT is the temperature difference between film and substrate, and the integral is over the area of contact between film and substrate.

From equations (III- 18) and (III- 19) we have [57],

$$G_s(f) = A_f.\kappa_s.a^{-1}\sqrt{\left(1+\frac{a}{L_p}\right)^2 + \left(\frac{a}{L_p}\right)^2} \qquad \text{(III- 20)}$$

From equation (III- 20) and equation (III- 11), and substituting the value of $A_f = L^2 = 2\pi a^2$, we can find the relation between G_s and both the frequency f and the film area L^2 as follows,

$$G_s(f) = L.\kappa_s.\sqrt{2\pi}\sqrt{\left(1+\sqrt{\left(\frac{L^2 f}{2D}\right)}\right)^2 + \left(\frac{L^2 f}{2D}\right)} \qquad \text{(III- 21)}$$

From equation (III- 20) we can distinguish two behaviors, depending on the modulation frequency compared to the critical frequency $f_{cr} = 2D/ L^2$,

- At low frequency, so called **static regime**:

$$f << f_{cr} \text{ (or } L_p >> a) \Rightarrow G_s(0) = \kappa_s(L^2/a) = L.\kappa_s.\sqrt{2\pi} \qquad \text{(III- 22)}$$

which is equal to the thermal conductance of a volume with square area $A_f = L^2$ and thickness "a". In this range of frequencies, G_s is constant and independent of frequency.

- At high frequency, so called **dynamic regime**:

$$f >> f_{cr} \text{ (or } L_p << a) \Rightarrow G_s(f) = \kappa_s\sqrt{2}(L^2/L_P) = L^2\sqrt{2\pi f \kappa_s c_s} \qquad \text{(III- 23)}$$

which is equal to the thermal conductance of a volume with square area $A_f = L^2$ and thickness L_P. Hence, G_s depends on frequency and scales as $f^{0.5}$. Thus, we can calculate the critical frequency $f_{cr} = 2D/L^2$ at which L_p=a in Table 3-5 for our samples on STO, MgO and Si substrate by using the calculated values of D listed in Table 3-3.

Table 3-5 The calculated values of f_{cr} using calculated values of D from Table 3-4 for the different substrates materials and sample surfaces A_f at 300 K

$A_f = 2\pi a^2$ (μm^2)	a (μm)	STO	MgO	Si
50×50	20	3.1 kHz	12.3 kHz	76.2 kHz
100×100	40	784 Hz	3.1 kHz	19.1 kHz
200×200	80	196 Hz	770 Hz	4.8 kHz

The frequency f_{cr} is inversely dependent of sample surface (A_f), so the plateau region of the optical response will be reduced when using bigger sample size. Therefore, using smaller sample surface results in optical response closer to the basic first order model (cf. paragraph 3.4 of chapter I). Using the Equation (III- 20) we can plot the substrate thermal conductance (G_s) for STO substrate for different sample surfaces, as seen in Figure 3-31. It's obvious that the plateau region is bigger for lower sample surface, thus lower response time. In addition, G_s is proportional to L in the static regime, but it is proportional to L^2 in the dynamic regime.

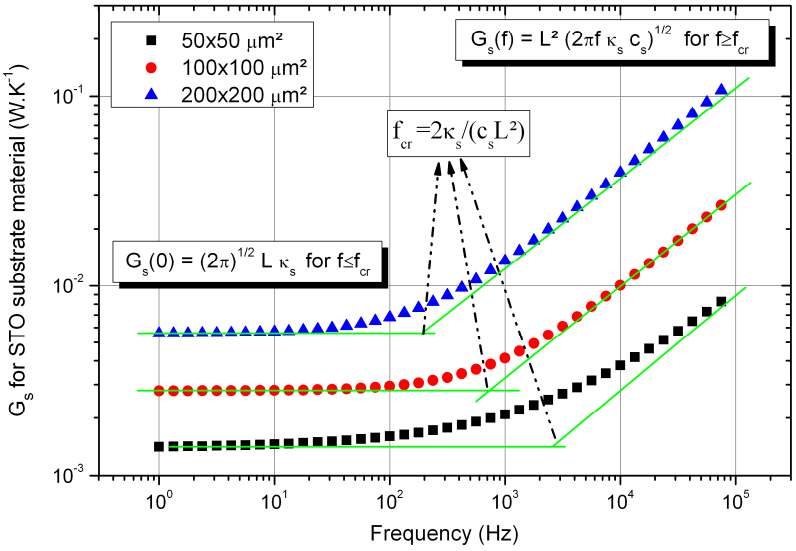

Figure 3-31. Modeled thermal conductance of STO substrate versus frequency at 300 K for different sample surfaces

According to thermal conductance of the substrate estimated from this model using the equation (III- 20), we can predict three zones for the optical responsivity dependence of frequency, as shown in Figure 3-32.

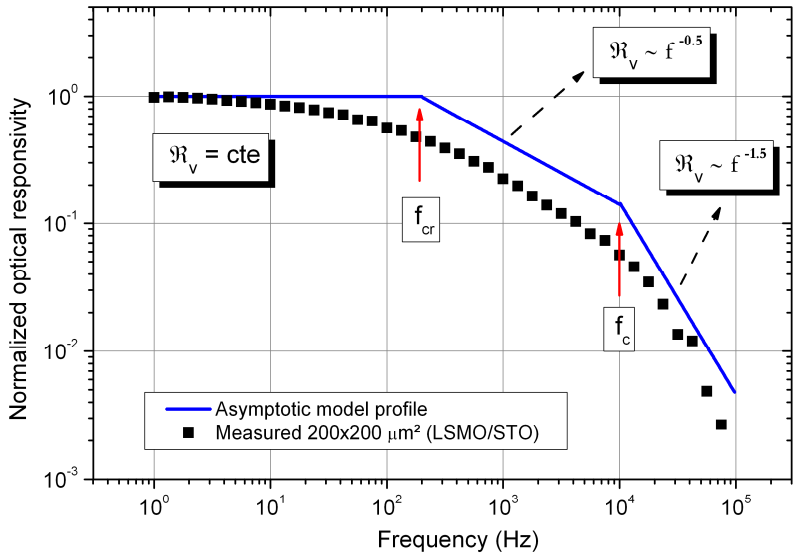

Figure 3-32. Asymptotic profile according to model and measured optical responsivity of G568_L200M7 sample at T_{opt} =330 K. The f_c value was chosen in arbitrary way

For frequency lower that f_{cr} the thermal conductance $G_s(f)$ is constant, and the optical responsivity is constant too. For frequency higher than the cut-off frequency f_c, the responsivity scales as $f^{-1.5}$. Finally, in the range of frequencies between f_{cr} and f_c we have an intermediate zone between the latter two zones, where the optical responsivity changes its scale with frequency from $f^{-0.5}$ to $f^{-1.5}$ according to the relative values of f_{cr} and f_c. Indeed, the value of f_c in the figure was chosen in arbitrary way for the sake of simplicity. The figure shows also the normalized measured optical responsivity for LSMO/MgO sample of dimension 200×200 µm² where it follows the indicated model.

On the other hand, we need to find out the relation of the thermal capacity of the substrate C_s, therefore its heated volume. Based on the concept of the proposed model, the heated volume of the substrate is $A_f \times a$ for frequencies less than f_{cr}, so that the thermal capacity of substrate will be constant because the heated volume is constant too. In contrast, we will consider the volume $A_f \times L_p$ for frequencies more than f_{cr}. This represents a rectangular volume of depth L_p, so the thermal capacity of substrate decreases as function of frequency since L_p decreases with f. Then, depending on the modulation frequency compared to the critical frequency f_{cr}, the analytical expression of C_s can be given by,

- At static regime, $f \leq f_{cr}$:

$$C_s(f) = L^3 c_s / \sqrt{2\pi} \qquad \text{(III- 24)}$$

In this range of frequencies, C_s is constant and independent of frequency.

- At dynamic regime, $f > f_{cr}$:

$$C_s(f) = L^2 \sqrt{\kappa_s c_s / (\pi f)} \qquad \text{(III- 25)}$$

Hence, C_s depends on frequency and scales as $f^{-0.5}$. Figure 3-33 shows the thermal capacitance of 100×100 µm² pixel size for STO, MgO, and Si substrates at 300 K.

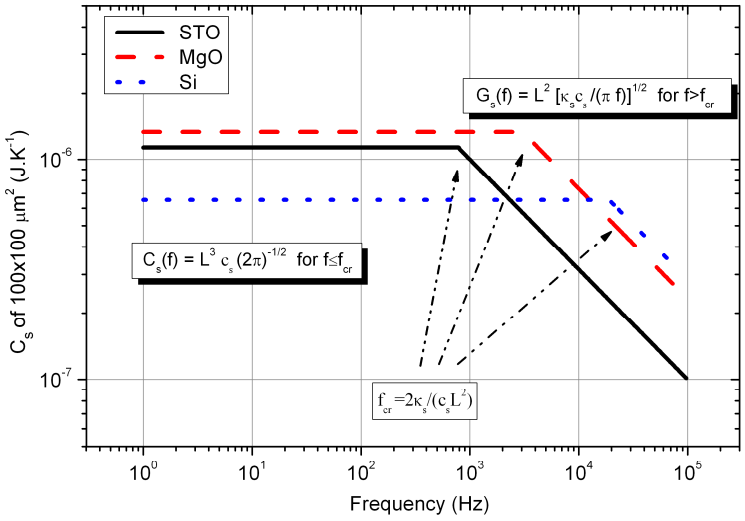

Figure 3-33. Model thermal capacitance of 100×100 µm² pixel surface for three substrate materials versus frequency at 300 K

2.7. Model analysis and experimental validation

As I did mention, the sample holder can be considered as an isothermal mass at a fixed temperature T_0. Then, the frequency response of the responsivity will be mainly influenced by the thermal parameter of the film (R_f, C_f) and of the substrate material (R_s, C_s), and by the thermal boundary resistance at the film-substrate interface (R_{fs}). From 1 Hz to 100 kHz, we have noticed in Figure 3-24 that the thermal diffusion length (L_p) for LSMO film is bigger than film thickness, therefore the film can be considered as an isothermal layer. Finally, we can rebuild the simplified equivalent circuit as:

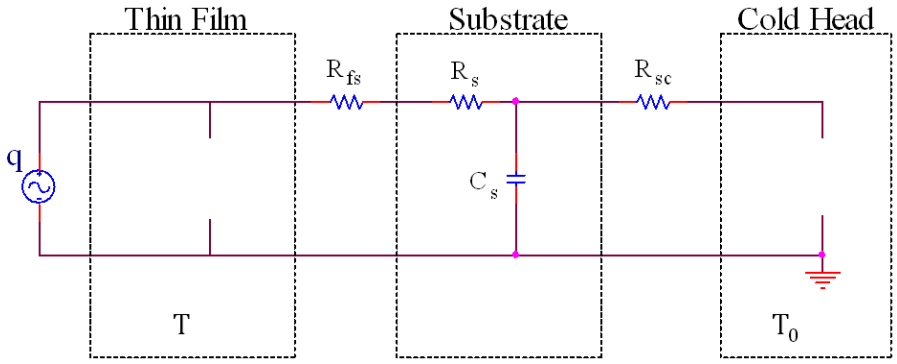

Figure 3-34. Equivalent electrical circuit of the one dimension thermal model in case of the thin film is an isothermal layer

2.7.1. Static regime ($f<<f_{cr}$)

From the equivalent electrical circuit model (see Figure 3-34), the total thermal conductance in the static regime is given by,

$$\frac{1}{G_{tot}} = \frac{R_{fs}}{A_f} + \frac{1}{G_s} \qquad \text{(III- 26)}$$

where G_s is the thermal conductance of the substrate. Here we supposed that the lateral heat flow is negligible in comparison with perpendicular one since the thermal conductivity of copper is higher than that of the three types of substrates (cf. Table 3-4).

Using the relation of $G_s(0) = (2\pi a)\kappa_s$ estimated by the spherical model for $f<<f_{cr}$, we can calculate the thermal conductance of substrate in the static regime.

Table 3-6 Calculated thermal conductance of the substrate materials (G_s) at 300 K

$A_f = 2\pi a^2$ (μm^2)	a (μm)	$G_s = 2\pi a\,\kappa_s$ (10^{-3} W·K^{-1})		
		STO	MgO	Si
50 × 50	20	1.4	6.4	19.6
100 × 100	40	2.8	12.8	39.1
200 × 200	80	5.6	25.6	78.2

Note that the value of the hemisphere radius "a" is less than the substrate thickness (300 µm or 1000 µm). Therefore, the heat flow does not exceed the substrate, and thus the roll of R_{sc} will be negligible and has no effect on the total equivalent thermal conductance. We therefore have,

$$\frac{R_{fs}}{A_f} = \frac{G_s - G_{tot}}{G_s \,.\, G_{tot}} \qquad \text{(III- 27)}$$

The values of G_{tot} are the total thermal conductance measured using electrical V-I and R-T measurements (cf. paragraph 1.2). They are summarized in Table 3-7. The effective surface is the ratio of the meander form surface to the square surface equipped by this meander. Indeed, G_{tot} was measured at temperature 330 K and not at T_{opt} since it does not change with temperature in this range (cf. paragraph 4.3 of chapter I). The uncertainty values present the standard deviation of the linear fitting used to estimate G_{tot} (cf. Paragraph 1.2.3).

Table 3-7 The measured G_{tot} for all square samples on different substrates at 330 K

	G_{tot} (10^{-3} W·K^{-1})				
Geometry	Effective surface (10^3 µm^2)	G568 (STO)	G623 (MgO)	G621 (STO/Si)	CA660-8 (STO/Si)
L×L = 50×50 , Meander form					
L50M5	2.1	---	4.9 ± 0.2	10.4 ± 0.6	9.8 ± 0.6
L50M7	1.8	0.7 ± 0.2	4.5 ± 0.2	11.7 ± 1.0	---
L×L = 100×100 , Meander form					
L100M3	9.7	---	---	22.5 ± 1.3	17.9 ± 2.0
L100M5	9.3	1.9 ± 0.2	10.3 ± 1.2	21.5 ± 1.5	17.4 ± 1.2
L100M7	9.0	1.9 ± 0.2	---	---	---
L×L = 200×200 , Meander form					
L200M5	38.3	---	20.3 ± 1.8	42.4 ± 2.8	33.4 ± 2.1
L200M7	38.1	3.5 ± 0.4	18.3 ± 1.6	43.9 ± 2.9	39.1 ± 2.5
L×L = 100×100 , Square form					
L100CR	10	1.5± 0.2	9.8 ± 0.2	20.3 ± 1.0	18.1 ± 1.2

Therefore, using G_s from Table 3-6 and G_{tot} from Table 3-7 we can estimate the thermal interface film-substrate resistance R_{fs} between the film and the substrate for square samples, as we can see in Table 3-8.

Table 3-8 Estimation of the interface film-substrate thermal resistance (R_{fs}) of square samples at 330 K

	R_{fs} (m^2·K·W^{-1})				
Geometry	Effective surface (10^3 µm^2)	G568 (STO)	G623 (MgO)	G621 (STO/Si)	CA660-8 (STO/Si)
L×L = 50×50 , Meander form					
L50M5	2.1	---	1.2×10^{-7}	1.1×10^{-7}	1.3×10^{-7}
L50M7	1.8	20.5×10^{-7}	1.6×10^{-7}	0.9×10^{-7}	---
L×L = 100×100 , Meander form					
L100M3	9.7	---	---	1.9×10^{-7}	3.0×10^{-7}
L100M5	9.3	18.1×10^{-7}	1.9×10^{-7}	2.1×10^{-7}	3.2×10^{-7}
L100M7	9.0	18.7×10^{-7}	---	---	---
L×L = 200×200 , Meander form					
L200M5	38.3	---	4.1×10^{-7}	5.4×10^{-7}	6.9×10^{-7}
L200M7	38.1	42.4×10^{-7}	6.2×10^{-7}	3.7×10^{-7}	5.1×10^{-7}
L×L = 100×100 , Square form					
L100CR	10	31.6×10^{-7}	2.6×10^{-7}	2.4×10^{-7}	3.0×10^{-7}
AVERAGE		***(26.3±10.6)×10^{-7}***	***(2.9±1.9)×10^{-7}***	***(2.5±1.6)×10^{-7}***	***(3.7±2.0)×10^{-7}***

In the case of LSMO/STO/Si samples, we have a 20-nm-thick buffer layer of a STO material. The thermal barrier height (20nm/κ_s) would be rather small 1.8×10^{-9} $m^2\cdot K\cdot W^1$, so it's of the evidence that the presence of this buffer layer will not affect the value of R_{fs} between LSMO film and Si substrate. The negligible role of buffer layer on R_{fs} has been reported also in [29][30], so the buffer layers have only a modest effect on R_{fs} [29]. We have two different values for STO/Si substrate (G621 and CA660-8 samples), this can be related to the different fabrication technical method and conditions (cf. Appendix A).

The minimal R_{fs} values are in the order of magnitude of 10^{-7} $K\cdot m^2\cdot W^1$ estimated for LSMO/MgO (and LSMO/STO/Si) structure with the 8% (and -0.8%) lattice mismatch (cf. Appendix A) between the film and the substrate or the buffer layer. The maximal values of R_{fs} is in the order of 10^{-6} $K\cdot m^2\cdot W^1$ estimated for LSMO/STO structures with the 0.8% lattice mismatch. As a result, the role of lattice mismatch on the interface thermal resistance is not evident. This conclusion is also noticeable regarding literature results in Table 3-3 for YBCO film. Indeed, the actual value of R_{fs} depends on the surface quality of the interfaces, as well as on the specific details of the deposition [29].

2.7.2. Dynamic regime ($f>>f_{cr}$)

The transfer function of the electrical circuit equivalent model (as seen in Figure 3-34) writes as:

$$\frac{T-T_0}{q} = \frac{1}{G_{tot}(f)+j\omega C_s(f)} \qquad \text{(III- 28)}$$

This way we can write the modulus of the response function as follows,

$$\left|\frac{T-T_0}{q}\right| = \frac{1}{G_{tot}(f)\sqrt{1+\omega^2[C_s(f)/G_{tot}(f)]^2}} \qquad \text{(III- 29)}$$

To calculate the response modulus as a function of the frequency, we estimate $G_{tot}(f)$ using the value of $G_s(f)$ from Equation (III- 20) and the average value of R_{fs} from Table 3-8. Therefore, we can validate this model by comparing the calculated and measured frequency responses of all samples. The overall expression of $G_{tot}(f)$ can be presented, using equation (III- 20) and (III- 27) as:

$$G_{tot}(f) = \frac{L^2.\kappa_s\sqrt{2\pi}\sqrt{(1+\frac{L\sqrt{f}}{\sqrt{2D}})^2+(\frac{L\sqrt{f}}{\sqrt{2D}})^2}}{L+\kappa_s.R_{fs}\sqrt{2\pi}\sqrt{(1+\frac{L\sqrt{f}}{\sqrt{2D}})^2+(\frac{L\sqrt{f}}{\sqrt{2D}})^2}} \quad \text{(III- 30)}$$

To calculate the value of the thermal capacity of the substrate, we used the relations given in equation (III- 24) and equation (III- 25).

The Figure 3-35 shows the normalized (at 1 Hz) measured and calculated optical responsivity of all sample sizes and substrates materials.

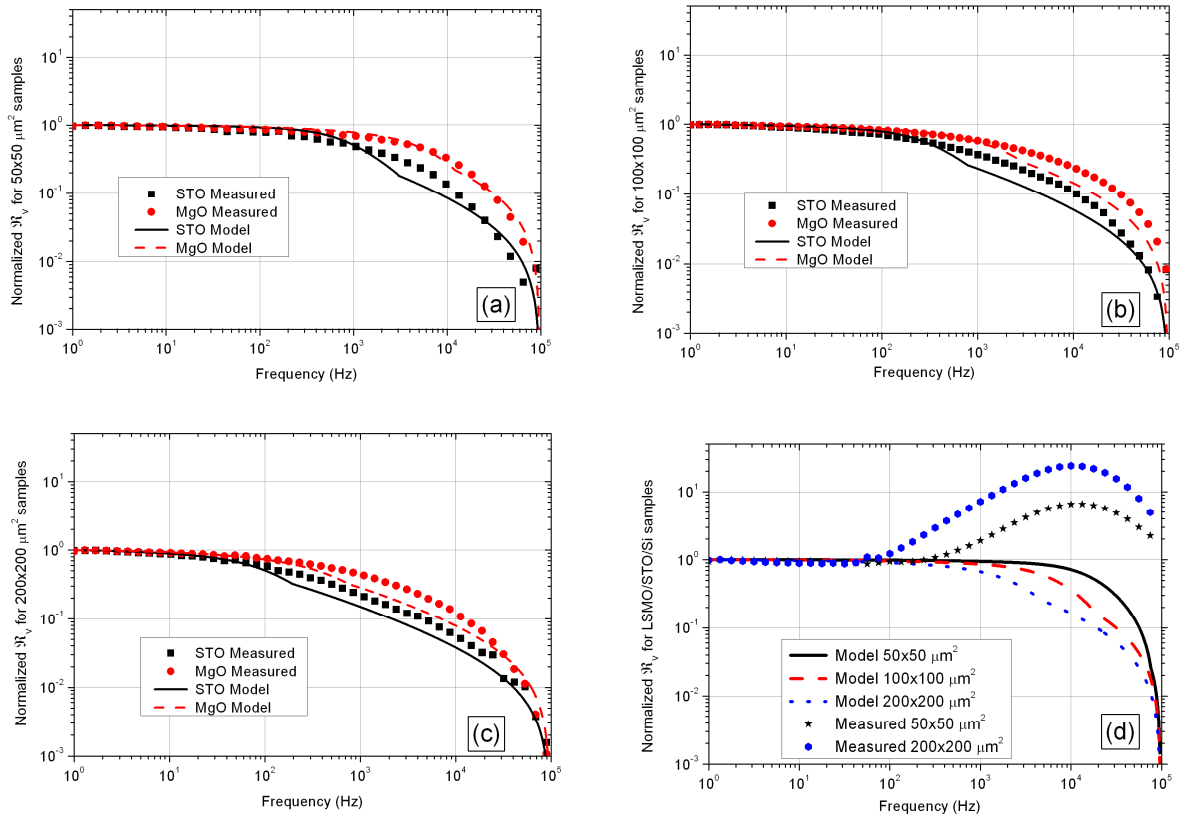

Figure 3-35. Measured and calculated normalized (at 1 Hz) optical responsivity at T_{opt} of LSMO film on STO (G568) and MgO (G623) substrates materials for (a)50×50 µm² sample size, (b)100×100 µm² sample size, (c)200×200 µm² sample size, (d) and LSMO/STO/Si (G621) samples

This figure shows that measurements achieve a good consistence with calculation issued from the proposed thermal model for STO and MgO substrate materials.

Measurements and calculation both display the same tendency for the three pixel sizes. To accurately evaluate the difference between model and measurement, we calculate this difference for all frequencies (1 Hz to 100 kHz). This difference is limited to a maximum value of about 15% (or 10%) for LSMO/STO (or LSMO/MgO) 50×50 µm² samples, of about 8% (or 4%) for LSMO/STO (or LSMO/MgO) 100×100 µm² samples, and of about 2% for 200×200 µm² samples for both types. The origin of this difference is mainly related to the analytical model. The noticed discontinuity in the model graph issued from the discontinuity of substrate thermal conductance value (C_s) between static and dynamic regimes (which occurs at f_{cr}). Finally, the analytical model can be used with an error less than 15% for all kinds of samples to predict the optical responsivity versus modulation frequency.

Indeed, we couldn't achieve this comparison for Si substrate because of the non-bolometric component obtained in the optical responsivity measurements of these samples at high frequency, as seen in Figure 3-35(d).

2.7.3. Conclusion

We obtain finally a validate model for film-on-substrate structure, which estimates the total thermal conductance of this structure, and consequently the optical responsivity. The small corner shown in the modeled frequency response, which occurred near the frequency f_{cr}, is a result of the combination between the studied zones. This is principally coming up from the estimation of the heated volume, then the thermal capacity of substrate, before and after f_{cr}. We can notice that this model is better for MgO substrate, but it's also valid for STO substrate. In total, the measured responsivity as a function of modulation frequency is well described as expected for the three zones (constant, $\sim f^{-0.5}$, $\sim f^{-1.5}$) as we can see in Figure 3-35.

As conclusion, we can use the present model of the total thermal conductance to analyze and optimize the bolometric performance of the film-on-substrate structure, as we will see in section 3 of this chapter.

2.8. Static thermal conductance & substrate material

To achieve higher responsivity of bolometer, a lower thermal conductance, G_{tot}, that links the film with its environment has to be achieved. In general, the major parameter that can influence G_{tot} is the thermal conductivity (κ_s) of the substrate material and the thermal

boundary resistance (R_{fs}) of the film-substrate interface. We will try in this paragraph to estimate G_{tot} using the model proposed in section 2 as a function of pixel surface (A_f=L×L).

Going back to equation (III- 30), we can extract the static model of the total thermal conductance as a function of sample size L.

$$G_{tot}(0) = \frac{L^2}{R_{fs} + (\kappa_s \sqrt{2\pi})^{-1} L} \qquad \text{(III- 31)}$$

From this equation we can estimate the total thermal conductance using the average value of R_{fs} (cf. Table 3-8). Figure 3-36 shows a comparison between measured and calculated $G_{tot}(0)$ using equation (III- 31) for different substrates. It confirms a good consistence between measurements and calculation, especially for small pixel sizes. The higher difference noticed at L=200 µm, especially for STO/Si substrate, maybe raised from the relatively higher uncertainty measurements of G_{tot} for this pixel size. Also, it could also be related to neglecting the effect of STO buffer layer when estimating the interface thermal resistance (R_{fs}).

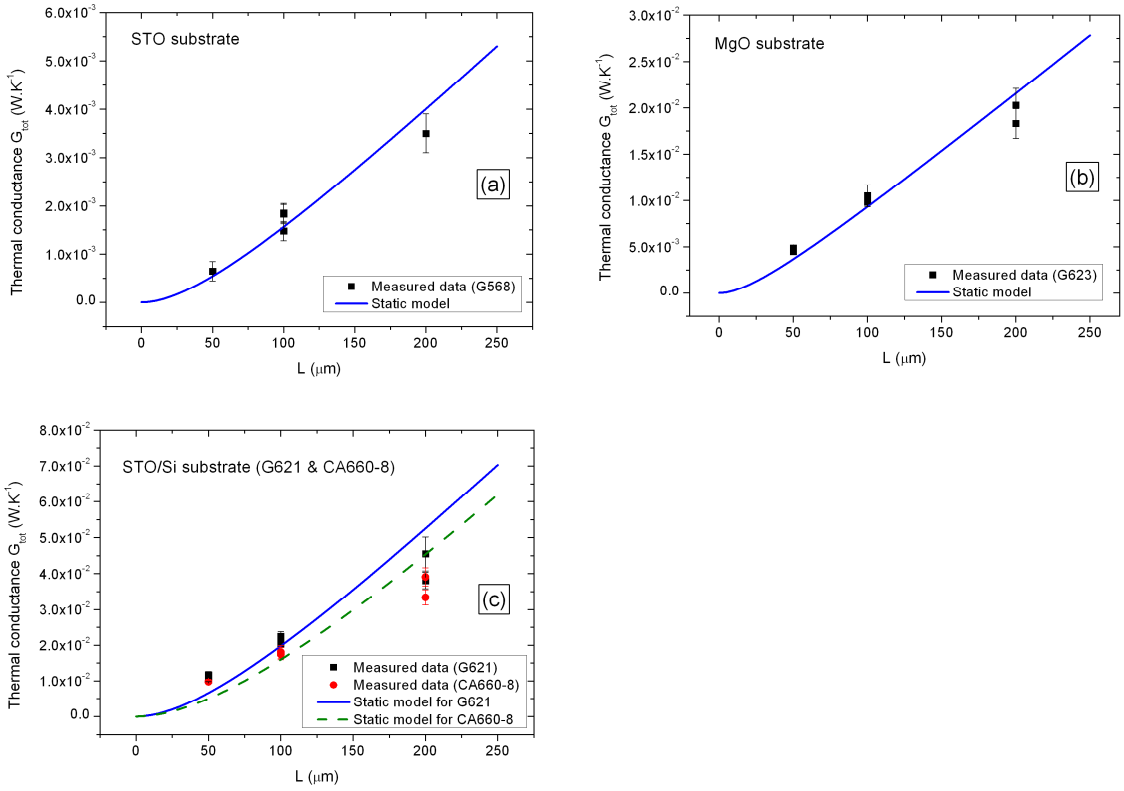

Figure 3-36. The total static thermal conductance measured and calculated using equation (III- 31) at 300 K for STO (a), MgO (b), and Si (c) substrates and for square samples

The effect of substrate is almost negligible for small sizes, near about 10 µm size. At these sizes the penetration length becomes so small and so does G_s. In other way, G_s will be no more dominant, and the total thermal conductance will be affected by both G_s and L^2/ R_{fs}.

Finally, and by using this model for the total thermal conductance of film on substrate structure, we can estimate the DC optical responsivity as a function of sample size.

3. Analysis and optimization of pixel geometry

In this section I will explore the effect of sensor pixel geometry on the performance of a bolometer, using the measurement results and calculation data issued from the proposed thermal model. The geometry parameters are pixel surface, film thickness, and number of strips. In addition, I will try to find out the benefits of the meander form in comparison with the square form of same surface.

3.1. Theoretical estimation

I will investigate in this paragraph the optimization of the main figures of merit of a thermal detector (optical responsivity $\Re_v$, thermal time constant τ_{eff}, noise equivalent power NEP, and specific detectivity D*) depending on pixel detector geometry, therefore on the parameters L, n, t_f, and on the substrate material.

In all calculations, the nominal values at 300 K for β (2% K^{-1}) and ρ (2×10^{-5} Ω·m) of LSMO material will be used. We also assumed that the film thickness equals 75 nm, the film absorption η equals 1, the temperature equals 300 K, $\alpha_H/n=10^{-30}$ m^3, and the strips spacing d equals 2 µm.

3.1.1. Optical responsivity $\Re_v$ & thermal time constant τ_{eff}

Using the basic bolometer model of a thin film on substrate, and considering the proposed model of the thermal conductance detailed in section 2, the relation of optical responsivity of a bolometer, i.e., the output signal voltage per unit incident radiated power is given by:

$$\Re_v(\omega) = \frac{\eta\, I_b\, R\ \beta}{\left(G_{tot}(\omega) - I_b^2\, R\, \beta\right)\sqrt{1+\omega^2\tau_{eff}^2}} \qquad \text{(III- 32)}$$

where R is the electrical resistance of bolometer, $\omega=2\pi f$ where f is the modulation frequency. Indeed, this relation does not present, any more, a first order system. Also, the τ_{eff} depends on the frequency, and therefore it does not present any physical meaning. The τ_{eff} is given by:

$$\tau_{eff}(\omega) = \frac{C_S(\omega)}{G_{tot}(\omega) - I_b^2\, R\, \beta} \qquad \text{(III- 33)}$$

where $C_S(\omega)=c_p\, \rho_v\, A_f\, L_p$ is the substrate thermal capacity, which depends on ω because the heated volume depends on the thermal diffusion length, L_p, which in turn depends on f, as explained in paragraph 2.5 of this chapter.

Therefore, to get higher responsivity, higher R, lower G_{tot}, and maximum allowed I_b are required. A bolometer with positive TCR can be current biased if this current does not exceed certain value called optimal current I_{opt} (cf. equation (I-22) in chapter I). Therefore, the optimum responsivity, for which $I_b=I_{opt}$, can be presented as follows,

$$\Re_{v-opt}(\omega) = \frac{\eta\sqrt{0.3\, R\ \beta}}{\left(0.7\sqrt{G_{tot}(\omega)}\right)\sqrt{1+\omega^2\left(\frac{C_S(\omega)}{0.7\, G_{tot}(\omega)}\right)^2}} \qquad \text{(III- 34)}$$

Equation (III- 34) points out that optimum optical responsivity increases only as a square root of increasing the electrical resistance or decreasing the thermal conductance. Therefore, we can extract the DC optimum responsivity as given in equation (III- 35).

$$\Re_{v-opt}(0) = \eta.\ \frac{\sqrt{0.3\, R\, \beta}}{\left(0.7\sqrt{G_{tot}(0)}\right)} \qquad \text{(III- 35)}$$

Using equations (III- 3), (III- 31**)**, and (III- 35), the developed DC optimum responsivity can be given as:

$$\Re_{v-opt}(0) = \frac{\eta\sqrt{0.3\,\beta\,\rho}}{(0.7)\sqrt{t_f}} \times \sqrt{n\left[\frac{L(n-2)+3(n-1)d}{L-(n-1)d}+1.12\right]} \times \sqrt{\frac{R_{fs}\,\kappa_s\sqrt{2\pi}+L}{L^2\,\kappa_s\sqrt{2\pi}}} \qquad \text{(III- 36)}$$

This relation proposes that $\Re_{v\text{-}opt}(0)$ decreases as function of L and square root of t_f, and increases for higher n. Figure 3-37(a) shows the variation of the DC optimum optical responsivity as a function of pixel size (L) for three values of number of strips, n (3, 5, 7) using STO substrate material. It shows that lowering L value leads to achieve higher optical responsivity. Indeed, there is a practical technological limit concerning the values of L, n, d, and W. For example, for L=10 µm, n=5, and d=2 µm as minimum resolution of lithography, then the strip width W=0.4 µm which is not realizable practically for the resolution limit reason (W must be equal to or higher than 2 µm).

To clarify the role of substrate material on the DC optimal responsivity I will plot, as seen in Figure 3-37(b), the calculated $\Re_{v\text{-}opt}(0)$ for the three substrate materials, with the number of strips, n, equals 5.

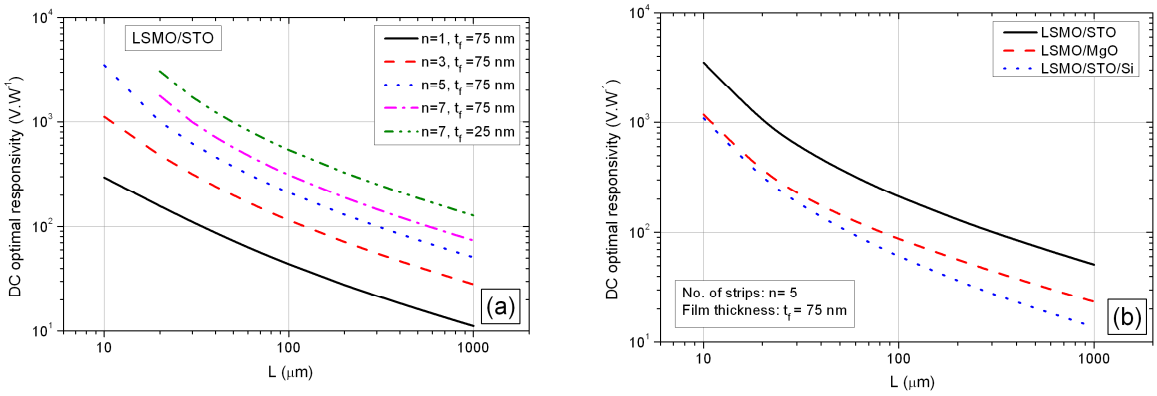

Figure 3-37. The calculated DC optimal responsivity versus pixel size, L, for (a) square and meander geometries with n number of strips and STO substrate material, (b) for 5 strips and 75 nm film thickness, and for the three types of substrate materials

The calculated optimal DC responsivity increases by increasing the number of strips n, because this increases the electrical resistance of a fixed surface pixel (L×L). Another way to increase the electrical resistance, and so the optimal responsivity, is to decrease the film thickness (t_f). In addition, to achieve higher responsivity a substrate material with lower thermal conductivity should be used, which is the case of STO. The convergence between MgO and STO/Si graphs for lower value of L is related to the fact that R_{fs} is no longer

negligible (cf. equation (III- 36)), and that R_{fs} has almost the same value for these substrate materials (cf. Table 3-8).

From equation (III- 34) we can figure out the effective thermal time constant at the optimal bias current, which is written as,

$$\tau_{eff-opt}(\omega) = \frac{C_s(\omega)}{0.7\ G_{tot}(\omega)} \qquad \text{(III- 37)}$$

Indeed, both the thermal capacity of heated volume, C_s (cf. equation (III- 25)), and the total thermal conductance, G_{tot} (cf. equation (III- 30)), depend on the frequency. Then $\tau_{eff-opt}$ depends on the frequency, therefore it has no physical meaning. The frequency where $\tau_{eff-opt}$ decreases rapidly is the critical frequency f_{cr} (cf. paragraph 2.6 and Table 3-5). Given that the value of response time estimated from the optical responsivity at -3dB (τ_{-3dB}) too is smaller than f_{cr} (cf. Table 3-5 and Table 3-9), therefore, $\tau_{eff-opt}$ can be considered as almost invariable versus frequency. This way, by using the static model for C_s and G_{tot}, the relation of $\tau_{eff-opt}$ can be given as,

$$\tau_{eff-opt}(f < f_{cr}) = \frac{C_s(0)}{0.7\ G_{tot}(0)} = \frac{A_f\ a\ c_p\ \rho_v}{\dfrac{0.7\ L^2}{R_{fs} + (L/\kappa_s\sqrt{2\pi})}} = \frac{L\left(R_{fs}\ \kappa_s\sqrt{2\pi} + L\right)}{0.7\ (2\pi)D} \qquad \text{(III- 38)}$$

The value of $\tau_{eff-opt}$ increases for higher L values, and decreases for substrate material with higher thermal diffusivity D (cf. Table 3-4). Also, $\tau_{eff-opt}$ is independent of the number of strips, n. This is compatible with the measured total thermal conductance presented earlier in Table 3-7.

To conclude, the model shows that minimizing pixel size leads to achieve higher DC optimal responsivity and faster response of the bolometer. Also, choosing the substrate material is a key factor for the performance of the bolometer. Higher thermal conductivity of substrate material leads to lowering the DC responsivity and achieve faster response.

3.1.2. Noise Equivalent Power & specific detectivity

There are several main noise sources which limit sensor performance: photon noise, phonon noise, thermal noise, excess (or 1/f) noise, and measuring system noise (cf. paragraph 3.5.3 of chapter I). The total noise equivalent power at the optimal bias current NEP_{opt} equals to:

$$NEP_{opt}(\omega) = \sqrt{NEP^2_{phonon-opt}(\omega) + NEP^2_{thermal-opt}(\omega) + NEP^2_{\frac{1}{f}-opt}(\omega) + NEP^2_{Amp-opt}(\omega)} \qquad \text{(III- 39)}$$

At the optimal bias current, the noise equivalent power for phonon fluctuations is given by:

$$NEP_{phonon-opt}(\omega) = \sqrt{4\, k_B T^2 \times 0.7 G_{tot}(\omega)} \qquad \text{(III- 40)}$$

The $NEP_{phonon-opt}$ is proportional to the square root of the total thermal conductance of film-on-substrate structure (G_{tot}) in the pass-band frequencies.

Using the optimal responsivity equation (III- 34), we can extract the thermal NEP at the optimal bias current, as follows:

$$NEP_{thermal-opt}(\omega) = \frac{0.7\ \sqrt{4\, k_B\, T\, G_{tot}(\omega)}}{\eta\ \sqrt{0.3\ \beta}}\ \sqrt{1 + \omega^2 \left(\frac{C_S(\omega)}{0.7\ G_{tot}(\omega)}\right)^2} \qquad \text{(III- 41)}$$

Equation (III- 41) points out that $NEP_{thermal-opt}$ is independent of the sample electrical resistance value, and decreases (in the pass-band frequencies) as a square root of G_{tot} with respect to the optimal bias current.

Using the optimal responsivity equation (III- 34) and $V=(0.3G_{tot}R/\beta)^{-1/2}$ at the optimal bias current, we can extract the corresponding 1/f noise equivalent power, as follows:

$$NEP_{\frac{1}{f}-opt}(\omega) = \frac{0.7\ G_{tot}(\omega)\ \sqrt{\alpha_H / n}}{\eta\ \beta \sqrt{\Omega\, f}}\ \sqrt{1 + \omega^2 \left(\frac{C_S(\omega)}{0.7\ G_{tot}(\omega)}\right)^2} \qquad \text{(III- 42)}$$

Equation (III- 42) points out that corresponding $NEP_{1/f\text{-}opt}$ increases with increasing G_{tot} at low frequencies (cf. equation (III- 30)), and decreases as a square root of the sample film volume (Ω). Also, it is independent of the sample electrical resistance value.

Figure 3-38 shows the graph of each NEP type and the total NEP as function of pixel size (L) at 30 Hz, 300 K, n=5, and by using the nominal values. Indeed, the NEP of the measurement system has been neglected since, at 30 Hz, it shows a white noise equivalent to that of about 1.2 kΩ electrical resistance, which could be ignored in comparison with that of sample resistance (about 6 kΩ).

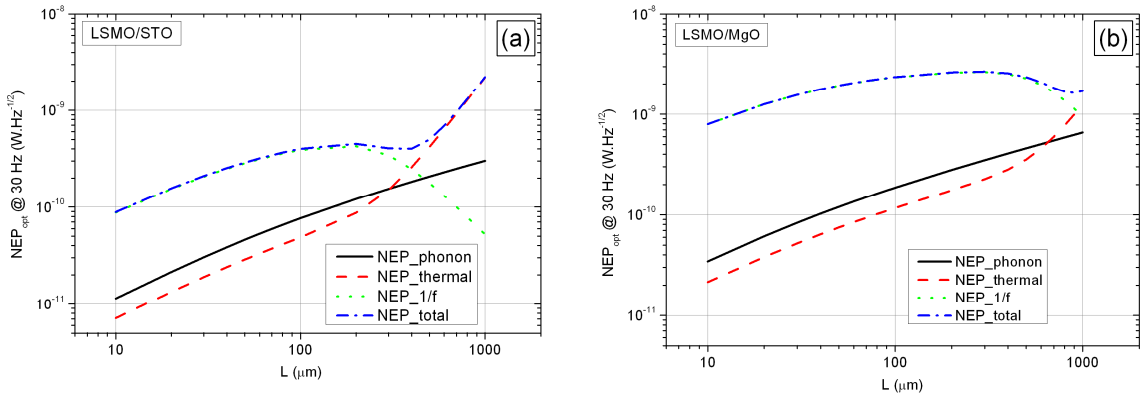

Figure 3-38. The calculated total NEP (at 30 Hz, I_{opt}, 300 K) versus pixel size for STO (a) and MgO (b) substrate material, and for an nominal LSMO material

As we can see from this graph, the total calculated NEP increases with increasing L. In addition, also notable in the latter relations, $NEP_{1/f}$ is the dominant one. But for high value of L the $NEP_{thermal}$ will be the dominant one, especially for STO substrate.

Figure 3-39(a) shows the total NEP for STO, MgO, STO/Si substrate materials at 30 Hz versus L, and Figure 3-39(b) shows the total NEP at 30 Hz for L=50µm and n=5 for STO, MgO, and STO/Si substrate materials. This identifies the role of the substrate material on the total NEP. We note that, globally, the NEP increases for material having higher thermal conductivity (cf. Table 3-4), especially at low frequencies. Hence, the STO substrate seems to be the best choice.

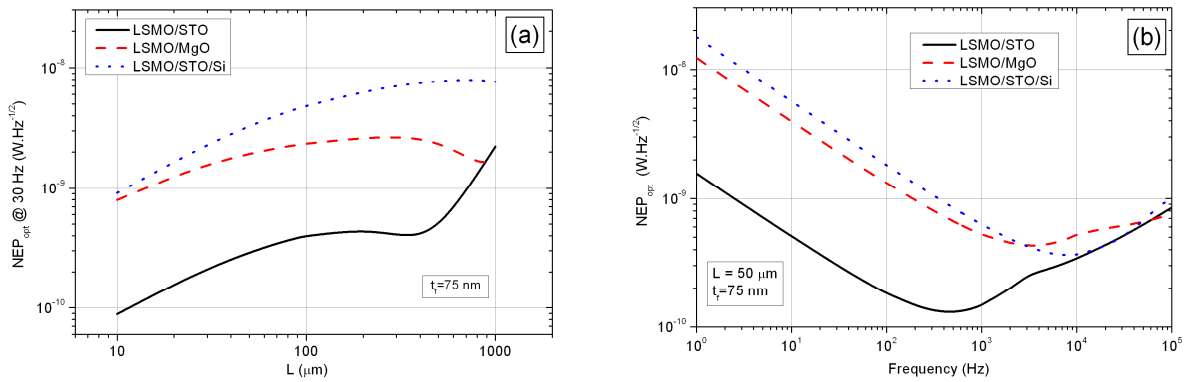

Figure 3-39. (a) The calculated total NEP_{opt} (at 30 Hz, 300 K, t_f=75 nm, and I_{opt}) versus L for an nominal LSMO film on the three substrate materials, (b) The total NEP_{opt} (L=50µm, 300 K, t_f=75 nm, and I_{opt}) versus the modulation frequency for the three substrate materials

Finally, minimizing the pixel size with reducing the 1/f noise and using substrate material having lower thermal conductivity value will provide an optimal NEP performance at low frequency (30 Hz). In addition, a 10^{-10} W·Hz$^{-1/2}$ NEP value could be achieved by these 1/f noise limited bolometers. This value is still about one order of magnitude higher than that achieved by a-Si or VO_2 (cf. Table 1-8 and Table 1-9 of chapter I) mainly because our samples have non-suspended structures.

To normalize bolometer performance per area unit, the specific detectivity D* is used (cf. paragraph 3.4.4 of chapter I). Figure 3-40 shows the specific detectivity, D^*_{opt}, at 30 Hz and I_{opt} (for increasing value of L) versus the estimated optimal response time, $\tau_{eff\text{-}opt}$, (cf. equation (III- 38)). The substrate material with the lowest thermal conductivity (which is the case of STO substrate) leads to achieve the highest D^*_{opt} up to 10^8 cm·W^{-1}·Hz$^{1/2}$. This substrate material achieves the highest D^*_{opt} but the slowest response time, of about 10 ms.

In addition, D^*_{opt} scales as the square root of $\tau_{eff\text{-}opt}$, therefore, this reveals a constant impulse detectivity D_i (cf. equation (I-32) in chapter I) of about 3×10^8 cm·J^{-1} for STO substrate.

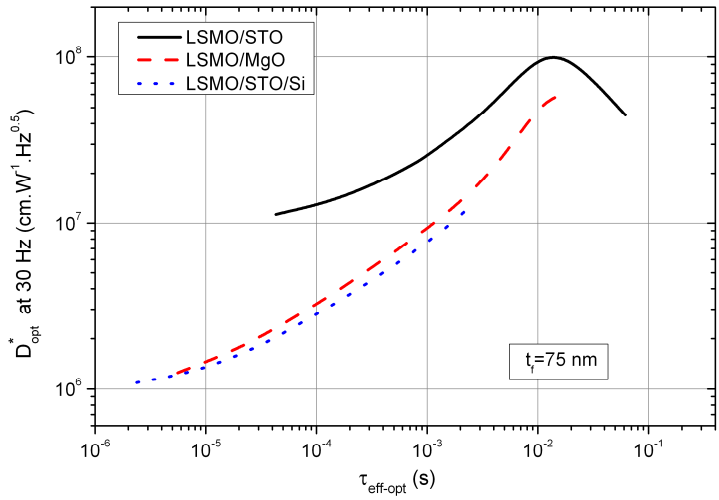

Figure 3-40. The calculated D^*_{opt} (at 30 Hz, 300 K, and I_{opt}) for increasing L values versus the optimal effective thermal time constant for the three types of substrate materials and film thickness of 75 nm

To conclude, a lower thermal conductivity substrate material achieves higher D^*_{opt} with higher τ_{-3dB_opt}. Consequently, a compromise between these two parameters must be done relatively to the substrate material to then choose the optimal pixel size L for such application. Thus, the design of bolometer with optimal performance (D*, τ) is a compromise matter between pixel size, L, and thermal properties ($c_p \times \rho_v$, κ_s) of substrate material.

3.2. Measurement analysis & comparison with the model

This paragraph focuses on analyzing the achieved measurements of detector figures of merit. Thus, the role of pixel size, number of strips, and substrate material will be explored one by one. Indeed, measurements of figures of merit have been done at a given bias current, then, and by using the extrapolation, its values at the optimal bias current were estimated. In addition, a comparison with calculation issued from the proposed model will be presented.

3.2.1. Effect of pixel surface

To compare the effect of pixel geometry (pixel size, number of strips, film thickness) and the effect of substrate material on the bolometer performance, I will summarize all relevant results in one table (see Table 3-9).

First, in this paragraph, I will deal with the effect of pixel size. I will compare three sizes: L=50, 100, 200 µm with the same number of strips, n (7 for STO substrate, and 5 for MgO and Si substrates) of LSMO samples deposited on different substrates. The presented values (last three columns) are estimated by extrapolation at the optimal bias current (I_{opt} as in paragraph 3) which is calculated using the measured values of G_{tot} and dR/dT. The NEP_{opt} and D^*_{opt} values are calculated at modulation frequency of 30 Hz.

I will discuss in the next subparagraphs all performance parameters one by one.

Table 3-9 Main estimated figures of merit for all samples on different substrates at T_{opt}

	Geometry	**L×L′(µm) n**	**G_{tot} (10^{-3} W·K^{-1})**	**τ_{-3dB} τ_{-3dB_opt} (µs)**	**$d\Re_v/dI_b$ (10^3 V·W^{-1}·A^{-1})**	**$\Re_{v\text{-}opt}$ (V·W^{-1})**	**NEP_{opt} (10^{-10} W·Hz$^{-1/2}$)**	**D^*_{opt} (10^{+6} cm·Hz$^{1/2}$·W^{-1})**
G568 (LSMO/ STO)	L50M7	50×50 7	0.7	679 969	1783	1040	3.6	11.8
	L100CR	100×100 1	1.5	3183 4534	16	47	48.3	2.1
	L100M5	100×100 5	1.9	1550 2212	131	227	11.7	8.3
	L100M7	100×100 7	1.8	1525 2178	248	318	8.0	11.8
	L200M7	200×200 7	3.5	3617 5166	133	232	11.6	16.8
G623 (LSMO/ MgO)	L50M5	50×50 5	4.9	138 197	106	280	44.2	1.0
	L50M7	50×50 7	4.5	159 227	172	394	17.2	2.5
	L100M5	100×100 5	10.3	374 534	19	102	85	1.1
	L200M5	200×200 5	20.3	965 1379	11	73	64.6	3.0
G621 (LSMO/ STO/Si)	L50M5	50×50 5	10.4	15 21	97	298	55.2	0.8
	L200M5	200×200 5	38.1	50 70	11	77	421	0.5
CA660-8 (LSMO/ STO/Si)	L50M5	50×50 5	9.8	15 21	53	224	218	0.2
G455 LSMO/ STO)	L220W20	220×110 4	3.1	7579 10824	97	228	40.0	3.4
	L300W100	300×870 8	8.1	10976 15670	20	128	33.3	14.9
CA656-7 (LSMO/ STO/Si)	L150W50	220×110 4	40.3	180 257	2	40	293	0.6
	L400W100	220×110 4	72.0	---	3	38	---	---

3.2.1.1. DC Optical responsivity

It's not directly evident to compare samples in terms of optical responsivity, since it depends on the bias current (cf. equation (III- 32)). Therefore, to eliminate the role of biasing current, I will compare the measured $d\Re_v/dI_b$ which is independent of bias current instead of the measured $\Re_v$. Table 3-9 shows clearly that we get more responsivity per bias current by minimizing L, which is consistent with theoretical calculations and model (cf. Figure 3-37). Figure 3-41 shows the variation tendency of $d\Re_v/dI_b$ as function of L. Here, it decreases for higher value of L for all substrate materials. Therefore, to get more responsivity L must be smaller (cf. equation (III- 36)). For example, $d\Re_v/dI_b$ rises by about one order of magnitude if L becomes 50 µm instead of 200 µm. This conclusion comes from the fact that smaller pixel gives higher electrical resistance, then higher dR/dT value (for β constant). But minimizing pixel size is still restricted by technological fabrication limits (resolution of lithography).

The samples G455 and CA656-7 have a rectangular form, so I calculated the equivalent square surface for each one, and then calculated the equivalent value of L.

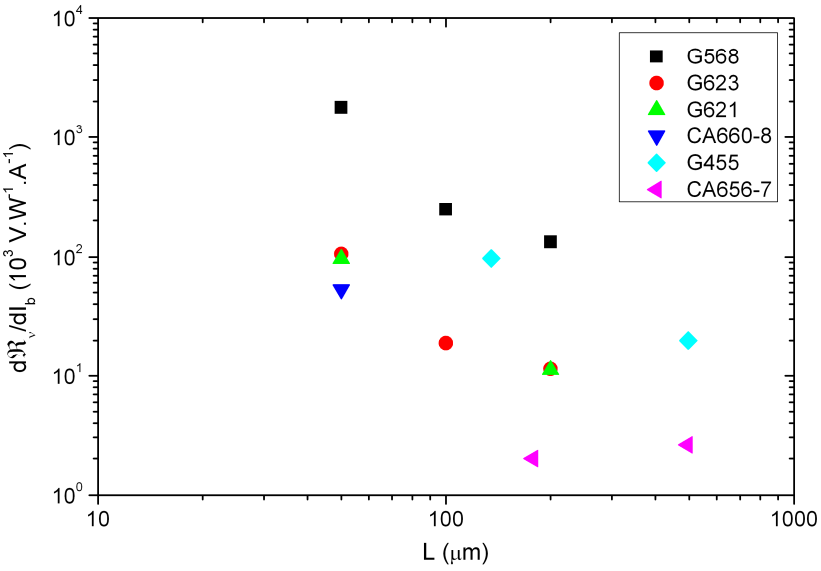

Figure 3-41. Measured optical responsivity per bias current of LSMO films versus pixel size L for different substrate materials and at T_{opt}

Another important conclusion from Table 3-9 is that the meander form pixel (L100M7) gives higher DC responsivity (in term of estimated $\Re_{v\text{-}opt}$ or measured $d\Re_v/dI_b$) in

comparison with square one (L100CR). This gives a good reason for the utility of meander pixels, but this have to be confirmed for more measurements on different substrates.

To estimate the optimal responsivity for any pixel size, we will try to validate the model relation for DC optimal responsivity. The Figure 3-42 shows the calculated $\Re_{v\text{-}opt}$ using equation (III- 35) and the estimated one using the measured $\Re_v$ (at I_b) supposing the linearity of $\Re_v$ as function of bias current, which has been verified practically for all samples. Practically, we couldn't realize measurements at the optimal current due to the limitation of readout electronics, which is related to the DC output voltage saturation (V_{out_dc}) or to the input voltage (V_i) limitation (cf. paragraph 6.4 of chapter II). This graph shows a good agreement between estimated and calculated DC optimal responsivity. The small divergence from the calculation could be related to difference between nominal and real values for TCR and ρ of LSMO film. In addition, this small divergence is also influenced by the estimation of the interface film-substrate thermal resistance, R_{fs}.

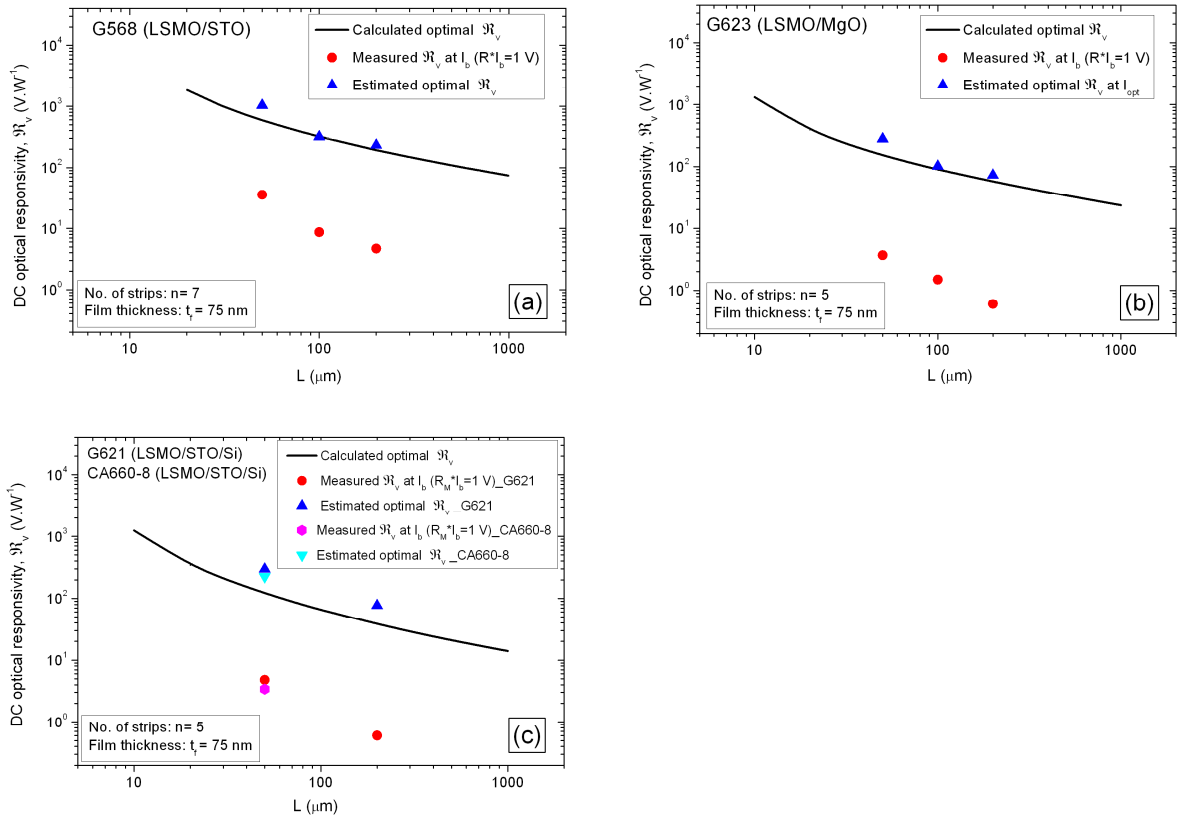

Figure 3-42. Measured, estimated and calculated DC optical responsivity at T_{opt} versus pixel size of LSMO films on STO (a), MgO (b), and Si (c) substrate materials for square samples

3.2.1.2. Response time

Using values of measured response time (τ_{-3dB}) and estimated optimal response time ($\tau_{-3dB\text{-}opt}$) from Table 3-9, and the calculated effective optimal thermal time constant ($\tau_{eff\text{-}opt}$) issued from equation (III- 38), we can plot the response time at I_{opt} versus the pixel size L for both model and measurements (see Figure 3-43).

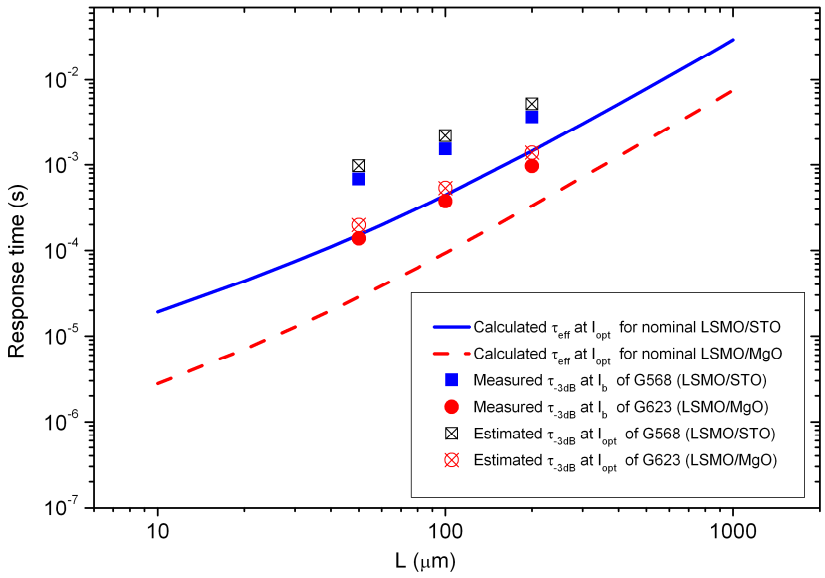

Figure 3-43. Measured and calculated response time versus pixel size L of LSMO films (of thickness 75 nm) on STO and MgO substrate materials at T_{opt} for square samples

Both, measurement and model show the same trend. The observed difference may be related to the approximation in values of C_s (cf. equation (III- 24)) and G_{tot} (cf. equation (III- 31)) at static regime. In addition, the measured values were estimated at -3dB from the frequency response (cf. Figure 3-13) but actually the system is not a true first order one (cf. equation (III- 29)).

Finally, larger pixel size achieves slower response time. Also, measurements exhibit slower response times in comparison with the model for STO and MgO substrate materials. In the case of Si substrate samples, it was not possible to estimate τ_{-3dB} due to the non bolometric contribution in the optical response (cf. Figure 3-14). Therefore, I will consider the τ_{eff} estimated from the thermal model in order to have a not so wrong estimation of the bolometer time constant (cf. Figure 3-35(d)). Thus, for samples of G621 and CA660-8, we have an

estimated response time equals to 15 µs, 50 µs, 192 µs (or 21, 70, 271 µs at I_{opt}) for 50×50 µm², 100×100 µm², 200×200 µm² sample sizes, respectively.

3.2.1.3. Noise Equivalent Power (NEP)

Figure 3-44 shows the calculated and estimated NEP at 30 Hz and at I_{opt} versus pixel sizes L for different substrates. The difference comes basically from that the value of Hooge parameter α_H/n (cf. paragraph 1.4.2) is not the same for all the samples. Therefore, knowing that the 1/f noise is dominant at 30 Hz for all samples, using the mean value of this parameter for the three pixel size (2×10^{-30} m^3 for LSMO/STO and LSMO/MgO, and 6×10^{-29} m^3 for LSMO/STO/Si) concludes to a good agreement between measurement and calculation. In addition, the TCR value is also not the same for all samples and is different from the nominal value used in calculation (2% K^{-1}). By considering all these parameters, the measured NEP is in good agreement with the calculated one. Finally, Wu [62] has reported α_H/n value equals to 2×10^{-30} m^3 for rectangular non-suspended LSMO/STO/Si sample, and Liu [10] has reported α_H/n value equals to 1×10^{-30} m^3 for suspended LSMO/STO/Si sample. This difference could be related to non-uniformity of current density in the corners of meander pattern. Therefore, improvement of NEP value of about three decades can be achieved by using the suspended structure. This is related to the lower α_H/n value and lower thermal conductance value (~10^{-6} $W\cdot K^{-1}$ for suspended structure).

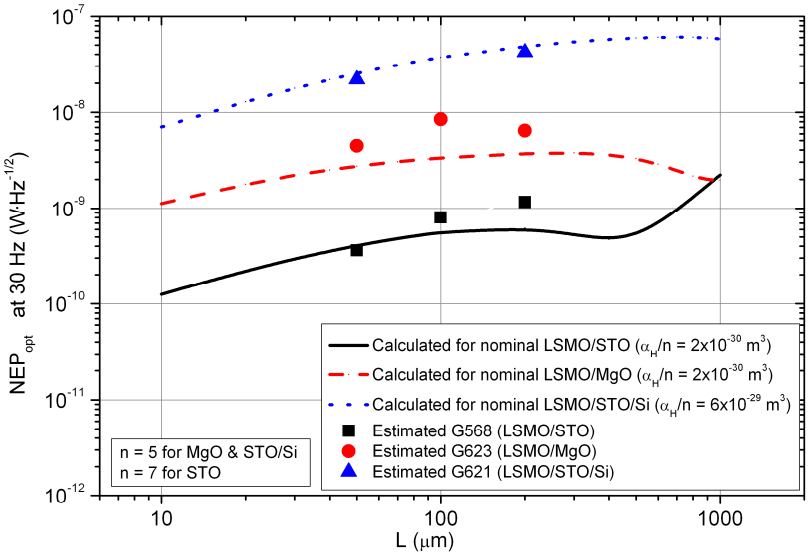

Figure 3-44. Calculated and estimated NEP_{opt} (at 30 Hz, I_{opt}, T_{opt}) versus pixel size L of LSMO film on STO, MgO, and Si substrates for square samples

3.2.1.4. Specific detectivity D*

Figure 3-45 shows the calculated and estimated values of specific detectivity at 30 Hz and I_{opt} versus pixel size for LSMO films on STO, MgO, and STO/Si substrates.

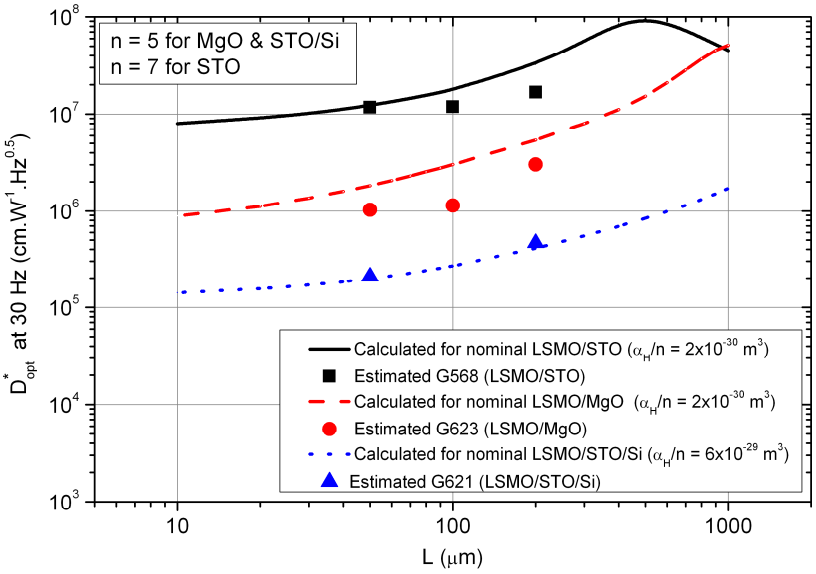

Figure 3-45. Calculated and estimated specific detectivity (at 30 Hz, I_{opt}, T_{opt}) versus pixel size for LSMO film on the different substrates for square samples

We notice that D^*_{opt} rises for higher L, with an increasing rate depending on the substrate material (or on its thermal conductivity). We get a good agreement between measurement and calculation when using α_H/n values (2×10^{-30} m^3 for LSMO/STO and LSMO/MgO, and 6×10^{-29} m^3 for LSMO/STO/Si) higher than the nominal one. Finally, the STO substrate, that has the lowest thermal conductivity, could achieve the highest specific detectivity (about 10^8 $cm\cdot W^{-1}\cdot Hz^{0.5}$ for L=500 µm). This value is of the same order of magnitude as the ones achieved by other uncooled bolometer materials (cf. Table 1-8 and Table 1-9 of chapter I) even though if our samples have non-suspended structures.

3.2.2. Effect of number of strips

Using Table 3-9 we can explore the effect of the number of strips (n) on the sample performance. Thus, we can compare the performance between samples of same substrate and same surface, but having different number of strips. For G568, we have three 100×100 µm² comparable samples: square (L100CR), 5 strips (L100M5), and 7 strips (L100M7). For G623,

we have two 50×50 µm² comparable samples: 5 strips (L50M5), and 7 strips (L50M7). Unfortunately, we did not fabricate other samples with more number of strips variations. The samples with 7 strips (G568_L100M7 and G623_L50M7) present higher DC optical responsivity in comparison with samples with 5 strips (G568_L100M5 and G623_L50M5), in terms of $d\Re_v/dI_b$ or $\Re_{v\text{-}opt}$ (see Figure 3-46(a)). Also, specific detectivity D^*_{opt} increases as a function of number of strips (see Figure 3-46(b)). It raises about one order of magnitude when the number of strips raises one order of magnitude, for G568 sample (cf. equation (III- 36)).

The response time τ_{-3dB} is still almost invariable for samples with different number of strips and same surface, since it is mainly related to the pixel volume (cf. Table 3-9). This is compatible with measurement of thermal conductance G_{tot}, which confirms that G_{tot} is almost invariable as function of the number of strips (n=3, 5, 7). Also, the heated volume, then the volume thermal capacity, is still almost constant for these values of n. This result has to be confirmed for higher values of number of strips, n, as one perspective of this work.

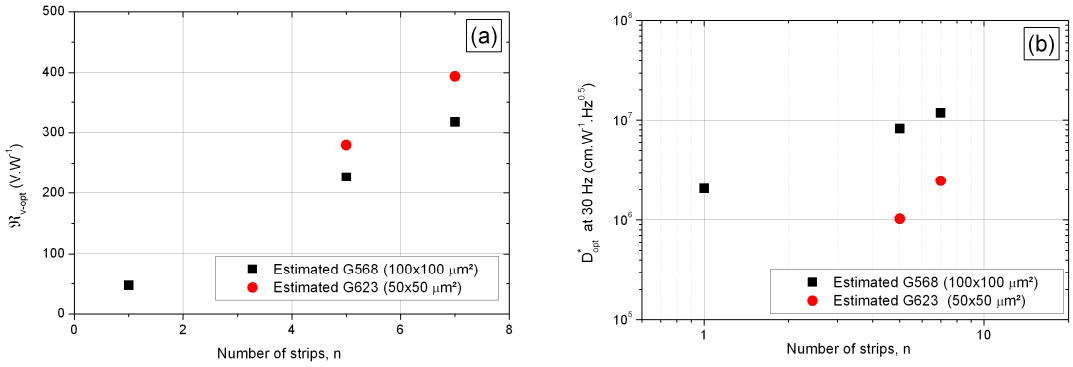

Figure 3-46. Optical responsivity (a) and specific detectivity (b) versus number on strips for LSMO film on STO and MgO substrates at I_{opt} and T_{opt}

As a conclusion, increasing the number of strips has positive effect on sample performance. But this is still limited by fabrication possibilities and maybe the noise performance. This has to be proven experimentally for higher number of strips as a perspective of this work.

3.2.3. Effect of substrate material

In this paragraph I will explore the role of substrate material on the performance of our samples in terms of detector's figures of merit. Using the Table 3-9 we can compare the performance of 50×50 µm² samples deposited on different substrates (STO, MgO, and Si).

The main difference in the substrate material properties is the thermal conductivity κ_s, which influence all figures of merit. We can conclude that higher optical responsivity is achieved by substrate material with higher thermal conductivity κ_s (STO in comparison with MgO and Si substrates), as seen in Figure 3-47(a).

The optimal specific detectivity for samples on different substrate versus response time $\tau_{-3dB-opt}$ is plotted in Figure 3-47(b). We notice that substrate material with higher thermal conductivity results in lower optimal specific detectivity but faster response (for Si substrate). These samples achieve a constant impulse detectivity D_i of about 2×10^8 cm·J^{-1} which is compatible with that achieved by the model (3×10^8 cm·J^{-1}).

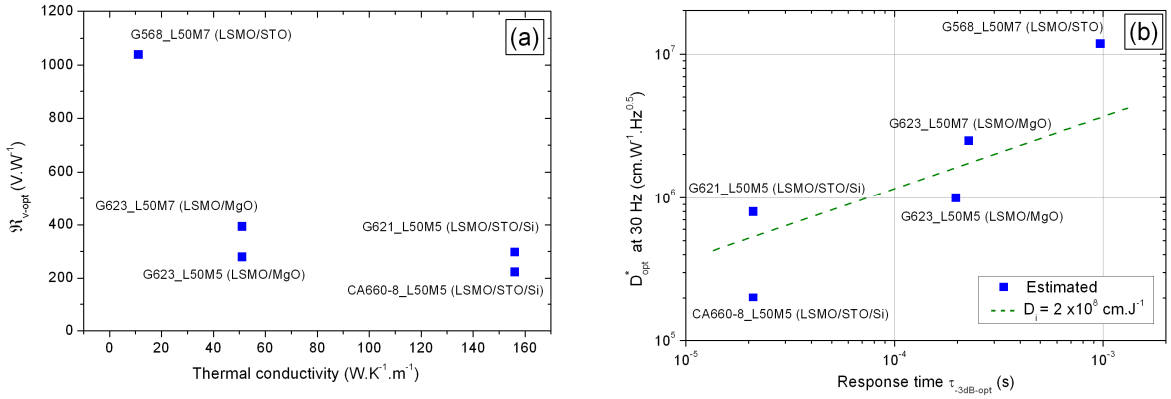

Figure 3-47. Optical DC responsivity for 50×50 µm² samples (at I_{opt} and T_{opt}) on different substrates versus substrate thermal conductivity κ_s (a) and versus thermal time constant (b)

The sample with Si substrate (CA660-8) has an optimal specific detectivity about two orders of magnitude lower than that of STO substrate (G568), but it has faster response and moderate optical responsivity (cf. Figure 3-47(b)). Indeed, the main advantage of using Si substrate is achieving the compatibility of sensor integration with the readout electronic fabrication technology. Finally, the choice of substrate, and then the compromise between specific detectivity and response speed can be done according to the final application.

3.3. Measurement results for a suspended structure

This paragraph is dedicated for presenting measurement results of the suspended structure sample CA660-22 (cf. paragraph 8.3 of chapter II). It is a suspended microbridge (length 50 µm or 100 µm, width 4 µm, thickness 75 m) of LSMO film onto STO buffered Si substrate. This sample is relevant to another research work done by S. Liu (a PhD student in

our laboratory). Suspended structure has its own model [10] which is different from non-suspended model. Figure 3-48 show the measured ρ, dR/dT, and TCR versus temperature for these two microbridges.

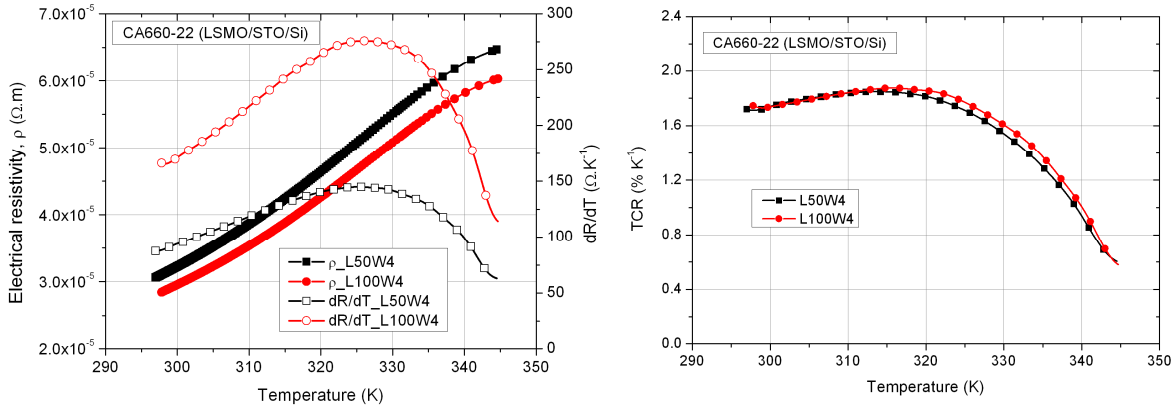

Figure 3-48. Electrical resistivity and dR/dT (a) and TCR (b) versus temperature of LSMO/STO/Si (G660-22) samples

The electrical resistivity was calculated from R-T measurement by using equation (III-3). Samples show electrical resistivity values at 300 K (cf. Table 3-10) close to nominal value (2×10^{-5} Ω·m at 300 K) for LSMO thin films [3]. This confirmed the good quality of the film.

Based on R-T measurements, Table 3-10 summarizes all the measured and calculated values of $(dR/dT)_{max}$, the optimal working temperature (T_{opt}), the TCR at T_{opt}, the maximum TCR values (TCR_{max}), and the electrical resistivity (ρ) at 300K for CA660-22 (LSMO/STO/Si) sample. The values of obtained TCR_{max} are of the same order of magnitude as the ones reported in literature (~ 2 % K^{-1}) [3][5]. These values are the same as that measured for non-suspended structure (cf. Table 3-1).

Table 3-10 The measured values issued from the R-T measurement for suspended structure samples

	Geometry	L×L′ (μm)	ρ @300K (10^{-5}Ωm)	T_{opt} (K)	$(dR/dT)_{max}$ (Ω·K^{-1})	TCR at T_{opt} (%K^{-1})	TCR_{max} (%K^{-1})	T_m (K)
CA660-22 LSMO/STO/Si	**L50W4**	50×4	3.2	325	145	1.7	1.9	315
	L100W4	100×4	3.0	325	277	1.8	1.9	316

The variation of the optical responsivity as a function of the laser power modulation frequency at different bias currents for CA660-22(L50W4) and CA660-22(L100W4) samples is shown in Figure 3-49(a), Figure 3-49(b), respectively.

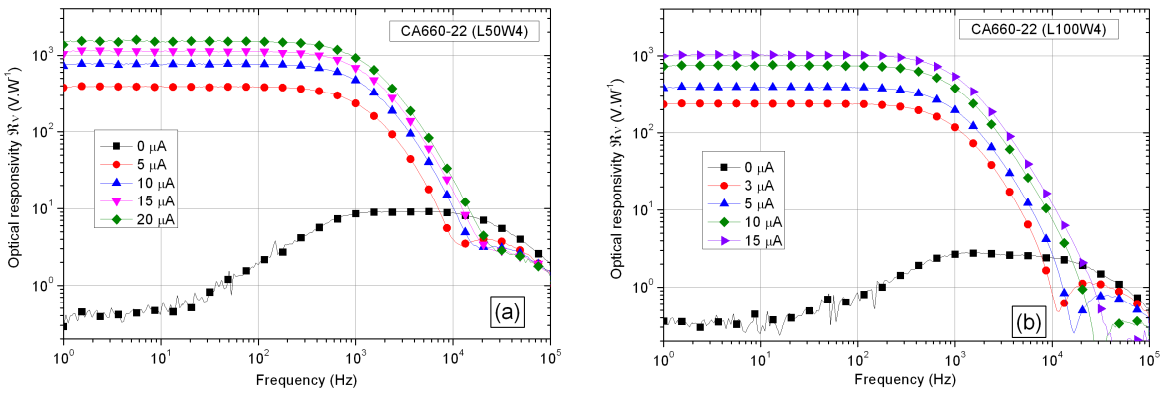

Figure 3-49. Optical responsivity at T_{opt} versus laser modulation frequency at different bias currents for CA660-22_L50W4 sample (a), and CA660-22_L100W4 sample (b)

Actually, these two samples show low pass behavior with response time at -3dB equals to 203 µs and 238 µs for L50W4 and L100W4, respectively. The measured optical responsivity shows a good linearity as a function of bias current. Moreover, the non-bolometrical behavior is also observed in suspended structure samples, but it is too small (about 1% of bolometrical response) in comparison with that observed in non-suspended structure (more that 100% of bolometrical response) samples (cf. Figure 3-15).

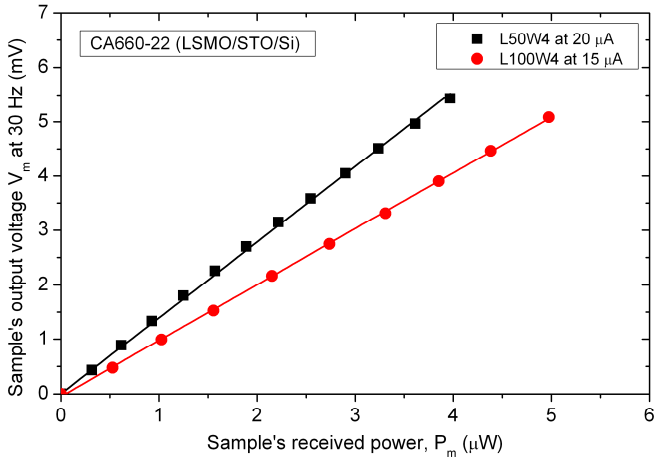

Figure 3-50. The output voltage (V_m) versus the received power (P_m) at T_{opt} and at modulation frequency 30 Hz for (a) CA660-22(L50W4) sample, (b) CA660-22(L100W4) sample. The lines are guides for the eyes

Figure 3-50 show the sample's output voltage (V_m) versus the power received by the sample (P_m) at fixed temperature (T_{opt}) and at fixed bias current (I_b). It shows that V_m increases linearly with increasing P_m at a given bias current for each sample. The slopes values are consistent with the measured optical responsivity, as seen in Figure 3-49(a) and Figure 3-49(b). Table 3-11 summarizes the main figure of merit that was measured and extrapolated (for the performance at I_{opt}) from measurements.

Table 3-11 Main measured figures of merit for suspended structure samples at T_{opt}

	Geometry	**LxL′(μm) n**	**G_{tot} (10^{-6} W·K^{-1})**	**τ_{-3dB} τ_{-3dB_opt} (μs)**	**$d\Re_v/dI_b$ (10^3 V·W^{-1}·A^{-1})**	**$\Re_{v\text{-}opt}$ (V·W^{-1})**	**NEP_{opt} (10^{-10} W·Hz$^{-1/2}$)**	**D^*_{opt} (10^{+6} cm·Hz$^{1/2}$·W^{-1})**
CA660-22 (LSMO/STO/Si)	L50W4	50×4 1	2.4	203 288	76511	7803	3.6	4.0
	L100W4	100×4 1	3.5	238 339	72287	6921	7.0	2.9

The measured optical responsivity (in terms of $d\Re_v/dI_b$) for suspended structure (CA660-22) is about three orders of magnitude higher in comparison with non-suspended one (CA660-8 and G621). This is mainly raised from the fact that a suspended structure has a thermal conductance (~10^{-6} W·K^{-1}) three orders of magnitude lower than that of non-suspended structure (~10^{-3} W·K^{-1}) [10]. Indeed, the thermal conductance Gtot has been measured using the method explained in paragraph 1.2.3 of this chapter. Globally, the NEP_{opt} for CA660-22 samples is one order of magnitude lower than that for CA660-8 and G621, consequently, the D^*_{opt} is limited to $4\times10^{+6}$ cm·Hz$^{1/2}$·W^{-1} for these samples. This is mainly related to the higher noise level observed with these samples, which comes from a very high voltage contact resistance. This drawback was resolved when using the B-mask design to fabricate suspended samples [10].

3.4. Results summary and comparison

The Figure 3-51 summarizes the specific detectivity as a function of response time for all studied samples estimated at I_{opt} and T_{opt}. Also, it shows a comparison of our results with other uncooled bolometer materials. In the case of LSMO/STO/Si (star symbol) we used the response time estimated from the model. The little dispersion of D^*_{opt} for samples on same substrate is related to the difference of number of strips (n), where it is bigger for higher values of n. The overall tendency of all samples shows that D^*_{opt} is proportional to the square

root of response time, hence, getting a fixed value of impulse detectivity (D_i). A maximum D^*_{opt} is achieved (~10^7 cm·Hz$^{1/2}$·W^{-1}) for the substrate that has the lowest thermal conductivity (case of STO) but then the slowest response time. The LSMO/STO/Si samples show the faster response with moderate specific detectivity.

The best specific detectivity achieved is about three orders of magnitude lower than that achieved by Liu for LSMO/CTO/Si with suspended structure [10]. This is mainly related to the fact that this sample used suspended structure (like all other reference samples). Then, it has a thermal conductance four orders of magnitude lower than that in our samples. Thus, by lowering the thermal conductance of our samples by using suspended structure (with a thermal conductance of about 10^{-6} W·K^{-1}), we can enhance the specific detectivity by about three orders of magnitude. Consequently, the suspended LSMO films can show D* close to that of BLIP thermal detector. We have to mention here that our samples with suspended structure did not show competitive results due to their fabrication mask which results in high noise level. This drawback was overcome using the B-mask design, as we can see in the result of Liu [10]. In other way, our results realise the faster response time, which is mainly related to the highest value of thermal conductance of the used unsuspended structure.

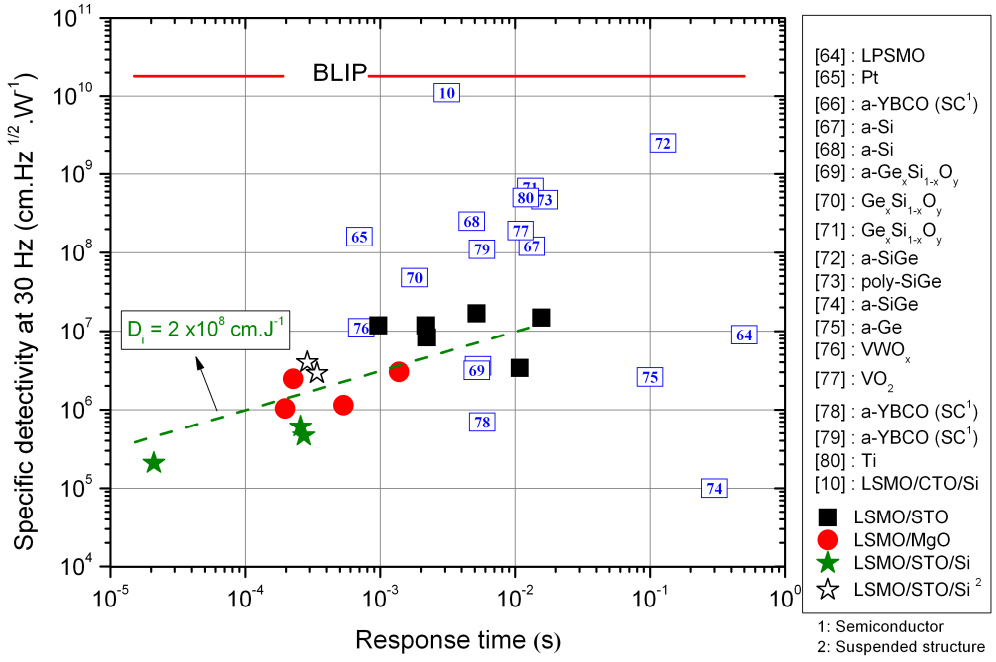

Figure 3-51. Comparison of estimated optimal specific detectivity at 30 Hz versus thermal time constant with literature values for uncooled bolometers

4. Chapter conclusion

The performance of LSMO thin films on different substrate materials, as uncooled radiation thermal detector, has been evaluated. This includes measurement of thermal and electrical parameters needed to qualify the performance of the bolometer by identifying the classical figures of merit. Then, the optical responsivity to a radiation heating source was measured, and its thermal origin also was identified. In addition, noise measurement was achieved, and then NEP and D* were evaluated. These measurements were done at one bias current, and then extrapolated at the optimal one.

The proposed thermal model for film-on-substrate structure estimates the total thermal conductance of this structure, and consequently the optical responsivity. This model shows a dependence of this thermal conductance on frequency, hence, the overall frequency response of the optical responsivity is not a simple first order system. This model shows good agreement with measurements, and explains well the variation of optical responsivity versus frequency. Then the effective thermal time constant has no more physical sense. This way, the response time was evaluated at -3dB.

The interface thermal resistance (R_{fs}) between LSMO film and substrate materials was estimated for the first time. It shows a value of 21×10^{-7}, 2.2×10^{-7}, 2.8×10^{-7} $m^2\cdot K\cdot W^1$ for STO, MgO, and STO/Si substrate materials, respectively. The presence of STO buffer layer doesn't seem to affect the value of R_{fs} between LSMO film and Si substrate. Also, the role of lattice mismatch on the interface thermal resistance is not evident.

The effect of pixel geometry on the performance of LSMO thin film bolometer, using the measurement results and model calculation data has been analyzed. In addition, the role of substrate material on this performance has been investigated. We get more optical responsivity for smaller pixel size and higher number of strips, n. In addition, the meander form pixel gives better responsivity in comparison with square one. The measured response time is almost invariable for samples with different n and same surface, since it is mainly related to the pixel volume. The fastest response time was estimated of about 20 µs for 50×50 μm^2 in the case of STO/Si substrate.

The noise measurement shows that 1/f noise is the dominant one, and a NEP value of about 10^{-10} $W \cdot Hz^{-1/2}$ for STO substrate could be achieved by these 1/f-noise limited bolometers. The specific detectivity, D*, rises for higher L values, and for higher n values. A maximum value of D* was evaluated at 30 Hz, T_{opt}, and I_{opt} of about 10^8 $cm \cdot W^{-1} \cdot Hz^{0.5}$ for STO substrate material. The NEP and D* show a good compatibility with calculation.

The role of substrate material shows that faster response is achieved by substrate materials with higher thermal conductivity, but then the responsivity and detectivity will then be smaller. The choice of substrate material, based on the compromise between detectivity and response speed, can be done according to the final application. Finally, the design of bolometer with optimal performance is mainly related to pixel size, number of strips, and thermal conductivity of the substrate material.

References for Chapter III

[1] http://cobweb.ecn.purdue.edu/~janes/EE557/Electrical_Characterization.pdf

[2] http://www.dnu.no/arkiv1/multek_pwb_designguide.pdf3.

[3] Y. Okimoto, T. Katsufuji, T. Ishikawa, T. Arima, and Y. Tokura "Variation of electronic structure in $La_{1-x}Sr_xMnO_3$ ($0 \leq x \leq 0.3$) as investigated by optical conductivity spectra", Phys. Rev. B, vol. 55, p. 4206, (1997).

[4] B. Raquet, J. Coey, S. Wirth, and S. von Molnar, "1/f noise in the half-metallic oxides CrO_2, Fe_3O_4, and $La_{2/3}Sr_{1/3}MnO_3$," Phys. Rev. B, vol. 59, pp. 12435-12443, (1999).

[5] A. Lisauskas, S. Khartsev, and A. Grishin, "Studies of 1/f Noise in $La_{1-x}M_xMnO_3$ (M= Sr, Pb) Epitaxial Thin Films," J. Low Temp. Phys., vol. 117, pp. 1647–1651, (1999).

[6] J. Dho, Y.N. Kim, Y.S. Hwang, J.C. Kim, and N.H. Hur, "Strain-induced magnetic stripe domains in $La_{0.7}Sr_{0.3}MnO_3$ thin films", Appl. Phys. Lett., vol. 82, p.1434, (2003).

[7] K. Daoudi, T. Tsuchiya, I. Yamaguchi, T. Manabe, S. Mizuta, and T. Kumagai, "Substrate effect on the temperature coefficient of resistance of $La_{0.7}Ca_{0.3}MnO_3$ thin films prepared by metal organic deposition", Journal of Electroceramics, vol. 16, pp. 527-532, (2006).

[8] J-H. Kim, A. M. Grishin, H. H. Radamson, "Properties of $La_{0.75}Sr_{0.25}MnO_3$ films grown on Si substrate with $Si_{1-x}Ge_x$ and $Si_{1-y}C_y$ buffer layers",Thin Solid Films, vol. 515, pp. 411-415, (2006).

[9] R. Prasad, H. K. Singh, M. P. Singh, W. Prellier, P. K. Siwach et al., "Thickness dependent transport properties of compressively strained $La_{0.88}Sr_{0.12}MnO_3$ ultrathin films", J. Appl. Phys., vol. 103, (2008).

[10] S. Liu, "Fabrication et caractérisation électrique et thermique de microbolomètres non refroidis suspendus à base de couches minces $La_{0.7}Sr_{0.3}MnO_3$ sur silicium", Phd thesis, university of Caen Basse-Normandie, (2013).

[11] H. Neff, "Modeling and optimization of high-T_c superconducting bolometers: The effect of film thickness", J. Appl. Phys. Vol. 69, p. 8375, (1991).

[12] T. Tsuchiya, T. Yoshitake, Y. Shimakawa, Y. Kubo, Y. Yamaguchi, T. Manabe, T. Kumagai, and S. Mizuta, "Preparation and characterization of $La_{0.8}Sr_{0.2}MnO_3$ thin films by an excimer laser mod process for a bolometer", Appl. Phys. A, Vol. 79, pp. 1537-1539, (2004).

[13] M. Rajeswari, C. H. Chen, A. Goyal, C. Kwon, M. C. Robson, R. Ramesh, T. Venkatesan, and S. Lakeou, "Low-frequency optical response in epitaxial thin films of $La_{0.67}Ca_{0.33}MnO_3$ exhibiting colossal magnetoresistance", Appl. Phys. Lett., vol. 68, p. 3555, (1996).

[14] J. H. Hao, X. T. Zeng, and H. K. Wong, "Optical response of single-crystal (La,Ca)MnO_3 thin films", J. Appl. Phys. vol. 79, p. 1810, (1996).

[15] A. Aryan, J-M Routoure, B. Guillet, P. Langlois, C. Fur, J. Gasnier, C. Adamo, D. G. Schlom and L. Méchin, "Optical Characterisation of $La_{0.7}Sr_{0.3}MnO_3$ Thin Film Based Uncooled Bolometers", IARIA Sensor Devices Proceeding, pp. 61-65, (2012).

[16] A. J. Kreisler, V. S. Jagtap, and A. F. Dégardin, "Infrared Response in the 95 to 300 K Temperature Range of Detectors Based on Oxygen-depleted Y-Ba-Cu-O Thin Films", Physics Procedia, vol. 36, pp. 223-228, (2012).

[17] B. Guillet, S. Wu, B. Cretu, R. Talmat, H. Achour, C. Barone, S. Pagano, E. Sassier, and J.M. Routoure, " Uncertainties in the estimation of low frequency noise level extracted from noise spectral density measurements", Noise and Fluctuations (ICNF) Proceeding, pp. 433-436, (2011).

[18] F. Kreith, R. M. Manglik, M. S. Bohn, "Priciple of heat transfert", 7th edition, Cengage Learning, pp. 10–90, (2011).

[19] J. H. Lienhard, "A Heat Transfer Textbook", 3rd edition, Phlogiston Press-Cambridge, pp. 4-77, (2008).

[20] T. L. Bergman, A. S. Lavine, F. P. Incropera, D. P. Dewitt, "Fundamental of Heat and Mass Transfer", 7th Edition, John Wiley & Sons, pp. 68-95, (2011).

[21] A. Bozbey, "YBCO Transition Edge Bolometers: Effect of Superconductivity Transition on the Phase and Magnitude of Response", Thesis of MS, Bilkent University, (2003).

[22] M. Nahum, S. Verghese, P. L. Richards, and K. Char, "Thermal boundary resistance for $YBa_2Cu_3O_{7-\delta}$ films", Appl. Phys. Lett., vol. 59, p. 2034, (1991).

[23] M. Kelkar, P. E. Phelan and B. Gu, "Thermal boundary resistance for thin-film high-TC superconductors at varying interfacial temperature drops", Int. J. Heat Mass Transfer. vol. 40, pp. 2631-2645, (1997).

[24] C. D. Marshall, I. M. Fishman and M. D. Fayer, "Ultrasonic wave propagation and barrier-limited heat flow in thin films of $YBa_2Cu_3O_{7-\delta}$", Phys. Rev. B, vol. 43, pp. 2696-2699, (1991).

[25] C. D. Marshall, I. M. Fishman, R. C. Dorfman, C. B. Eom and M. D. Fayer, "Thermal diffusion, interfacial thermal barrier, and ultrasonic propagation in $YBa_2Cu_3O_{7-\delta}$ thin films: Surface-selective transient-grating experiments", Phys. Rev. B, vol. 45, pp. 10009–10021, (1992).

[26] C. D. Marshall, A. Tokmakoff, I. M. Fishman, C. B. Eom, Julia M. Phillips and M. D. Fayer, "Thermal boundary resistance and diffusivity measurements on thin $YBa_2Cu_3O_{7-\delta}$ films with MgO and $SrTiO_3$ substrates using the transient grating method", J. Appl. Phys., vol. 73, p. 850, (1993).

[27] S. Zeuner, H. Lengfellner, and W. Prettl, "Thermal boundary resistance and diffusivity for YBa2Cu3O7-x films", Phys. Rev. B, vol. 51, pp. 11903–11908, (1994).

[28] Y. V. Medvedev, Y. M. Nikolaenko, A. M. Grishin, and S. I. Khartsev, "The Diagnostics of Thermal Kinetic Coefficients for the Optimization of Film Bolometer Properties", Tech. Phys. vol. 47, p.114 (2002).

[29] Y. M. Nikolaenko, Y. V. Medvedev, Y. A. Genenko, M. Ghafari, and H. Hahn, "Interface thermal resistance of nanostructured FeCoCu film and Si substrate", Phys. Stat. Sol., vol. 3, pp. 1343-1346, (2006).

[30] Y. M. Nikolaenko, Y. V. Medvedev, M. Ghafari, H. Hahn, and I. N. Chukanova, "Thermal Boundary Resistance of a Granular Film–Substrate Interface", Tech. Phys. Let., vol. 32, pp. 904-907, (2006).

[31] V. Jagtap, A. Scheuring, M. Longhin, A. Kreisler, and A. Dégardin, "From Superconducting to Semiconducting YBCO Thin Film Bolometers: Sensitivity and Crosstalk Investigations for Future THz Imagers",IEEE Transactions on Applied Superconductivity, vol. 19, pp. 287-292, (2009).

[32] H. Muta, K. Kurosaki, and S. Yamanaka, "Thermoelectric properties of reduced and La-doped single-crystalline $SrTiO_3$", J. Alloys Compd., vol. 392, p. 306, (2005).

[33] A. Durán, F. Morales, L. Fuentes, and J. M. Siqueiros, "Specific heat anomalies at 37, 105 and 455 K in $SrTiO_3$:Pr", J. Phys. Condens. Matter, vol. 20, p. 085219, (2008).

[34] Y. Suemune, "Thermal conductivity of $BaTiO_3$ and $SrTiO_3$ from 4 to 300 K", Jpn. J. Phys. Soc., vol. 20, p. 174, (1965).

[35] D-W. Oh, J. Ravichandran, C-W. Liang, W. Siemons, and B. Jalan , "Thermal conductivity as a metric for the crystalline quality of $SrTiO_3$ epitaxial layers", Appl. Phys. Lett., vol. 98, p. 221904, (2011).

[36] S. Wiedigen, T. Kramer, M. Feuchter, I. Knorr, and N. Nee, "Interplay of point defects, biaxial strain, and thermal conductivity homoepitaxial $SrTiO_3$ thin films", Appl. Phys. Lett., vol. 100, p. 061904, (2012).

[37] E. Breckenfeld, R. Wilson, J. Karthik, A. Damodaran, D. Cahill, and L. Martin, "Effect of Growth Induced (Non)Stoichiometry on the Structure, Dielectric Response, and Thermal Conductivity of $SrTiO_3$ Thin Films", Chem. Mater., vol. 24, p. 331, (2012).

[38] S. S. Todd and R. E. Lorenson, "Heat Capacities at Low Temperatures and Entropies at 298.16°K. of Metatitanates of Barium and Strontium", J. Am. Chem. Soc., vol. 74, p. 2043, (1952).

[39] A. M. Hofmeister, "Thermal diffusivity of oxide perovskite compounds at elevated temperature", J. Appl. Phys., vol. 107, p. 103532, (2010).

[40] Standard Thermodynamic Properties of Chemical Substances, CRC Press LLC, (2000).

[41] David R. Lide, ed., CRC Handbook of Chemistry and Physics, Internet version, 90th Edition, CRC Press, Boca Raton, FL., (2005).

[42] R.W. Powell, C.Y. Ho and P.E. Liley, "Thermal Conductivity of Selected Materials", NSRDS-NBS8, National Bureau of Standards Reference Data Series, (1966).

[43] G. A. Slack, " Thermal Conductivity of MgO, Al_2O_3, $MgA1_2O_4$, and Fe_3O_4 Crystals from 3 to 300°K", Phys. Rev., vol. 126, p. 427, (1962).

[44] A. C. Victor and T. B. Douglas, "Thermodynamic properties of magnesium oxide and beryllium oxide from 298 to 1200 °K" J. Res. Nat. Bur. Stand. Sec. A, Phys. Ch., vol.67A, no. 4, p. 325, (1963).

[45] K. Itatani, T. Tsujimoto, A. Kishimoto, " Thermal and optical properties of transparent magnesium oxide ceramics fabricated by post hot-isostatic pressing", J. Eur. Ceram. Soc., vol. 26, p. 639, (2006).

[46] A. Seko, F. Oba, A. Kuwabara, and I. Tanaka, " Pressure-induced phase transition in ZnO and ZnO-MgO pseudobinary system: A first-principles lattice dynamics study", Phys. Rev. B, vol. 72, p. 024107, (2005).

[47] L.-Y. Lu, Y. Chenga, X.-R. Chena, J. Zhu, "Thermodynamic properties of MgO under high pressure from first-principles calculations", Physica B, vol. 370, p. 236, (2005).

[48] C. J. Glassbrenner and G. A. Slack, "Thermal Conductivity of Silicon and Germanium from 3K to the Melting Point", Phys. Rev., vol. 134, p. A1058, (1964).

[49] B. Abklks, D. S. Bkkrs, G. D. Cody and J. P. Dismukes, "Thermal Conductivity of Ge-Si Alloys at High Temperatures", Phys. Rev., vol. 125, p. 44, (1961).

[50] L. M. Wang, J. -H. Lai, J. -L. Wu, Y. -K. Kuo, and C. L. Chang, "Effects of Ru substitution for Mn on $La_{0.7}Sr_{0.3}MnO_3$ perovskites", J. Appl. Phys., vol. 102, p. 023915, (2007).

[51] I. El-Kassab, A.M. Ahmed, P. Mandal, K. Barner, A. Kattwinkel, and U. Sondermann, "Heat conductivity of $La_{1-x}Sr_xMnO_3$ surface layers", Physica B, vol. 305, p. 233, (2001).

[52] Y. K. Kuo , R. T. Jiang , L. M. Wang, "Anomalous Behavior in Ru-doped $La_{0.7}Sr_{0.3}MnO_3$ perovskites", Chinese J. of Physics, vol. 43, p. 745, (2005).

[53] H.-Y. Lee, H.-J. Liu, C.-H. Hsu, and Y.-C. Liang, "Preparation of $La_{0.7}Sr_{0.3}MnO_3$ /$LaNiO_3$ magnetic oxide superlattice structure by rf sputtering", Thin Solid Films, vol. 494, p. 325, (2006).

[54] M. N.Khlopkin, G. Kh.Panova, A. A. Shikov, V. F. Sinyavskiĭ, and D. A. Shulyatev, "Heat Capacity of $La_{1-x}Sr_xMnO_3$ Single Crystals in Different Magnetic States", Phys. of Solid State, vol. 42, p. 114, (2000).

[55] M. Fardmanesh, "Analytic Thermal Modeling for dc to Midrange Modulation Frequency Response of Thin Film High-Tc Superconductive Edge-Transition Bolometers", Applied Optics, vol. 40, pp. 1080-1088, (2001).

[56] M. Fardmanesh, A. Rothwarf, and K. J. Scoles, "Low and Midrange Modulation Frequency Response for YBCO Infrared Detectors: Interface Effects on the Amplitude and Phase", IEEE Trans. on Appl. Supercond., Vol. 5, pp. 7-13, (1995).

[57] T-L. Hwang, S. E. Schwarz, and D. B. Rutledge, "Microbolometers for infrared detection", Appl. Phys. Lett., vol. 34**,** p. 773, (1979).

[58] Q. Hu and P. L. Richards, "Design analysis of a high Tc superconducting microbolometer", Appl. Phys. Lett., vol. 55, p. 2444, (1989).

[59] P. L. Richards, "Bolometers for infrared and millimeter waves", J. Appl. Phys., vol. 76, p. 1, (1994).

[60] S. Verghese, P. L. Richards, K. Char, and S. A. Sachtjen, "Fabrication of an infrared bolometer with a high Tc superconducting thermometer", IEEE Trans. Magn., vol. 27, pp. 3077-3080, (1991).

[61] L. Méchin, J.-M. Routoure, B. Guillet, F. Yang, S. Flament, and D. Robbes, "Uncooled bolometer response of a low noise $La_{0.7}Sr_{0.3}MnO_3$ thin film" J. Appl. Phys, vol. 87, p. 204103, (2005).

[62] L. Méchin, C. Adamo, S.Wu, B. Guillet, S. Lebargy, C. Fur, J.-M. Routoure, S. Mercone, M. Belmeguenai, and D. G. Schlom, " Epitaxial $La_{0.7}Sr_{0.3}MnO_3$ thin films thin films grown on $SrTiO_3$ buffered silicon substrates by reactive molecular-beam epitaxy", Phys. Status Solidi A, vol. 209, p. 1090, (2012).

[63] S. Wu, "Bruit basse fréquence dans des couches minces $La_{0.7}Sr_{0.3}MnO_3$ gravées: vers la réalisation de microcapteurs performants", Phd thesis, university of Caen Basse-Normandie, (2012).

[64] A. Lisauskas, S. I. Khartsev, and A. Grishin, "Tailoring the colossal magnetoresistivity: $La_{0.7}(Pb_{0.63}Sr_{0.37})_{0.3}MnO_3$ thin-film uncooled bolometer ", Appl. Phys. Lett., vol. 77, p. 756 (2000).

[65] K. C. Liddiard, "Thin Film Resistance Bolometer IR detectors", Infrared Phys., vol. 24, pp. 57-64, (1984).

[66] V. S. Jagtap, A. Scheuring, M. Longhin, A. J. Kreisler, and A. F. Dégardin, "From Superconducting to Semiconducting YBCO Thin Film Bolometers: Sensitivity and Crosstalk Investigations for Future THz Imagers", IEEE T. Appl. Supercon., vol. 19, (2009).

[67] X-M Liu, H-J Fang, and L-T Liu, "Study on new structure uncooled a-Si microbolometer for infrared detection", Microelectron. J., vol. 38, pp. 735–739, (2007).

[68] T. Ma, Y. Liu, and T. Li, "A (100) direction front-etched membrane structure for a micro-bolometer",J. Micromech. Microeng., vol. 19, p. 129901, (2009).

[69] M. M. Rana and D. P. Butler, "High responsivity a-$Si_xGe_{1-x}O_y$:H Microbolometers," IEEE Sensors J., vol. 7, pp. 1413–1419, (2007).

[70] E. Iborra, M. Clement, L.V. Herrero, and J. Sangrador, "IR uncooled bolometers based on amorphous $Ge_xSi_{1-x}O_y$ on silicon micromachined structures", J. Microelectromech. S., vol. 11, pp. 322–328, (2002).

[71] A.H.Z. Ahmed and R.N. Tait, "Characterization of an amorphous $Ge_xSi_{1-x}O_y$ microbolometer for thermal imaging applications", IEEE T. Electr. Dev., vol. 52, pp. 1900- 1906, (2005).

[72] M. Moreno**,** A. Kosarev, A. Torres and R. Ambrosio, "Fabrication and performance comparison of planar and sandwich structures of micro-bolometers with Ge thermo-sensing layer" , Thin Solid Films, vol. 515, pp. 7607-7610, (2007) .

[73] L. Dong, R. Yue, and L. Liuff, "An uncooled microbolometer infrared detector based on poly-SiGe thermistor", Sensor Actuator A, vol. 105, pp. 286–292, (2003).

[74] M. Garcia, R. Ambrosio, A. Torres, and A. Kosarev, "IR bolometers based on amorphous silicon germanium alloys", J. Non-Cryst. Solids, vol. 338–340, pp. 744–748, (2004).

[75] A. Torres, A. Kosarev, M.L. Garcia Cruz, and R. Ambrosio, "Uncooled micro-bolometer based on amorphous germanium film", J. Non-Cryst. Solids, vol. 329, pp. 179–183, (2003).

[76] N. Chi-Anh, H-J. Shin, K. Kim, Y-H. Han, and S. Moon, "Characterization of uncooled bolometer with vanadium tungsten oxide infrared active layer", Sensor Actuator A, Vol. 123–124, pp. 87-91, (2005).

[77] C. Chen, X. Yi, X. Zhao, and B. Xiong, "Characterizations of VO_2-based uncooled microbolometer linear array", Sensor Actuator A, vol. 90, pp. 212-214, (2001).

[78] A. J. Kreisler, V. S. Jagtap, and A. F. Dégardin, "Infrared Response in the 95 to 300 K Temperature Range of Detectors Based on Oxygen-depleted Y-Ba-Cu-O Thin Films", Physics Procedia, vol. 36, pp. 223-228, (2012).

[79] S. A. Dayeh, D. P. Butler, and Z. Celik-Butler, "Micromachined infrared bolometers on flexible polyimide substrates", Sensor Actuator A, vol. 118, pp. 49–56, (2005).

[80] H.K. Lee, J.B.Yoon, E. Yoon, S.B. Ju, Y.J. Yong, W. Lee and S.G. Kim, "A High Fill-Factor Infrared Bolometer using Micromachined Multilevel Electrothermal Structures", IEEE T. Electr. Dev., vol. 46, pp. 1489-1491, (1999).

CONCLUSION

GENERAL CONCLUSION

The main goal of this thesis is the characterization, geometry optimization, and thermal modeling of LSMO thin films deposited on different substrates. Therefore, I worked on the evaluation of the performance of this material used as uncooled radiation thermal detector in the near infrared wavelength. This characterization includes measurements of the electrical, thermal, and optical properties. Measurement of LSMO film electrical resistance as a function of the temperature concludes to estimate its TCR value. Also, estimate the thermal conductance is necessary since it influences the optical responsivity and response time. In addition, the optical responsivity to a radiation heating source had to be measured, then its bolometric (thermal) origin had to be identified. Furthermore, noise measurement of bolometer is also one important characteristics for sensor application since it allows the estimation of its noise equivalent power (NEP) and specific detectivity (D*) which presents the main detector's figure of merit.

The first step of this work was dedicated to design, realize, and characterize an optical and electrical measurement setup, which had the objectives to achieve trustful and repeatable measurements over a large range of frequency (1 Hz–100 kHz). It allows realizing all the characterization steps of LSMO samples as a thermal radiation detector. It employ a semiconductor laser diode (635 nm, 5 mW), with a homemade electronic driver circuit. A laser beam was used to optically heat the tested sample, after passing through a series optical elements driving the beam, by a stable electronically modulated power. The incident power on the sample can be directly measured by using a high speed photodiode. Moreover, the laser diode spot shape and size has been identified and measured.

The tested sample is glued to a copper plate, and then fixed into a vacuum chamber equipped with an optical window. The regulation of sample holder temperature was achieved by a temperature controller with stability of 15 mK, with the possibility of heating the sample in the range 300-350 K. Using a four-point electrical technique, the sample was current biased using a homemade quasi-ideal DC current source, then the output voltage of the LSMO sample was measured using a homemade voltage amplifier.

The measured electrical resistance versus temperature of the LSMO thin film samples deposited on STO and MgO substrate (using PLD technique) and on Si substrate (using MBE technique) shows a performance very close to that of un-patterned films, therefore, verify the good quality of fabrication. The measured electrical resistivity at 300 K is in the range of 1.6-

4.1 mΩ·cm, which is close to the classical reported value of 2 mΩ·cm at 300 K for LSMO thin films. Indeed, a few samples show higher resistivity values. This could be related to the quality of the film, or to the fact that the film thickness is not uniform all over the sample surface. The measured TCR values for all the studied samples are in the range 1.6% - 3.0% K^{-1}, and reach their maximum value in 300-335 K of temperature range. The obtained TCR values of the studied LSMO samples are conformed to that given in literature, which provides a typical value of 2% K^{-1}.

Measurements show that we got higher TCR value for lower lattice mismatch (δ). This way, to enhance the optical responsivity and then the NEP, it is better to choose a substrate that has lower δ with the film, as in the case of STO substrate. Another analysis shows that TCR value of the LSMO film is inversely proportional to its electrical resistivity (ρ). This result is consistent with the good quality of the film, in terms of epitaxial structure. In addition, we can notice that TCR increases for higher film thickness. This result has already been reported many times in the literature.

The frequency response of the optical responsivity shows a low-pass behavior, but the trend is different following the sample surface. In addition, the cut-off frequency depends on the sample surface and substrate material. Therefore, a basic bolometer model cannot be used to identify this behavior. The developed thermal model of thin-film-on-substrate structure analyses the heat diffusion into the substrate, taking into account the film-substrate interface. This model proposes a hemisphere contact between the film and the substrate, with a radial heat flux into substrate. The film-substrate interface thermal resistance (R_{fs}) has been estimated for the first time in LSMO thin films. It is in the order of magnitude of 10^{-7} $K \cdot m^2 \cdot W^1$ for LSMO/MgO and LSMO/Si films. The maximal values of R_{fs} is in the order of 10^{-6} $K \cdot m^2 \cdot W^1$ estimated for LSMO/STO. The role of lattice mismatch on the interface thermal resistance was not obvious. The actual value of R_{fs} depends on the surface quality of the interfaces, as well as the specific details of the deposition. The proposed model shows that the effect of substrate is almost negligible for small sizes, near about 10×10 μm^2. Hence, the substrate thermal conductance will be no more dominant, and the total thermal conductance will be more affected by the interface thermal resistance (R_{fs}).

The model of film-on-substrate structure was validated for different substrate materials. It proposes an analytical model which enables us to calculate the responsivity as a

function of modulation frequency. Model and measurements show the same frequency response trend, with a good consistence between them for STO and MgO substrate materials. The difference between model and measurement, for all frequencies, is limited to a maximum value of about 8% (or 4%) for LSMO/STO (or LSMO/MgO) 100×100 µm² samples. Actually, this comparison was not done on Si substrate due to a non bolometric contribution that mask the bolometric behavior, especially at high frequency.

The effect of sensor pixel geometry (pixel surface, number of strips, and film thickness) and the role of the substrate material (STO, MgO, Si) on the performance of a bolometer have been analyzed. The measurement of DC optical responsivity ($\Re_v$) shows that it decreases for substrate material with higher thermal conductivity and so does the specific detectivity. Thus, its value decreases from 1040, 394, to 224 $V \cdot W^{-1}$ (at I_{opt} and at 1 Hz) for 50×50 µm² LSMO/STO, LSMO/MgO, and LSMO/Si films, respectively. The measured $\Re_v$ at 1 Hz shows a good linearity relationship with the bias current. Also, a linear dependence between the sample's output voltage and the received radiated power has been clearly observed. In addition, the thermal origin of this responsivity has been verified.

The suspended structure samples shows higher optical responsivity comparing to non-suspended ones since it has a lower thermal conductivity of about four orders of magnitude. Also, the meander pixel form of LSMO/STO shows better performance in comparison with square one with same surface. On the other hand, the samples with higher number of strips show a higher optical responsivity and higher specific detectivity. The response time is still almost invariable for samples with different number of strips and same surface, since it is mainly related to the pixel volume. This is compatible with measurement of thermal conductance.

The study of the role of substrate material shows that faster response (τ_{-3dB}) is achieved by substrate material with higher thermal conductivity. Its value at I_{opt} decreases from 970, 200, to 21 µs for 50×50 µm² LSMO/STO, LSMO/MgO, and LSMO/Si films, respectively. The measurements demonstrate slower response time in comparison with calculation for STO and MgO substrate materials. This could be related to the approximation of thermal capacitance and conductance at static regime. In addition, the measured values were estimated at -3dB from the frequency response but actually the system is not a true first order. Finally, measurements and calculations show the same variation tendency, where larger pixel size achieves slower response time.

The noise measurements show that the 1/f noise is dominant at 30 Hz for all samples. The measured NEP shows a good agreement with calculated one issued from the proposed model. NEP increases for higher pixel size, for all substrate material. In other way, it increases for material having higher thermal conductivity, especially at low frequencies. Hence, the STO substrate seems to be the best choice. A value of about 10^{-10} $W \cdot Hz^{-1/2}$ could be achieved by these 1/f noise limited bolometers. This value is still about one order of magnitude lower than that achieved by a-Si or VO_2 which employ a suspended structure. Finally, minimizing the pixel size with reducing the 1/f noise and using substrate material having lower thermal conductivity value will provide an optimal NEP performance at low frequency (30 Hz).

The measured specific detectivity (D*) increases for higher pixel size, with an increasing rate depending on the substrate material. It shows a good agreement with calculation. The substrate material with lower thermal conductivity (STO material) leads to achieve the higher value of D*. We estimated a value of 2×10^7 $cm \cdot W^{-1} \cdot Hz^{1/2}$ at 30 Hz and I_{opt} for 200×200 µm² LSMO/STO sample. In contrast it achieves the slower response time, of about 5.2 ms. Consequently, a compromise between these two parameters, therefore pixel size and substrate material, will be the key factor for the intended final application. The achieved value of D* is about two orders of magnitude lower than that achieved by other uncooled bolometer materials. But by using suspended structure, LSMO shows D* value close to that of Background Limited Infrared Photodetector (BLIP).

In the case of Si substrate, the specific detectivity is limited to 0.2×10^6 $cm \cdot Hz^{1/2} \cdot W^{-1}$ but with fast response of about 21 µs and moderate responsivity of 242 $V \cdot W^{-1}$ (at I_{opt} for 50×50 µm²). This response time is comparable to that of photon detectors, therefore, LSMO/STO/Si films could be competitive candidate for applications requires moderate responsivity and fast response. The other advantage of using Si substrate is achieving the compatibility of sensor integration with the readout electronic fabrication technology, hence, using LSMO/STO/Si for thermal imaging applications. In addition, other important application could be single device non-contact thermometers (pyrometer) and non-destructive gas sensors. In this case, the suspended structure can be used since it provides better performance (about 3 orders of magnitude). Also, developing antennas coupled devices could offer the opportunity for LSMO bolometers to find application in far infrared and THz detection, where an absorbing layer is needed.

APPENDICES

Appendix A

Films deposition & properties

1. Thin film deposition conditions

The studied LSMO thin films were deposited on STO (001) and MgO (001) substrates by PLD (Pulsed Laser Deposition) technique (done by Laurence Méchin at GREYC) at temperature of 720 °C in a O_2 pressure of 0.35 mbar (*i.e.* 34.7 Pa), and on 20 nm thick STO buffered Si (001) substrates by reactive MBE (Molecular Beam Epitaxy) technique (done by C. Adamo at Cornell university - USA) at 670 °C in a distilled ozone background pressure of 5×10^{-7} Torr (*i.e.* 6.7×10^{-5} Pa). The LSMO film thickness was fixed at 100 nm for the first series and at 75 nm for the second series. Indeed, only the sample G621 of the second series was slightly different. In this sample, a 65 nm thick LSMO film was deposited by PLD on top of a 10 nm thick LSMO/20 nm STO first deposited by MBE on a high resistivity silicon substrate (ρ>1 kΩ.cm) by MBE at Cornell University [1]. All samples were epitaxially grown with (001) orientation as seen in the X-ray diffraction patterns in the θ–2θ configuration (cf. Figure I).

1.1. 1st series of 100 nm thick LSMO films (A-mask)

Figure I shows the X-ray diffraction patterns in the θ–2θ configuration of the two LSMO films of the 1st series. Table I summarizes the out-of-plane lattice parameter c_{LSMO} of LSMO films deposited on STO and on STO/Si, and c_{STO} of STO deposited on silicon. The Full Width at Half Maximum (FWHM) of the 002 LSMO peak in the ω-scan configuration is shown in Figure II.

Table I: Deposition conditions and out-of-plane lattice parameter for 100 nm LSMO films

	Substrate	Deposition technique	Temperature (°C)	Pressure (mbar)	c_{LSMO} (nm)	c_{STO} (nm)	FWHM (°)
G455	$SrTiO_3$ (001)	PLD	720	0.35	0.3856	-	0.14
CA656-7	$SrTiO_3$/Si (001)	MBE	670	6.7×10^{-7}	0.3852	0.3893	0.26

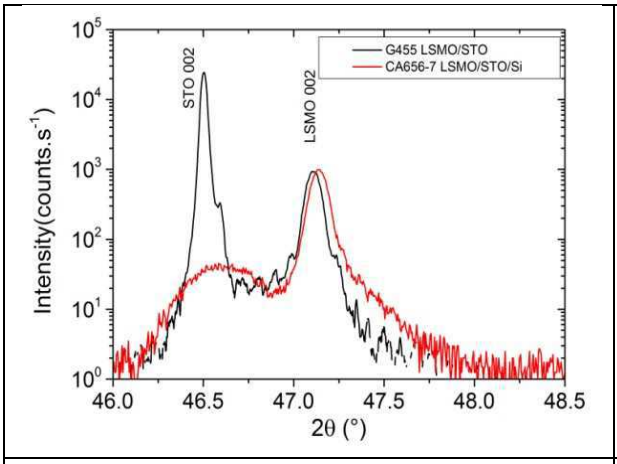

Figure I: XRD patterns in the θ–2θ configuration of the studied 100 nm thick LSMO films on STO and on STO/Si

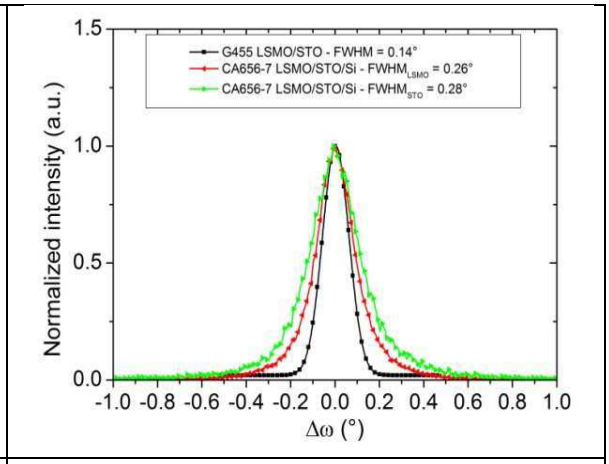

Figure II: XRD patterns in the ω–scan configuration of the studied 100 nm thick LSMO films on STO and on STO/Si

1.2. 2nd series of 75 nm thick LSMO films (B-mask)

Figure III shows the X-ray diffraction patterns in the θ–2θ configuration of the 4 LSMO films of the 2nd series. The out-of-plane lattice parameter c_{LSMO} of LSMO films deposited on STO and on STO/Si, and c_{STO} of STO deposited on silicon are reported in Table II. The value of $\varepsilon_{[001]}$ is negative on STO and on STO/Si substrates but positive on MgO substrate (cf. Table II).

The FWHM of the 002 LSMO peak in the ω-scan configuration varied from 0.10° for G568 (LSMO/STO(001)) up to 1.46° for G623 (LSMO/MgO(001)), as expected from the lattice mismatch between LSMO and these substrates (cf. Figure IV). The FWHM of the 002 LSMO peak in the ω-scan configuration for the two LSMO/STO/Si samples were very close (0.24° and 0.22°).

Table II: Deposition conditions and out-of-plane lattice parameter for 75 nm LSMO films

	Substrate	Deposition technique	Temperature (°C)	Pressure (mbar)	c_{LSMO} (nm)	c_{STO} (nm)	FWHM (°)
G568	$SrTiO_3$ (001)	PLD	720	0.35	0.3854	-	0.10
G623	MgO (001)	PLD	720	0.35	0.3893	-	1.46
G621	STO/Si (001) (ρ>1kΩ.cm)	PLD	720	0.35	0.3842	0.3891	0.24
CA660-8	STO/Si (001)	MBE	670	6.7×10^{-7}	0.3847	0.3893	0.22

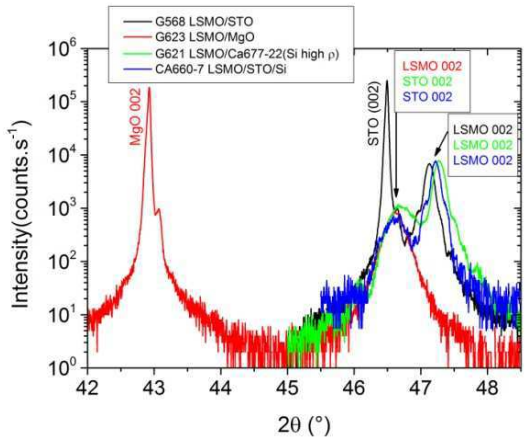

Figure III: XRD patterns in the θ–2θ configuration of the studied 75 nm thick LSMO films on STO, MgO and on STO/Si

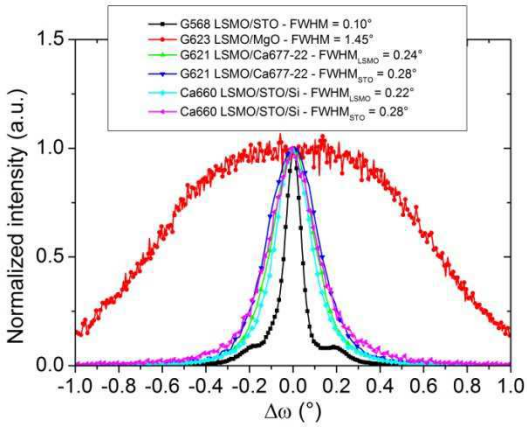

Figure IV: XRD patterns in the ω–scan configuration of the studied 75 nm thick LSMO films on STO, MgO and on STO/Si.

2. Electrical properties of the unpatterned LSMO films

2.1. 1st series of 100 nm thick LSMO films (A-mask)

Figure V shows the variation of electrical resistivity and TCR as function of temperature for 100 nm thick LSMO films of the 1st series, and Table III summarizes the main resulted values.

Table III: Electrical resistivity and TCR values for 100 nm thick LSMO thin films

	Substrate	ρ at 300 K (Ω.m)	TCR_{max} (% K^{-1})	T_m (K)
G455	$SrTiO_3$ (001)	4.0×10^{-5}	2.3	324
CA656-7	$SrTiO_3$/Si (001)	3.9×10^{-5}	2.0	314

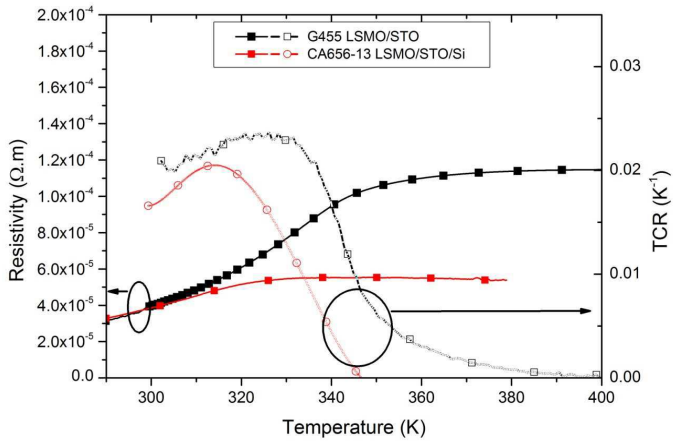

Figure V. The electrical resistivity and TCR versus temperature for unpatterned 100 nm thick LSMO films

2.2. 2nd series of 75 nm thick LSMO films (B-mask)

Figure VI shows the variation of electrical resistivity and TCR as function of temperature for 75 nm thick LSMO films of the 2nd series, and Table IV summarizes the main resulted values.

Table IV: Electrical resistivity and TCR values for 75 nm thick LSMO thin films

	Substrate	ρ at 300 K (Ω.m)	TCR_{max} (% K^{-1})	T_m (K)
G568	$SrTiO_3$ (001)	3.9×10^{-5}	2.4	325
G623	MgO (001)	7.5×10^{-5}	1.7	306
G621	$SrTiO_3$/Si (001) (ρ>1kΩ.cm)	3.5×10^{-5}	2.9	325
CA660-7	$SrTiO_3$/Si (001)	3.2×10^{-5}	1.9	316

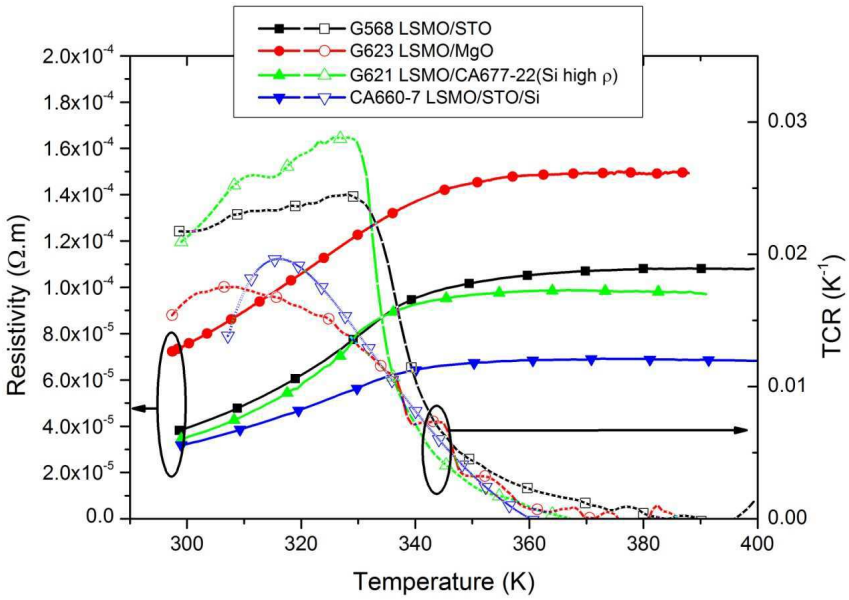

Figure VI. The electrical resistivity and TCR versus temperature for unpatterned 75 nm thick LSMO films

3. Lattice mismatch film-substrate

In order to understand the role of substrate material on the performance of LSMO film-on-substrate bolometer, we will need firstly to consider the lattice parameters for the film

and the substrate. The lattice mismatch (δ) between in-plane lattice parameters of film (a_{film}) and substrate ($a_{substrate}$) is defined as,

$$\delta = \frac{a_{substrate} - a_{film}}{a_{substrate}} \qquad \text{(A-1)}$$

Consequently, one can induce either in-plane tensile (for $\delta > 0$) or compressive (for $\delta < 0$) strain, as we can see in 0. Bulk LSMO exhibits hexagonal, orthorhombic or rhombohedral perovskitic structures. When prepared in the form of epitaxial thin films on well matched crystalline substrates such as cubic STO (with $a_{STO} = c_{STO} = 0.3905$ nm), its crystallographic structure differs from that of the bulk to become pseudo-cubic (with $a_{LSMO}=c_{LSMO}=0.3873$ nm), where "a" and "c" are the in-plane and out-of-plane lattice parameters, respectively [2].

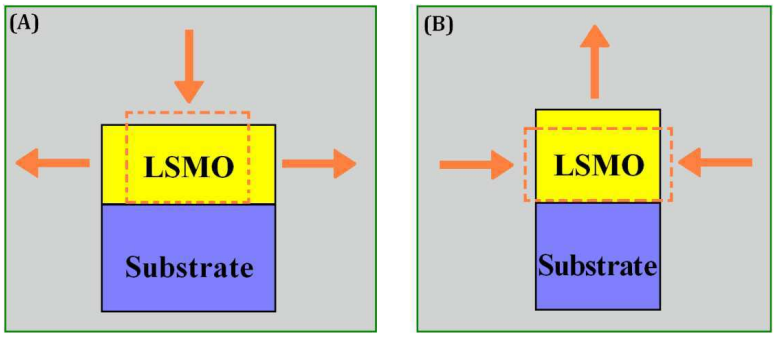

Figure VII. Tensile (A) or compressive (B) strain between LSMO film and substrate

Table V: Lattice parameter and lattice mismatch for LSMO on different substrates materials at 300 K

	Structure	**a (nm)**	**δ (%)**
LSMO film	Pseudo cubic	0.3873 [2]	---
STO substrate	Cubic	0.3905 [3]	0.82
STO film	Cubic	0.3894 [1]	0.54
MgO substrate	Cubic	0.4216 [3]	8.14
Si substrate	Cubic	0.5431	-0.85 (rotated by 45°)

The out-of-plane lattice parameter c_{LSMO} of LSMO films deposited on STO and on STO/Si, and c_{STO} of STO deposited on silicon is also reported in [1]. The measured c_{STO} value of STO was 0.3894 nm for all LSMO/STO/Si films, which gives $\delta = 0.54$ % (to be compared

with δ = 0.82 % when LSMO is deposited on STO substrates). The lattice mismatch between LSMO and substrate is then smaller on STO/Si than on STO. As expected from the positive δ values between LSMO and STO in both series of samples, LSMO films are strained showing an out-of-plane lattice parameter smaller than bulk value (i.e. an in-plane tensile strain).

4. Film patterning by photolithography

Photolithography is the basic technique usually used for the fabrication of microstructures. In other way, it is to transfer the desired film patterns on a substrate, as we can see in Figure VIII. This technique requires producing a quartz chrome mask (or plastic) representing patterns to be transferred.

After the film deposition on the substrate, a photoresist layer to ultraviolet (UV) radiation is deposited over the film uniformly. Then, it exposed through the mask using a UV lamp ($\lambda \cong 365$ nm) for a predetermined time (3 to 5 second, according to the aging of the lamp). The substrate is finally immersed into a strong base to "develop" (as in photography) the transferred image. The remaining photoresist on the film will serve as a mask for the etching step where the film pattern will be formed. The final step is to remove the remaining photoresist.

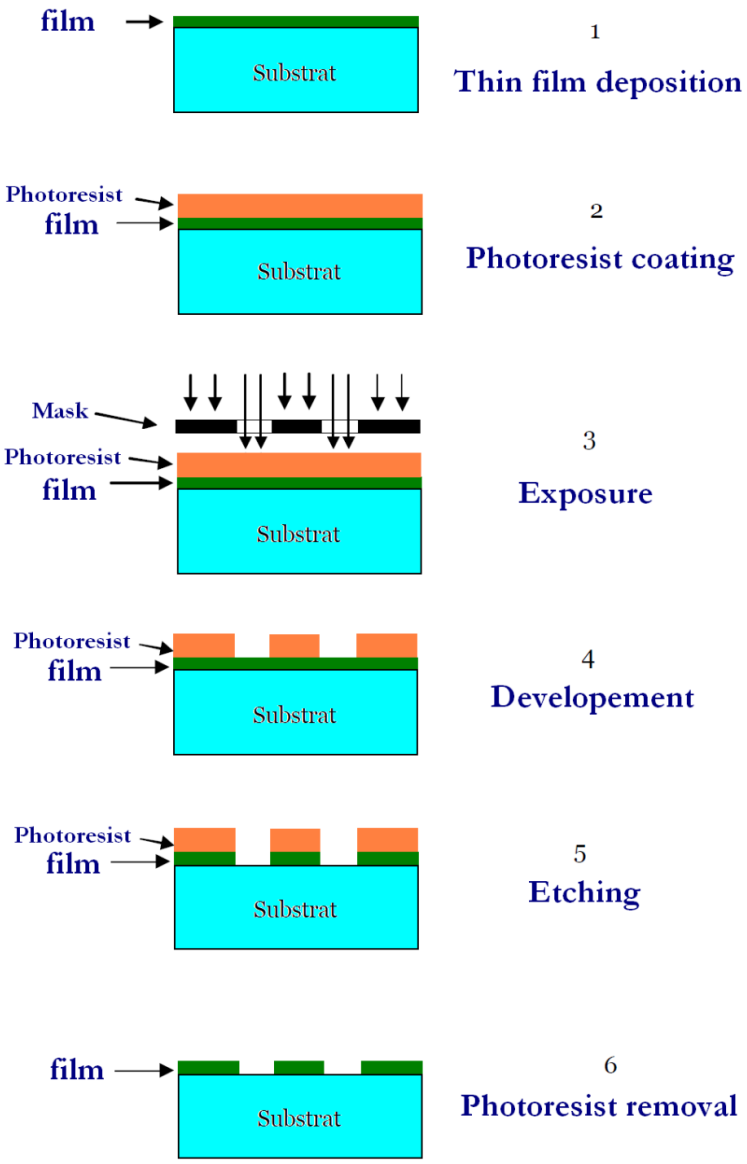

Figure VIII. Main steps of photolithography patterning

References

[1] L. Méchin, C. Adamo, S.Wu, B. Guillet, S. Lebargy, C. Fur, J.-M. Routoure, S. Mercone, M. Belmeguenai, and D. G. Schlom, ”Epitaxial $La_{0.7}Sr_{0.3}MnO_3$ thin films thin films grown on $SrTiO_3$ buffered silicon substrates by reactive molecular-beam epitaxy”, Phys. Status Solidi A,vol. 209, p. 1090, (2012).

[2] A. Hammouche, E. Siebert, A. Hammou, Mat. Res. Bull., 24 (3) 367 (1989).

[3] Société CRYSTEC GmbH, http://www.crystec.de/crystec-e.html.

Appendix B

Schematic of electronic circuits

1. Laser diode driver circuit

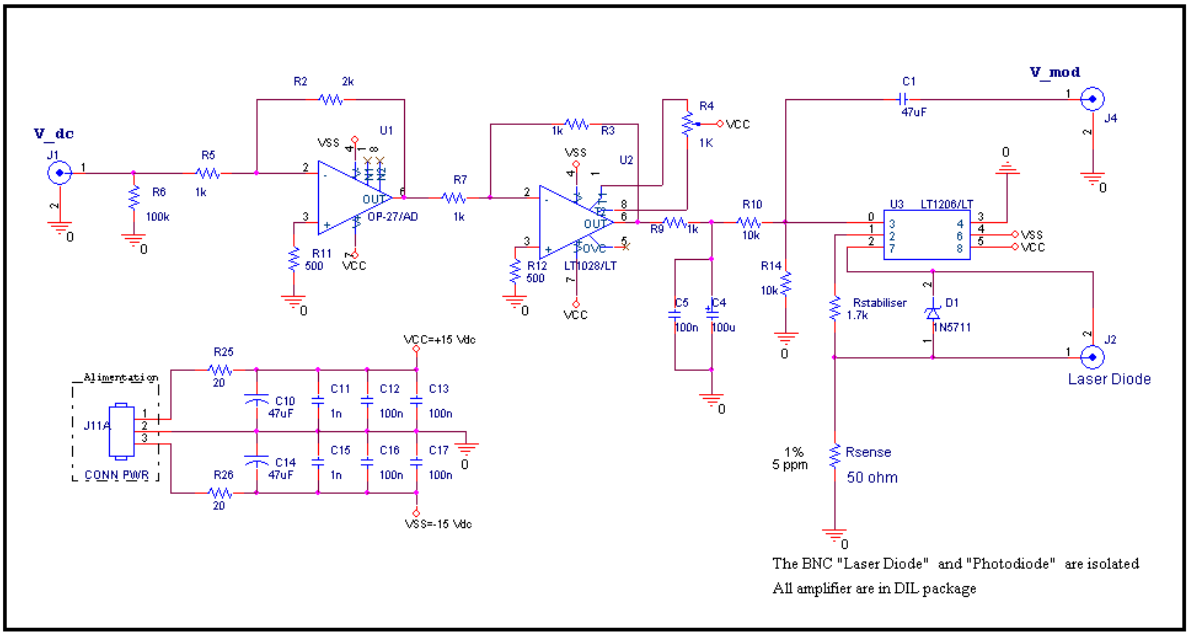

2. Photodiode I/V converter circuit

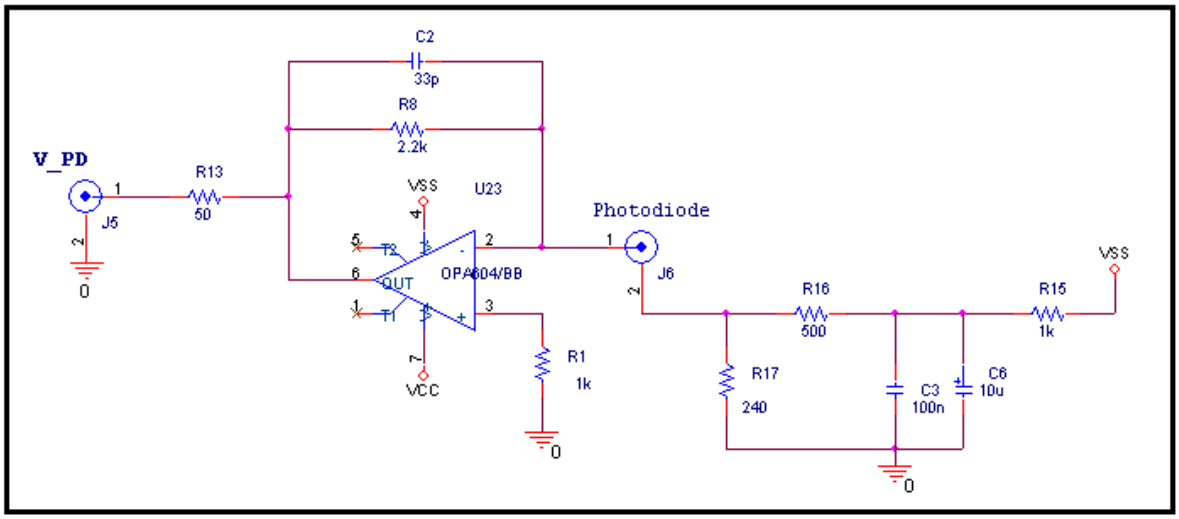

Symbols

α_s	The thermoelectric (or Seebeck) coefficient of the thermocouple [$V \cdot K^{-1}$]
α_H/n	The normalized Hooge parameter [m^3]
β	Temperature coefficient of resistance [$\%K^{-1}$]
γ	The efficiency of the laser diode [$W \cdot A^{-1}$]
δ	The lattice mismatch between in-plane lattice parameters of film and substrate [dimensionless]
η	The absorption coefficient of thermal detector material [dimensionless]
κ	The material thermal conductivity [$W \cdot K^{-1} \cdot m^{-1}$]
κ_s	The thermal conductivity of the substrate material [$W \cdot K^{-1} \cdot m^{-1}$]
λ	The wavelength [m]
λ_{max}	The wavelength at maximum radiation of a blackbody [m]
π_p	The pyroelectric coefficient [$C \cdot m^{-2} \cdot K^{-1}$]
ρ	The electrical resistivity [$\Omega \cdot m$]
ρ_v	The mass density [$kg \cdot m^{-3}$]
σ_{SB}	The Stefan-Boltzmann constant [$W \cdot m^{-2} \cdot K^{-4}$]
τ	The thermal response time of thermal detector [s]
τ_{-3dB}	The response time at -3 decibel [s]
$\tau_{-3dB\text{-}opt}$	The response time at -3 decibel at optimal bias current [s]
τ_{eff}	The effective thermal time constant [s]
$\tau_{eff\text{-}opt}$	The effective thermal time constant at optimal bias current [s]
ω	The pulsation [$rad \cdot s^{-1}$]
Ω	The real volume of the sensitive element [m^3]
Φ	The modulated radiation signal [W]
Φ_0	The maximum value of modulated radiation signal [W]
(r,θ,ϕ)	The spherical coordinate system [m, °, °]
χ	The correction factor [dimensionless]
$\Re_i$	The current optical responsivity [$A \cdot W^{-1}$]
$\Re_v$	The optical voltage responsivity [$V \cdot W^{-1}$]
a	The hemisphere radius of the contact model between the film and the substrate [m]
a_{LSMO}	The in-plane lattice parameter of LSMO film [m]
$a_{substrate}$	The in-plane lattice parameter of substrate material [m]
A	The detector element area [m^2]
A_1	The constant used to fit the transfer function of readout electronics [dimensionless]
A_2	The constant used to fit the transfer function of readout electronics [Hz]
A_3	The constant used to fit the transfer function of readout electronics [Hz]
A_f	The area of heated surface [m^2]
C	The thermal capacitance of the thermal detector [$J \cdot K^{-1}$]
C_{cu}	The heat capacity of the sample holder [$J \cdot K^{-1}$]
C_f	The heat capacity of the film material [$J \cdot K^{-1}$]
C_s	The heat capacity of the substrate material [$J \cdot K^{-1}$]
Ct1	A fitting constant [$V^2 \cdot Hz^{-1}$]
Ct2	A fitting constant [$V^2 \cdot Hz^{-1}$]
c_0	The velocity of light in vacuum [$m \cdot s^{-1}$]
c_p	The specific heat capacity at constant pressure [$J \cdot kg^{-1} \cdot K^{-1}$]
c_s	The volumetric heat capacity of the substrate material [$J \cdot K^{-1} \cdot m^{-3}$]
c_{LSMO}	The out-of-plane lattice parameter of LSMO film [m]
c_{STO}	The out-of-plane lattice parameter of STO material [m]

Symbols and Abbreviations

D	The thermal diffusivity of the material [$m^2 \cdot s^{-1}$]
d	The spacing between strips in the meander shape [m]
D*	The specific detectivity [$cm \cdot Hz^{1/2} \cdot W^{-1}$]
D^*_{BLIP}	The specific detectivity of detector limited by photon noise of the environment [$cm \cdot Hz^{1/2} \cdot W^{-1}$]
D_{1/e^2}	The beam diameter where the irradiance drop to $1/e^2$ of its maximal value [m]
D_{FWHM}	The beam diameter where the irradiance drop to the half of its maximal value [m]
D_i	The impulse detectivity [$cm \cdot J^{-1}$]
E(x,y)	The intensity or irradiance of the Gaussian laser beam [$W \cdot m^{-2}$]
E_0	The peak intensity of the Gaussian laser beam [$W \cdot m^{-2}$]
E_b (T)	The total radiation energy of a blackbody [$W \cdot m^{-2}$]
e^2_{nA}	The voltage noise spectral density of the amplification stage of the readout electronics [$V^2 \cdot Hz^{-1}$]
e^2_{nRCI}	The voltage noise spectral density of the current contact resistance [$V^2 \cdot Hz^{-1}$]
e^2_{nRCV}	The voltage noise spectral density of the voltage contact resistance [$V^2 \cdot Hz^{-1}$]
e^2_{nRm}	The voltage noise spectral density of the studied sample [$V^2 \cdot Hz^{-1}$]
e^2_{ns}	The voltage noise spectral density of the current source [$V^2 \cdot Hz^{-1}$]
e^2_{n-in}	The voltage noise spectral density at the input of the amplification stage [$V^2 \cdot Hz^{-1}$]
e^2_{n-out}	The voltage noise spectral density at the output of the amplification stage [$V^2 \cdot Hz^{-1}$]
f	The frequency [Hz]
f_{-3dB}	the cut-off frequency at -3 decibel [Hz]
f_c	The cut-off frequency of a system [Hz]
f_{cr}	the critical frequency of the substrate material [Hz]
f_L	The knee frequency of the substrate material [Hz]
G	The thermal conductance of the thermal detector [$W \cdot K^{-1}$]
G_f	The thermal conductance of the thin film [$W \cdot K^{-1}$]
G_{ac}	The gain of the alternative voltage output of the readout electronics [dimensionless]
G_{dc}	The gain of the continuous voltage output of the readout electronics [dimensionless]
G_{eff}	The effective thermal conductance of bolometer material [$W \cdot K^{-1}$]
G_s	thermal conductance of the substrate material [$W \cdot K^{-1}$]
G_{tot}	The total thermal conductance of film-on-substrate structure [$W \cdot K^{-1}$]
h	The Planck's constant [J·s]
I_+, I_-	The positive and negative current terminals of the studied sample, respectively [A]
I_b	The bias current of bolometer [A]
I_{dc}	The laser-diode's DC current needed for operation in laser emission region [A]
I_{mod}	The laser-diode's AC current used to modulate the radiated laser power of laser diode[A]
I_{emb}	The thermal runaway current [A]
I_{op}	The forward current that generate rated output power P_o [A]
I_{opt}	The optimal bias current [A]
I_{th}	The threshold current of the laser diode [A]
i^2_{ns}	The current noise spectral density of the current source [$A^2 \cdot Hz^{-1}$]
i^2_{nA}	The current noise spectral density of the measurement system amplification stage [$A^2 \cdot Hz^{-1}$]
h_c	The surface interface thermal conductance [$W \cdot K^{-1} \cdot m^{-2}$]
k_B	The Boltzmann's constant [$J \cdot K^{-1}$]
L, L'	The length and width of the sample, respectively [m]
L_P	the thermal diffusion length [m]
M(λ,T)	The spectral radiance of the electromagnetic radiation emitted by a perfect blackbody [$W \cdot m^{-3}$]
n	The number of strips in the sample [dimensionless]
N_p	The carrier number [m^{-3}]
NEP	The noise equivalent power [$W \cdot Hz^{-1/2}$]
NEP_{opt}	The noise equivalent power at the optimal bias current [$W \cdot Hz^{-1/2}$]

Symbols and Abbreviations

NEP_{phonon}	The phonon noise equivalent power [$W \cdot Hz^{-1/2}$]
$NEP_{phonon-opt}$	The phonon noise equivalent power at the optimal bias current [$W \cdot Hz^{-1/2}$]
$NEP_{thermal}$	The thermal noise equivalent power [$W \cdot Hz^{-1/2}$]
$NEP_{thermal-opt}$	The thermal noise equivalent power at the optimal bias current [$W \cdot Hz^{-1/2}$]
$NEP_{1/f}$	The 1/f noise equivalent power [$W \cdot Hz^{-1/2}$]
$NEP_{1/f-opt}$	The 1/f noise equivalent power at the optimal bias current [$W \cdot Hz^{-1/2}$]
NEP_{Amp}	The measurement system noise equivalent power [$W \cdot Hz^{-1/2}$]
$NEP_{Amp-opt}$	The measurement system noise equivalent power at the optimal bias current [$W \cdot Hz^{-1/2}$]
P_i	The incident radiation power on the sample [W]
P_J	The energy released due to the Joule heat at T temperature [W]
P_{J0}	The energy released due to the Joule heat at T_0 temperature[W]
P_{LD}	The output radiated power of laser diode [W]
P_m	The portion of incident power (P_i) that is received by the sample [W]
P_o	The rated output power of the laser diode [W]
P_{PD}	The radiated power measured by the photodiode [W]
P_{tot}	*The total power of the laser beam [W]*
q	The absorbed radiated heat flow at the surface of the sample [W]
q''	The volumetric heat generation [$W \cdot K^{-3}$]
R	The electrical resistance [Ω]
R_0	The electrical resistance that control the output bias current of the current source [Ω]
R_m	The electrical resistance of the film [Ω]
R_{CV}	The total voltage contact resistance [Ω]
R_{CV+}	The voltage contact resistance of the positive voltage pad [Ω]
R_{CV-}	The voltage contact resistance of the negative voltage pad [Ω]
R_{CI}	The total current contact resistance [Ω]
R_{CI+}	The current contact resistance of the positive current pad [Ω]
R_{CI-}	The current contact resistance of the negative current pad [Ω]
R_{sense}	The current sensing electrical resistance of the laser diode driver [Ω]
R_{bd}	The boundary resistance between two solid surfaces [$m^2 \cdot K \cdot W^{-1}$]
R_{fs}	Thermal interface resistance at the film-substrate interface [$m^2 \cdot K \cdot W^{-1}$]
R_{sc}	Thermal interface resistance at the substrate- sample holder interface [$m^2 \cdot K \cdot W^{-1}$]
R_{cu}	The thermal resistance of the sample holder, respectively [$K \cdot W^{-1}$]
R_f	The thermal resistance of the film material, respectively [$K \cdot W^{-1}$]
R_s	The thermal resistance of the substrate material, respectively [$K \cdot W^{-1}$]
S_v	The voltage noise spectral density [$V^2 \cdot Hz^{-1}$]
S_v^{therm}	The voltage thermal-noise spectral density [$V^2 \cdot Hz^{-1}$]
S_v^{phonon}	The voltage phonon-noise spectral density [$V^2 \cdot Hz^{-1}$]
$S_v^{1/f}$	The voltage 1/f noise spectral density [$V^2 \cdot Hz^{-1}$]
S_v^{Amp}	The measurement system voltage noise spectral density [$V^2 \cdot Hz^{-1}$]
T	The temperature [K]
t	The time [s]
t_f	The detector element thickness [m]
t_s	The thickness of the substrate [m]
T_0	The temperature of thermostat [K]
T_B	The background temperature [K]
T_c	The Curie temperature [K]
T_D	The detector temperature [K]
T_m	The temperature where we have a maximum of TCR [K]

T_{opt}	The optimal working temperature [K]
$TR_{C\text{-}rf}$	The transmission rate of reflected light in the cubic beam splitter [dimensionless]
$TR_{C\text{-}tr}$	The transmission rate of transmitted light in the cubic beam splitter [dimensionless]
TR_{f100}	The transmission rate of convergent lens with 100 mm focal distance [dimensionless]
TR_{f225}	The transmission rate of convergent lens with 225 mm focal distance [dimensionless]
TR_{win}	The transmission rate of the vacuum chamber window [dimensionless]
V_+ , V_-	The positive and negative voltage terminals of the studied sample, respectively [V]
V_{dc}	The DC voltage used to achieve the DC working point of the laser diode [V]
V_i	The DC voltage that control the output bias current of the current source [V]
V_I	The DC voltage equivalent to the laser diode drive current [V]
V_m	The output voltage across the film [V]
V_{mod}	The AC voltage used to achieve modulation of the laser diode [V]
V_{out_ac}	The alternative voltage output of the readout electronics [V]
V_{out_dc}	The continuous voltage output of the readout electronics [V]
V_P	The DC voltage equivalent to the power radiated by the laser diode [V]
V_{PD}	The photodiode output signal proportional to P_{PD} [V]
V_T	The DC voltage equivalent to the temperature of the laser diode box [V]
w	The beam width where the irradiance drop to $1/e^2$ of its maximal value [m]
W	The strips width of the meander shape [m]
w_x , w_y	The $1/e^2$ radius of the Gaussian laser beam in the x and y directions, respectively [m , m]
Z_s	The output impedance of the current source [$V \cdot A^{-1}$]

Abbreviations

ACC	Automatic Current Control
APC	Automatic power control
BLIP	Background Limited Infrared Photodetector
CCD	Charge Coupled Device
CMR	Colossal Magneto-Resistance
CNI	spin-canted insulator
CW	Continuous wave
dB	decibel
Erf	The error function
FI	Ferromagnetic Insulator
FM	Ferromagnetic Metal
FWHM	Full width half maximum
LAO	$LaAlO_3$
LSMO	$La_{0.7}Sr_{0.3}MnO_3$
MBE	Molecular Beam Epitaxy
NEP	Noise Equivalent Power
PI	Paramagnetic Insulator
PLD	Pulsed Laser Deposition
PM	Paramagnetic Metal
STO	$SrTiO_3$
TCC	Temperature Coefficient of Capacitance
TCR, β	Temperature Coefficient of Resistance

Titre : Bolomètres non refroidis à base de couche minces $La_{0,7}Sr_{0,3}MnO_3$: modèle thermique, caractérisations électrique et optique

Résumé
Ce travail évalue la potentialité de couches minces LSMO ($La_{0,7}Sr_{0,3}MnO_3$) déposées sur substrat comme détecteur de rayonnement à température ambiante, en exploitant la variation de sa résistance électrique au voisinage de 300 K. Un banc de mesure optique a été mise en place (conception et réalisation) pour achever cet objectif. Ce banc a été utilisé pour caractériser les échantillons LSMO comme détecteur de rayonnement bolométrique. Un modèle thermique analytique détaillé de la structure couche-mince-sur-substrat est proposé. Il interprète les variations de la sensibilité optique par rapport la fréquence de modulation de la puissance laser rayonnée. La discussion du modèle comprend la présentation de la diffusion de la chaleur dans le substrat et la résistance thermique d'interface couche-substrat. Ce modèle a été analysé et validé à l'aide des résultats de mesure de plusieurs surfaces de détection (méandre forme) pour différents matériaux de substrat. La valeur de la résistance thermique de l'interface couche-substrat a été estimée pour les différents substrats. La caractérisation de bolomètre inclut les paramètres thermiques et électriques, comme le TCR et la conductance thermique, nécessaires pour qualifier sa performance. Ainsi, la mesure et l'analyse de sensibilité optique et le bruit de plusieurs pixels surfaces sur différents substrats sont présentés. Le rôle de pixel géométrie (pixel surface, l'épaisseur du film, nombre de méandres) et le matériau de substrat ($SrTiO_3$, MgO, $SrTiO_3$/Si) sur les performances du bolomètre est étudiée, en utilisant les résultats de mesure et les données de calcul issus du modèle. La détectivité spécifique mesurée augmente pour une taille du pixel plus grand et une conductivité thermique du substrat plus petit. On estime 2×10^7 $cm\cdot W^{-1}\cdot Hz^{1/2}$ pour échantillon 200×200 µm² LSMO/STO. Pour LSMO/Si, un temps de réponse 21 µs été obtenue pour 50×50 µm², ce qui est comparable à celui des détecteurs photonique.

Mots clés: Détecteurs de rayonnement infrarouge, Oxydes de manganèse, Couches minces

---

Title: Uncooled bolometer based on $La_{0.7}Sr_{0.3}MnO_3$ thin films: Thermal model, electrical and optical characterizations

Abstract
The aim of this thesis is to evaluate LSMO ($La_{0,7}Sr_{0,3}MnO_3$) thin films deposited on substrate as room temperature radiation detector, by using the variation of its resistance electric near 300 K. An optical measurement setup has been designed and realized to achieve this objective. This setup was to characterize the LSMO samples as bolometrical radiation detector. A detailed thermal model of thin-film-on-substrate structure is proposed. It interprets the variation of the optical responsivity versus the modulation frequency of laser radiation power. The discussion of this model includes presenting the heat diffusion into substrate, and the film-substrate interface thermal resistance. This model has been analyzed and validated using the measurement results of many detection surfaces (meander shape) and substrate materials. The value of film-substrate interface thermal resistance was estimated for different substrates. The bolometer characterization includes the thermal and electrical parameters, like TCR and thermal conductance, needed to qualify its performance. Also, measurement and analysis of optical responsivity and noise for many different pixel surfaces on different substrates is presented. The role of detector geometry (pixel surface, film thickness, and number of strips) and substrate material ($SrTiO_3$, MgO, $SrTiO_3$/Si) on the bolometer performance is studied by using the measurement results and calculation data issued from the proposed model. The measured specific detectivity increases for higher pixel size and lower substrate material thermal conductivity. We estimated 2×10^7 $cm\cdot W^{-1}\cdot Hz^{1/2}$ for 200×200 µm² LSMO/STO sample. For LSMO/Si, estimation of 21 µs response time was achieved for 50×50 µm², which is comparable to that of photon detectors.

Keywords: Infrared detectors, Manganese oxides, Thin films

Université de Caen Basse-Normandie, ENSICAEN, CNRS,
GREYC- équipe électronique
6 Bd. Maréchal Juin, 14050 Caen cedex, FRANCE